

UNCLASSIFIED

AD NUMBER

AD501433

CLASSIFICATION CHANGES

TO: unclassified

FROM: confidential

LIMITATION CHANGES

TO:  
Approved for public release, distribution  
unlimited

FROM:  
Distribution authorized to U.S. Gov't.  
agencies and their contractors;  
Administrative/Operational use; Apr 1969.  
Other requests shall be referred to Air  
Force Rocket Propulsion Lab, Edwards AFB  
CA.

AUTHORITY

Apr 1981, Group 4, DoD 5200.10, 26 July  
1962; AFPRL LTR 5 FEB 1986

THIS PAGE IS UNCLASSIFIED

**CONFIDENTIAL**

**AD 501433**

**2.75-IN. FOLDING FIN AIRCRAFT ROCKET (U)**

**FINAL REPORT**

**VOLUME II**

**APPENDIXES**

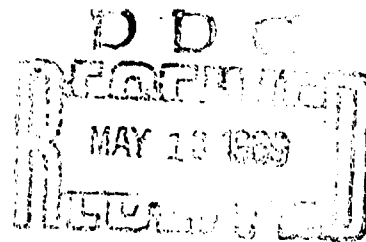
**Contract F04611-67-C-0114**

**Report AFRPL-TR-69-90**

**April 1969**

**G. Dolgonas  
H. A. Krayenbuhl**

**Reproduced From  
Best Available Copy**



**CONFIDENTIAL**

Report AFRPL-TR-69-90

2.75-IN. FOLDING FIN AIRCRAFT ROCKET (U)

FINAL REPORT

VOLUME II

APPENDIXES

Contract F04611-67-C-0114

G. Dolgonas  
H. A. Krayenbuhl

April 1969  
STATEMENT #3 ~~CONFIDENTIAL~~

In addition to security requirements which must be met, this document is subject to export controls and each transmittal to a foreign national may be made only with the approval of the "RPAIR-STINFO" Prepared for:

AIR FORCE ROCKET PROPULSION LABORATORY  
Research and Technology Division  
Edwards, California 93523

DOWNGRADED AT 5 YEAR INTERVALS;  
DECLASSIFIED AFTER 12 YEARS  
DOD DIR 5200.10

GROUP 4  
DOWNGRADED AT 3 YEAR INTERVALS; DECLASSIFIED AFTER 12 YEARS.

"THIS DOCUMENT CONTAINS INFORMATION AFFECTING THE NATIONAL DEFENSE OF THE UNITED STATES WITHIN THE MEANING OF THE ESPIONAGE LAWS, TITLE 18, U.S.C., SECTIONS 793 AND 794. ITS TRANSMISSION OR THE REVELATION OF ITS CONTENTS IN ANY MANNER TO AN UNAUTHORIZED PERSON IS PROHIBITED BY LAW."

3297

**AEROJET-GENERAL CORPORATION**  
A SUBSIDIARY OF THE GENERAL TIRE & RUBBER COMPANY

**CONFIDENTIAL**

# UNCLASSIFIED

Report AFRPL-TR-69-90

## NOTICES

In addition to security requirements which apply to this document and must be met, each transmittal outside the agencies of the U. S. Government must have prior approval of the Air Force Rocket Propulsion Laboratory.

When U. S. Government drawings, specifications, or other data are used for any purpose other than a definitely related government procurement operation, the government thereby incurs no responsibility nor any obligation whatsoever; and the fact that the government may have formulated, furnished, or in any way supplied the said drawings, specifications, or other data is not to be regarded by implication or otherwise, as in any manner licensing the holder or any other person or corporation, or conveying any rights or permission to manufacture, use, or sell any patented invention that may in any way be related thereto.

Do not return this copy. When not needed, destroy in accordance with pertinent security regulations.



# UNCLASSIFIED

Report AFRPL-TR-69-90

## FOREWORD

This report presents the results of the 2.75-inch Folding Fin Aircraft Rocket improvement program conducted for the Air Force Rocket Propulsion Laboratory by the Aerojet-General Corporation at Sacramento, California, under Contract F04611-67-C-0114. The program was administered under the direction of Captain M. P. Konieczny, RPMMA, and Mr. Lee Meyer, RPMMA, Project Officers.

The Aerojet program managers were T. Bowden and G. Dolgonas. The work reported herein was conducted from July 1967 through October 1968. This report contains no classified information extracted from other classified documents, except for performance parameters quoted from the contract statement of work. The Aerojet report number assigned to this document for local identification is 3297-01F. This technical report has been reviewed and approved by C. R. Cooke, Chief, Solid Rocket Division, Air Force Rocket Propulsion Laboratory.

UNCLASSIFIED

# UNCLASSIFIED

Report AFRPL-TR-69-90

## ABSTRACT

Contract F04611-67-C-0114 covers the design, development, testing and delivery of an improved rocket for the flechette warhead. Work included (1) design, analysis, and component tests; (2) development tests; (3) Preliminary Flight Rating Tests; and (4) delivery of improved rocket motors. Analyses included design trade-off studies, aerodynamics analysis, and manufacturing optimization studies. The improved design was successfully demonstrated through the preliminary flight rating tests and through flight tests, both ground-launched and aircraft-launched. Performance, reliability, and accuracy are within contract requirements.

This final report is in two volumes. Volume I contains the program accomplishments and Volume II contains the Appendixes.

UNCLASSIFIED

# UNCLASSIFIED

Report AFRPL-TR-69-90

## TABLE OF CONTENTS

	<u>Appendix</u>
Stability and Control	A
Stress Analysis	B
Weights and Balance	C
Environmental Test	D

UNCLASSIFIED

**UNCLASSIFIED**

Report AFKPL-TR-69-90

**APPENDIX A**

**STABILITY AND CONTROL**

**UNCLASSIFIED**

**UNCLASSIFIED**  
Report AFRPL-TR-69-90, Appendix A

Improved 2.75" FFAR  
STABILITY AND CONTROL REPORT  
Volume I

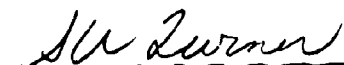
January 18, 1968

Approved:

  
A.W. Ernest, Manager  
Aerothermodynamics Dept.

  
W. Hatalaky

  
R.P. Arnold

  
S.W. Turner

SPACE DIVISION  
Aerojet-General Corporation

**UNCLASSIFIED**

# UNCLASSIFIED

Report AFRPL-TR-69-90, Appendix A

## TABLE OF CONTENTS

<u>Section</u>	<u>Page No.</u>
1.0 INTRODUCTION . . . . .	1
2.0 SUMMARY . . . . .	2
3.0 CONCLUSIONS . . . . .	3
4.0 ANALYSES AND DISCUSSION OF RESULTS . . . . .	5
4.1 GENERAL . . . . .	5
4.2 AERODYNAMICS . . . . .	7
4.2.1 Final Computer Input Data . . . . .	7
4.2.2 Symbols and Nomenclature . . . . .	7
4.2.3 Rigid Body Aerodynamics . . . . .	9
4.2.4 Loads Determination and Distribution . . . . .	18
4.2.5 Method of Analysis . . . . .	21
4.2.6 Tail Effectiveness and Variation . . . . .	22
4.2.7 Transient Effects . . . . .	24
4.2.8 References . . . . .	25
4.3 AEROELASTICITY . . . . .	26
4.3.1 Introduction . . . . .	26
4.3.2 Discussion . . . . .	26
4.3.3 Results of the Analysis . . . . .	29
4.4 AERODYNAMIC HEATING . . . . .	37
4.4.1 Introduction . . . . .	37
4.4.2 Fin Heating . . . . .	38
4.4.3 Aerothermoelastic Analysis of the Fins . . . . .	40
4.4.4 Motor Case Heating . . . . .	40
4.4.5 Aerodynamic Heating and Ablation Program . . . . .	42
4.4.6 References . . . . .	45

UNCLASSIFIED

# UNCLASSIFIED

Report AFRPL-TR-69-90, Appendix A

## TABLE OF CONTENTS - Cont'd.

<u>Section</u>	<u>Page No.</u>
5.0 APPENDICES	
5.1 PRELIMINARY ANALYSIS . . . . .	66
5.1.1 Aerodynamics . . . . .	66
5.1.2 Preliminary Aeroelasticity . . . . .	87
5.2 WIND TUNNEL TEST . . . . .	89
5.2.1 Summary . . . . .	89
5.2.2 Introduction . . . . .	89
5.2.3 Symbols and Nomenclature . . . . .	89
5.2.4 Model Description . . . . .	92
5.2.5 Run Schedule . . . . .	94
5.2.6 Basic Data Presentation . . . . .	96
5.2.7 Estimated Accuracy . . . . .	98
5.2.8 Results and Discussion . . . . .	99
5.2.9 Processed Data Presentation and Discussion . . . . .	100
5.2.10 Recommendations and Conclusions . . . . .	102
5.2.11 References . . . . .	102

## ILLUSTRATIONS

<u>Figure No.</u>		
4.1-1	2.75 FFAR Improved Configuration . . . . .	6
4.2-1	Drag Coefficient as a Function of Mach Number, Power On $S_{Ref} = 0.0412 \text{ ft}^2$ . . . . .	10
4.2-2	AEDC Wind Tunnel Test VA 0706, Normal Force Slope as a Function of Mach Number, $\alpha = -4^\circ$ to $+4^\circ$ , $\phi = 0^\circ$ . . .	11
4.2-3	AEDC Wind Tunnel Test VA 0706, Center of Pressure as a Function of Mach Number, $\alpha = -4^\circ$ to $+4^\circ$ , $\phi = 0^\circ$ . . .	12

UNCLASSIFIED

# UNCLASSIFIED

Report AFRPL-TR-69-90, Appendix A

## ILLUSTRATIONS - Cont'd.

<u>Figure No.</u>		<u>Page No.</u>
4.2-4	Tail Center of Pressure as a Function of Mach Number .	13
4.2-5	$C_{N\delta}$ Normal Force Coefficient Derivative, per radian For Two Fins in Pitch . . . . .	14
4.2-6	Roll Driving Coefficient as a Function of Mach Number .	15
4.2-7	Roll Damping Coefficient as a Function of Mach Number .	16
4.2-8	Pitch Damping Coefficient as a Function of Mach Number	17
4.2-9	Jet Damping as a Function of Time . . . . .	19
4.2-10	Body Running Load at $M = 1.4, 2.4, 3.5$ . . . . .	22
4.3-1	Load Points used for Structural Influence Coefficients	33
4.3-2	Structural Influence Coefficients L.E. Deflections due to L.E. Loads . . . . .	34
4.3-3	Fin Spanwise Load Distributions . . . . .	37
4.3-4	Flex Fin Lift/Rigid Fin Lift vs $q C_{N\alpha} \left( \frac{C_{N\alpha_F}}{C_{N\alpha_R}} \right)$	38
4.3-5	Flex Fin Normal Force/Rigid Fin Normal Force vs $q C_{N\alpha} \left( \frac{C_{N\delta_F}}{C_{N\delta_R}} \right)$ . . . . .	39
4.3-6	Flex Fin Rolling Moment/Rigid Fin Rolling Moment vs $q C_{N\alpha} \left( \frac{C_{l\delta_F}}{C_{l\delta_R}} \right)$ . . . . .	40
4.3-7	Flex Fin Rolling Moment/Rigid Fin Rolling Moment vs $q C_{l\alpha} \left( \frac{C_{l_{PF}}}{C_{l_{PR}}} \right)$ . . . . .	41
4.3-8	Total Flex Lift/Total Rigid Lift vs Mach Number $\left( \frac{C_{N\alpha_F}}{C_{N\alpha_R}} \right)$ Body + Tail . . . . .	43
4.3-9	Incremental Static Stability Margin vs Mach Number . .	44
4.3-10	Ratio of Elasticized Pitch Damping to Rigid Pitch Damping vs Mach Number . . . . .	45
4.3-11	Body Running Load at $M = 1.4, 2.4, 3.5$ . . . . .	49

UNCLASSIFIED



# UNCLASSIFIED

Report AFRPL-TR-69-90, Appendix A

## ILLUSTRATIONS - Cont'd.

<u>Figure No.</u>		<u>Page No.</u>
4.3-12	Mass Distribution . . . . .	50
4.3-13	EI Distribution . . . . .	51
4.3-14	Net Limit Maximum Aeroelastic Shear . . . . .	52
4.3-15	Net Limit Maximum Aeroelastic Bending Moment . . . . .	53
4.3-16	Net Limit Maximum Axial Load . . . . .	54
4.4-1	Fin Cross-Section Showing Temperature Points . . . . .	57
4.4-2	Temperature History for Three Fin Points . . . . .	58
4.4-3	Fin Span Temperature at Burnout . . . . .	59
4.4-4	Motor Case Temperature History . . . . .	64
 <u>Appendices</u>		
5.1.1-1	Drag Coefficient as a Function of Mach Number, Power On, $S_{Ref} = .0412 \text{ ft}^2$ . . . . .	72
5.1.1-2	Normal Force Coefficient Slope as a Function of Mach Number, $S_{Ref} = .0412 \text{ ft}^2$ . . . . .	73
5.1.1-3	Center of Pressure as a Function of Mach Number $\alpha = 0 - 4^\circ$ . . . . .	74
5.1.1-4	Tail Center of Pressure as a Function of Mach Number .	75
5.1.1-5	$C_{N\delta}$ Normal Force Coefficient Derivative, per radian For Two Fins in Pitch . . . . .	76
5.1.1-6	Roll Driving Coefficient as a Function of Mach Number .	77
5.1.1-7	Roll Damping Coefficient as a Function of Mach Number .	78
5.1.1-8	Pitch Damping Coefficient as a Function of Mach Number	79
5.1.1-9	Jet Damping as a Function of Time . . . . .	80
5.1.1-10	Transient $C_{N\alpha}$ as a Function of Mach Number . . . . .	81
5.1.1-11	Transient Center of Pressure as a Function of Mach Number . . . . .	82
5.1.1-12	Transient $C_{N\delta}$ as a Function of Mach Number . . . . .	83
5.1.1-13	Transient $C_{l\delta}$ as a Function of Mach Number . . . . .	84
5.1.1-14	Transient $C_{lp}$ as a Function of Mach Number . . . . .	85
5.1.1-15	Transient $C_{mq}$ as a Function of Mach Number . . . . .	86

UNCLASSIFIED

# UNCLASSIFIED

Report AFRPL-TR-69-90, Appendix A

## ILLUSTRATIONS - Cont'd.

<u>Figure No.</u>		<u>Page No.</u>
5.1.2-1	Stability Margin vs % Exposed Span . . . . .	88
5.2-1	2.75 FFAR Configuration Definition . . . . .	103
5.2-2	Wind Tunnel Model 2.75" Folding Fin Aircraft Rocket . .	104
5.2-3	Test Reynold's Number as a Function of Mach Number . .	105
5.2-4	Configuration 1 (Body Alone) . . . . .	106
5.2-5	Configuration 2 (Body Tail with Straight Tail Fins) M = 2.50, BT <sub>1</sub> . . . . .	107
5.2-6	Configuration 2 (Body Tail with Straight Tail Fins) M = 3.0, BT <sub>1</sub> . . . . .	108
5.2-7	Configuration 2 (Body Tail with Straight Tail Fins) M = 3.5, BT <sub>1</sub> . . . . .	109
5.2-8	Configuration 2, BT <sub>1</sub> , Mach No. 2.5 . . . . .	110
5.2-9	Configuration 2, BT <sub>1</sub> , Mach No. 3 . . . . .	111
5.2-10	Configuration 2, BT <sub>1</sub> , Mach No. 3.5 . . . . .	112
5.2-11	Configuration 3, (Body Tail with Bent Tail Fins) M = 2.5, BT <sub>2</sub> . . . . .	113
5.2-12	Configuration 3 (Body Tail with Bent Tail Fins) M = 3.0, BT <sub>2</sub> . . . . .	114
5.2-13	Configuration 3 (Body Tail with Bent Tail Fins) M = 3.5, BT <sub>2</sub> . . . . .	115
5.2-14	Configuration 3 (Body Tail with Bent Tail Fins) M = 4.02, BT <sub>2</sub> . . . . .	116
5.2-15	Configuration 3, BT <sub>2</sub> , Mach No. 2.5 . . . . .	117
5.2-16	Configuration 3, BT <sub>2</sub> , Mach No. 3 . . . . .	118
5.2-17	Configuration 3, BT <sub>2</sub> , Mach No. 3.5 . . . . .	119
5.2-18	Configuration 3, BT <sub>2</sub> , Mach No. 4.05 . . . . .	120
5.2-19	Drag Coefficient as a Function of Mach Number, Power On, S <sub>Ref</sub> = 0.0412 ft <sup>2</sup> . . . . .	121
5.2-20	Normal Force Slope as a Function of Mach Number, $\alpha = -4^\circ$ to $+4^\circ$ , $\phi = 0^\circ$ . . . . .	122
5.2-21	Center of Pressure as a Function of Mach Number, $\alpha = -4^\circ$ to $+4^\circ$ , $\phi = 0^\circ$ . . . . .	123

UNCLASSIFIED

# UNCLASSIFIED

Report AFRPL-TR-69-90, Appendix A

## ILLUSTRATIONS - Cont'd.

<u>Figure No.</u>		<u>Page No.</u>
5.2-22	Rolling Moment as a Function of Mach Number at Zero Angle of Attack . . . . .	124
5.2-23	Roll Driving Derivative as a Function of Mach Number $\alpha = 0^\circ$ . . . . .	125
5.2-24	Rolling Moment Coefficient due to Folded Tail Fin Tips as a Function of Mach Number, $\alpha = 0^\circ$ . . . . .	126

## TABLES

<u>Table No.</u>		
4.3-1	Fin Structural Influence Coefficients Angular Deflection due to a Unit Streamwise Torque . .	31
4.3-2	Fin Structural Influence Coefficients Angular Deflection Due to a Unit Load . . . . .	32

UNCLASSIFIED

# UNCLASSIFIED

Report AFRPL-TR-69-90, Appendix A

## 1.0 INTRODUCTION

The Stability and Control Report for the Improved 2.75 in. FFAR is written in two volumes. The basic purpose of these volumes is to document and substantiate stability and general aerodynamic characteristics of the vehicle together with the flight dynamic behavior. Of specific interest are the burst point dispersion characteristics and an evaluation of aircraft safety from the standpoint of the possibility of the rocket flight path intersecting the aircraft; establishment of acceptable behavior in these areas is tantamount to establishing satisfactory stability characteristics of the rocket.

In the present volume, Volume I, the basic aerodynamic characteristics of the vehicle are established together with the aeroelastic corrections to these parameters necessary to the determination of the true forces and moments acting on the vehicle. These data are primarily used as input data to the dispersion and aircraft safety studies reported in Volume II.

Reported herein are not only the results pertinent to the flight configuration selected (essentially unchanged from the extant 2.75 in. FFAR configuration), but also the preliminary studies made of various modified configurations prior to the final design configuration. These studies are reported in the appendices, Section 5.1.

Because of the diverse nature of the studies presented, each major subsection carries its own list of symbols and references.

UNCLASSIFIED

## UNCLASSIFIED

Report AFRPL-TR-69-90, Appendix A

### 2.0 SUMMARY

The basic rigid body aerodynamic parameters for the vehicle are developed and presented. Included in the presentation is a discussion and presentation of the wind tunnel test results obtained from full scale tests conducted as part of this program in Tunnel A at the Arnold Engineering Development Center. Comparisons are made with results of previous wind tunnel tests and the sources of discrepancies are discussed and resolved.

Quasi-steady aeroelastic corrections to the rigid body aerodynamics are obtained; these corrections, together with the rigid body aerodynamic parameters, are used as input to work reported in Vol. II. These corrections include the effects of tail fin elasticity and body bending effects.

Critical flight conditions for body loads and fin loads are determined and the attendant loads are evaluated. Aeroelastic effects are included in the evaluation where required.

Aerodynamic heating effects are examined and the resultant fin and motor case temperatures are determined. Additionally, the effects of aero-thermoelasticity on the fin characteristics are examined.

In addition to the results presented for the final configuration, preliminary work conducted for the purpose of optimizing the tail configuration with respect to dispersions is also reported herein.

UNCLASSIFIED

# UNCLASSIFIED

Report AFRPL-TR-69-90, Appendix A

## 3.0 CONCLUSIONS

The following conclusions are derived from the work reported in this volume. Final conclusions on dispersions and aircraft safety are contained in Vol. II.

1. The results of the full scale wind tunnel tests corroborate the previously available scale model tests except for drag and body alone centers of pressure.
2. Drag coefficients based on the new data are on the order of 1.5% higher than those based on earlier data even when appropriate roughness corrections are applied to the skin friction drag of the previous tests. These figures are for drags corrected to flight Reynold's numbers. The difference is attributed to more realistic representation of flight hardware (joints, gaps, grooves, etc.) in the latest tests.
3. Body alone centers of pressure based on the latest test data are about 1.8 calibers forward of those of previous tests. This is attributed largely to inaccuracies due to the relative smallness of the forces to be measured. The new centers of pressure, when used in conjunction with tail-on centers of pressure, produce a more reasonable location for the centers of pressure of lift due to the tail than did previous data.
4. The tail effectiveness in producing lift drops off rapidly above Mach 1 to around 50% of theoretical at  $M = 1.5$  and does not return to theoretical levels till around  $M = 4$ . This indicates poor section characteristics due to leading edge bluntness and section thickness. The tip portions of the fins are probably ineffective in most of this range.
5. Static aeroelastic effects produce fin lift effectiveness losses of up to 40% at maximum dynamic pressure. The attendant loss in static margin is about 2 calibers at this condition.

UNCLASSIFIED

## UNCLASSIFIED

Report AFRPL-TR-69-90, Appendix A

6. Even with the low fin effectiveness and aeroelastic effects, the minimum static margin is about 5 calibers which is more than adequate.
7. For the elastic fin, reduction in the fin panel length by 30% only slightly reduced the minimum static margin.
8. The maximum body load condition occurred at  $t = 2.0$  sec. The maximum  $3\sigma$  body bending moment is 187 in-lb. The maximum fin load occurs at  $t = .08$  sec while the rocket is still in the aircraft flow field. The  $3\sigma$  maximum root bending moment is, conservatively, 106 in-lb.
9. Motor case external temperatures reach  $260^{\circ}\text{F}$  maximum due to aerodynamic heating.
10. Mean temperatures on the leading edge wedge section of the fins reach a maximum of slightly over  $600^{\circ}\text{F}$ .
11. Aerothermoelastic effects on the fins are negligible.

UNCLASSIFIED

# UNCLASSIFIED

Report AFRPL-TR-69-90, Appendix A

## 4.0 ANALYSES AND DISCUSSION OF RESULTS

### 4.1 GENERAL

In this section, the analyses performed for the final configuration are presented and discussed. The corresponding preliminary studies performed to assist in selection of the final configuration (see Vol. II) are presented in the Appendices, Section 5.0. Since much of the final work is a repeat of the preliminary effort with different inputs, considerable cross-referencing is made with Section 5.0 in order to eliminate unnecessarily repetitive descriptions of the methods employed.

Also, the wind tunnel test results, presented in Section 5.2 are the basis for the final aerodynamic data given in Section 4.2.

The final configuration analyzed herein is shown in Figure 4.1-1. The configuration shown (see Vol. II for the basis of selection) is geometrically unchanged from the current 2.75 in. FFAR.

UNCLASSIFIED



UNCLASSIFIED

Report AFRPL-TR-69-90, Appendix A

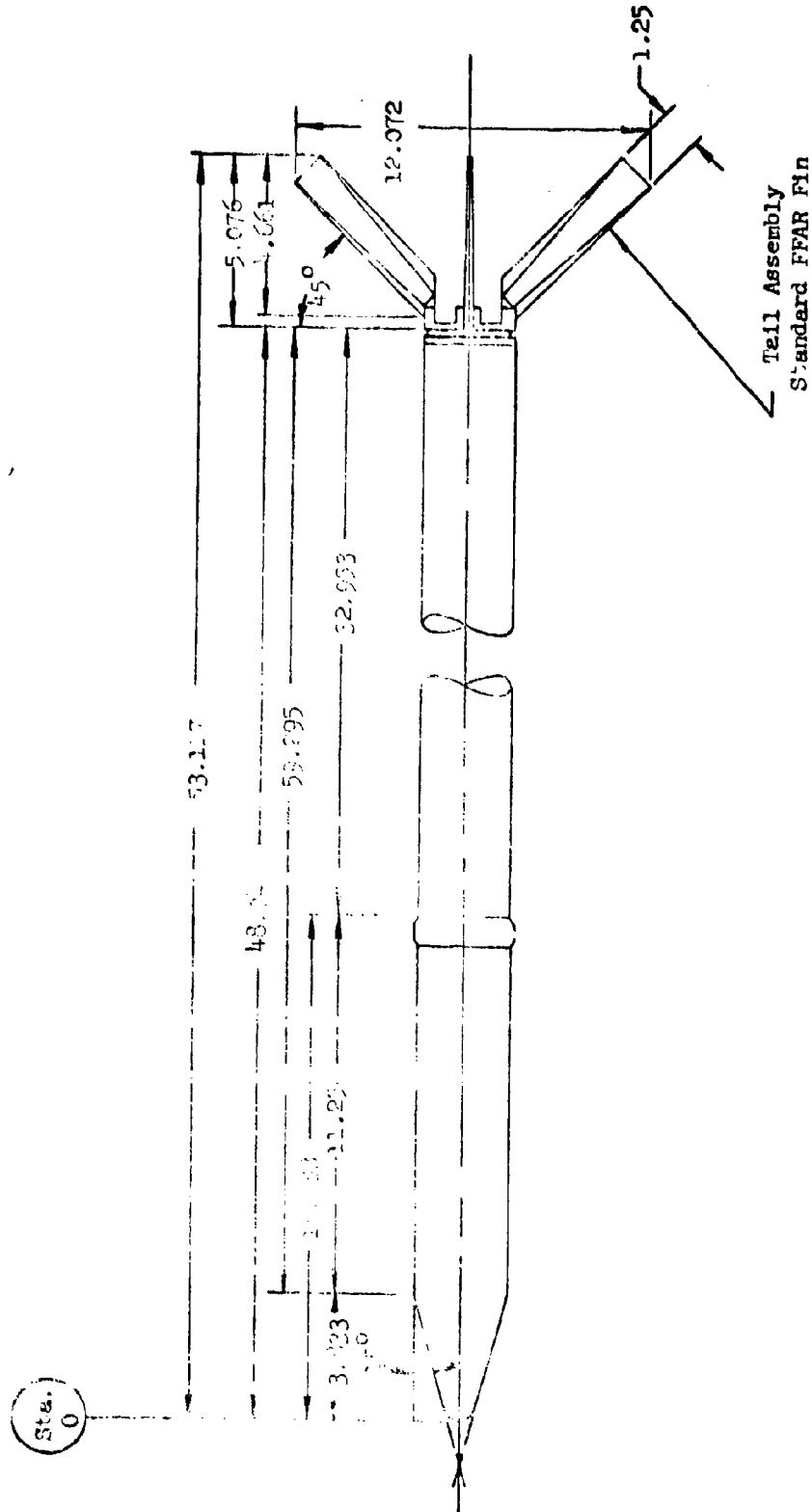


Figure 4.1.1-1

2.75 FFAR Improved Configuration

UNCLASSIFIED

# UNCLASSIFIED

Report AFRPL-TR-69-90, Appendix A

## 4.2 AERODYNAMICS

### 4.2.1 FINAL COMPUTER INPUT DATA

This section presents the final aerodynamic data used in the dispersion and aircraft safety studies reported in Vol. II.

### 4.2.2 SYMBOLS AND NOMENCLATURE

The following are the symbols and notation which are used in the presentation of the aerodynamic characteristics of the 2.75 FFAR vehicle.

$C_{D_0}$	zero lift drag coefficient
$C_{m\dot{\alpha}}$	pitch damping coefficient, per radian
$C_{l\dot{\alpha}}$	roll damping coefficient, per radian
$C_{l\dot{\beta}}$	roll driving coefficient, per radian
$C_N$	normal force coefficient
$C_{N\alpha}$	normal force coefficient slope, 1/radian
$C_{N\dot{\beta}}$	normal force coefficient derivative, per radian
$D$	body diameter, reference length, ft
$\frac{dw}{dh}$	wind shear, 1/sec
$h$	altitude, ft
$I$	fin polar moment of inertia, slug-ft <sup>2</sup>
$k_w, K_w, K_D$	interference factors from NACA TR 1307
$L$	missile length, ft
$M$	Mach number
$M/\dot{\alpha}$	jet damping derivative, ft-lb/rad/sec
$M_\alpha$	aerodynamic spring constant, ft-lb/rad
$\dot{m}$	mass flow rate slug/sec
$\mathcal{M}$	torque on tail fins, ft-lb
$N$	normal force, lb
$q$	dynamic pressure lb/ft <sup>2</sup>
$S$	body cross-sectional area, reference area, ft <sup>2</sup>

UNCLASSIFIED

# UNCLASSIFIED

Report AFRPL-TR-69-90, Appendix A

t	time, sec
T	thrust, lb
u	gust velocity, ft/sec
V	velocity, ft/sec
w	wind velocity, ft/sec
X	body station, inches, ft
$X_{cp}$ $(\frac{X_{cp}}{d})$	center of pressure, diameters
$\alpha$	angle of attack, deg, rad
$\alpha_{RSS}$	root-sum-square angle of attack, deg
$\delta_F$	tail fin misalignment, deg
$\delta_T$	thrust misalignment, deg
$\Delta\alpha$	incremental increase in angle of attack due to airplane flow field, deg
$\Delta t$	time increment for fin opening
$\lambda$	running load, lb/ft
$\phi$	roll position angle, deg
$\omega_n$	pitch frequency, rad/sec
$\lambda$	aerodynamic wavelength in pitch, ft
$\theta$	tail fin angle, radians
$\ddot{\theta}$	tail fin angular acceleration, rad/sec <sup>2</sup>

## Subscripts

B	body
BT	body-tail
BT-B	body-tail minus body
g	gust
S	shear
w	wind
C.G.	center of gravity
e	rocket exit plane

UNCLASSIFIED

## UNCLASSIFIED

Report AFFPL-TR-69-90, Appendix A

### 4.2.3 RIGID BODY AERODYNAMICS

The final aerodynamic characteristics determined for the 2.75 FFAR vehicle are presented for a rigid or undeflected vehicle. Corrections for elasticity effects are given in Section 4.3. The configuration for which these characteristics are being presented is in Figure 4.1-1. The aerodynamic characteristics were primarily determined from the wind tunnel test data as presented in Appendix 5.2, with theoretical analysis methods for the other computations such as the rotary derivatives.

#### 4.2.3.1 BASIC AERODYNAMIC CHARACTERISTICS

Figure 4.2-1 presents the zero lift drag coefficient as a function of Mach number. These data are for the power-on condition. These data were taken from Appendix 5.2, Wind Tunnel Data. The corrections to obtain this curve from the wind tunnel data is discussed in Appendix 5.2 and in the Method of Analysis, 4.2.5. Figures 4.2-2 and 4.2-3 are also from the same source. These figures present  $C_{N_\alpha}$ , the normal force coefficient slope, and  $X_{cp/d}$ , the body alone, and body-tail, centers of pressure as a function of Mach number. The data apply to the 2.75 FFAR vehicle over the vehicle linear range of angle of attack. Figure 4.2-4 presents the tail center of pressure as a function of Mach number. These data were taken from Appendix 5.1.1.

There are aeroelastic corrections which are applied to the rigid body aerodynamics to get aeroelastic data. These are discussed in Section 4.3.

#### 4.2.3.2 FORCE AND ROTARY DERIVATIVES

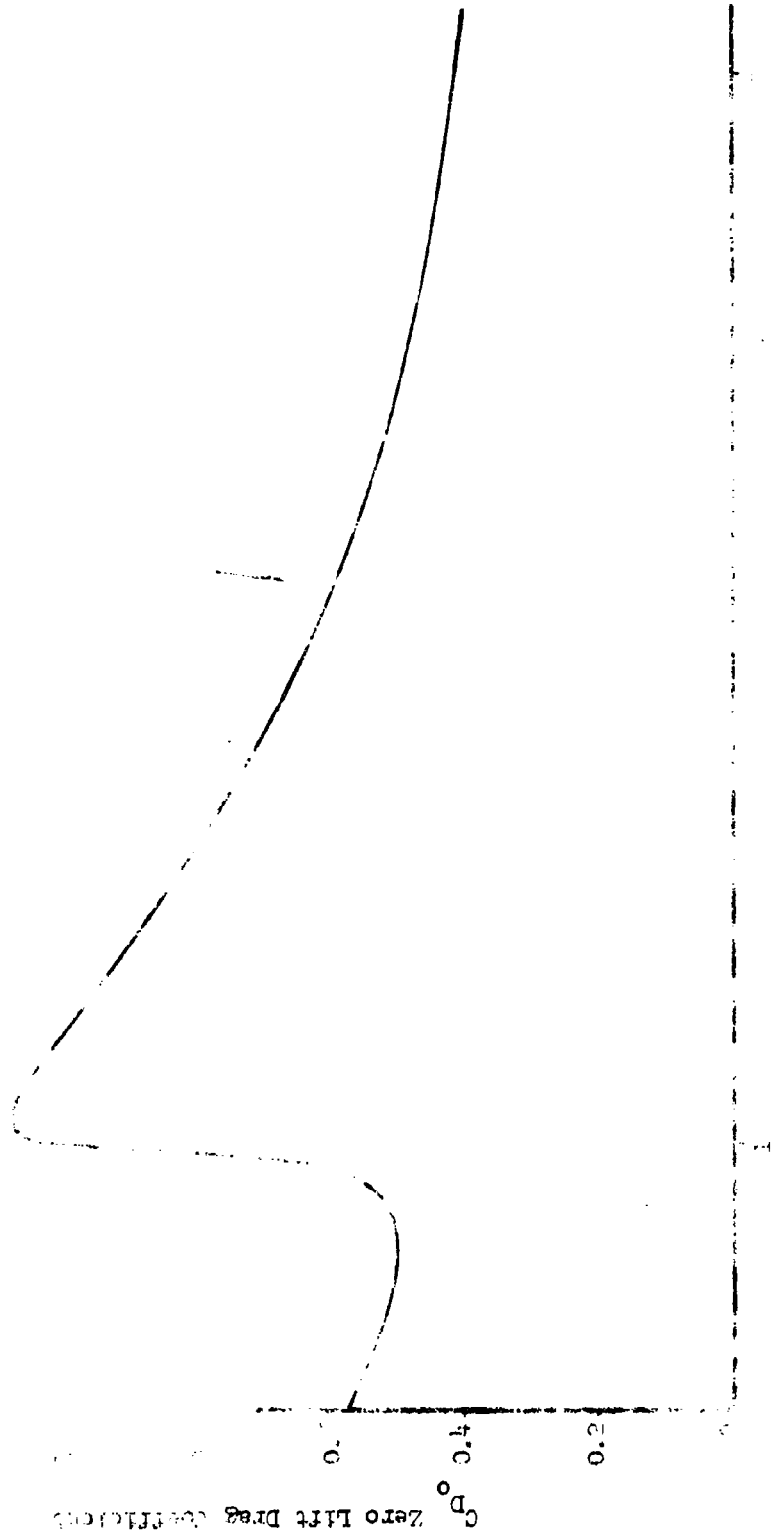
Figure 4.2-5 presents  $C_{N_6}$  the tail power derivative as a function of Mach number. These data are for two tail panels deflected in pitch. The data were taken from Appendix 5.1.1. The roll driving coefficient and roll damping coefficient are presented in Figures 4.2-6 and 4.2-7. These data were computed using the data in References 1 and 2 and are corroborated by experimental data from Appendix 5.2. These derivatives are presented as a function of Mach number for the linear range of angles of attack. Figure 4.2-8

UNCLASSIFIED

# UNCLASSIFIED

Report AFRPL-TR-69-90, Appendix A

of the data as a function of the Reynolds number,  $Re$ . On  $Re = 0.0412 \times 10^6$

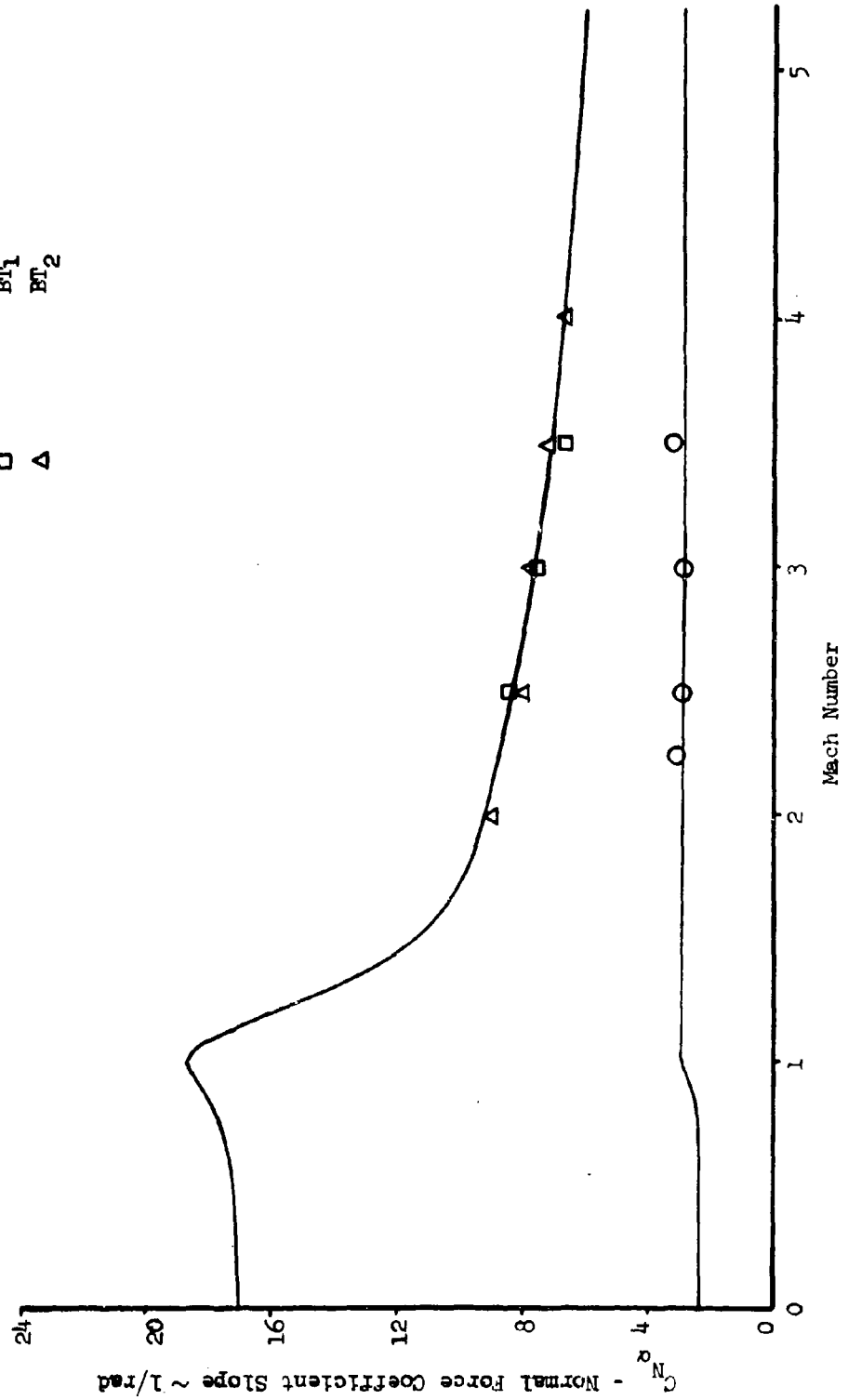


UNCLASSIFIED

UNCLASSIFIED

Report AFRPL-TR-69-90, Appendix A

Figure 4.2-2  
2.75 FFAR Vehicle  
AFDC Wind Tunnel Test VA 0706  
Normal Force Slope as a Function  
of Mach Number  
 $\alpha = -4^\circ$  to  $+4^\circ$ ,  $\phi = 0^\circ$



UNCLASSIFIED

UNCLASSIFIED

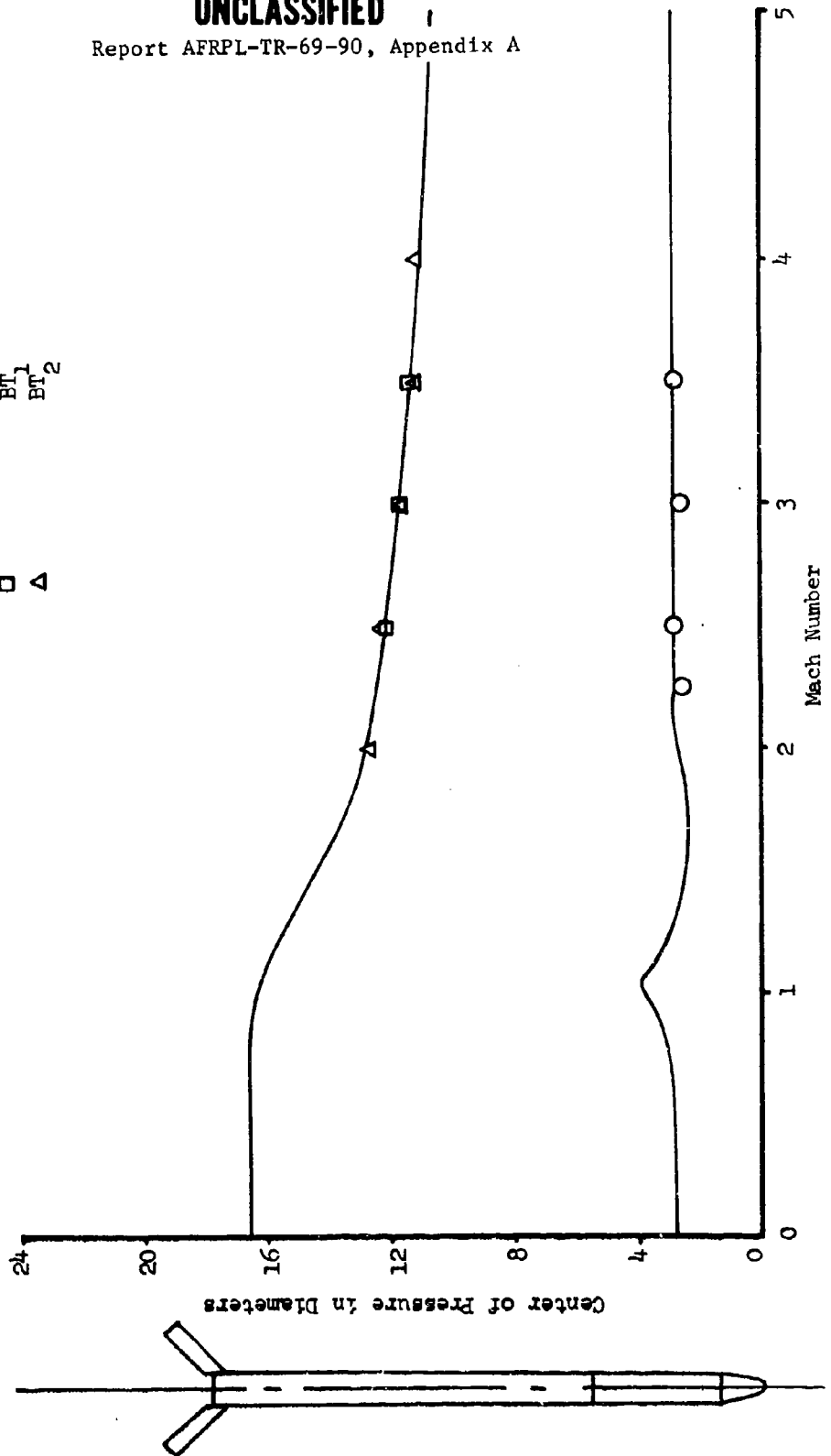
Report AFRPL-TR-69-90, Appendix A

Figure 4.2-3  
2.75 FFAR Vehicle  
AEDC Wind Tunnel Test VA 0706  
Center of Pressure as a Function  
of Mach Number

$\alpha = -4^\circ$  to  $+4^\circ$ ,  $\phi = 0^\circ$

Configuration  
B  
BT<sub>1</sub>  
BT<sub>2</sub>

Symbol  
O  
□  
△

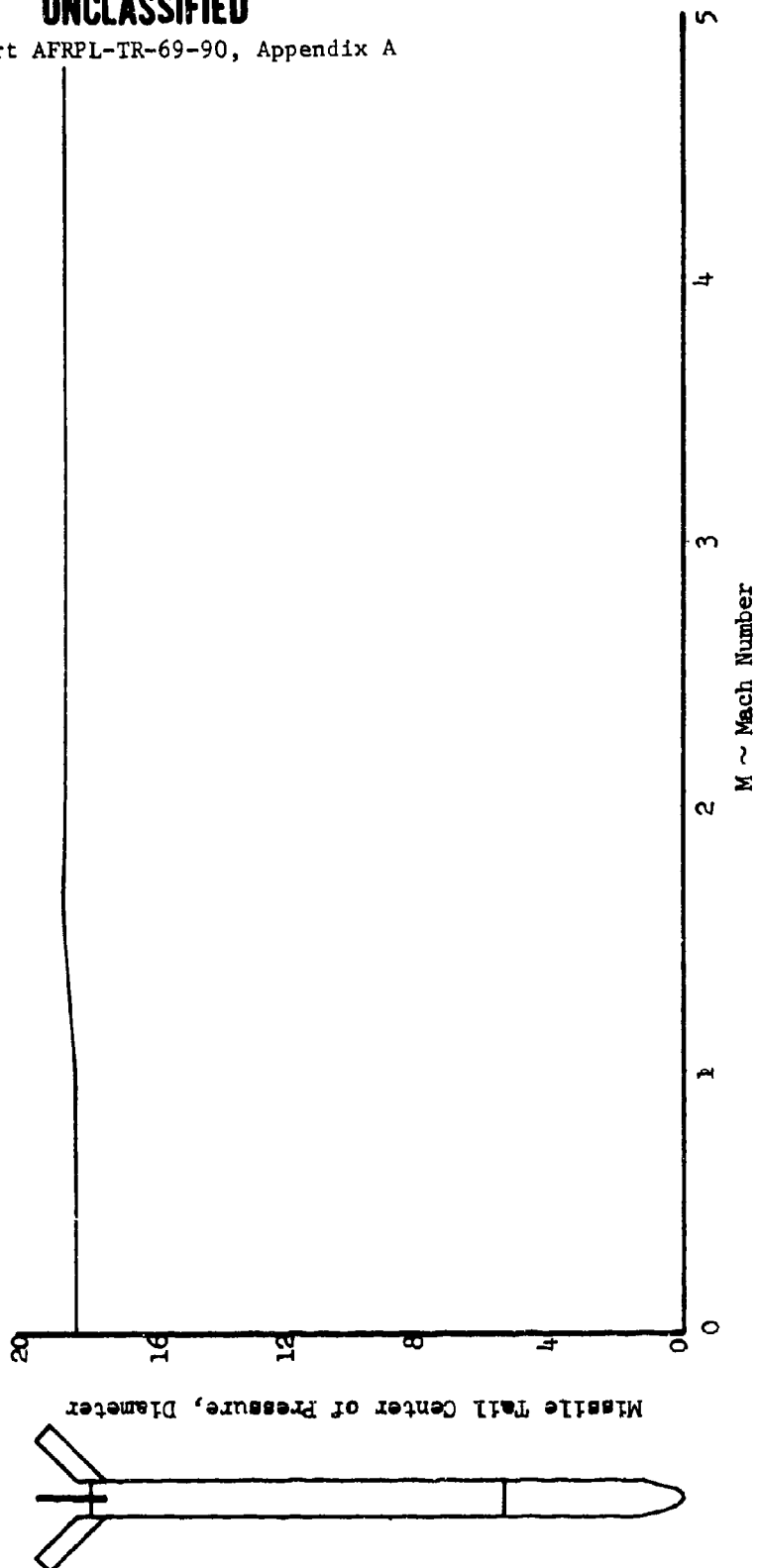


UNCLASSIFIED

UNCLASSIFIED

Report AFRPL-TR-69-90, Appendix A

Figure 4.2-4  
2.75 FFAR Vehicle  
Tail Center of Pressure as a  
Function of Mach Number



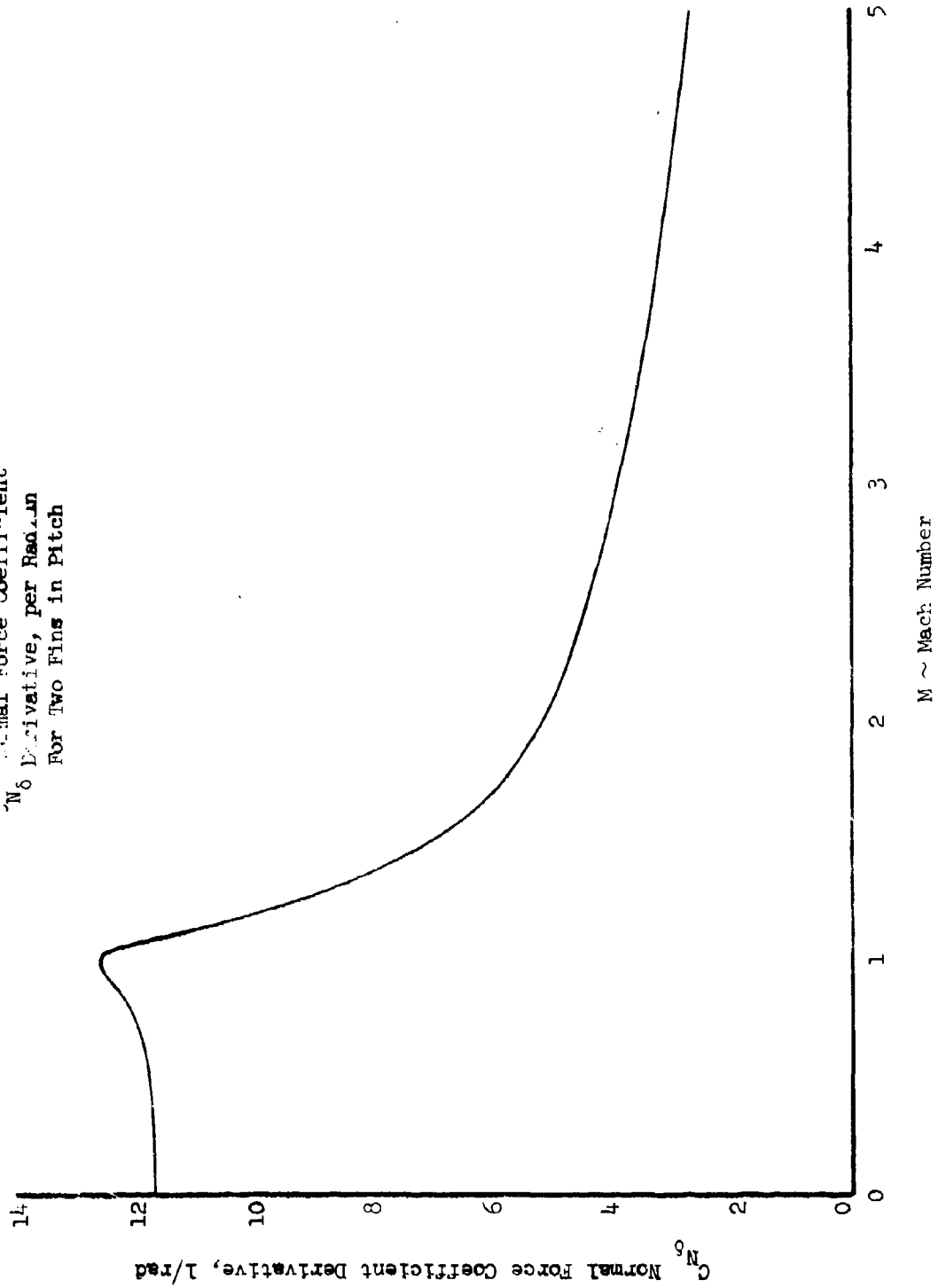
UNCLASSIFIED



UNCLASSIFIED

Report AFRPL-TR-69-90, Appendix A

Figure 4.2-5  
1.75 FFAR Vehicle  
 $C_{N\delta}$  Normal Force Coefficient  
Derivative, per Radian  
For Two Fins in Pitch

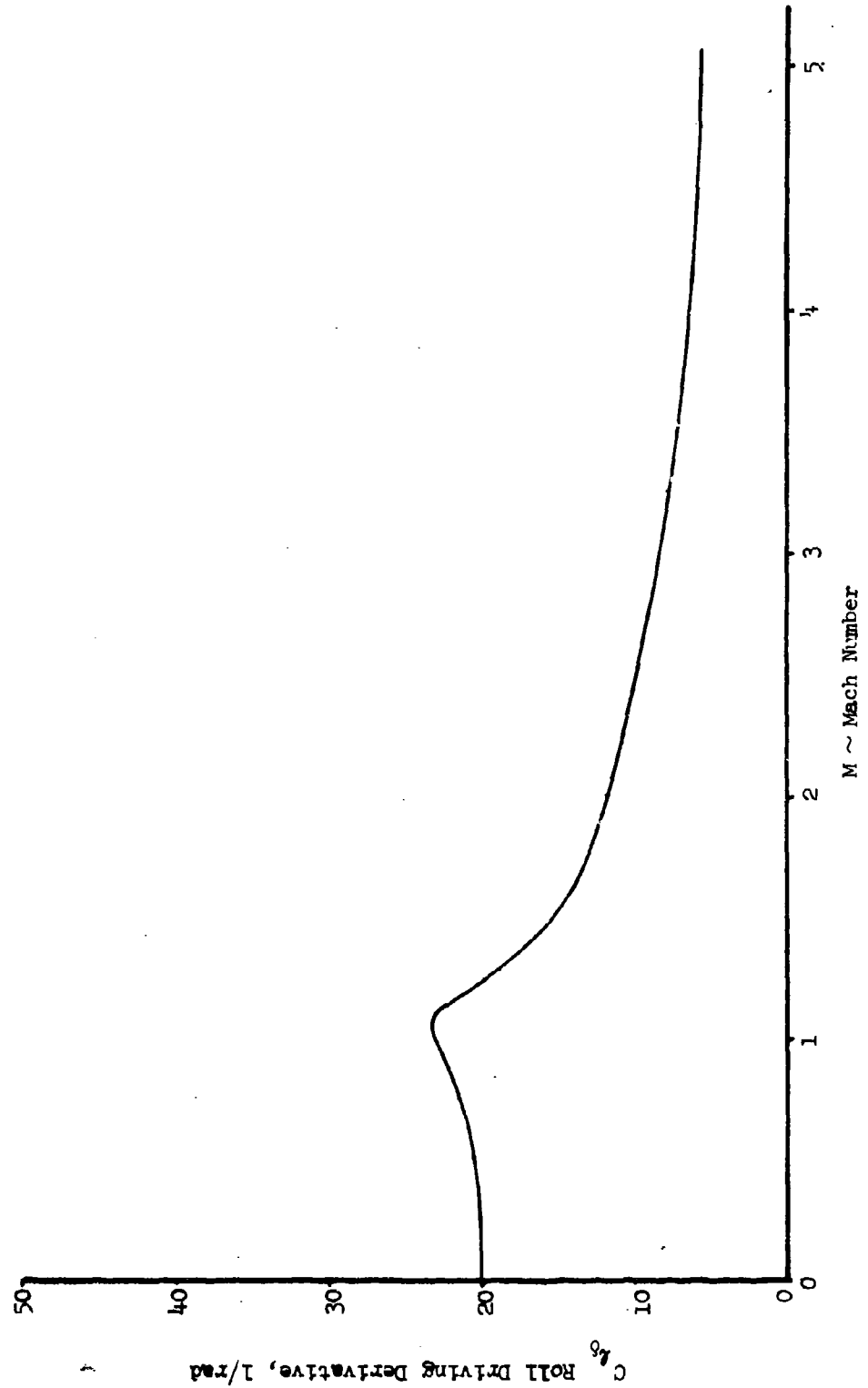


UNCLASSIFIED

UNCLASSIFIED

Report AFRPL-TR-69-90, Appendix A

Figure 4.2-6  
2.75 FTAR Vehicle  
Roll Driving Coefficient as a  
Function of Mach Number

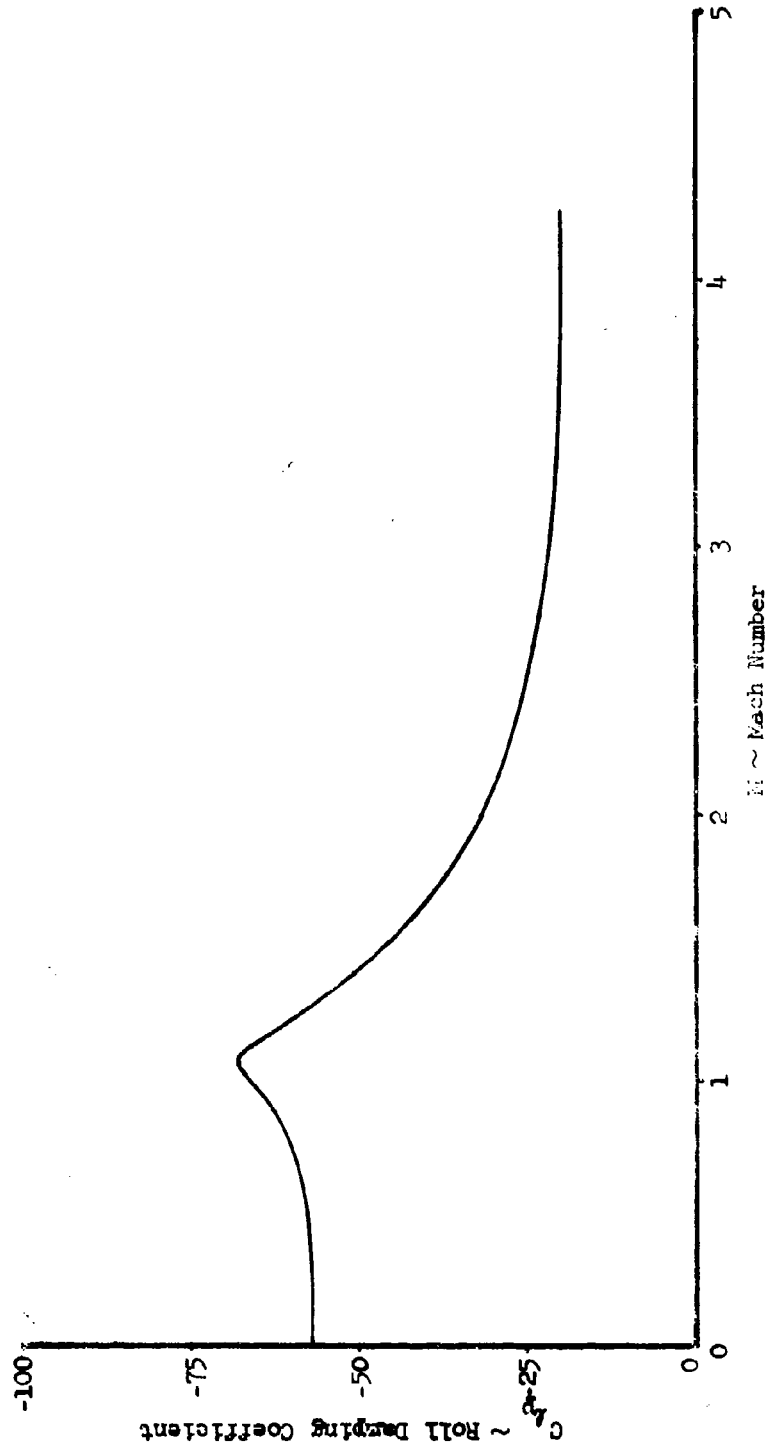


UNCLASSIFIED

# UNCLASSIFIED

Report AFRPL-TR-69-90, Appendix A

2.15 F102 Vehicle  
Roll Damping Coefficient as a  
Function of Mach Number

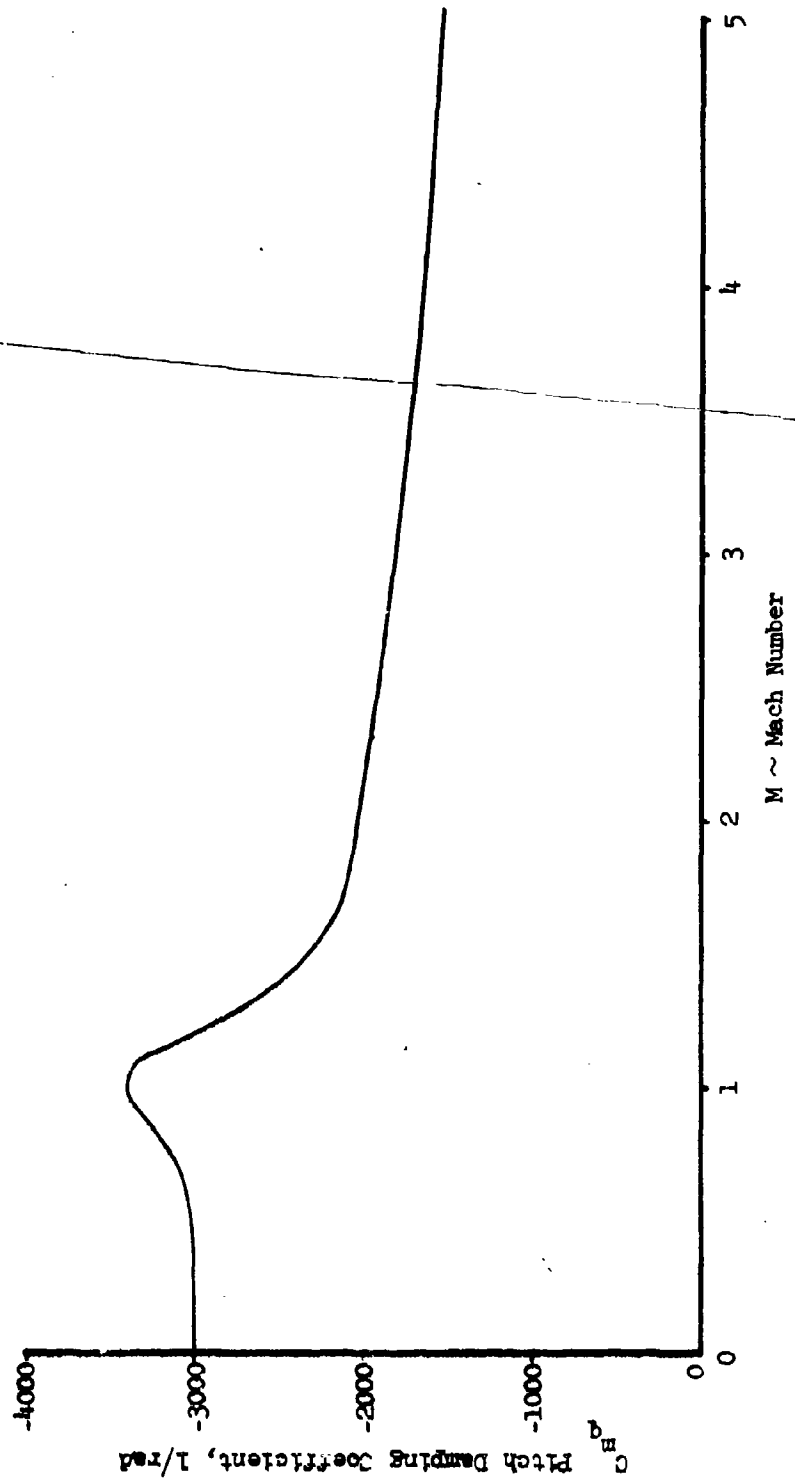


UNCLASSIFIED

UNCLASSIFIED

Report AFRPL-TR-69-90, Appendix A

Figure 4.2-8  
2.75 FTAR Vehicle  
Pitch Damping Coefficient as a  
Function of Mach Number



UNCLASSIFIED

# UNCLASSIFIED

Report AFRPL-TR-69-90, Appendix A

presents the pitch damping coefficient,  $C_{mq}$ , as a function of Mach number. These data were appropriated from Appendix 5.1.1. Figure 4.2-9 presents the jet damping derivative  $M/\dot{\theta}$  as a function of time. These values were computed just as shown in Appendix 5.1.1, but with a burning time of 2.75 seconds. The previous rocket motor version had a shorter value of burning time ( $t_B = 2.15$  sec).

The methods used in determining the force and moment coefficients and their derivatives are discussed in Section 4.2.5.

## 4.2.4 LOADS DETERMINATION AND DISTRIBUTION

In order to accurately determine the maximum loads and the distribution of the loads, it was necessary to determine the angles of attack. This was done as described below.

The angle of attack computed was on a 1 $\sigma$  probability basis. Four sources were used in this determination. These were; wind, shear and gust, thrust misalignment, tail fin misalignment, and aircraft flow field. These individual values were computed in intervals  $\Delta t \approx 0.1$  sec from launch to burnout. The results of these computations were root-sum-squared to obtain the angle of attack. The body and tail normal loads were computed using the normal force coefficient  $C_{N}$  from Section 4.2.3.1 and the dynamic pressure from the trajectory. The maximum tail normal force load was determined to occur at  $t = .08$  seconds at which time the missile is still in the airplane flow field and the vehicle velocity is low enough to generate a sizeable angle of attack due to wind. The individual values of angle of attack are given below in tabular form.

For  $t = .08$  seconds and  $M = 1.02$ ,

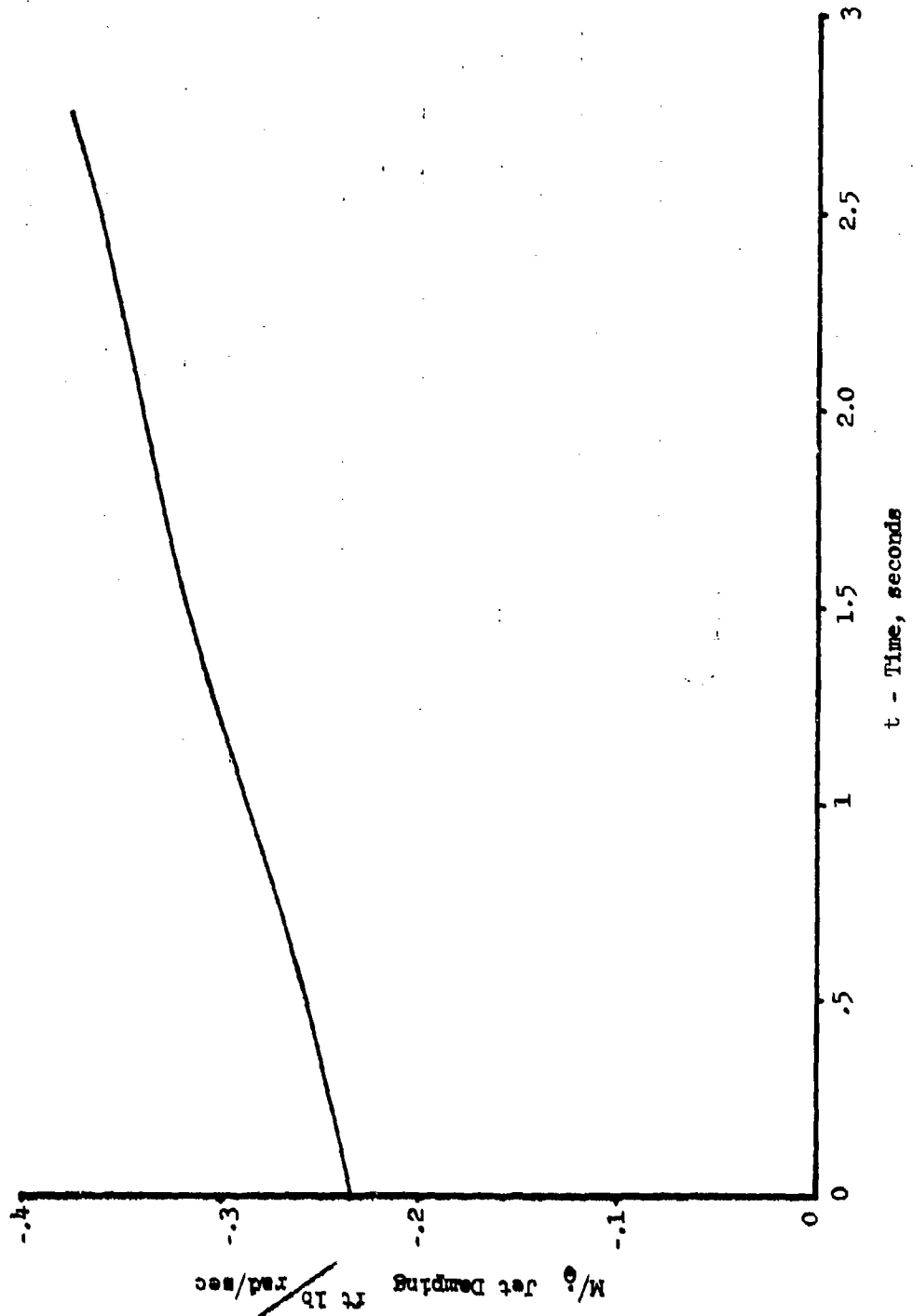
Item	Magnitude	Source	$\Delta\alpha$
Wind Shear	$dw/dh = .017$ 1/sec	Reference (1)	$.679^\circ$
Wind gust	$u = 13.34$ ft/sec	Reference (2)	$.4610^\circ$
Thrust Misalignment	$\delta_T = .125^\circ$	From Project Office	$.124^\circ$
Fan Misalignment	$\delta_F = .125^\circ$	From Project Office	$.1091^\circ$
Airplane Flow Field		From 6-d Trajectory	$2.000^\circ$

UNCLASSIFIED

UNCLASSIFIED

Report AFRPL-TR-69-90, Appendix A

Figure 4.2-9  
2.75 FFAR Vehicle  
Jet Damping as a Function of Time



UNCLASSIFIED

# UNCLASSIFIED

Report AFRPL-TR-69-90, Appendix A

The RSS angle of attack for these values is:

$$\alpha_{RSS} = \sqrt{(.679)^2 + (.124)^2 + (.1091)^2 + (2)^2}$$

$$\alpha_{RSS} = 2.12 \text{ deg } (1\sigma)$$

The tail load resulting from this angle of attack was computed to be:

$$N_T = C_{N_\alpha} \alpha q S = (3)(15.90)\left(\frac{2.12}{57.3}\right)(1387)(.0412) = 100.78 \text{ lb } (3\sigma)$$

A similar procedure was followed for the maximum body load. The individual angles of attack for the maximum body load is given below.

For  $t = 2$  seconds and  $M = 3.37$

Item	Magnitude	Source	$\Delta\alpha$
Wind Shear	$dw/dh = .016 \text{ 1/sec}$	Reference (1)	$.0273^\circ$
Wind Gust	$u = 13.34 \text{ ft/sec}$	Reference (2)	$.2035^\circ$
Thrust Misalignment	$\delta_T = .125^\circ$	From Project Office	$.054^\circ$
Fin Misalignment	$\delta_f = .125^\circ$	From Project Office	$.1665^\circ$
Airplane Flow Field		From 6-d Trajectory	$0^\circ$

The RSS angle of attack for these values is:

$$\alpha_{RSS} = \sqrt{(.2035)^2 + (.054)^2 + (.1665)^2}$$

$$\alpha_{RSS} = 0.2684 \text{ deg } (1\sigma)$$

The body load resulting from this angle of attack was computed to be:

$$N_B = C_{N_\alpha} \alpha q S = (3)(2.8)\left(\frac{.2684}{57.3}\right)(16591)(.0412) = 26.87 \text{ lb } (3\sigma)$$

Both these values are for a  $3\sigma$  probability level.\*

\*Note that the  $3\sigma$  value given is probably quite conservative since the aircraft flow field effect, which is the main contributor, should probably not be trebled at this probability level.

# UNCLASSIFIED

Report AFRPL-TR-69-90, Appendix A

The body load was distributed using the data in Reference 3. The result is shown in Figure 4.2-10.

The maximum drag load on the tail fins was computed to be  $D_{\max} = 26.76$  lb per fin. This occurred at flight time  $t = 2.10$  seconds.

## 4.2.5 METHOD OF ANALYSIS

Primarily the data were analyzed precisely as discussed in Section 5.1.1. In this appendix the data from the two scale model wind tunnel tests were used as a beginning point. In this instance, the flight hardware model data were used. The data and methods are discussed below.

Basically the axial force data are obtained from the wind tunnel test by correcting for Reynold's number and base pressure power-on. The data of Reference 4 were used in these corrections and an RMS roughness of .001 inches (painted surfaces) was assumed. The equation below shows the correction:

$$C_{D_o} = C_A + \left[ -\Delta C_{D_f \text{ model body}} - \Delta C_{D_f \text{ model tails}} + \Delta C_{D_f \text{ flight body}} + \Delta C_{D_f \text{ flight tails}} \right] + \left( -C_{P_B} \frac{A_B}{S_{\text{Ref}}} \right)$$

The above corrections were applied to the full scale wind tunnel test data from Reference 5. These data were for Mach numbers  $M = 2.50$  to  $4.0$ . The scale model wind tunnel test data of Reference 6 in conjunction with a transonic computed data point were used to generate the remainder of the curve shown in Figure 4.2-1.

The normal force coefficient slopes and centers of pressure were taken directly from the full scale test data and are presented with no corrections.

The tail power derivative  $C_{N_\delta}$  was obtained by the equation below.

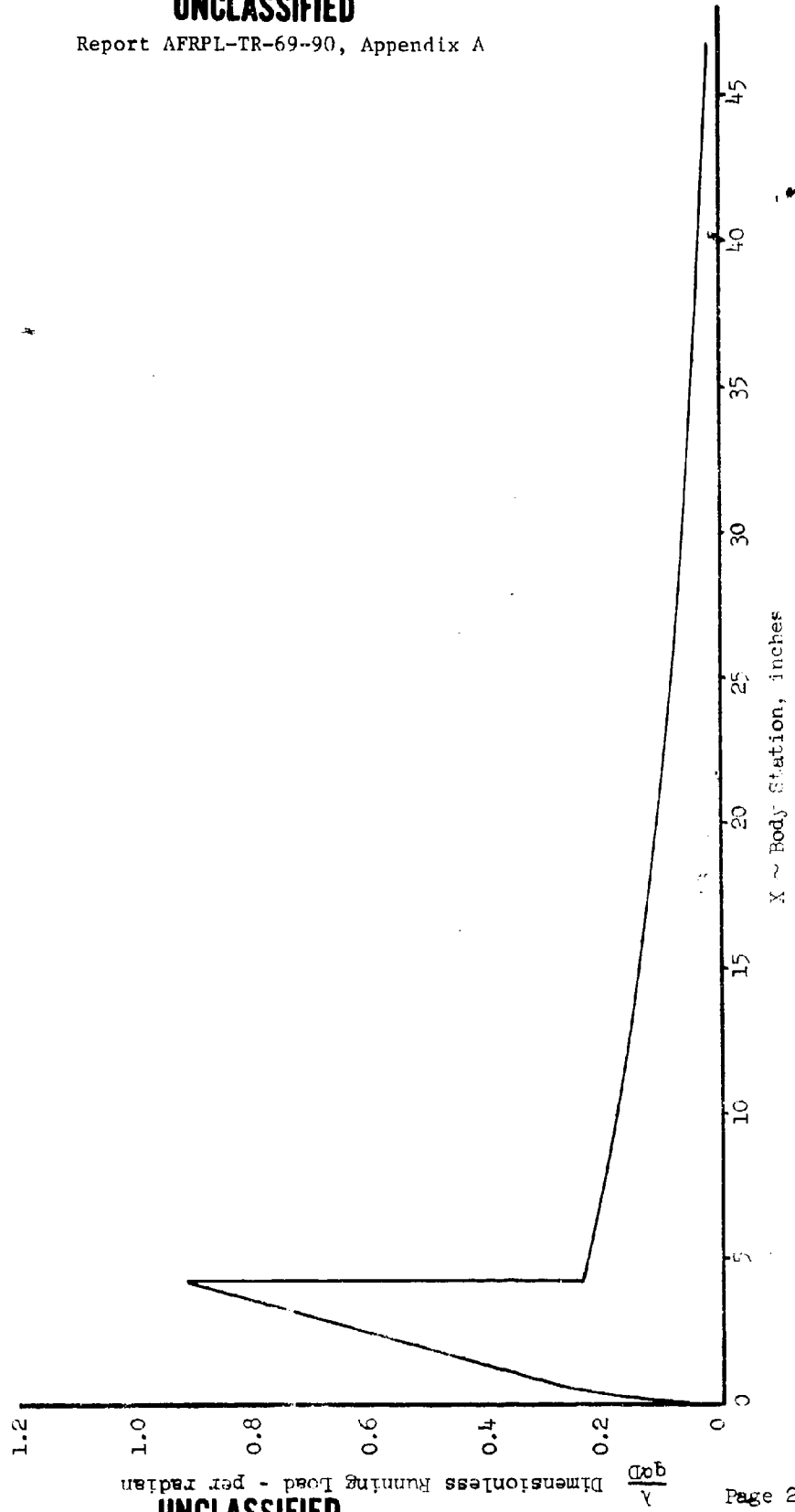
$$C_{N_\delta} = \frac{k_w}{K_w + K_B} \left[ C_{N_{\alpha_{BT}}} - C_{N_{\alpha_B}} \right]$$



UNCLASSIFIED

Report AFRPL-TR-69-90, Appendix A

Figure 4.2-10  
2.75 FFAR Vehicle  
Body Running Load at  $M = 1.4, 2.4, 3.5$   
Ref. Area  $5.94 \text{ in}^2$   
Ref. Length  $2.75 \text{ in.}$



UNCLASSIFIED

## UNCLASSIFIED

Report AFRPL-TR-69-90, Appendix A

The roll driving and damping derivatives were computed using the data of References 7 and 8.

The pitch damping derivative,  $C_{m_q}$  was computed by the equation presented below.

$$C_{m_q} = -2 C_{N_{\alpha_B}} \left( \frac{L - X_{CG}}{d} \right)^2 + (-2) C_{N_{\alpha_{BT-B}}} \left( \frac{X_{cp_T} - X_{CG}}{d} \right)^2$$

The jet damping derivative was computed as a function of time using the equation below.

$$\frac{M}{\dot{\theta}} = \dot{m} (X_e - X_{CG})^2$$

This expression was obtained from Reference 9.

### 4.2.6 TAIL EFFECTIVENESS AND VARIATION

One of the significant items to come out of the preliminary study is the relatively low effectiveness of the tail panels. At a Mach number of 1.5, they operate in the region of 60% of their theoretical computed effectiveness. This is as the result of a poor profile section and high thickness ratio. The subsonic and low supersonic lift curve slopes generated by these tails could be significantly improved by sharpening the leading edge and reducing the thickness ratio. However, the present tails are operative and an improvement program may be implemented in the future.

In the dispersion study, some variation in tail span studies were made. In these instances, the body tail-body data were ratioed according to the span and then the normal force coefficient slope, the drag coefficients and the rotary derivatives were modified accordingly. No attempt was made to account for the modified tips on the resulting tail configurations. This resulted in errors of +15 to 20% in some of the aerodynamic parameters but this was considered sufficiently accurate for the preliminary phase of the work

UNCLASSIFIED

## UNCLASSIFIED

Report AFRPL-TR-69-90, Appendix A

since the tail effectiveness values used could subsequently be related to fin span in a more accurate manner, i.e., the fin referred to as "70% span" in Vol. II may more accurately represent a fin of different physical span.

### 4.2.7 TRANSIENT EFFECTS

The fin opening times were computed using the differential equation presented below.

$$I \ddot{\theta} + m_{\text{aerodynamic}} + m_{\text{propulsive}} = 0$$

In the above equation the aerodynamic moment is that generated by the tail fin drag as the air courses about the fin. The propulsive moment is due to the chamber pressure acting on the quarter-inch diameter piston in the rocket base. This force is transmitted to the fins by an actuator attached to the piston. Substituting values in the above equation, the simplified equation below is obtained

$$\ddot{\theta} = -870 \sin \theta + 379 \cos^4 \theta$$

This equation was solved iteratively and the results indicate the time for the fins to open is  $\Delta t = .024$  seconds. These data were converted into Mach number for the appropriate launch condition. This is a procedure similar to that indicated in the transient analysis in Appendix 5.1.1.

UNCLASSIFIED

# UNCLASSIFIED

Report AFRPL-TR-69-90, Appendix A

## 4.2.8 REFERENCES

1. AFRCR TN 58-259, "Evaluation of an AN/GMD-2 Wind Shear Data for Development of Missile Design Criteria", by N. Dvoskin and N. Sissenwine.
2. NASA TN D-1249, "Statistical Wind Distribution Data for Use at NASA Wallops Station", by W.L. Weaver, A.G. Swanson, and J.F. Spurling, 1962.
3. NACA TR 1328, "A Second Order Shock Expansion Method Applicable to Bodies of Revolution Near Zero Lift", by C.A. Syvertson and D.H. Dennis, 1957.
4. "Fluid Dynamic Drag", by Sighard Hoerner, 1958.
5. AFRPL Aerojet 2.75 In. Rockets Project No. VA 0706, Tunnel 40 Inch Supersonic Tunnel Type Data, Tabulated Data Test, Completion Date Dec. 12, 1967, AEDC, Tullahoma, Tennessee.
6. AEDC TR 65-248, "Wind Tunnel Tests of a 2.75 FFAR,  $M = 0.6$  to 1.50".
7. NACA TM 1120, "The Lift Distribution of Sweptback Wings", by J. Weissinger, 1947.
8. "Aerodynamic Components of Aircraft at High Speeds", Volume VII, Princeton Series, Princeton University Press, 1957.
9. "Mathematical Theory of Rocket Flight", by J.B. Rosser, R.R. Newton, and G.L. Gross, McGraw-Hill Book Co., 1947.

UNCLASSIFIED

# UNCLASSIFIED

Report AFRPL-TR-69-90, Appendix A

## 4.3 AEROELASTICITY

### 4.3.1 INTRODUCTION

Preliminary analyses, presented in Section 5.1.2, indicate significant aeroelastic effects for the 2.75 FFAR. This is particularly true of the fins which, at maximum dynamic pressure, showed a large loss of lift and an attendant loss in vehicle static stability margin. A detailed body and fin aeroelastic analysis was, therefore, required to accurately predict these effects.

### 4.3.2 DISCUSSION

#### 4.3.2.1 GENERAL EFFECTS OF AEROELASTICITY

Aeroelastic effects must be considered for the flight dynamics, dispersion and loads analyses. This is required since aeroelasticity changes the dynamic response characteristics of the vehicle. For example, the loss in stability margin increases the vehicle angle of attack response to disturbances such as winds and fin and thrust misalignments. This, of course, is due to the reduction of aerodynamic restoring moments caused by body and fin elasticity. In addition, the elasticity of the fins changes the rolling characteristics of the vehicle due to changes in the damping and driving forces.

The effects of aeroelasticity are incorporated in the aforementioned analyses by use of elasticized force and moment data. These data are obtained from body and fin aeroelastic analyses for several Mach number and dynamic pressure combinations along the mission profile. The elasticized data are then used as input, for example, to the six-degree-of-freedom trajectory program from which the dynamic responses are obtained. The aeroelastic corrections are made on a quasi-static basis since past experience has shown that coupling between structural dynamic and rigid body dynamic terms has negligible effect on the rigid body mode responses for vehicles of this type.

UNCLASSIFIED

# UNCLASSIFIED

Report AFRPL-TR-69-90, Appendix A

## 4.3.2.2 METHODS OF ANALYSIS

### 4.3.2.2.1 Fin Aeroelasticity

The fin aeroelastic characteristics are determined from a closed form digital computer solution which is obtained by means of matrix inversion. The method used is completely documented in Reference 5. The solution is for the incremental angle of attack arising from fin bending and torsional characteristics. From this solution the elasticized forces and moments may be obtained.

Input data required for the fin aeroelastic analysis includes the following:

- 1) Spanwise airload distributions due to angle of attack (i.e., aerodynamic influence coefficients).
- 2) Spanwise distribution of chordwise centers of pressure.
- 3) Rigid fin angle of attack distribution.
- 4) Structural influence coefficients describing streamwise twist variation with applied bending and torsional moments.

### 4.3.2.2.2 Body Aeroelasticity

The aeroelastic body characteristics were determined by means of an iterative digital computer solution. The equations programmed and program usage are completely documented in References 1 and 2.

The analysis programmed considers the vehicle to be a free-free beam acted on by thrust and distributed aerodynamic drag and normal forces. The shears, bending moment and axial loads acting along the vehicle are obtained by integration of the applied loadings plus the distributed pitch and translational acceleration inertial reactions to the applied loads. The analysis also considers the column bending effects of thrust, drag and inertial loads acting in an axial direction on a vehicle which is bent in its pitch (or resultant) plane.

The body aeroelastic program does not calculate elastic fin characteristics. These are calculated as described in Section 4.3.2.2.1 and then input to the body program as an elasticized  $C_{N_\alpha}$  for the fins.

# UNCLASSIFIED

Report AFRPL-TR-69-90, Appendix A

## 4.3.3 RESULTS OF THE ANALYSIS

### 4.3.3.1 GENERAL APPROACH

The primary purpose of the aeroelastic analysis was to generate elasticized aerodynamic force and moment data to be used as input to the six-degree-of-freedom analysis. The secondary purpose was to determine aeroelastic structural design loads. This is discussed in Section 4.3.3.4. Pursuant to the primary purpose, aeroelastic body and fin analyses were performed for the following conditions:

<u>Mach No.</u>	<u>Velocity, fps</u>	<u>Dynamic Pressure, psf</u>
1.4	1562	2650
2.4	2678	8100
3.5	3906	18160

The above condition parameters are based upon a preliminary trajectory. Final trajectories showed differences in burning characteristics which would modify the inertial data for the conditions analyzed. However, it is felt that these differences are small and may be safely neglected. Since all conditions are at sea level, the Mach number-dynamic pressure relationships remain the same in either case.

The results obtained from these analyses are presented in the form of elastic force or moment to rigid force or moment ratios vs Mach number (or  $C_{N\alpha} q$  in the case of the fins). In the case of static stability margin the incremental margin vs Mach number is presented. Application of these ratios (or increments) to the rigid body data yields the desired elasticized aerodynamic force and moment data required for the six-degree-of-freedom dynamics analysis.

UNCLASSIFIED

# UNCLASSIFIED

Report AFRPL-TR-69-90, Appendix A

## 4.3.3.2 FIN AEROELASTIC CHARACTERISTICS

### 4.3.3.2.1 Fin Structural Influence Coefficients

The static aeroelastic fin analysis described in Section 4.3.2.2.1 requires structural influence coefficients which describe streamwise twists due to applied loads and applied streamwise torques. These coefficients may be determined theoretically or from structural test data. It was decided to determine these coefficients from test data for the 2.75 FFAR since the root constraint for this fin is difficult to describe analytically.

The influence coefficients were obtained experimentally at the Aerojet facility in Sacramento. They describe deflections at several points along the leading edge and trailing edge due to applied unit loads. A sketch of the fin geometry showing the load points considered is presented in Figure 4.3-1. Points 3+ and 7+, in Figure 4.3-1, have been added to improve the integration results in the aeroelastic analysis.

Typical plots of the deflections obtained from the tests are presented in Figure 4.3-2. This data is presented in the form of so-called "carpet" plots. A "carpet" plot is one in which the distance between the origin of each deflection curve along the abscissa represents the distance between the load points. Plotting the data in this fashion allows ready interpolation of influence coefficients for intermediate points. This procedure was necessary to facilitate the reduction of the data into the form of streamwise twists required for the aeroelastic analysis.

As stated above, it was necessary to reduce the deflection data into the form of streamwise twists due to loads applied at the elastic axis and due to applied streamwise torques. The procedure followed to obtain these data is described in the following paragraphs.

The twists due to unit loads applied at the elastic axis were obtained as follows:

- 1) The deflections of the L.E. and T.E. due to a 1/2 lb load applied at the L.E. and T.E. for each point were plotted.

UNCLASSIFIED



## UNCLASSIFIED

Report AFRL-TR-69-90, Appendix A

- 2) The deflections at the L.E. and T.E. of a streamwise chord through the load point were read off these curves.
- 3) The resulting twists were then determined from the following relationship:

$$\theta = \frac{\delta_{LE} - \delta_{TE}}{d}$$

where:  $\theta$  = Streamwise twist, rad

$\delta$  = L.E. or T.E. deflection, in.

$d$  = Streamwise chord length, in.

The twists due to unit applied streamwise torques were obtained as follows:

- 1) Influence coefficients were determined at the L.E. and T.E. of streamwise chords through the load points. These were obtained from the "carpet" plots.
- 2) The deflections at the L.E. and T.E. due to 1# up at the L.E. and 1# down at the T.E. for each point were determined.
- 3) The resulting twists were then determined from the following relationship:

$$\theta = \frac{\delta_{LE} - \delta_{TE}}{d^2}$$

Note that the  $d^2$  term gives the twist due to a unit applied torque.

The two structural twist influence coefficient matrices obtained in the above manner are presented in Tables 4.3-1 and 4.3-2. These are the matrices which were used in the aeroelastic computer program.

It should be noted here that the structural deflection data obtained from the tests gave aeroelastic results which were in close agreement with those obtained using theoretical structural influence coefficients. During the proposal effort theoretical influence coefficients were used which gave aerodynamic lift losses on the fin of approximately 35% at maximum  $q$ . For the final analysis, the influence coefficients obtained experimentally gave lift losses of approximately 40% at maximum  $q$  (see Figure 4.3-4.)

UNCLASSIFIED

# UNCLASSIFIED

Report AFRL-TR-69-90, Appendix A

Table 4.3-1  
2.75" FEAR  
FIN STRUCTURAL INFLUENCE COEFFICIENTS  
ANGULAR DEFLECTION DUE TO A UNIT STREAMWISE TORQUE  
Rad/in-lb

Row 1	.000130	.000223	.000304	.000438	.000630
Row 2	.000223	.000354	.000413	.000531	.000767
Row 3	.000320	.000431	.000748	.000450	.000748
Row 4	.000444	.000490	.000494	.000754	.000999
Row 5	.000640	.000751	.000698	.000934	.000910

Note: Element 1,1 represents the deflection at the most inboard point.

See Figure 4.3-1 for load points.

UNCLASSIFIED

Report AFRPL-TR-69-90, Appendix A

2. THE

### STRUCTURAL INFLUENCE COEFFICIENTS

head/1c

Row 1	- ,0000768	- ,00197	- ,0000000	- ,0000000	- ,00103
Row 2	- ,0000000	- ,0000118	- ,0000713	- ,0001111	- ,00183
Row 3	- ,0000083	- ,000501	- ,0000607	- ,00101	- ,00203
Row 4	- ,0000111	- ,000043	- ,0000618	- ,0010	- ,00227
Row 5	- ,0000000	- ,000000	- ,0000191	- ,000000	- ,00781

There is a small, but definite, difference in the position of the head of the male and female.

see Figure 1.5.7. Load point.

Report, AFRID-TR-1-90, . . .

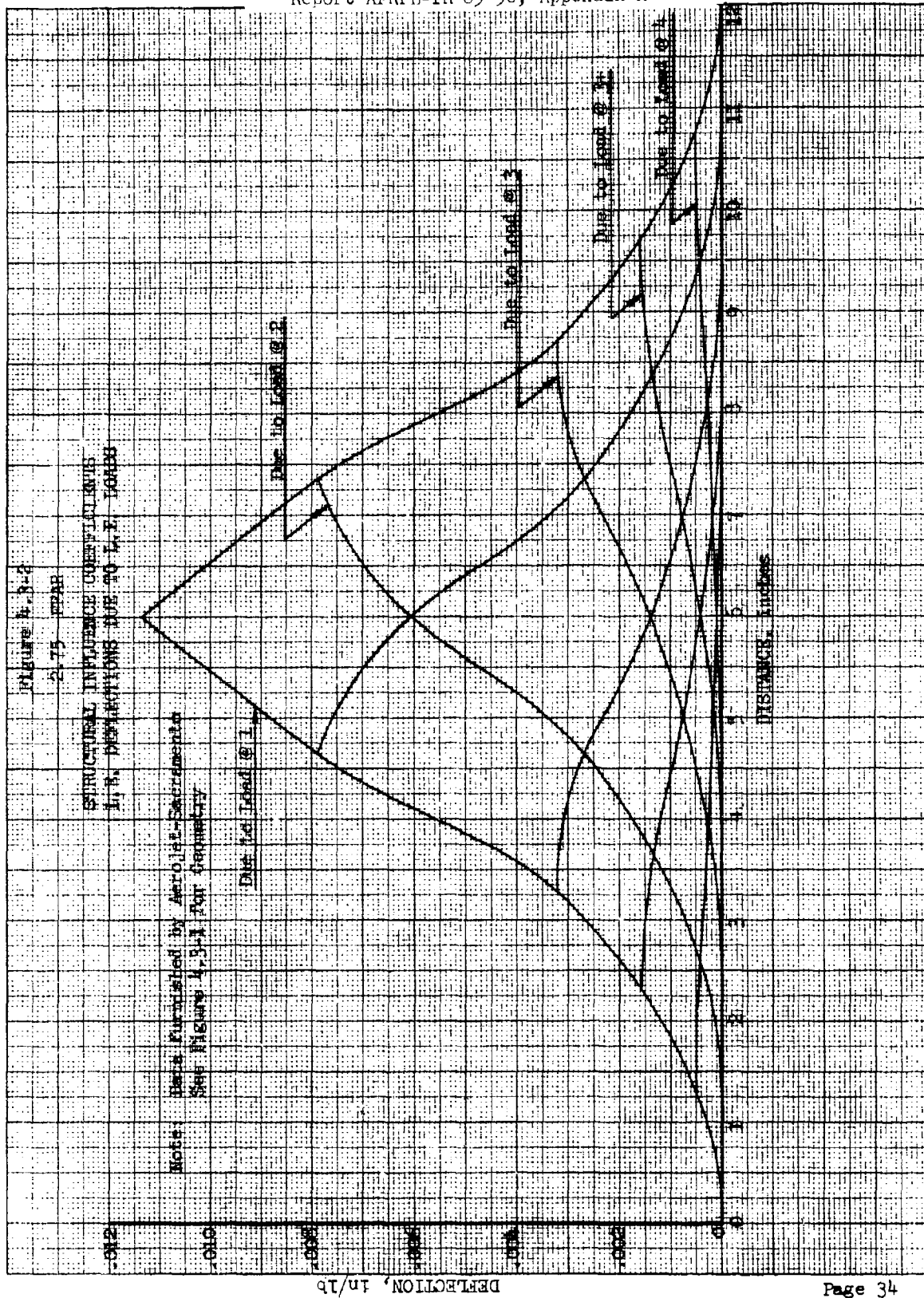
LOAD POINTS USED FOR STRUCTURAL INFLUENCE COEFFICIENTS

Fin Geometry,  $45^\circ$  Sw. on



UNCLASSIFIED

Report AFRPL-TR-69-90, Appendix A



UNCLASSIFIED

## UNCLASSIFIED

Report AFRPL-TR-69-90, Appendix A

### 4.3.3.2.2 Aerodynamic Influence Coefficients

The aeroelastic analysis requires an aerodynamic influence coefficient matrix to describe the changes in aerodynamic distributions due to fin twists. In the case of the 2.75 FFAR it was decided that these changes could adequately be described by strip theory. Strip theory assumes that the lift varies locally only with local deflections. Strip theory generally predicts aeroelastic increments accurately, even in Mach ranges where it gives inadequate prediction of rigid fin characteristics.

The influence coefficient matrix thus becomes a diagonal whose terms represent values of the fin span loading at the points of interest. This span loading is for the fin alone, not in the presence of the body. The span loadings used for Mach numbers 1.4, 2.4 and 3.5 are shown in Figure 4.3-3. These were derived from Reference 4.

Examination of wind tunnel data showed that the fin span loadings used (see Figure 4.3-3) over predicted the fin  $C_{N_\alpha}$ 's at the lower Mach numbers. This over prediction is due to a higher loading on the outboard panels than actually exists. The theoretical distributions, however, were the best available and were used in the analysis. Therefore, the aeroelastic effects at the lower Mach numbers are conservatively predicted.

It was necessary to perform the aeroelastic analysis for several cases at each Mach number. These were:

- 1) Due to fin deflection (driving).
- 2) Damping in roll.
- 3) Angle of attack in presence of the body.

In each of the above cases, the rigid span loadings were obtained by applying an appropriate angle of attack distribution to the aerodynamic influence coefficients. In the case of fin deflection this distribution was uniform. In the case of damping in roll it was linearly varying from the centerline of the vehicle. For the case of angle of attack in presence of the body, the body upwash had to be taken into account. This was done with the following relationship:

UNCLASSIFIED

# UNCLASSIFIED

Report AFRPL-TR-69-90, Appendix A

$$\alpha'(y) = \alpha(1 + R^2/y^2)$$

where:

- $\alpha'$  = local angle of attack including upwash correction
- $\alpha$  = uncorrected angle of attack
- $y$  = span distance from centerline of the vehicle
- $R$  = body radius

For all Mach numbers and rigid fin distributions, the chordwise centers of pressure were assumed to be at 47% of the local chord. Since chordwise bending is negligible for fins of such large structural aspect ratio, this also holds approximately true for the elasticized distributions.

## 4.3.3.2.3 Elasticized Fin Data

The results of the aeroelastic fin analysis are presented in the form of elastic to rigid ratios for the various types of loadings. These ratios may be applied to the rigid aerodynamic force and moment data to provide the desired elasticized data. The ratios are plotted vs  $C_{N_\alpha} q$ . Examination of the aeroelastic equations (Reference 5) shows that the distribution of the aeroelastic increment varies with the parameter  $C_{N_\alpha} q$ . A plot of Mach number is also provided for convenience in data preparation.

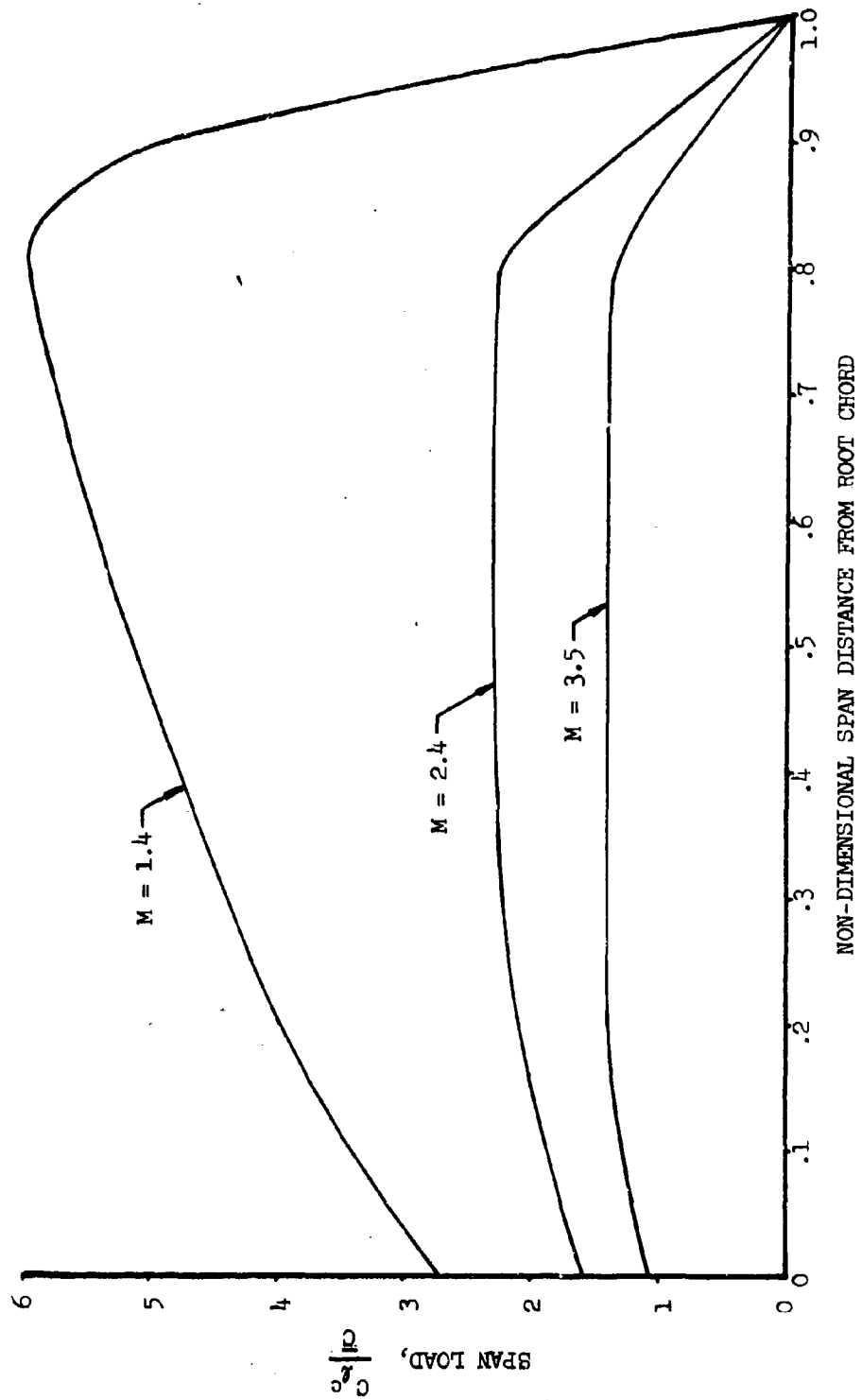
The ratios for fin lift,  $C_{N_\alpha}$ , are presented in Figure 4.3-4. This is to be used to determine the elasticized  $C_{N_\alpha}$  which is input to the body aeroelastic analysis. The ratios for fin normal force due to fin deflection (driving)  $C_{N_\delta}$ , are presented in Figure 4.3-5. The ratios for fin rolling moment due to fin deflection (driving)  $C_{l_\delta}$ , are presented in Figure 4.3-6. The ratios for damping in roll,  $C_{l_p}$ , are presented in Figure 4.3-7.

Examination of the steady roll equation shows that the change in steady roll rate due to elastic effects is the ratio of driving ratio to the damping in roll ratio. In case of the 2.75 FFAR there is an increase of 17% in the steady roll rate at maximum dynamic pressure due to elastic effects.

UNCLASSIFIED

Report AFRPL-TR-69-90, Appendix A

Figure 4.3-3  
2.75 FFAR  
FIN SPANWISE LOAD DISTRIBUTIONS  
DATA DERIVED FROM REFERENCE 4

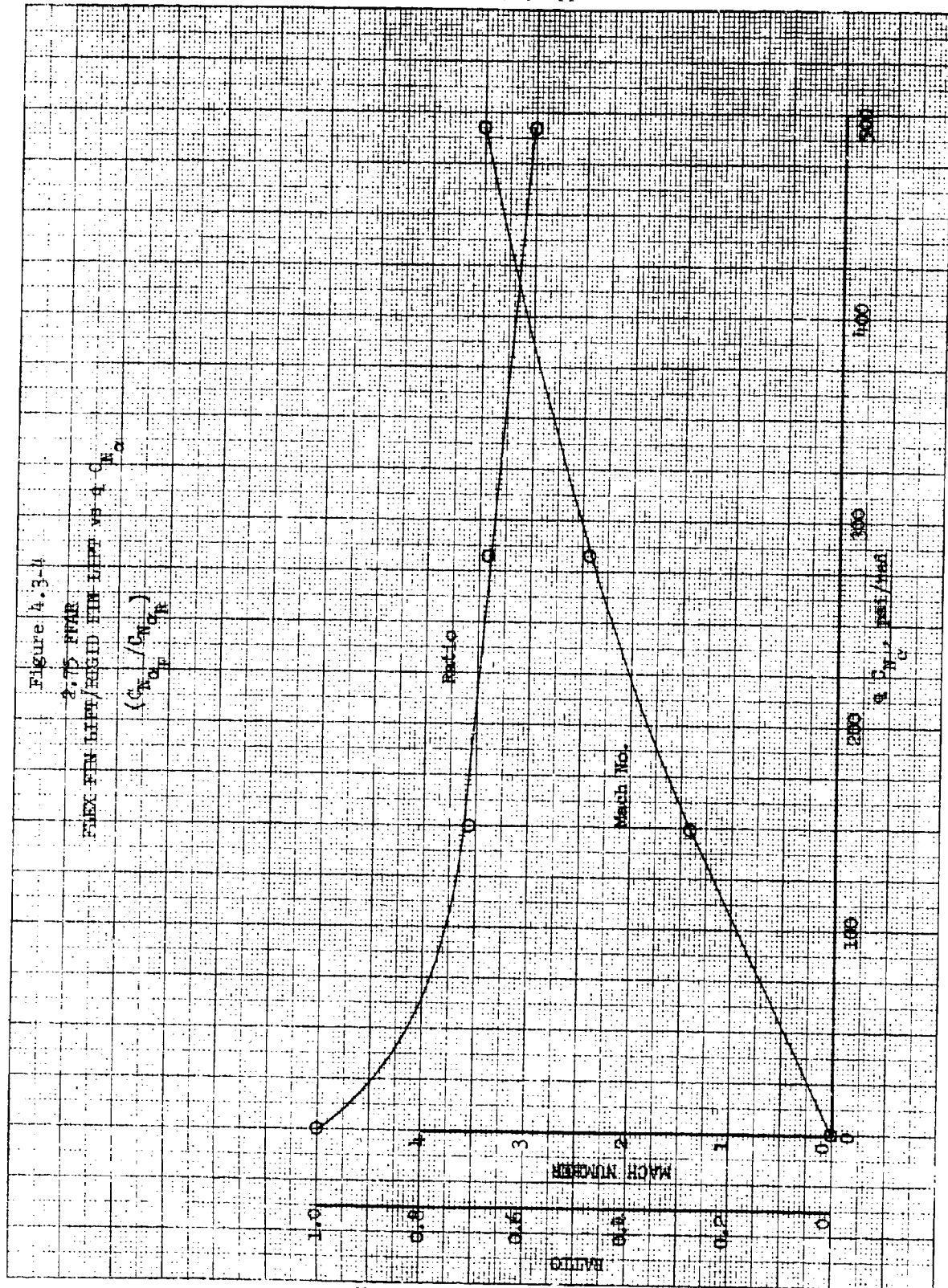


UNCLASSIFIED



UNCLASSIFIED

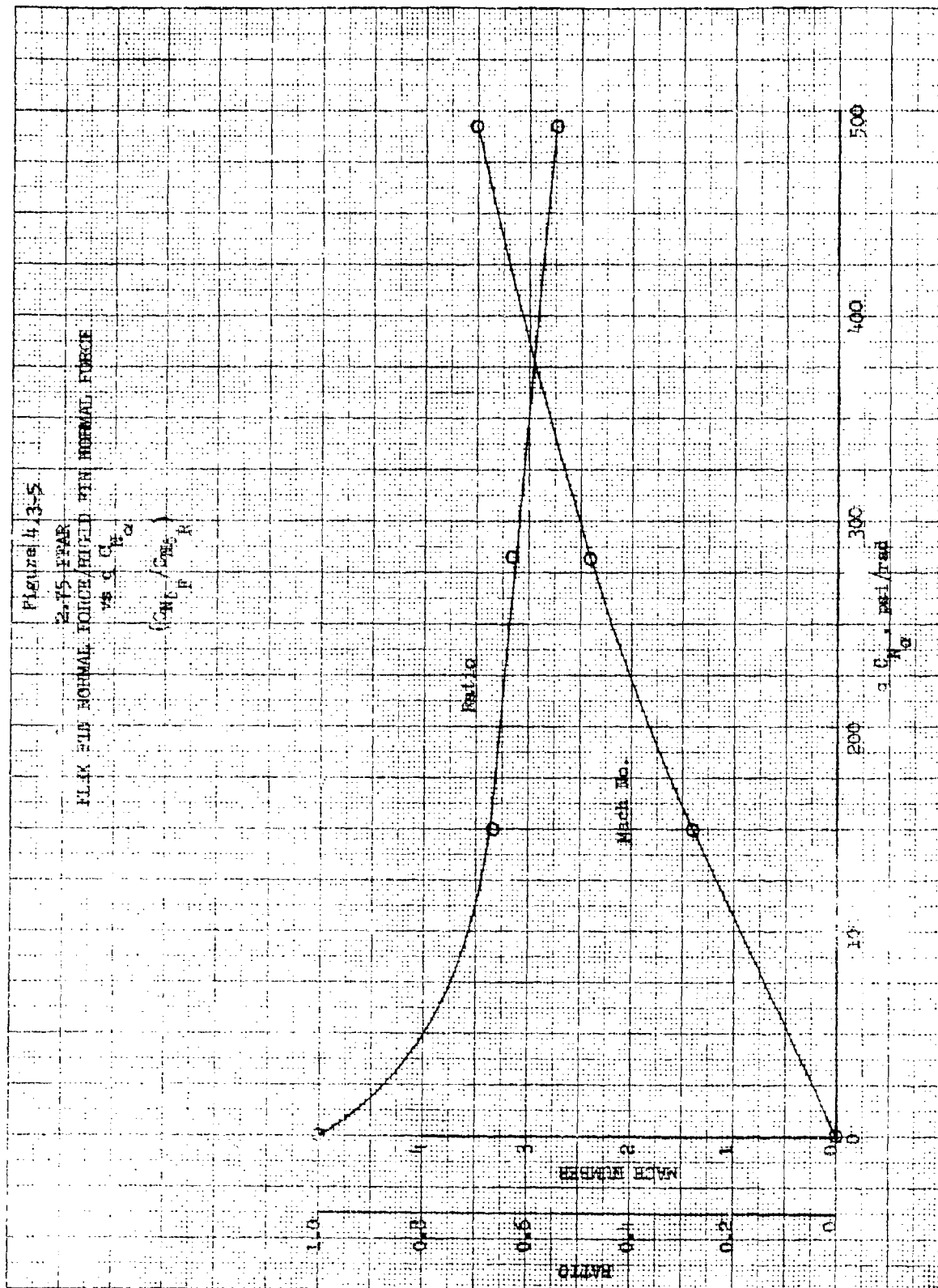
Report AFRPL-TR-69-90, Appendix A



UNCLASSIFIED

# UNCLASSIFIED

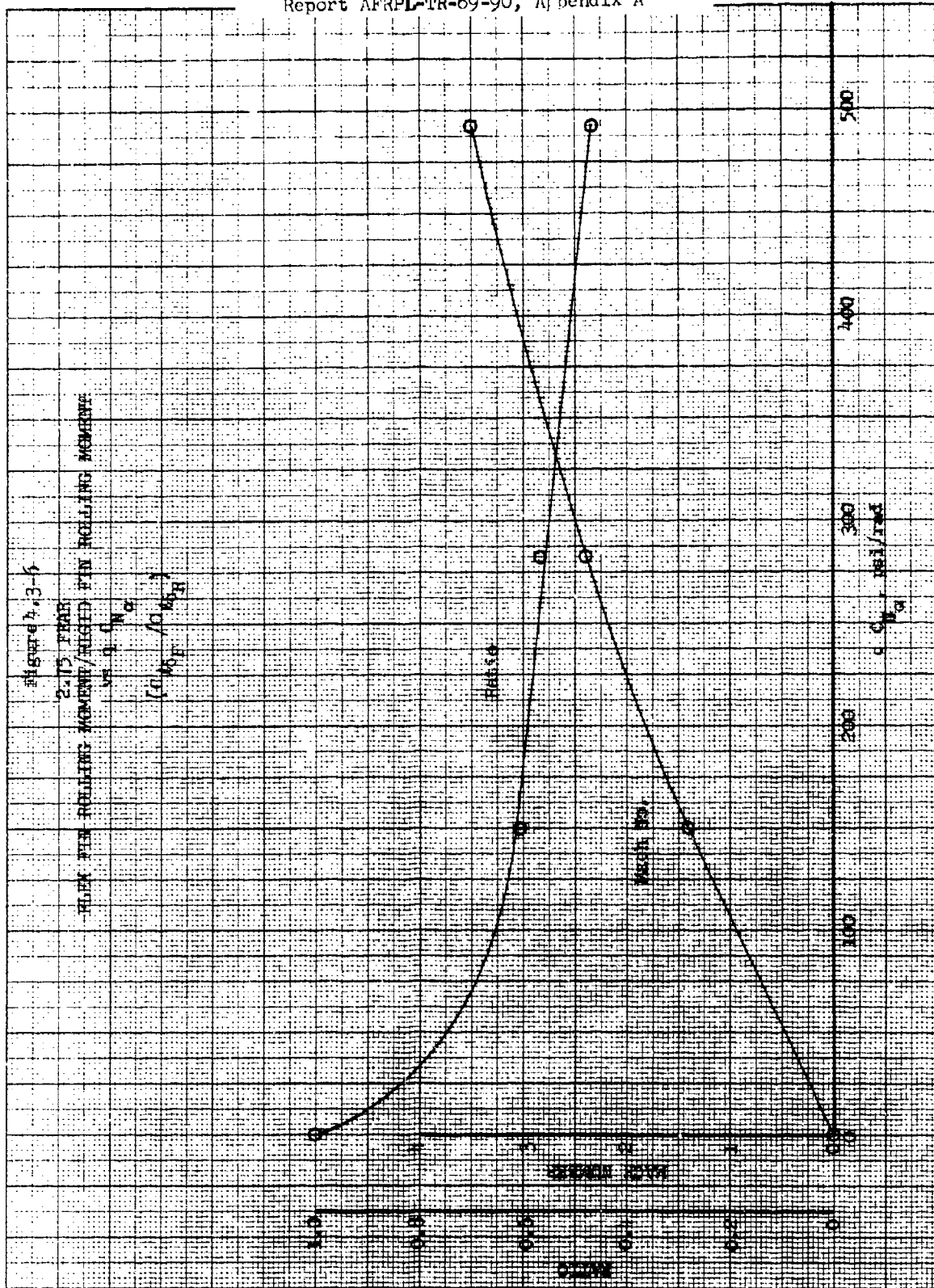
Report AFRPL-TR-69-90, Appendix A



UNCLASSIFIED

UNCLASSIFIED

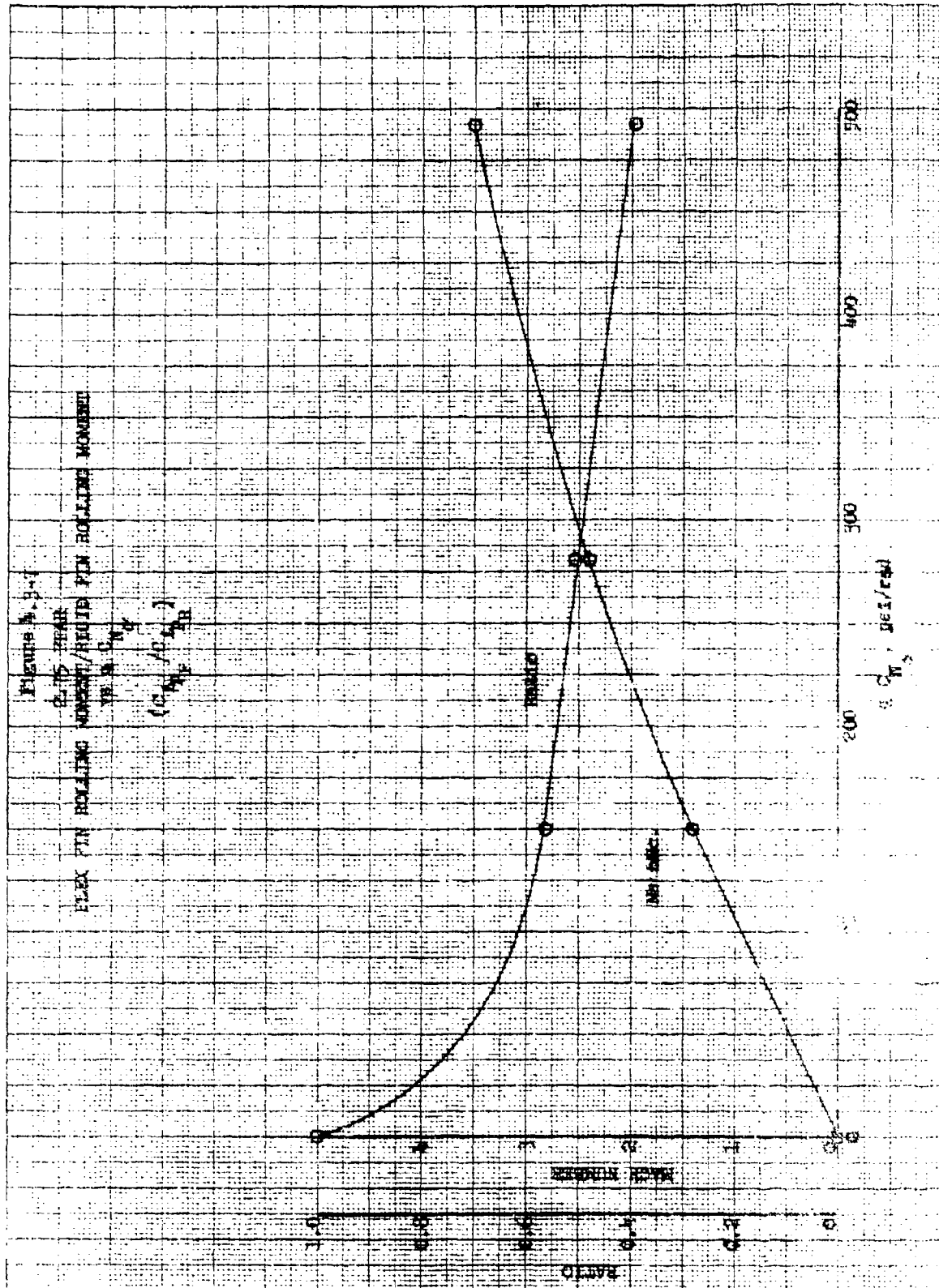
Report AFRPL-TR-69-90, Appendix A



UNCLASSIFIED

# UNCLASSIFIED

Report AFRL-TR-69-90, Appendix A



UNCLASSIFIED

## UNCLASSIFIED

Report AFRPL-TR-69-90, Appendix A

### 4.3.3.3 BODY AEROELASTIC CHARACTERISTICS

In order to accurately assess the change in static stability margin for the 2.75 FFAR it was necessary to account for the effects of body elasticity as well as fin elasticity. This was done according to the methods discussed in Section 4.3.2.2.2. The same Mach number-dynamic pressure combinations were analyzed as for the fins.

The mass distribution used for the analysis is presented in Figure 4.3-12. The body stiffness distribution (EI) used is shown in Figure 4.3-13. The mass and stiffness data were provided by the Aerojet-Sacramento facility. The lateral rigid body airload distribution used for the analysis is presented in Figure 4.3-11. Note that the same distribution applies with good accuracy for all Mach numbers of interest.\* This distribution represents the body aerodynamic influence coefficients. As in the case of the fins they are a diagonal matrix whose elements are the body airloading at various stations along the vehicle. They are used to describe the rigid body airloading and the change in airloading due to body bending. The tail loads used with this distribution do, however, vary significantly with Mach number. Elasticized values of tail  $C_{N_\alpha}$  based on the data of Section 4.3.3.2.3 were used with the distributions to completely define the body aerodynamics.

The elastic to rigid ratios of body plus fin lift are presented vs Mach number in Figure 4.3-8. The incremental static stability margin due to elasticity vs Mach number is presented in Figure 4.3-9. The elastic to rigid ratios of body plus fin damping in pitch moments are presented in Figure 4.3-10.

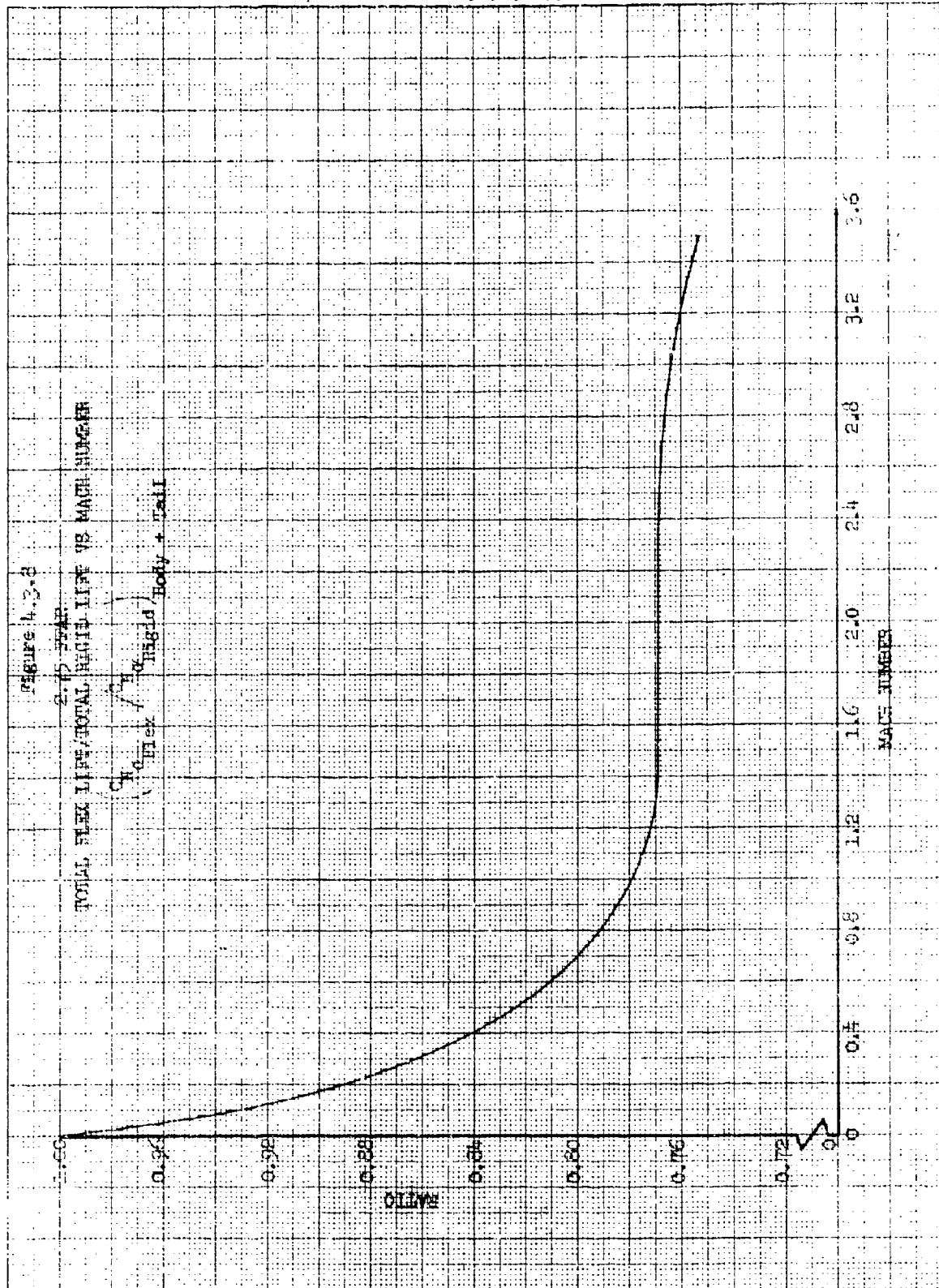
---

\* This would not be the case for transonic and subsonic Mach numbers, but the aeroelastic effects are small there in any case due to the lower dynamic pressures involved.

UNCLASSIFIED

UNCLASSIFIED

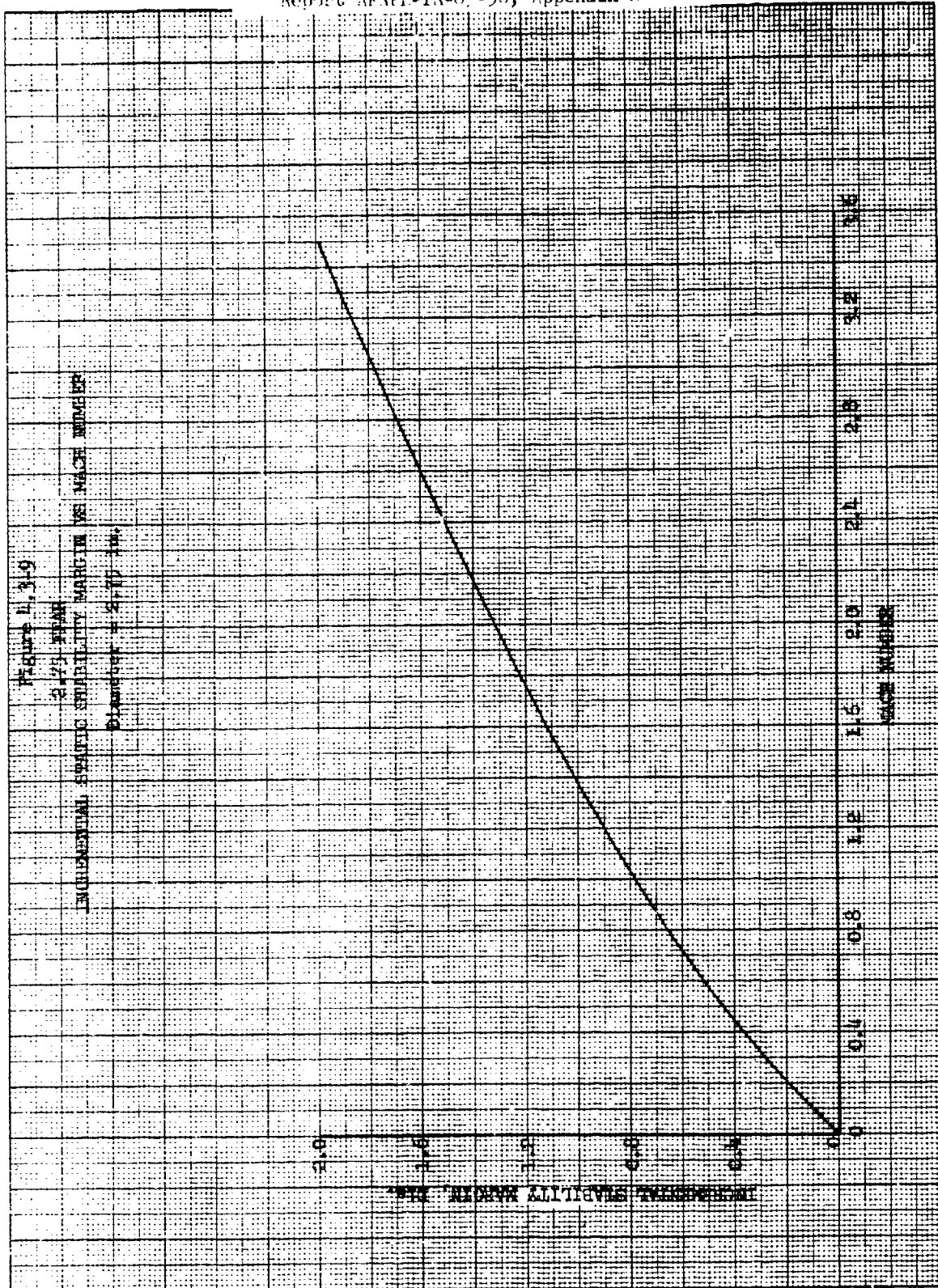
Report AFRPL-TR-69-90, Appendix A



UNCLASSIFIED

UNCLASSIFIED

Report AF3PI-TR-00-00, Appendix A

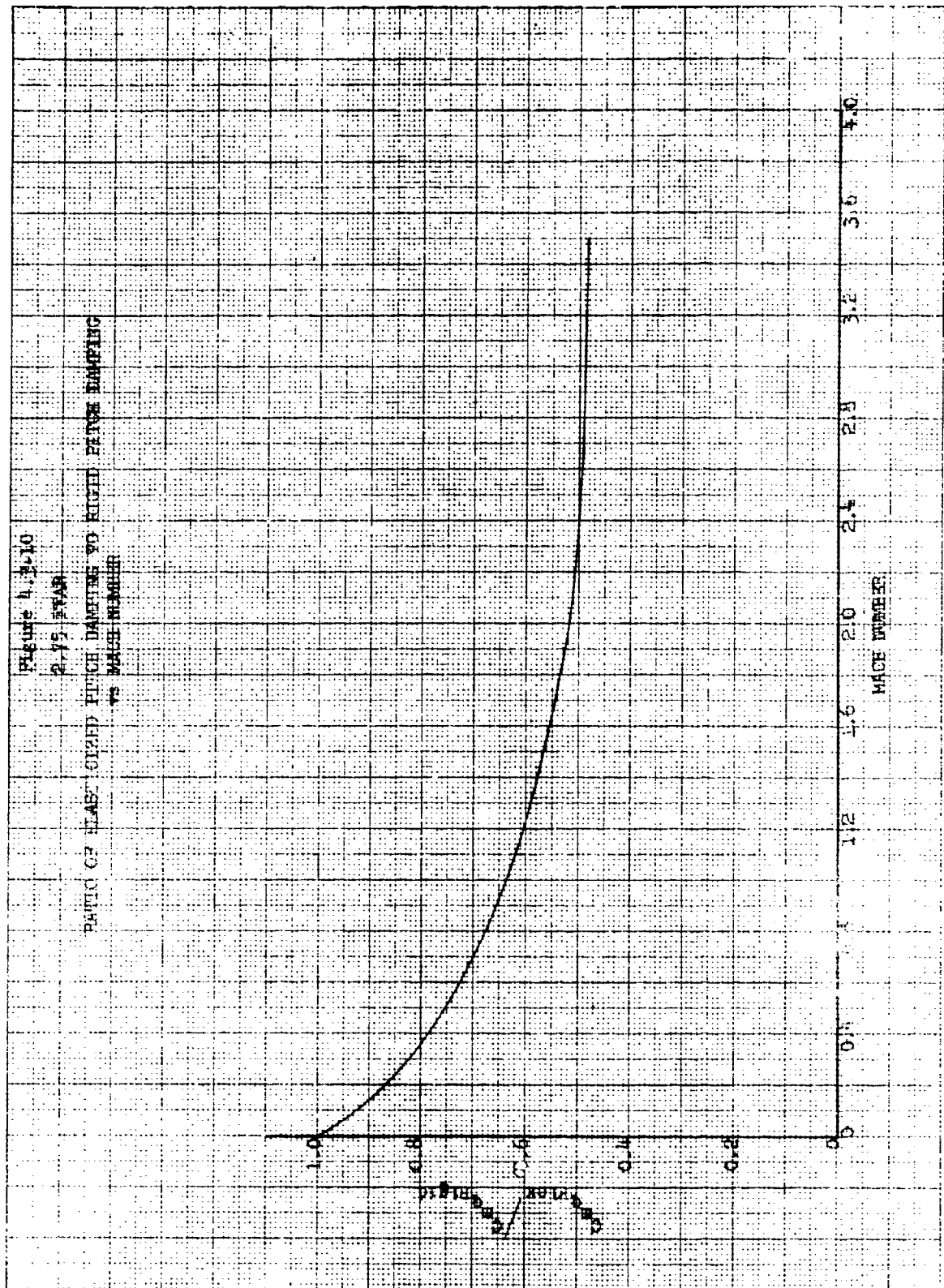


UNCLASSIFIED



UNCLASSIFIED

Report AFRPL-TR-69-90, Appendix A



UNCLASSIFIED

Page 45



# UNCLASSIFIED

Report AFRPL-TR-69-90, Appendix A

## 4.3.3.4 LOADS

### 4.3.3.4.1 General Discussion

In order to ensure the structural integrity of the vehicle, a flight loads analysis was performed. Much of the hardware under consideration has already been flight proven. However, the loads producing environment of this application is sufficiently more severe than previous applications to warrant such an analysis.

The work done for the aeroelastic analysis is directly applicable to the loads analysis. The aeroelastic analysis, for example, provides stability margin data from which the angle of attack may be determined. It also provides the elasticized distributions of shear and bending moment along the vehicle.

Two design body load conditions were considered. These were the maximum lateral load condition and the maximum axial load condition. These loads are discussed in the following sections.

### 4.3.3.4.2 Maximum Body Load Condition

The maximum lateral body load condition occurs at the time when

$C_{N_\alpha} \alpha q$  is a maximum, where:

$C_{N_\alpha}$  = Vehicle lift curve slope

$\alpha$  = Angle of attack

$q$  = Dynamic pressure

The determination of the rigid body conditions at the critical time where this occurs is discussed in Section 4.2. The critical time proved to be at 2.0 sec. The rigid body condition parameters prevailing at this time are as follows:

Time = 2.0 sec

Mach No. = 3.36

Dynamic Pressure = 16,591 psf

$3\sigma$  Rigid Body Angle of Attack = 0.805 deg.

UNCLASSIFIED

# UNCLASSIFIED

Report AFRPL-TR-69-90, Appendix A

The loads calculations must be based on elastic body angles of attack. The relationship used to determine the elasticized angle of attack is:

$$\alpha_F = \alpha_R \left( \frac{C_{N_{\alpha_R}} \Delta X_R}{C_{N_{\alpha_F}} \Delta X_F} \right)^{\frac{1}{2}}$$

where:

- $C_{N_{\alpha_R}}$  = Rigid body normal force curve slope
- $C_{N_{\alpha_F}}$  = Elastic body normal force curve slope
- $\alpha_R$  = Rigid angle of attack
- $\alpha_F$  = Elastic body angle of attack
- $\Delta X_R$  = Rigid body static stability margin
- $\Delta X_F$  = Elastic body static stability margin

The foregoing relationship is discussed in detail in Reference 3.

To obtain elastic body loads, the aeroelastic computer program is run first for an arbitrary angle of attack (say 1.0 degree). This provides the elasticized  $C_{N_{\alpha}}$  and  $\Delta X_F$  required to compute the elasticized angle of attack. The same data is then rerun with the actual value of the elasticized angle of attack to provide design values of shear and bending moment.

The rigid body angle of attack, as stated before, is 0.805 degrees. Consideration of elastic effects using the above relationship raises this value to 1.12 degrees.

The net limit design shears and bending moments for the maximum lateral load condition are presented in Figures 4.3-14 and 4.3-15. The distributed inputs used to determine these loads are the same as those used for the Mach 3.5 condition discussed in the aeroelastic analysis presented in Section 4.3.3.3.

UNCLASSIFIED

# UNCLASSIFIED

Report AFRPL-TR-69-90, Appendix A

## 4.3.3.4.3 Maximum Axial Load Condition

The maximum axial load condition occurs at the time of maximum axial acceleration for a 200 kt launch. The condition parameters at this time are:

t	= 1.87 sec
Mach number	= 2.77
Axial Acceleration	= 46.8 g's
Thrust	= 915 lb
Drag	= -237 lb

The mass distribution used for this condition is presented in Figure 4.3-12. The drag was assumed as a concentrated load acting at the base of the nose cone. The net limit design distribution of axial load based on this data is presented in Figure 4.3-16.

## 4.3.3.4.4 Maximum Fin Loads

The maximum design fin loads are discussed in Section 4.2. They occur at .08 seconds as the rocket leaves the launcher. No aeroelastic corrections were made to these loads since the dynamic pressures are quite low at this time. These rigid fin loads will be conservative in nature since aeroelastic effects would move the spanwise center of pressure inboard, thus reducing the bending moments. The rigid fin loads will be restated here, however, for completeness. The 3 $\sigma$  loads at the base of the fin are:

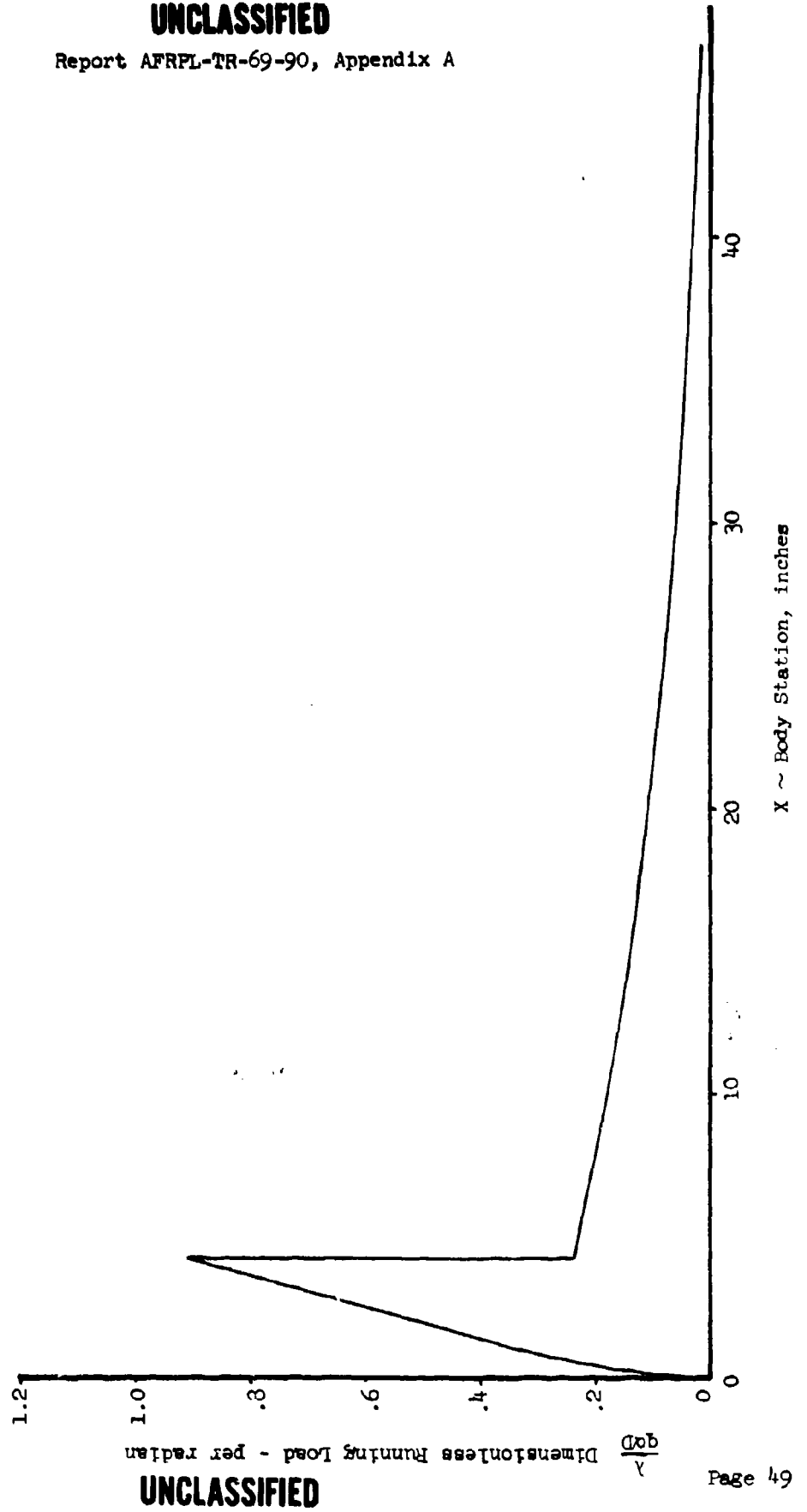
Fin Load	= 50.4 lb
Bending Moment	= 105.6 in-lb
Torsion	= 15.7 in-lb

UNCLASSIFIED

# UNCLASSIFIED

Report AFRPL-TR-69-90, Appendix A

Figure 4.3-11  
2.75 FFAR Vehicle  
Body Running Load at  $M = 1.4, 2.4, 3.5$   
Ref. Area  $5.94 \text{ in}^2$   
Ref. Length  $2.75 \text{ in.}$



UNCLASSIFIED

UNCLASSIFIED

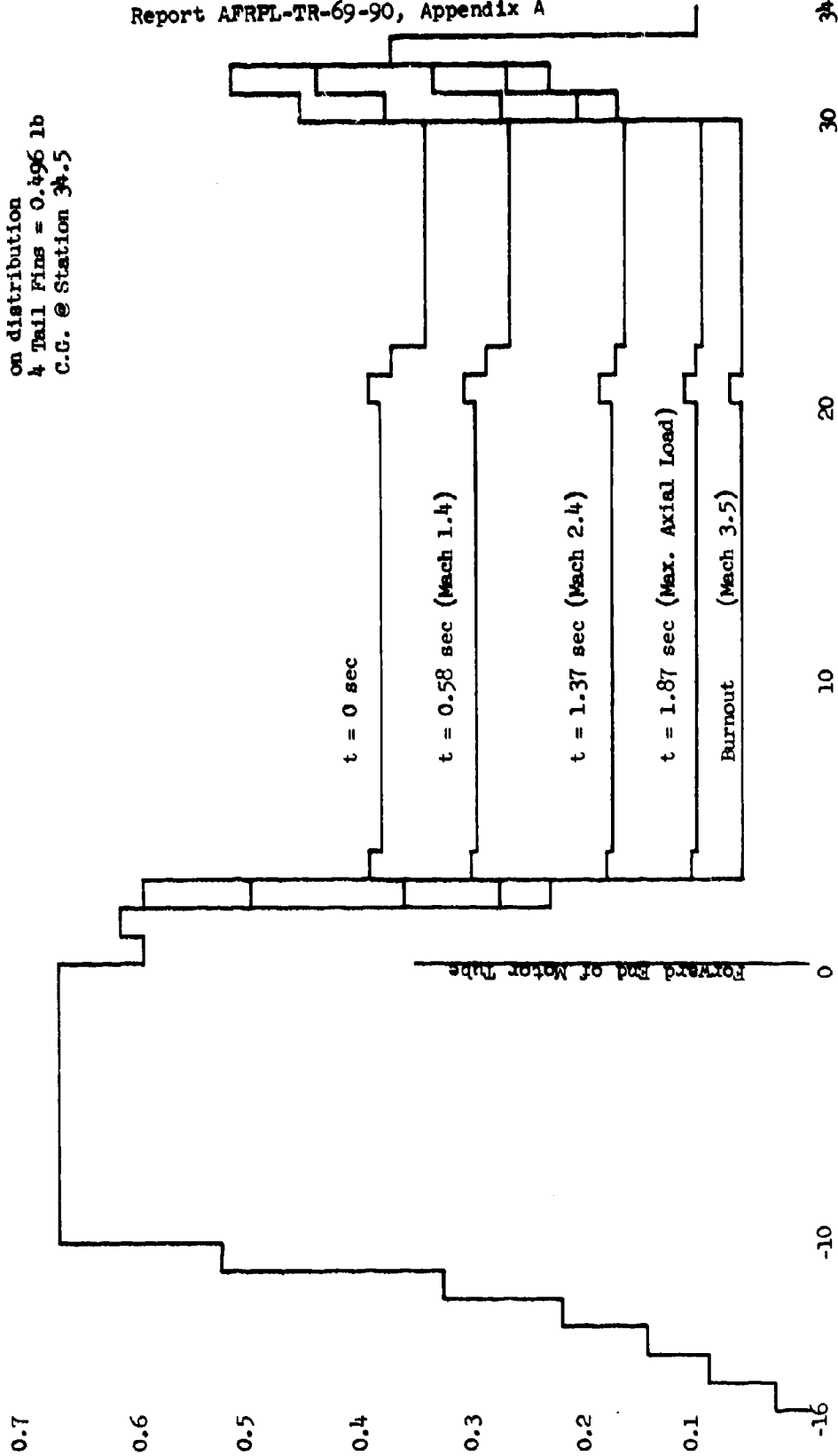
Report AFRPL-TR-69-90, Appendix A

Figure 4.3-12

2.75 FFAR

MASS DISTRIBUTION

Note: Tail Fins are not shown  
on distribution  
4 Tail Fins = 0.496 lb  
C.G. @ Station 34.5



UNCLASSIFIED

UNCLASSIFIED

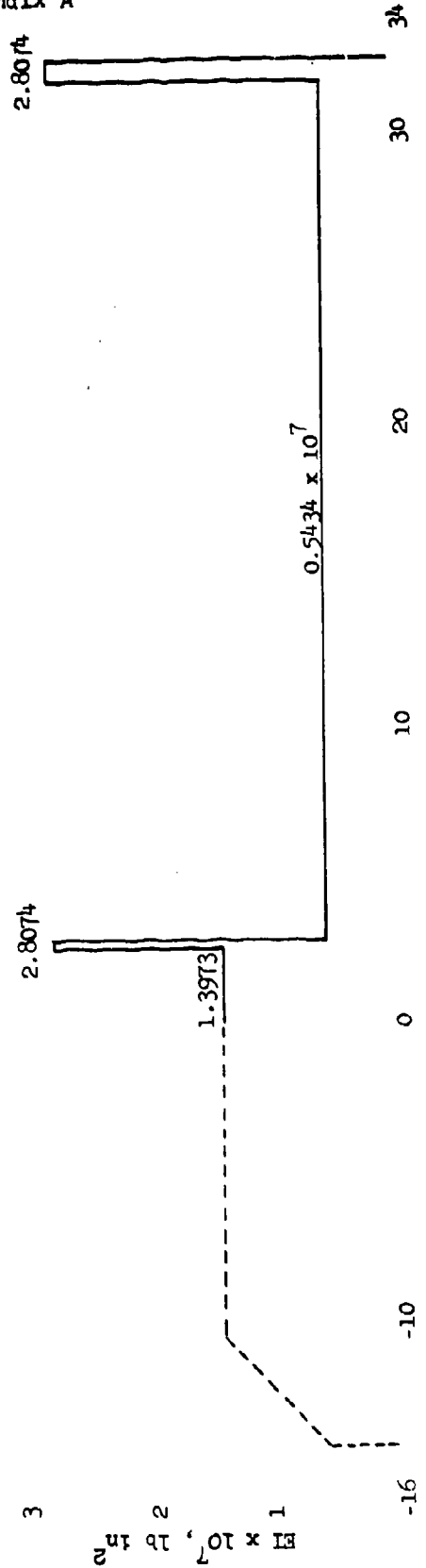
Report AFRPL-TR-69-90, Appendix A

Figure 4.3-13  
2.75" FFAR EI Distribution

Note: Motor station "0" is at forward end of motor tube.  
Payload EI (dotted line) is very rough estimate.

(Aft End)

(Forward End)

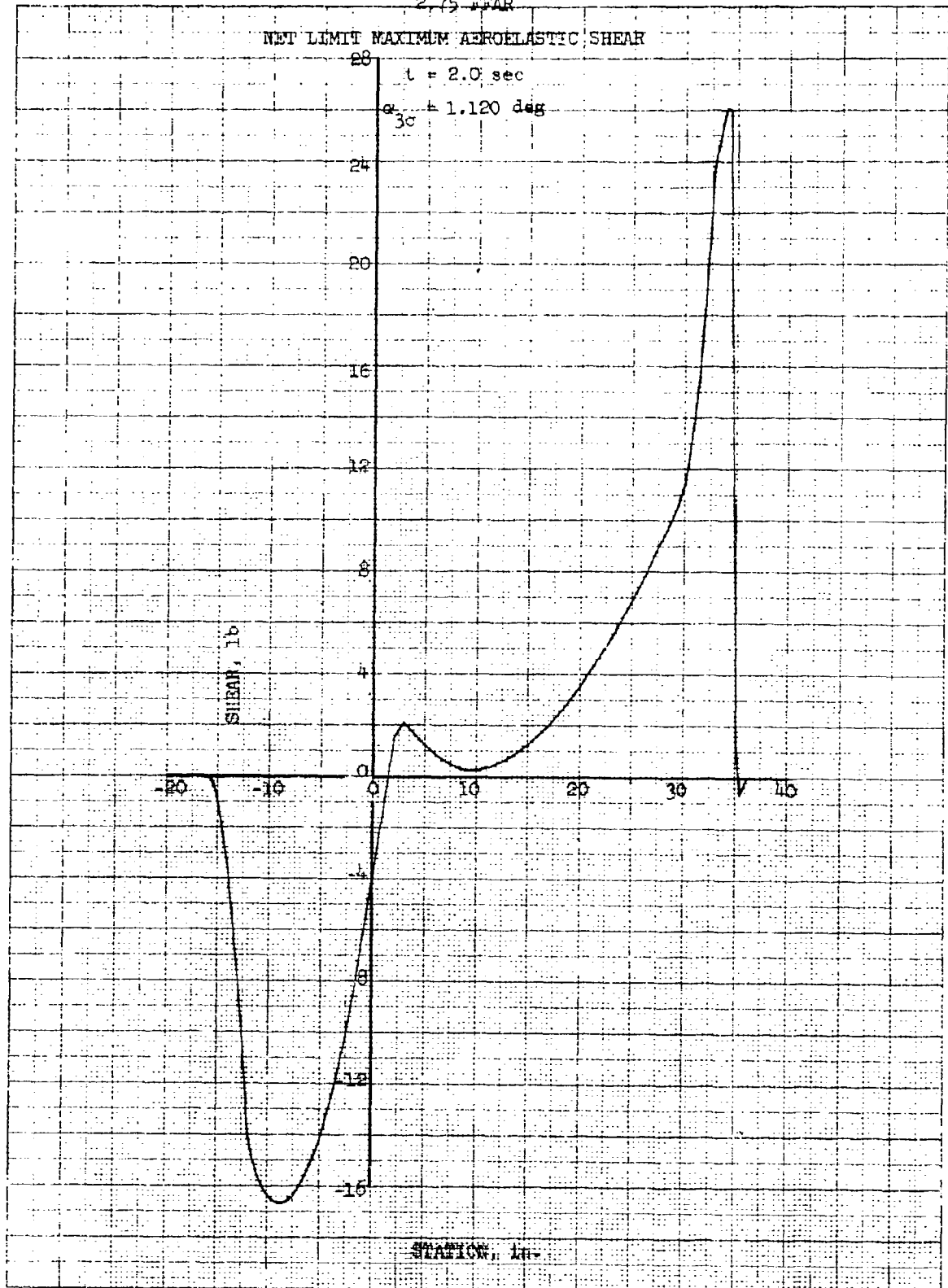


UNCLASSIFIED

UNCLASSIFIED

Report AFRPL-TR-69-90, Appendix A  
Figure 4.3-14

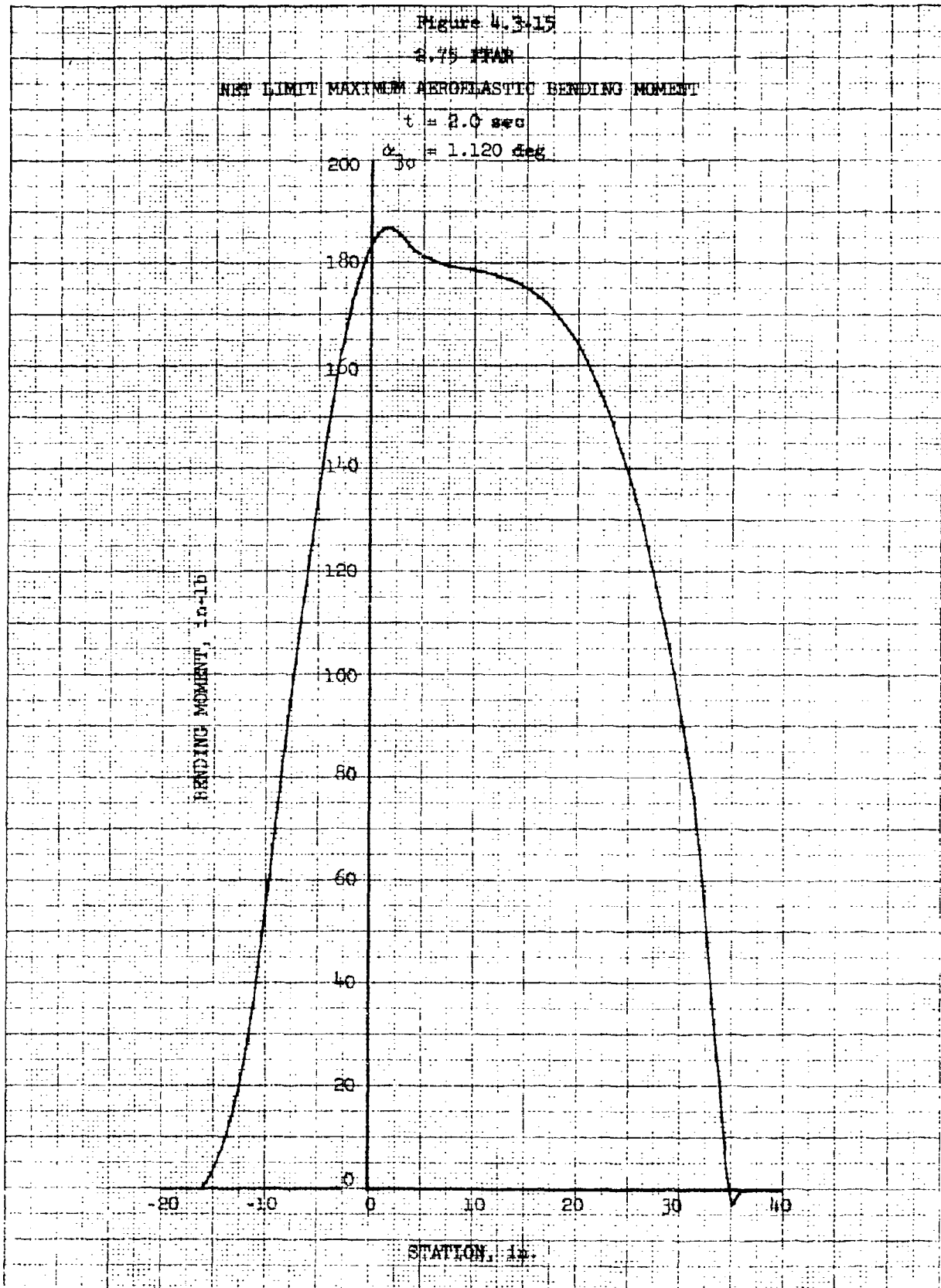
2.75 FFAR



UNCLASSIFIED

UNCLASSIFIED

Report AFRPL-TR-69-90, Appendix A

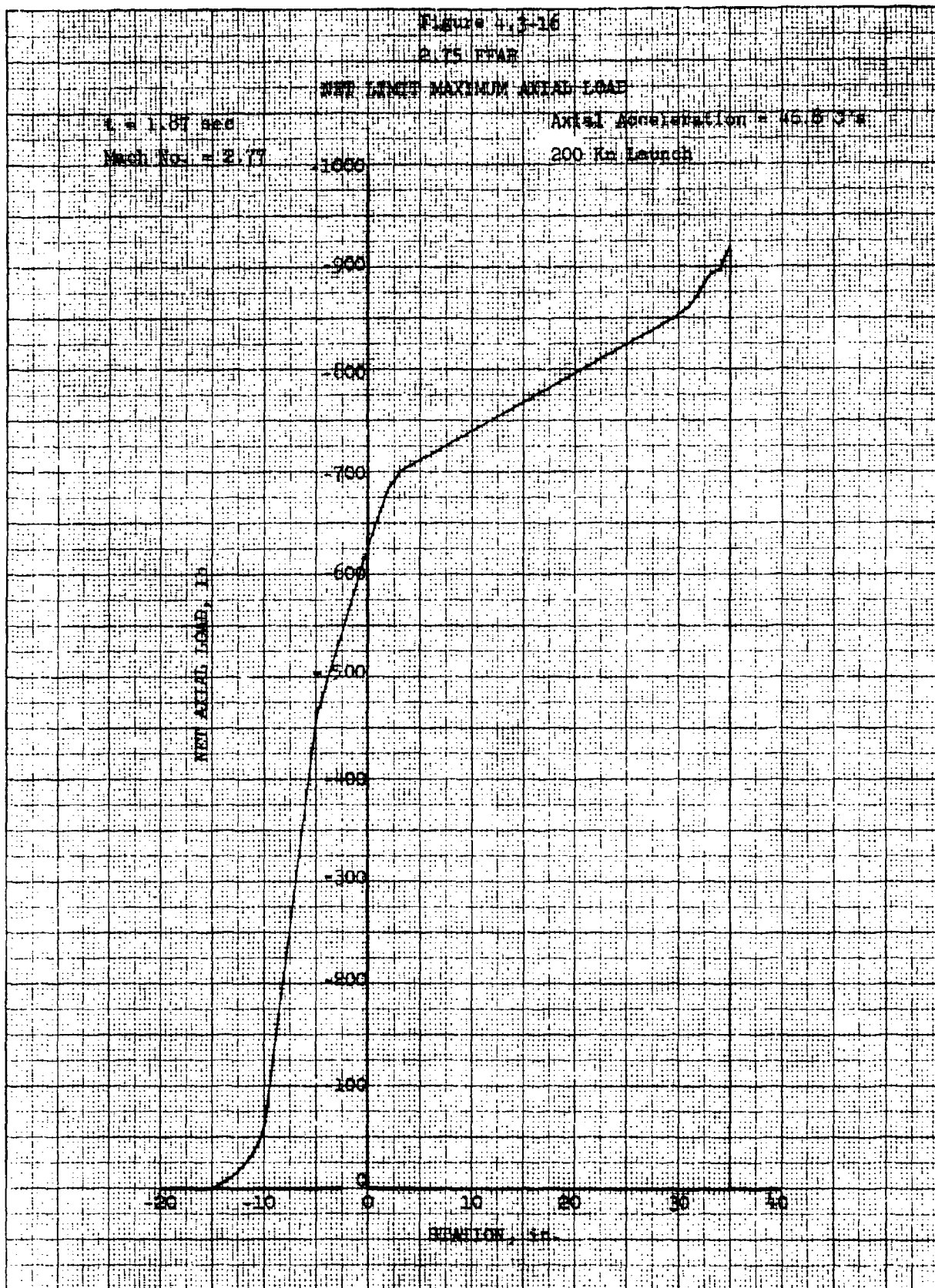


UNCLASSIFIED



# UNCLASSIFIED

Report AFRPL-TR-69-90, Appendix A



UNCLASSIFIED

## UNCLASSIFIED

Report AFRPL-TR-69-90, Appendix A

### 4.3.3.5 REFERENCES

1. Arnold, R.P., "Determination of Free-Free Static Aeroelastic Vehicle Loads, by Means of a Digital Computer Solution," Space-General Corporation IR&D Report No. 8, 20 Feb. 1964.
2. Arnold, R.P., "Addition of Cantilever Masses to the Static Aeroelastic Computer Program, D-60," Space-General Memo 5138:MO373, 10 August 1967.
3. Ernest, A.W., "Aerobee 350 Loads Changes due to Aeroelastic Shifts in Static Margin," Space-General Memo No. 5130:MO159, 16 December 1963.
4. Farrell, R.F., "A Rapid Method for Determination of Supersonic Line Aerodynamic Influence Coefficients," Bell Aircraft Report No. 9001-914002, 30 October 1956.
5. Bisplinghoff, R.F., Ashley, H., Halfman, R.T., "Aeroelasticity" Addison Wesley Publishing Company, Inc., Reading, Mass., 1955.

UNCLASSIFIED

# UNCLASSIFIED

Report AFRPL-TR-69-90, Appendix A

## 4.4 AERODYNAMIC HEATING

### 4.4.1 INTRODUCTION

This section of the report covers the aerodynamic heating analysis that was conducted for the fin and the rocket motor case. Section 4.4.2 discusses the heating on the fin and the resultant temperature histories. Section 4.4.3 discusses the analysis of the thermal elastic stress produced in the fin due to the temperature distribution across the fin span. The heating of a point on the rocket motor case is covered in Section 4.4.4. The trajectory used in the heating analysis was the 600 knot launch trajectory shown in Vol. II. The 600 knot launch was used in all cases. All temperatures were calculated by means of the "Aerodynamic Heating and Ablation" computer program which is discussed in the Section 4.4.5.

### 4.4.2 FIN HEATING

The three points on the fin cross-section for which temperatures have been calculated are shown in Figure 4.4-1. The cross-section is located at one-half of the fin span. Figure 4.4-2 shows the temperature histories for the three points. Figure 4.4-3 shows the maximum temperature distribution through the cross-section at 2.57 seconds after launch. The temperature distribution between  $X = .633$  and  $X = 1.266$  inches was estimated by the following approximation in the absence of radiation effects:

$$T \sim q \sim \frac{1}{\sqrt{X}}$$

based on laminar flat plate aerodynamic heat transfer.

The temperatures shown in the aforementioned figures are outside wall temperatures. However, the temperatures on the centerline of the cross-section were also determined and found to lag the outside temperatures by only a few °F at any time.

UNCLASSIFIED

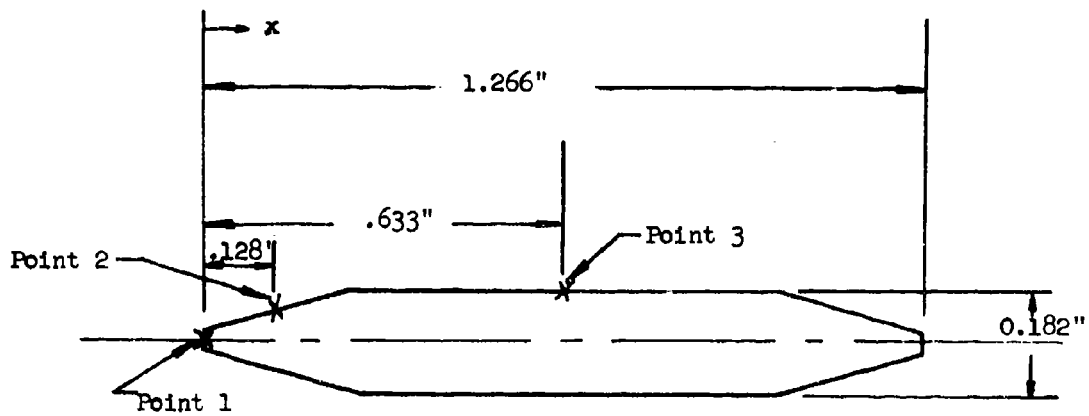
# UNCLASSIFIED

Report AFRPL-TR-69-90, Appendix A

Figure 4.4-1

2.75" FFAR

Fin Cross-Section Showing Temperature Points

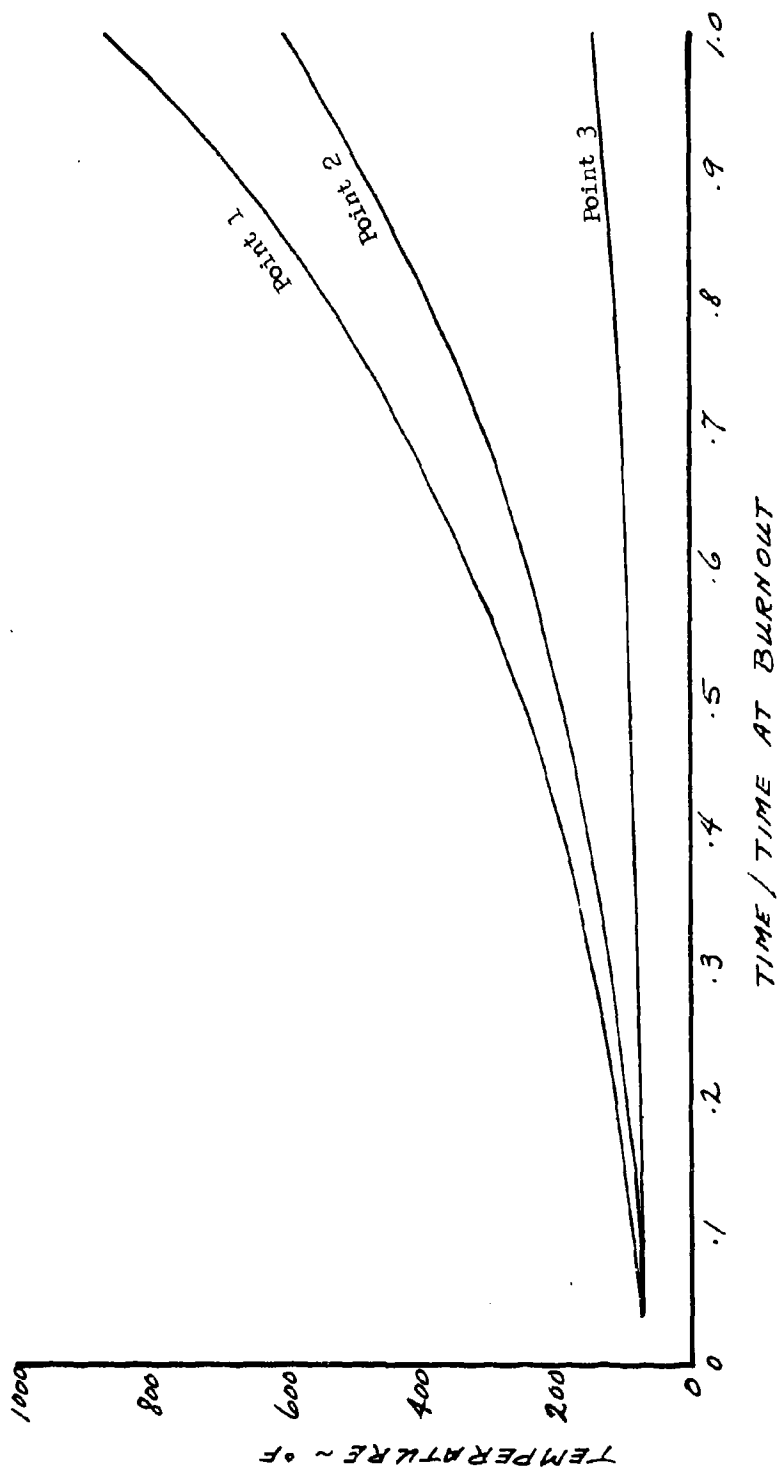


UNCLASSIFIED

UNCLASSIFIED

Report AFRPL-TR-69-90, Appendix A

Figure 4.4-2  
2.75" FFAR  
Temperature History for Three Fin Points

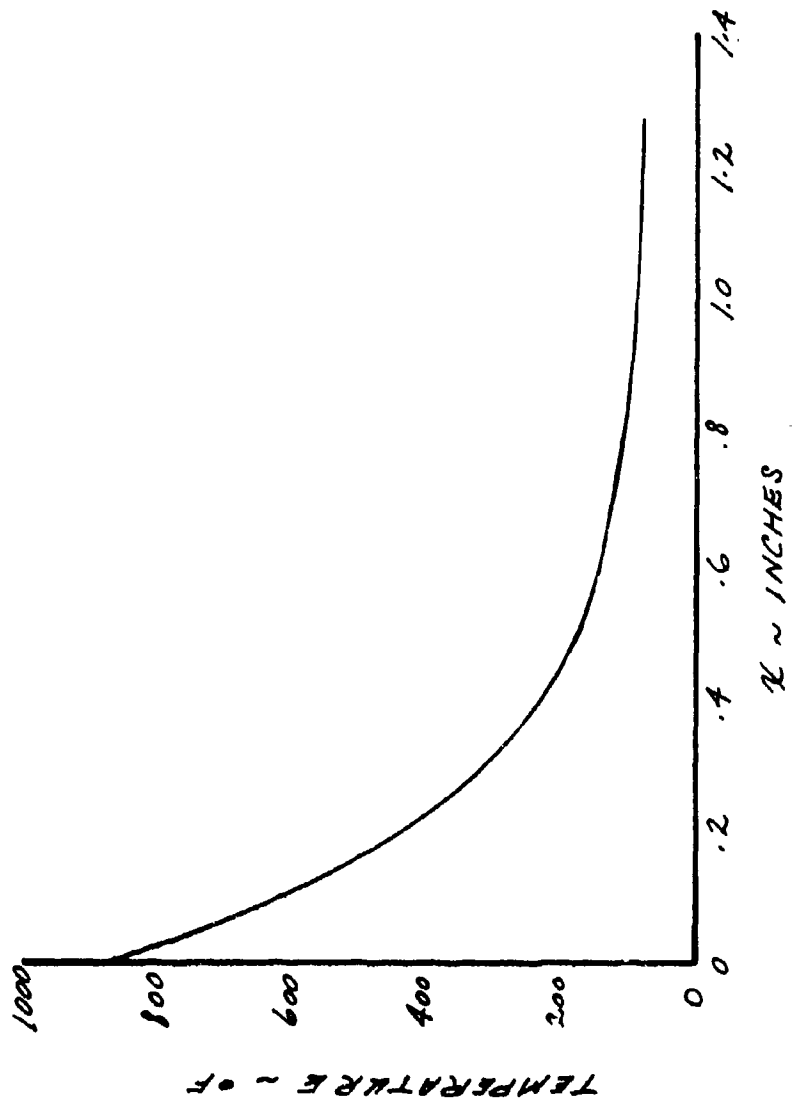


UNCLASSIFIED

UNCLASSIFIED

Report AFRPL-TR-69-90, Appendix A

Figure 4.4-3  
2.75" FFAR  
Fin Span Temperature at Burnout



UNCLASSIFIED

# UNCLASSIFIED

Report AFRPL-TR-69-90, Appendix A

The aerodynamic heating program that was used to calculate the various fin temperatures is restricted to one-dimension conduction at any point. However, due to the relatively high conductivity of aluminum and small fin cross-section and with convection applied to all sides of the fin, the problem becomes strongly two-dimensional. Based on previous experience and an approximate hand calculation the entire front wedge section of the fin was found to be at a temperature just slightly higher than 600°F and the temperature distribution through the cross-section was much more equalized.

## 4.4.3 AEROTHERMOELASTIC ANALYSIS OF THE FINS

Due to thermal gradients existing throughout the cross-section of the fin, thermoelastic stresses are set up with resultant component forces along the length of the fin. If a torque is now applied about the fin elastic axis, rotation of these stress resultants results in an additional torque. The net effect is a reduction of the effective torsional rigidity of the fin which can, in some cases, cause large aeroelastic effects. A brief analysis is carried out below to show that this problem is not significant for the fins employed here.

The stress in the fin cross-section caused by the temperature distribution was calculated by means of the following one-dimensional stress equation taken from Reference (1).

$$\sigma = -E\alpha \Delta T + E \left[ \frac{\int_A (E \alpha \Delta T) dA}{\int_A d(EA)} + \frac{x \int_A (E \alpha \Delta T) dA}{\int x^2 d(EA)} \right]$$

where:

- E is the temperature dependent modules of elasticity
- $\alpha$  is the coefficient of thermal expansion
- $\Delta T$  is the temperature change with time
- x is the cross-section axis distance
- A is the cross-sectional area.

UNCLASSIFIED

# UNCLASSIFIED

Report AFRPL-TR-69-90, Appendix A

The integrals were evaluated by hand for various points along the centerline of the cross-section. In applying this equation, the effect of temperature on Young's modulus, E, must also be accounted for.

The resultant effective reduction in torsional stiffness due to thermal stresses was calculated by means of the following equation from Reference 1. The ratio of effective torsional stiffness, GJ, to torsional stiffness without thermal stress,  $GJ_0$ , is

$$\frac{GJ}{GJ_0} = 1 + \frac{1}{GJ_0} \int \int_A \sigma(x^2 + z^2) dx, dz$$

The decrease in torsional stiffness was 204 lb-in<sup>2</sup>. This was a decrease of only 2.5 percent which is completely negligible.

In view of the somewhat approximate nature of the equations applied, a brief analysis was carried out to establish the significance of GJ variations in the present application. This was done employing a simple two-mode Galerkin's method computation as follows.

Taking  $\theta$  to be torsional rotation about the elastic axis,  $y$  the distance from the root along the elastic axis, and  $\delta$  the vertical deflection of the elastic axis we have

$$\frac{d\theta}{dy} = \frac{T}{GJ}$$

$$\frac{d^2\delta}{dy^2} = \frac{M}{EI}$$

and the incremental aeroelastic angle of attack is

$$\Delta\alpha \approx \theta \cos \Lambda - \frac{d\delta}{dy} \sin \Lambda$$

where  $\Lambda$  is the sweep angle.

UNCLASSIFIED



# UNCLASSIFIED

Report AFRPL-TR-69-90, Appendix A

The torque and bending moments are found as

$$T = \int_y^{\ell} \ell_{\alpha} (\alpha_R + \Delta\alpha) x dy'$$

and

$$M = \int_y^{\ell} \ell_{\alpha} (\alpha_R + \Delta\alpha)(y'-y) dy'$$

where  $\ell_{\alpha}$  is running load per unit angle of attack,  $\alpha_R$  is the rigid fin angle of attack, and  $x$  is the arm from the elastic axis to the line of aerodynamic centers. Using the above equations, it is apparent that  $\theta$  and  $\frac{d\delta}{dy}$  may be expressed as integral equations (i.e., having  $\theta$  and  $\frac{d\delta}{dy}$  also in the integrands). To apply Galerkin's method, we assume

$$\theta \approx k_1 y$$

and

$$\frac{d\delta}{dy} \approx k_2 y$$

i.e., linear twist and parabolic bending. The constants  $k_1$  and  $k_2$  are chosen to yield the best average values along the span by requiring

$$\int_0^{\ell} (\theta - k_1 y) dy = 0$$

and

$$\int_0^{\ell} \left( \frac{d\delta}{dy} - k_2 y \right) dy = 0.$$

The integral expressions obtained from the moment equations are substituted for  $\theta$  and  $\frac{d\delta}{dy}$  in these equations and then the  $\theta$  and  $\frac{d\delta}{dy}$  under the integrals are approximated by  $k_1 y$  and  $k_2 y$ . Carrying out the integrations results in two simultaneous algebraic equations for  $k_1$  and  $k_2$ . Setting the determinant of these equations equal to zero yields an equation for the divergence condition (i.e., the dynamic pressure at which an infinitesimal rigid angle of attack would produce a finite flexible angle of attack). The

UNCLASSIFIED

# UNCLASSIFIED

Report AFRPL-TR-69-90, Appendix A

resultant expression is

$$\left( q C_{N_{\alpha_T}} \right)_{\text{Divergence}} = \frac{2 \overline{EI}}{S_{\text{Ref}} l \cos \Lambda \left[ \frac{5}{12} \frac{\overline{EI}}{\overline{GJ}} x - \frac{11}{60} l \tan \Lambda \right]}$$

where  $q$  is dynamic pressure and  $C_{N_{\alpha_T}}$  is the tail lift curve slope based on area  $S_{\text{Ref}}$ .  $\overline{EI}$  and  $\overline{GJ}$  are some average values along the fin.

As expected for this highly swept fin, the  $q_{\text{Divergence}}$  is negative. Moreover, the first term in the bracket in the denominator is less than 1% of the second in the case of the 2.75 in. FFAR fin, i.e., torsion effects are negligible compared to bending. Therefore, the reduction in  $\overline{GJ}$  would have to be by a factor on the order of 10 in order to significantly affect the result.

It is concluded that aerothermoelastic effects are negligible for this fin.

## 4.4.4 MOTOR CASE HEATING

The wall temperature was calculated for a point on the motor case located at Station 35.40. The analysis considered an aluminum wall 0.070 inches thick. An adiabatic surface was assumed at the inside surface of the wall.

The temperature history for the outside of the motor case is shown in Figure 4.4-4. The inside temperature followed the outside temperature by a few degrees at any time.

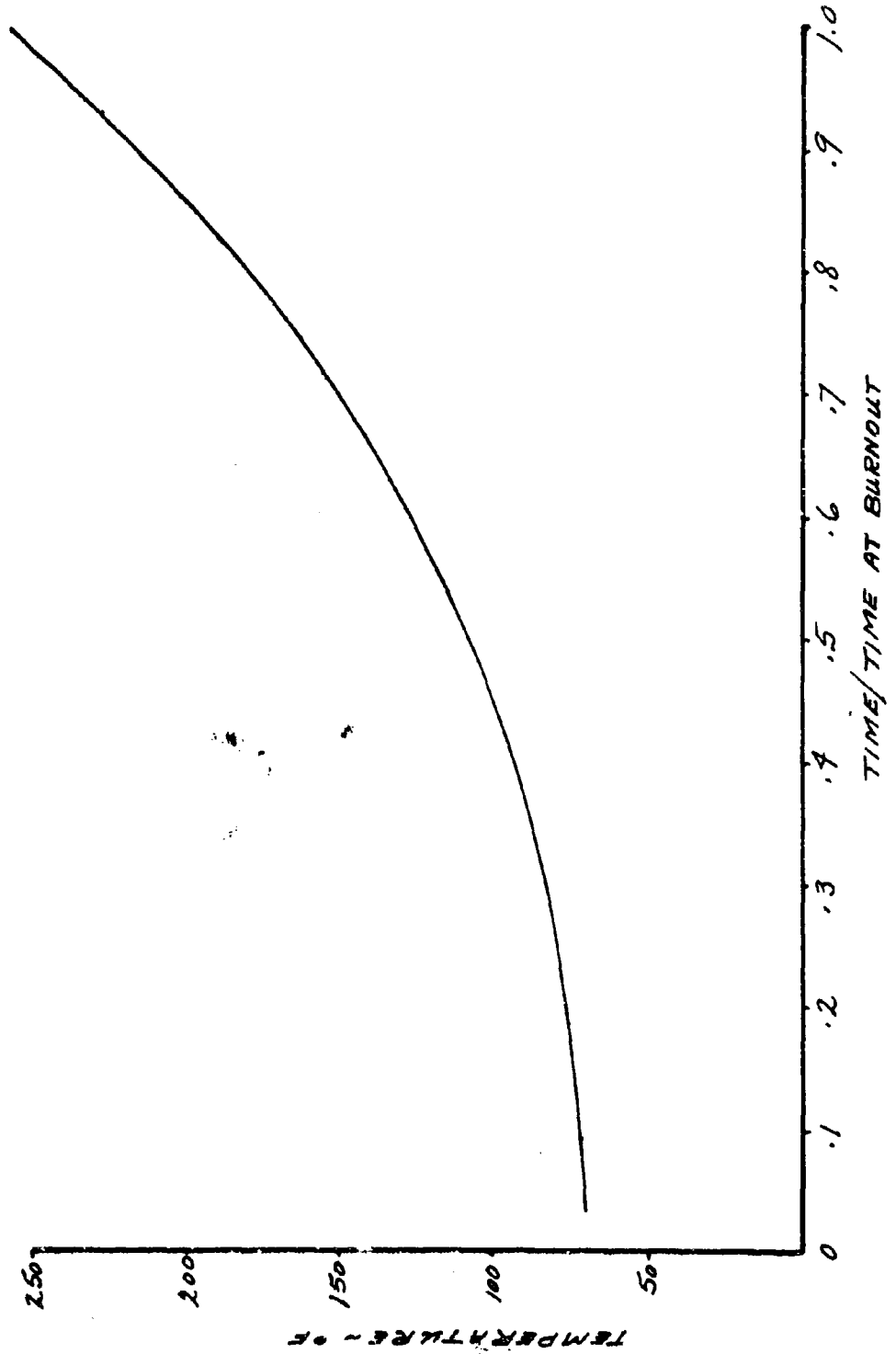
## 4.4.5 AERODYNAMIC HEATING AND ABLATION PROGRAM

The program analyzes the thermodynamic, mechanical, and chemical behavior of high speed body heat protection system following a specified trajectory. The energy balance, a non-linear, parabolic, partial differential equation for heat conduction through a one-dimensional medium, is solved

# UNCLASSIFIED

Report AFRPL-TR-69-90, Appendix A

Figure 4.4-4  
2.75" FFAR  
Motor Case Temperature History



UNCLASSIFIED

## UNCLASSIFIED

Report AFRPL-TR-69-90, Appendix A

using a finite difference approximation. Solution of the finite difference equations by the explicit method gives the temperature, density, and mass depolymerization profiles through the primary material, and the temperature profile through the secondary materials of the heat protection system as a function of time. The solution of the aerodynamic equations; which describe the mass and energy balances about the surface of the heat protection system, gives the surface heat and the mass flux which are used as boundary conditions for the finite difference equations.

### 4.4.6 REFERENCES

1. Bisplinghoff, R.L. "Some Structural and Aeroelastic Considerations of High-Speed Flight", JAS, April 1956, Vol. 23, No. 4.

UNCLASSIFIED

# UNCLASSIFIED

Report AFRPL-TR-69-90, Appendix A

## 5.0 APPENDICES

### 5.1 PRELIMINARY ANALYSIS

#### 5.1.1 AERODYNAMICS

For the preliminary aerodynamic data used as inputs to the digital computer, the data of References 1 and 2 were used. In the subsequent paragraphs of this section, the resulting data will be presented and an explanation of how these were determined.

##### 5.1.1.1 SYMBOLS AND NOMENCLATURE

$A_B$	Base area, $\text{ft}^2$
$C_A$	Axial force coefficient (from References 1 and 2 with zero base drag)
$C_{D_B}$	Base drag coefficient
$C_{D_f}$	Skin friction drag coefficient
$C_{D_0}$	Zero lift drag coefficient
$C_{l_p}$	Roll damping derivative, per radian
$C_{l_o}$	Roll driving derivative, per radian
$C_{m_q}$	Pitch damping derivative, per radian
$C_{N_\alpha}$	Normal force coefficient slope, per radian
$C_{N_\delta}$	Normal force coefficient derivative, per radian (for deflecting two tail fins in pitch)
$d$	Body diameter, reference length, ft ( $d = .229$ ft)
$k_w, K_w, K_P$	Interference factors from Reference 6
$L$	Body length, ft
$\dot{m}$	Mass flow rate, slug/sec
$M$	Mach number
$M/\dot{\theta}$	Jet damping derivative, $\text{ft-lb/radian per second}$
$S_{\text{Ref}}$	Body cross-sectional area, reference area, $\text{ft}^2$ ( $S_{\text{Ref}} = .0495 \text{ ft}^2$ )
$X_{cp}$	Center of pressure location, ft
$(X_{cp}/d)$	Center of pressure, diameters
$X_{cg}$	Center of gravity location, ft
$X_t$	Distance to rocket motor nozzle, ft

UNCLASSIFIED

# UNCLASSIFIED

Report AFRPL-TR-69-90, Appendix A

$\alpha$  angle of attack, degrees  
 $\delta$  tail deflection, degrees

## 5.1.1.2 BASIC CHARACTERISTICS

The configuration used in these analyses is from References 1 and 2 and it is presented in Figure 4.1.1.

Three items are involved in the basic data for the Improved 2.75 FFAR. These are;  $C_{D_0}$ , zero lift drag coefficient,  $C_{N_\alpha}$ , normal force coefficient slope, and  $(X_{cp}/d)$  center of pressure. These data are presented in Figures 5.1.1-1, 5.1.1-2, and 5.1.1-3 as a function of Mach number.

The drag coefficient as a function of Mach number is presented in Figure 5.1.1-1. The data are presented for power-on and power-off. Basically, these data are the axial force coefficient data of References 1 and 2 corrected for skin friction drag (Reynold's number effect) and base drag. In this instance it was assumed the model and flight vehicle had aerodynamically smooth surfaces, and the data of Reference 3 were used to compute the skin friction drag correction. The form of the correction is shown below.

$$\Delta C_{D_f} = -\Delta C_{D_f \text{ model body}} - \Delta C_{D_f \text{ model tails}} + \Delta C_{D_f \text{ flight body}} + \Delta C_{D_f \text{ flight tails}}$$

This correction was applied to the experimental data in References 1 and 2. Since the axial force data in References 1 and 2 are for zero base drag, it is necessary to compute the power-off and power-on base drag coefficients to be added to the experimental data. The form of this computation is

$$\Delta C_{D_B} = -C_{P_B} \frac{A_B}{S_{Ref}}$$

The  $C_{P_B}$  data in Reference 4 were used in this application and the base area varied for power-off and power-on by the area of the four exit nozzles. The corrected drag coefficient as presented in Figure 5.1.1-1 was obtained using the expression below.

## UNCLASSIFIED

Report AFRPL-TR-69-90, Appendix A

$$C_{D_0} = C_A + \Delta C_{D_f} + \Delta C_{D_B}$$

Figure 5.1.1-2 presents the normal force coefficient slope as a function of Mach number. These data are presented for body alone and for body tail and are the values as determined from References 1 and 2 with no corrections. Similarly Figure 5.1.1-3 presents body and body-tail centers of pressure as a function of Mach number from References 1 and 2 and have no corrections applied. Figure 5.1.1-4 presents the tail center of pressure as a function of Mach number as computed from the data in Reference 5. These data are to be used in the fin misalignment part of the dispersion study.

### 5.1.1.3 CONTROL POWER AND ROTARY DERIVATIVES

Figure 5.1.1-5 presents  $C_{N_\delta}$ , the pitch tail power derivative, as a function of Mach number. The experimental data in conjunction with the data in Reference 6 were used to determine this derivative. The expression below presents the form of the  $C_{N_\delta}$  expression.

$$C_{N_\delta} = \frac{k_w}{K_w + K_B} \left[ C_{N_{\alpha_{BT}}} - C_{N_{\alpha_B}} \right]$$

The roll driving derivative is presented in Figure 5.1.1-6. Presented is  $C_{\ell_\delta}$  as a function of Mach number. This expression was obtained from the  $C_{N_\delta}$  derivative by using the expression below.

$$C_{\ell_\delta} = 2 C_{N_\delta} \left( \frac{y}{d} \right)$$

The  $\left( \frac{y}{d} \right)$  is a non-dimensional moment arm which represents the lateral center of pressure location from the vehicle axis of symmetry. The value (2) stems from the fact that the  $C_{N_\delta}$  expression on the previous page is for two tail panels.

UNCLASSIFIED

# UNCLASSIFIED

Report AFRPL-TR-69-90, Appendix A

The roll damping derivative,  $C_{l_p}$ , is presented as a function of Mach number in Figure 5.1.1-7. This was computed using the expression below.

$$C_{l_p} = -2 (2 C_{N_\delta}) \left(\frac{l}{d}\right)^2$$

In this instance the  $\left(\frac{l}{d}\right)$  is also a lateral center of pressure but for a triangular loading on the tail fins.

Figure 5.1.1-8 presents the pitch damping coefficient as a function of Mach number. These data were generated using the  $C_{N_\alpha}$  data from Figure 5.1.1-2. The expressions below were used.

$$\begin{aligned} C_{m_{q_{body}}} &= -2 C_{N_{\alpha_B}} \left[ \frac{L - X_{cg}}{d} \right]^2 \\ C_{m_{q_{tails}}} &= -2 C_{N_{\alpha_{BT-B}}} \left( \frac{X_{cp_T} - X_{cg}}{d} \right)^2 \\ C_{m_{q_{Total}}} &= C_{m_{q_B}} + C_{m_{q_T}} \end{aligned}$$

The jet damping derivative as a function of time is presented in Figure 5.1.1-9. This term was estimated using the equation below.

$$\frac{M}{\dot{\phi}} = \dot{m} (X_t - X_{cg})^2$$

This expression was obtained from Reference 7.

## 5.1.1.4 OPENING TRANSIENT CHARACTERISTICS

Some indication of the manner in which the fins are extended and the resultant variation in aerodynamic coefficients is necessary for a proper launch simulation. This was estimated for the preliminary work. For these

UNCLASSIFIED



# UNCLASSIFIED

Report AFRL-TR-69-90, Appendix A

estimates the launch tube was assumed to be body length and the fins remained closed until the missile completely emerged. The Mach number computed at this instant was  $M = 0.717$ . This assumes the airplane velocity was 750 ft/sec. To determine the time for the fins to become fully extended, experimental data from Reference 8 were used. These data indicated the fins had completely extended and locked at a distance of 2 to 3 feet from the launcher. A distance of 2.5 feet was used and the erection time was computed to be  $t = .04$  sec. This results in a vehicle flight Mach number of  $M = 0.722$  for fins fully effective. These estimates were used to show the opening transient in the aerodynamic coefficients.

No transient was determined for the drag coefficient.

Presented in Figure 5.1.1-10 is  $C_{N_\alpha}$  as a function of Mach number. The four major events are ignition, full missile emergence from the launcher, 50% fin extension (spanwise) and full fin extension. Each of these events has been located in terms of Mach number in a nominal trajectory. The ignition event occurs at  $M = 0.672$  and the vehicle has fully emerged from the launcher at  $M = 0.717$ . At this time the vehicle possesses body alone aerodynamic characteristics. The fins are fully extended at  $M = 0.722$  and the vehicle has the aerodynamic characteristics of the body-tail configuration. A point was computed for a 50% extension of the fins and located midway between the body and body-tail data. This results in a reasonable representation of the  $C_{N_\alpha}$  function during the launch phase.

Presented in Figures 5.1.1-11 through 5.1.1-15 are the other transient aerodynamic characteristics including center of pressure, pitch damping coefficient, pitch tail power derivative, roll driving coefficient, and other data. These data are shown in transition as the fins are extended.

UNCLASSIFIED

# UNCLASSIFIED

Report AFRPL-TR-69-90, Appendix A

## 5.1.1.5 REFERENCES

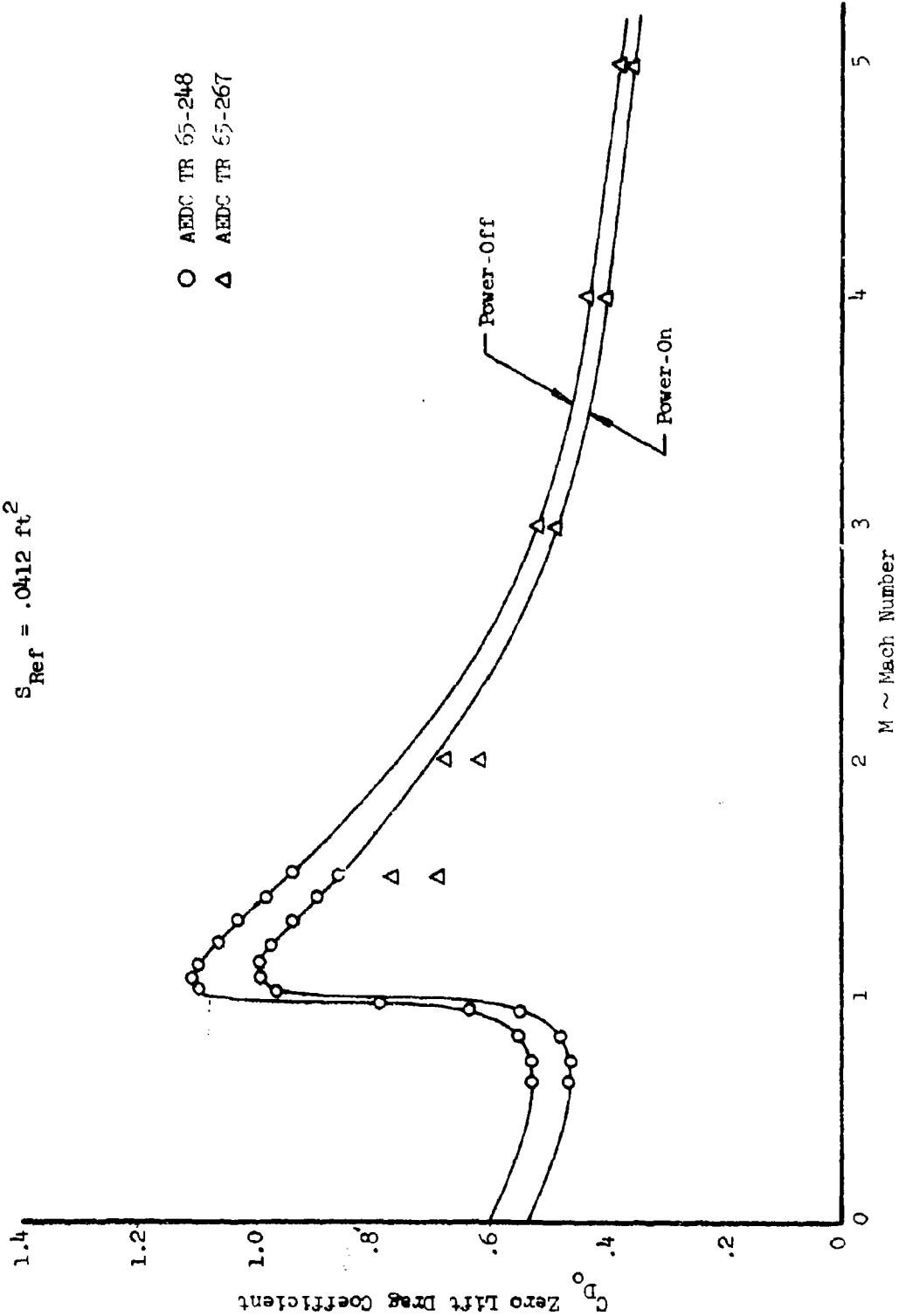
1. AEDC TR 65-248, "Wind Tunnel Tests of a 2.75 FFAR,  $M = 0.60$  to 1.50".
2. AEDC TR 65-267, "Wind Tunnel Tests of a 2.75 FFAR,  $M = 1.50$  to 5.0".
3. Journal of Aeronautical Sciences, "Turbulent Boundary Layer in Compressible Fluids", by E.R. VanDriest, Vol. 18, March 1951.
4. "Fluid Dynamic Drag", by Sighard Hoerner, 1958.
5. SGC TN 5135-0153, "Aerodynamic data for Swept and Tapered Wings", 1963.
6. NACA TR-1307, "Lift and Center of Pressure of Wing-Body-Tail Combinations at Subsonic, Transonic, and Supersonic Speeds", by W.C. Pitts, J.N. Nielsen, and G.E. Kaattari, 1957.
7. "Mathematical Theory of Rocket Flight" by J.B. Rosser, R.R. Newton, and G.L. Gross, McGraw-Hill Book Company, 1947.
8. "Interim Report on Launching Parameters for the 2.75 Inch AAFR Rocket", Fairbanks, D.H., NOTS TM No. 468, U.S. Naval Ordnance Test Station, Inyokern China Lake, Calif. 1951.

UNCLASSIFIED

# UNCLASSIFIED

Report AFRPI-TR-69-90, Appendix A

Figure 5.1.1.1-1  
Drag Coefficient as a Function  
of Mach Number Power-On  
 $S_{Ref} = .0412 \text{ ft}^2$

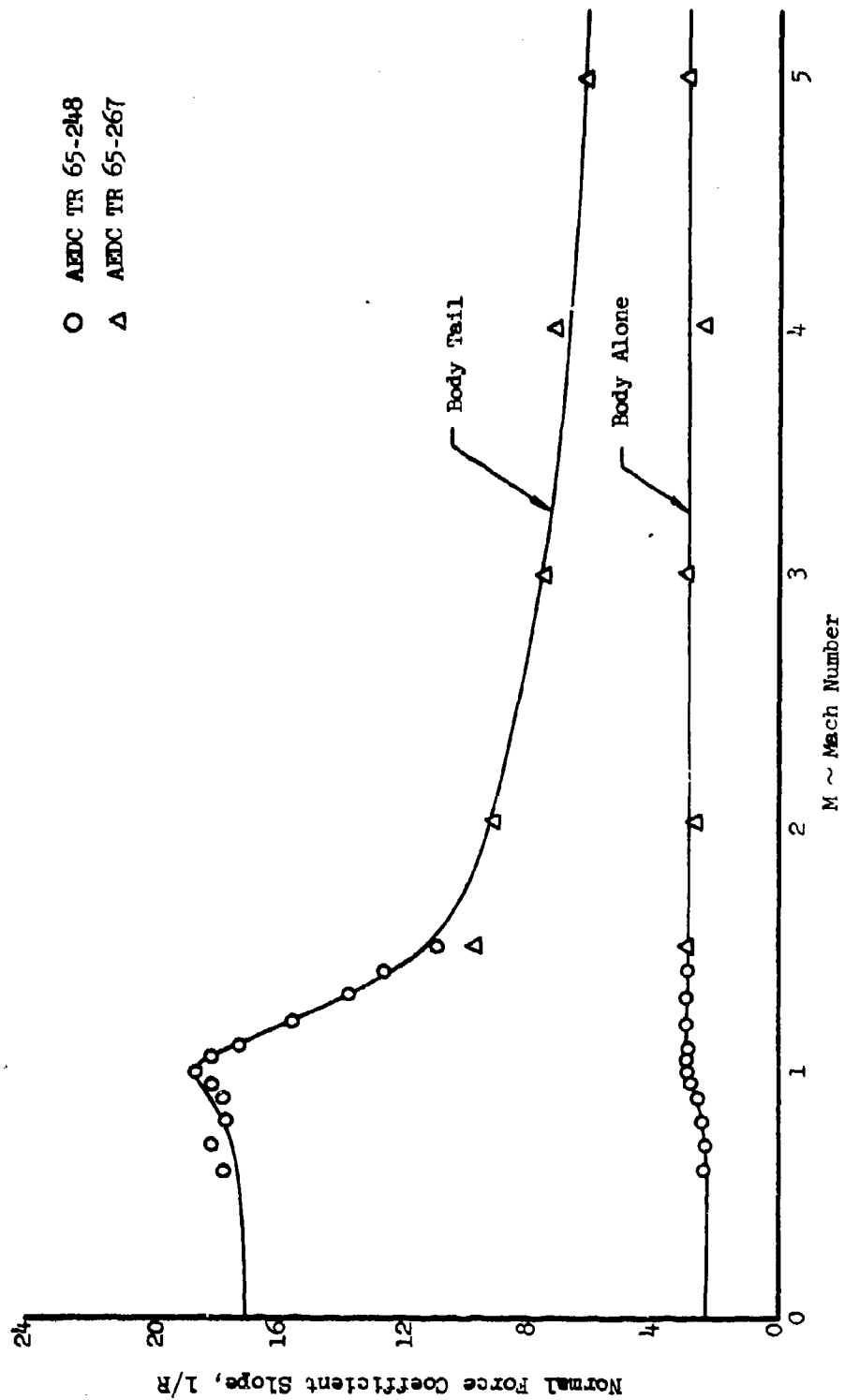


UNCLASSIFIED

UNCLASSIFIED

Report AFRPL-TR-69-90, Appendix A

Figure 5.1.1.1-2  
Normal Force Coefficient Slope  
as a Function of Mach Number  
 $S_{Ref} = .0412 \text{ ft}^2$

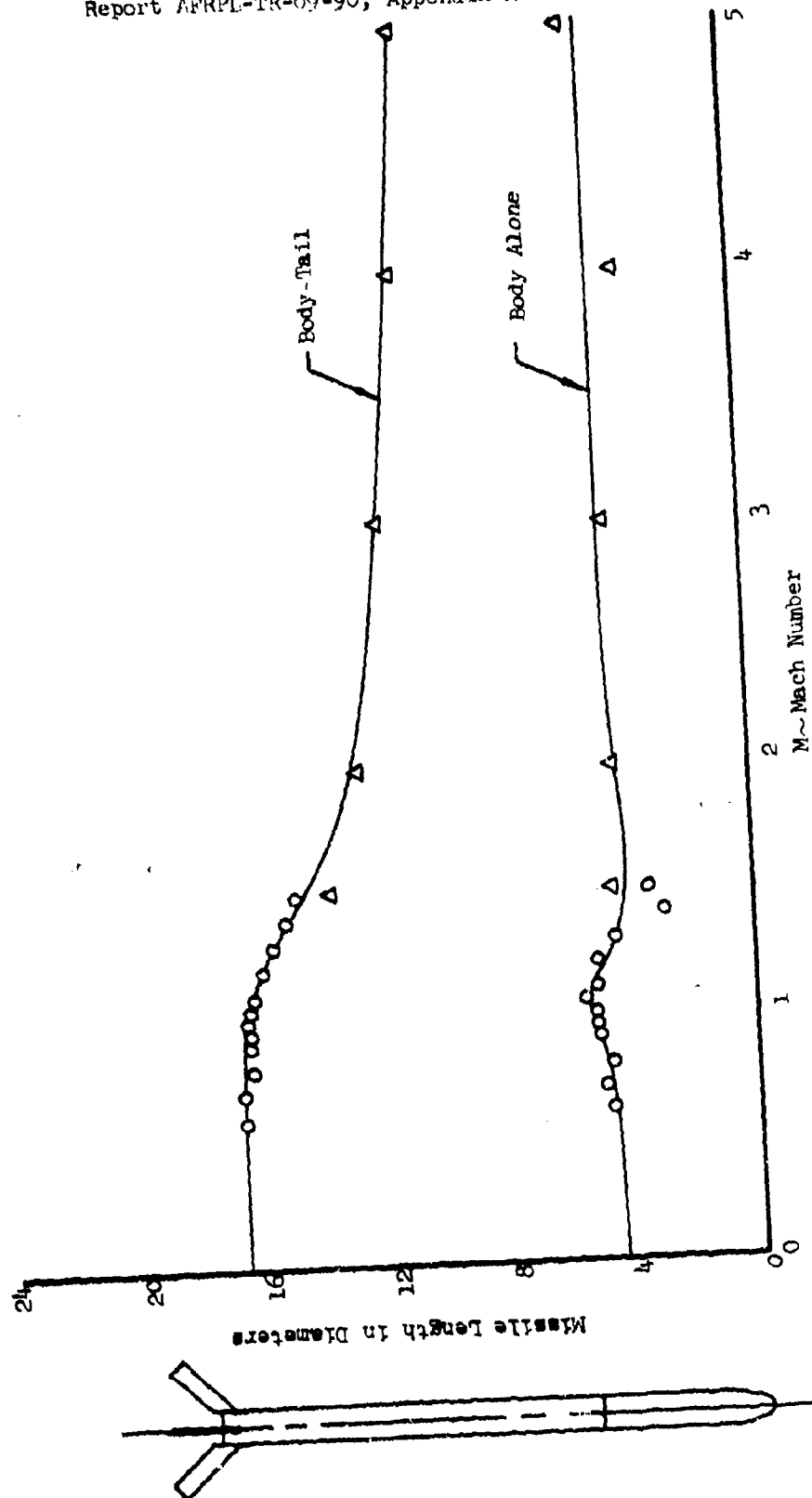


UNCLASSIFIED

UNCLASSIFIED

Report AFRPL-TR-69-90, Appendix A

Figure 5.1.1.1-3  
Center of Pressure as a Function  
of Mach Number  $\alpha = 0 - 40^\circ$

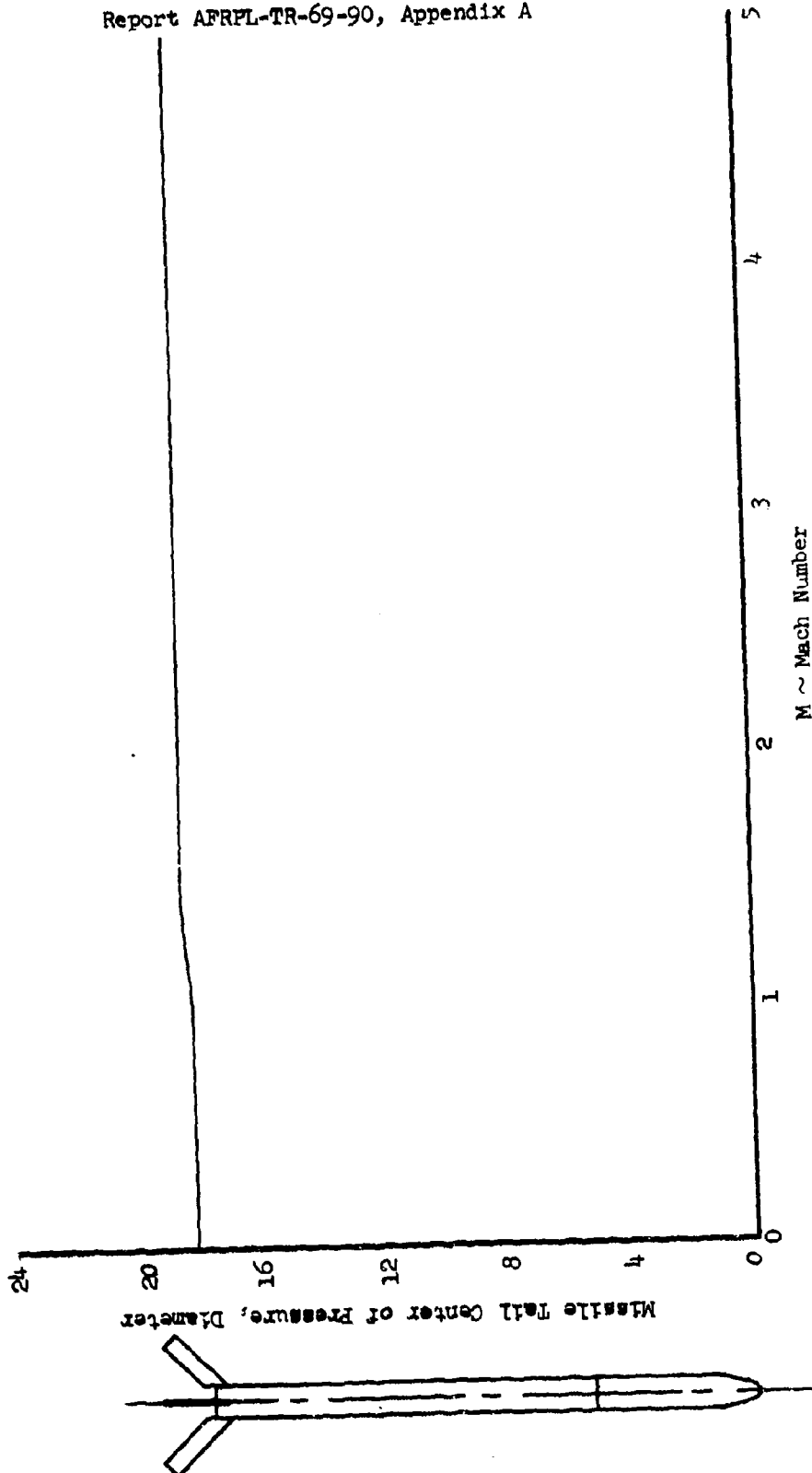


UNCLASSIFIED

UNCLASSIFIED

Report AFRPL-TR-69-90, Appendix A

Figure 5.1.1.1-4  
2.75 FVAR Vehicle  
Tail Center of Pressure as a  
Function of Mach Number

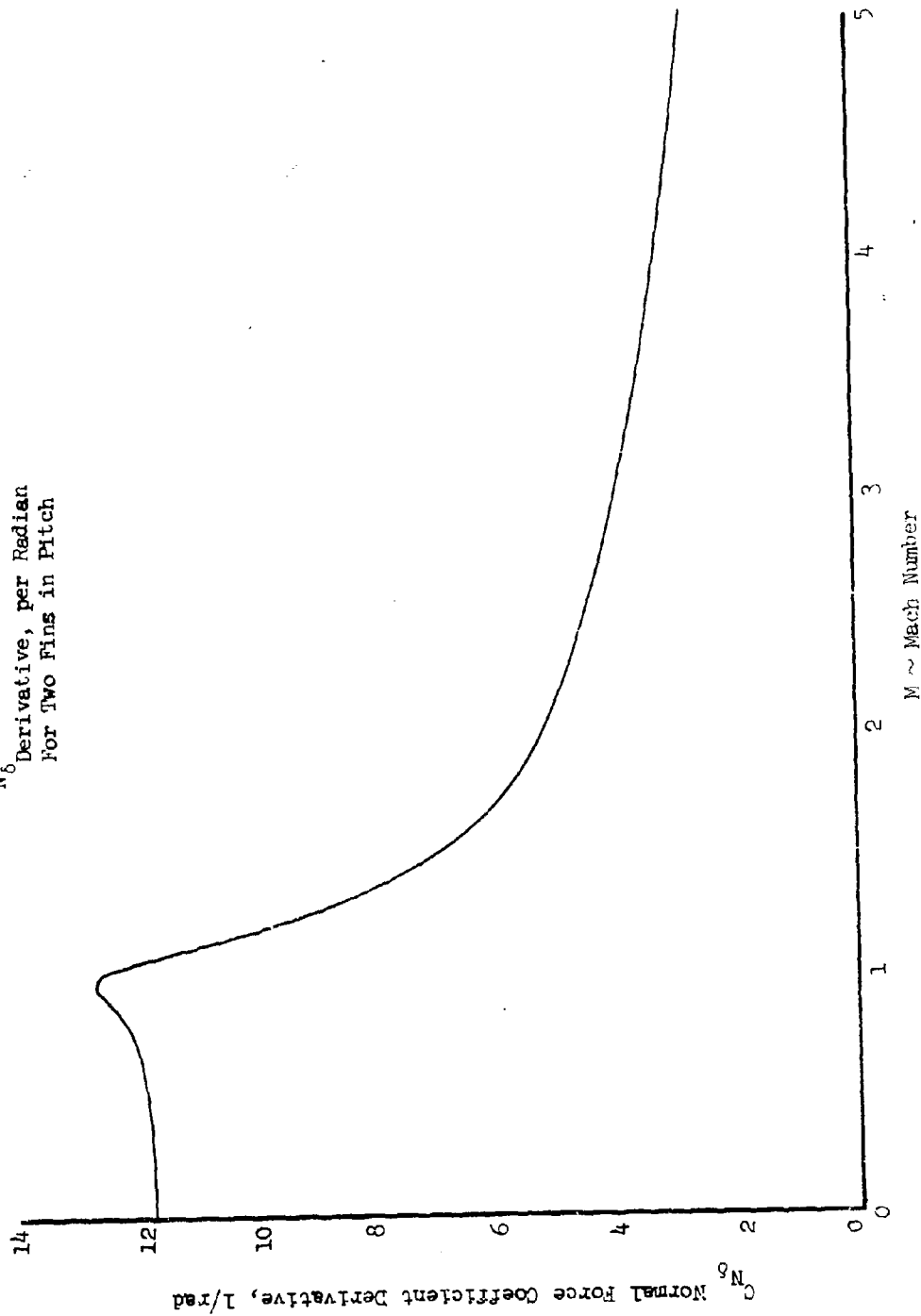


UNCLASSIFIED

UNCLASSIFIED

Report AFRPL-TR-69-90, Appendix A

Figure 5.1.1-5  
2.75 FFAR Vehicle  
 $C_{N\delta}$  Normal Force Coefficient  
Derivative, per Radian  
For Two Fins in Pitch

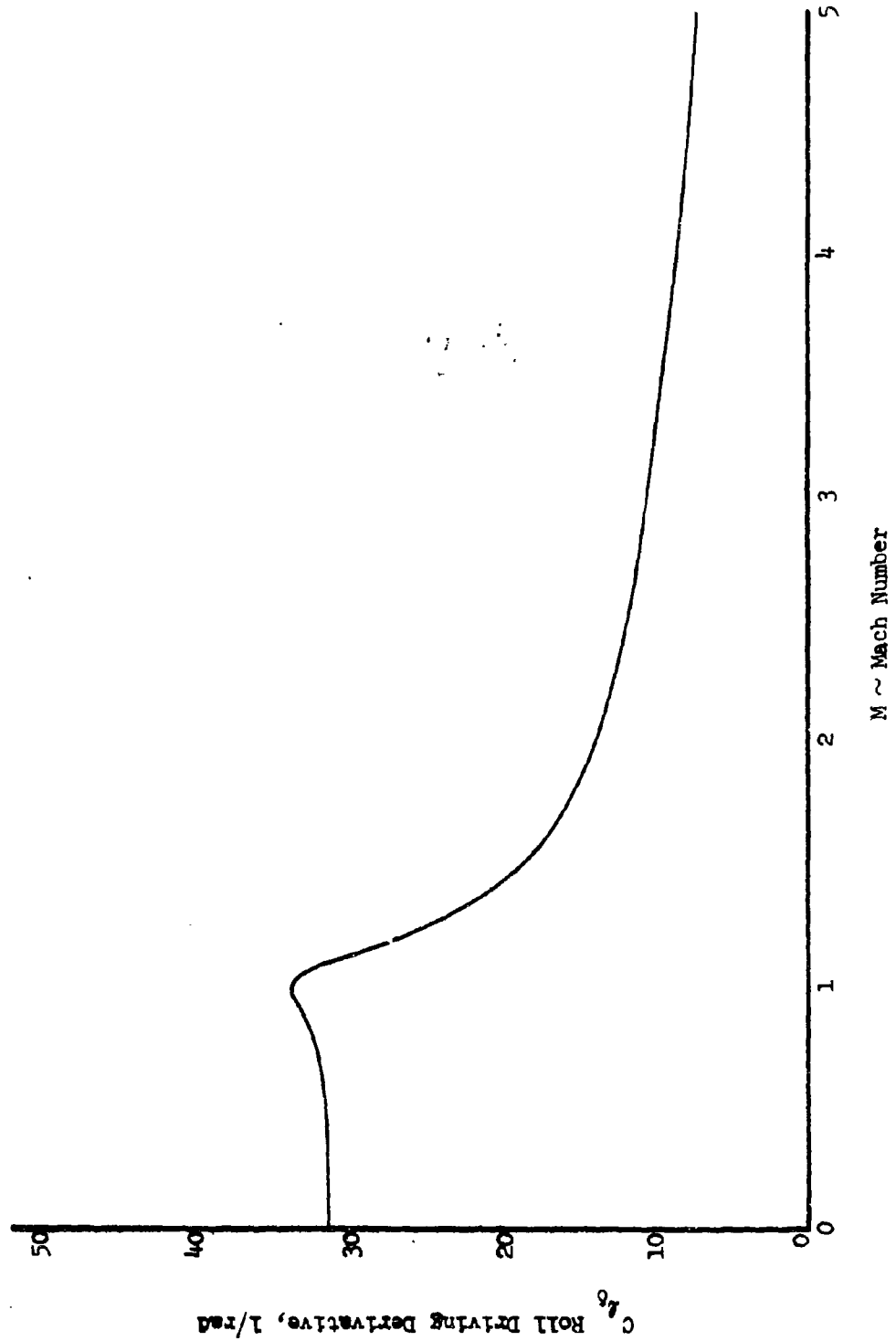


UNCLASSIFIED

UNCLASSIFIED

Report AFRPL-TR-69-90, Appendix A

Figure 5.1.1.1-6  
2.75 FFAR Vehicle  
Roll Driving Coefficient as a  
Function of Mach Number



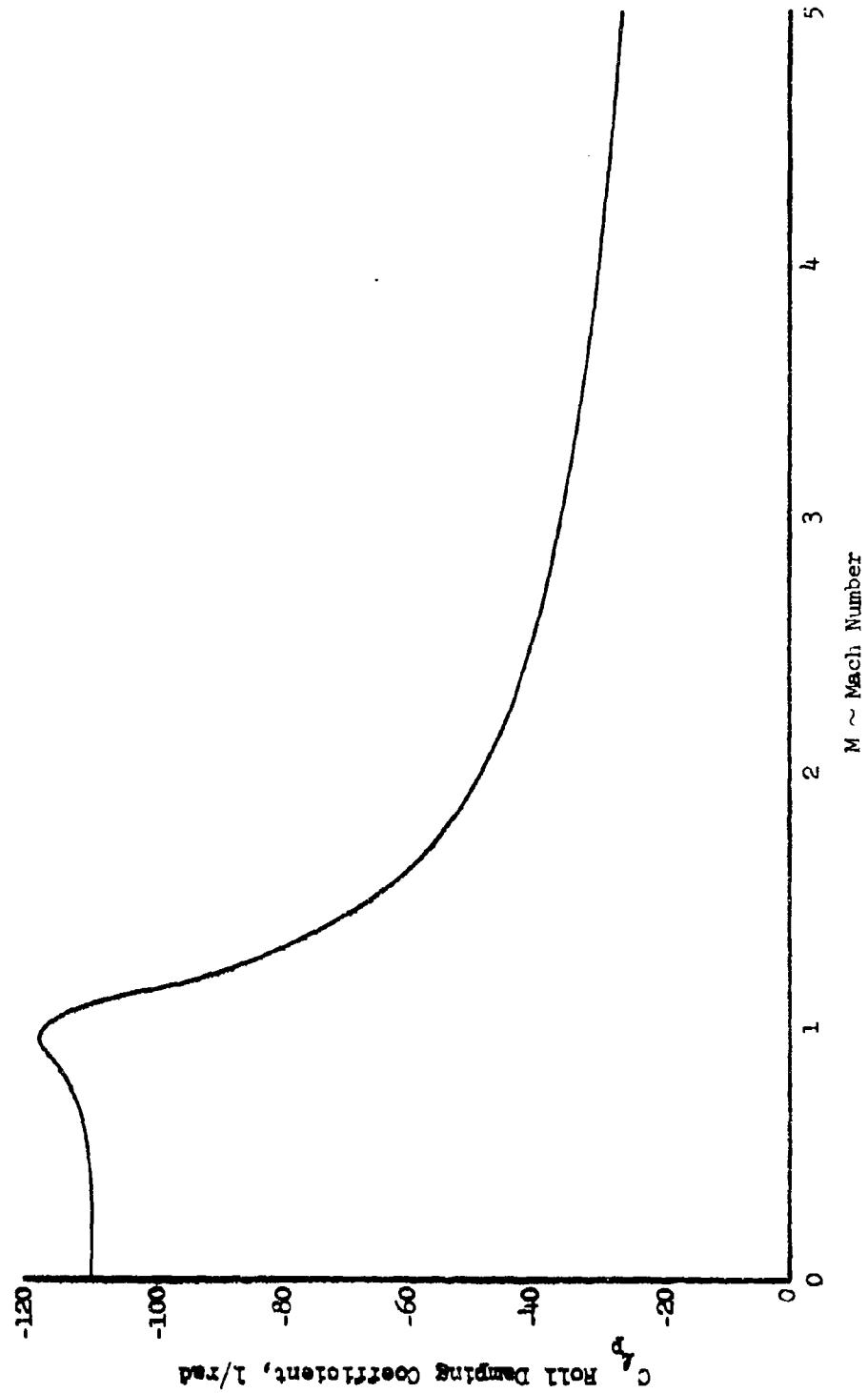
UNCLASSIFIED



UNCLASSIFIED

Report AFRPL-TR-69-90, Appendix A

Figure 5.1.1.1-7  
2.75 FFAR Vehicle  
Roll Damping Coefficient as a  
Function of Mach Number



UNCLASSIFIED

UNCLASSIFIED

Report AFRPL-TR-69-90, Appendix A

Figure 5.1.1.1-8  
2.75 FFAR Vehicle  
Pitch Damping Coefficient as a  
Function of Mach Number

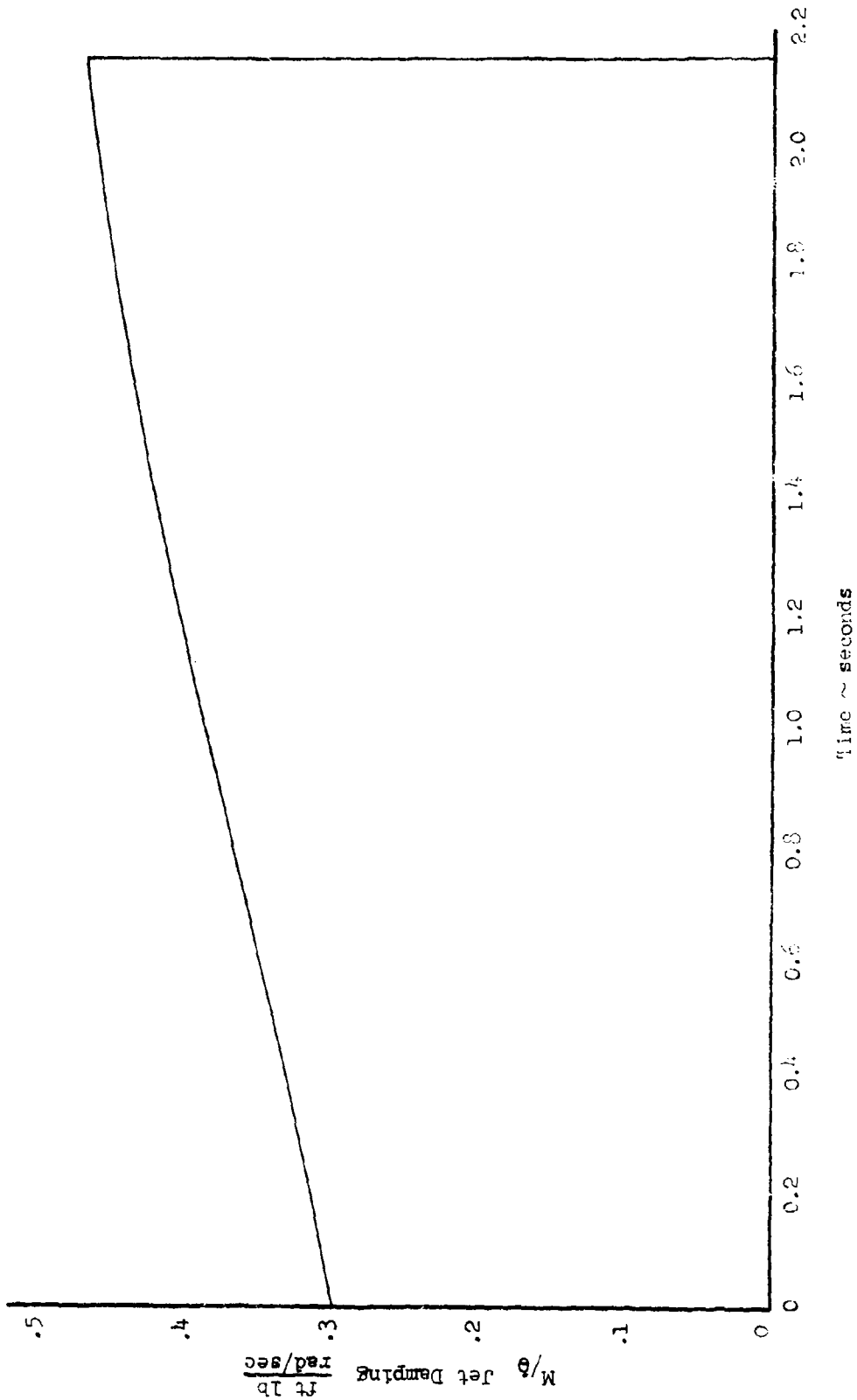


UNCLASSIFIED

UNCLASSIFIED

Report AFRPL-TR-69-90, Appendix A

Figure 5.1.1.1-9  
2.75 FFAR Vehicle  
Jet Damping as a Function of Time

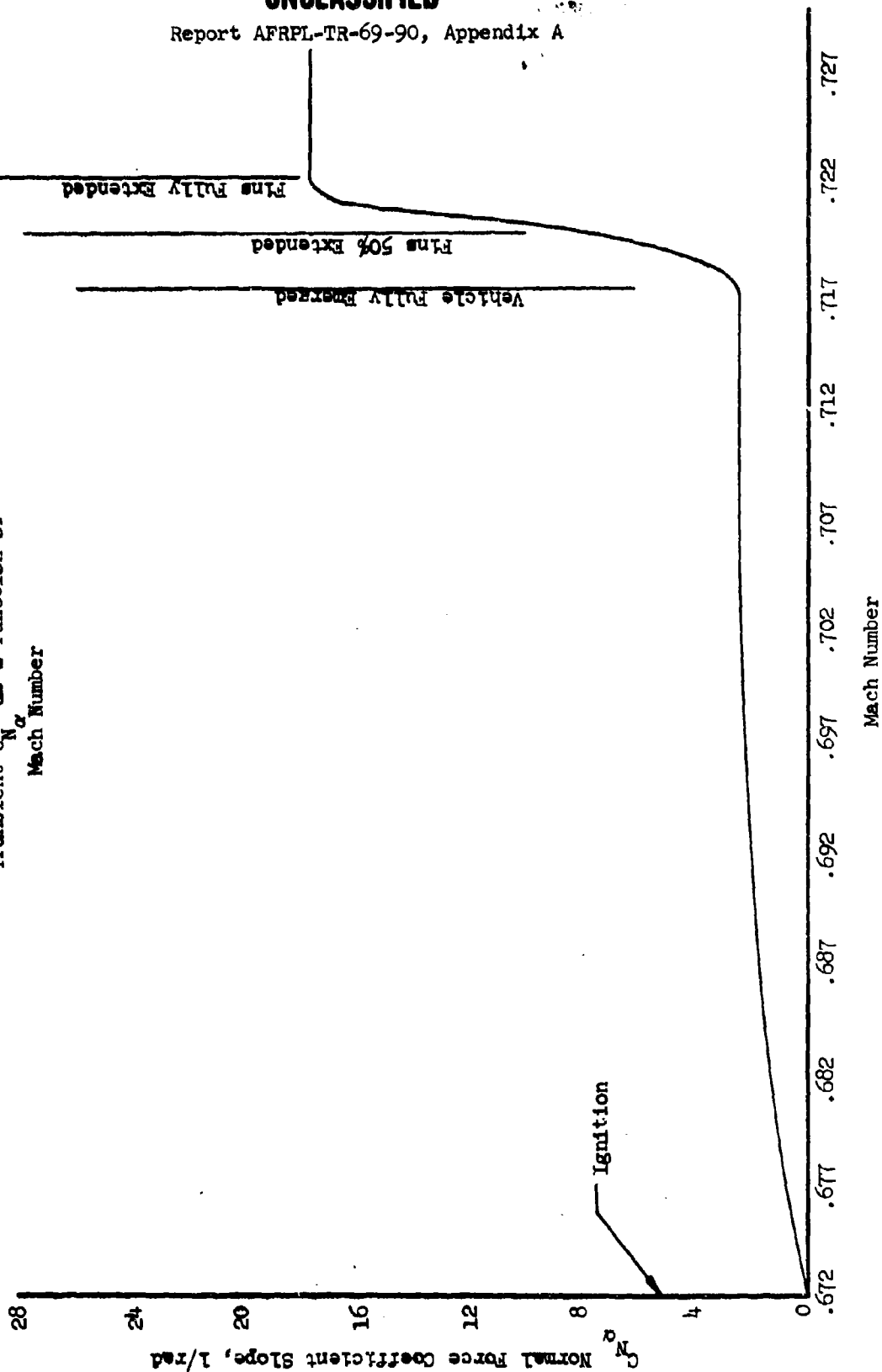


UNCLASSIFIED

UNCLASSIFIED

Report AFRPL-TR-69-90, Appendix A

Figure 5.1.1-10  
2.75 FFAR Vehicle  
Transient  $C_{N\alpha}$  as a Function of  
Mach Number

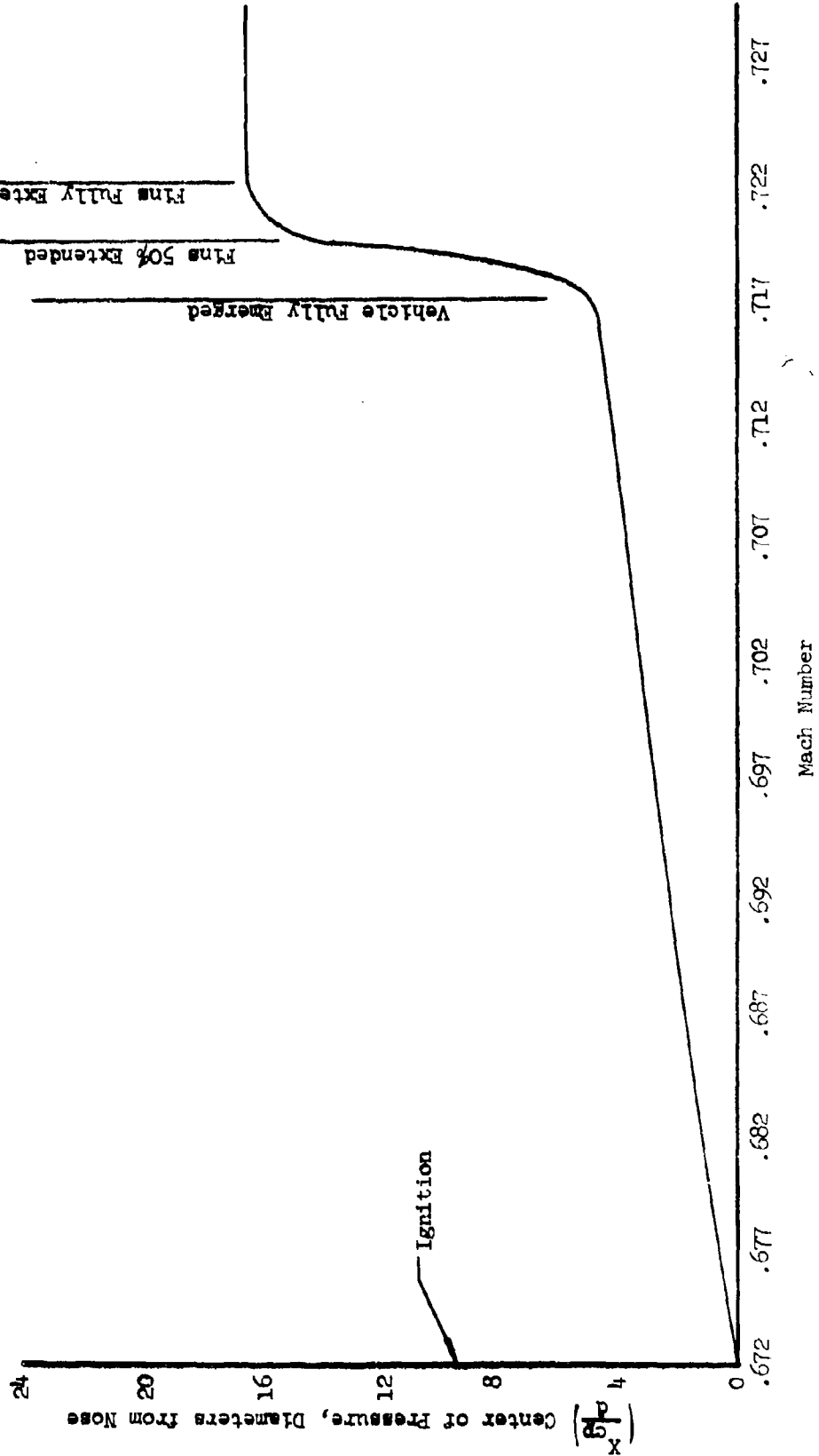


UNCLASSIFIED

UNCLASSIFIED

Report AFRPL-TR-69-90, Appendix A

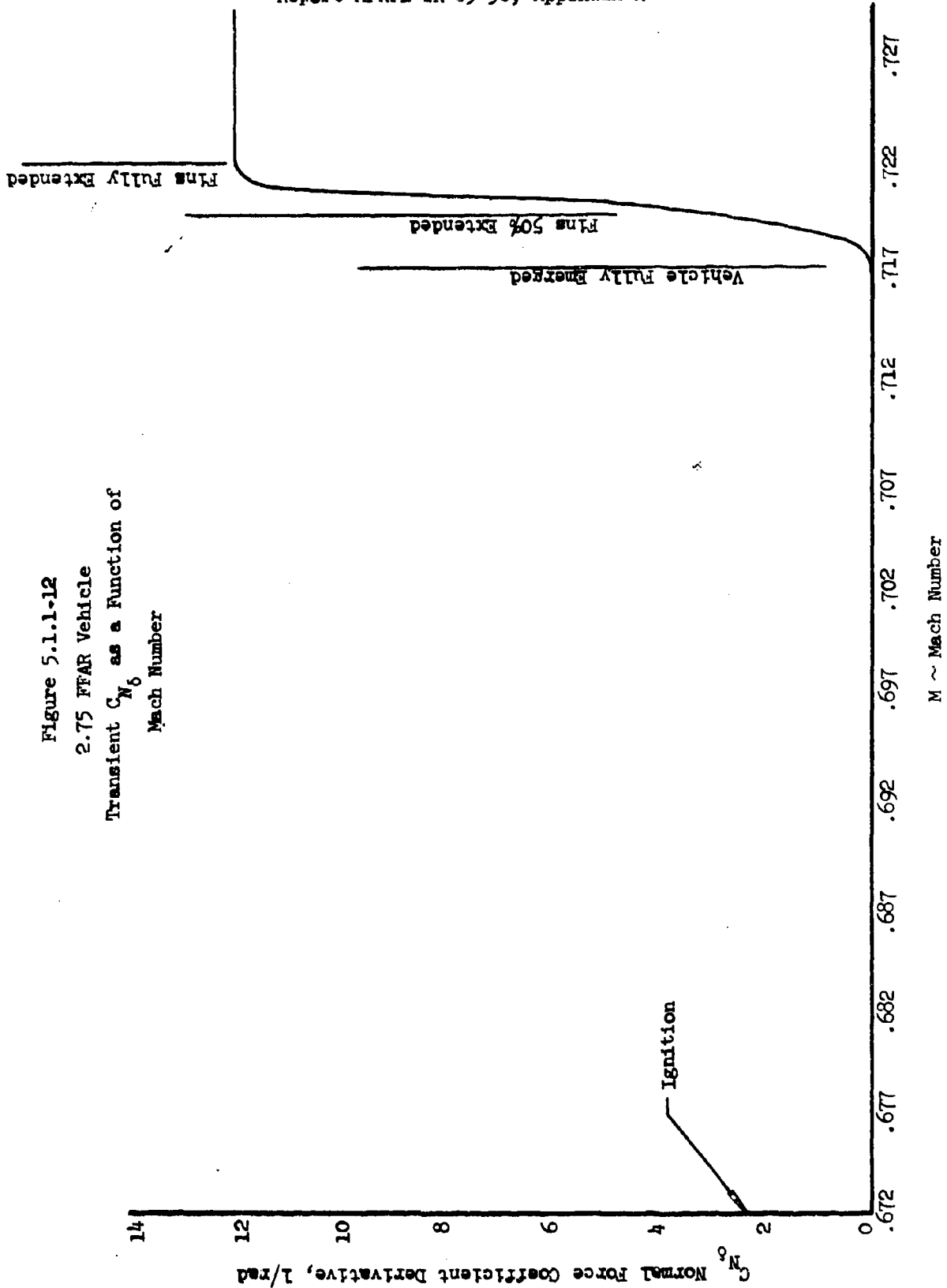
Figure 5.1.1-11  
2.70 FEAR Vehicle  
Transient Center of Pressure as a  
Function of Mach Number



UNCLASSIFIED

UNCLASSIFIED

Report AFRPL-TR-69-90, Appendix A

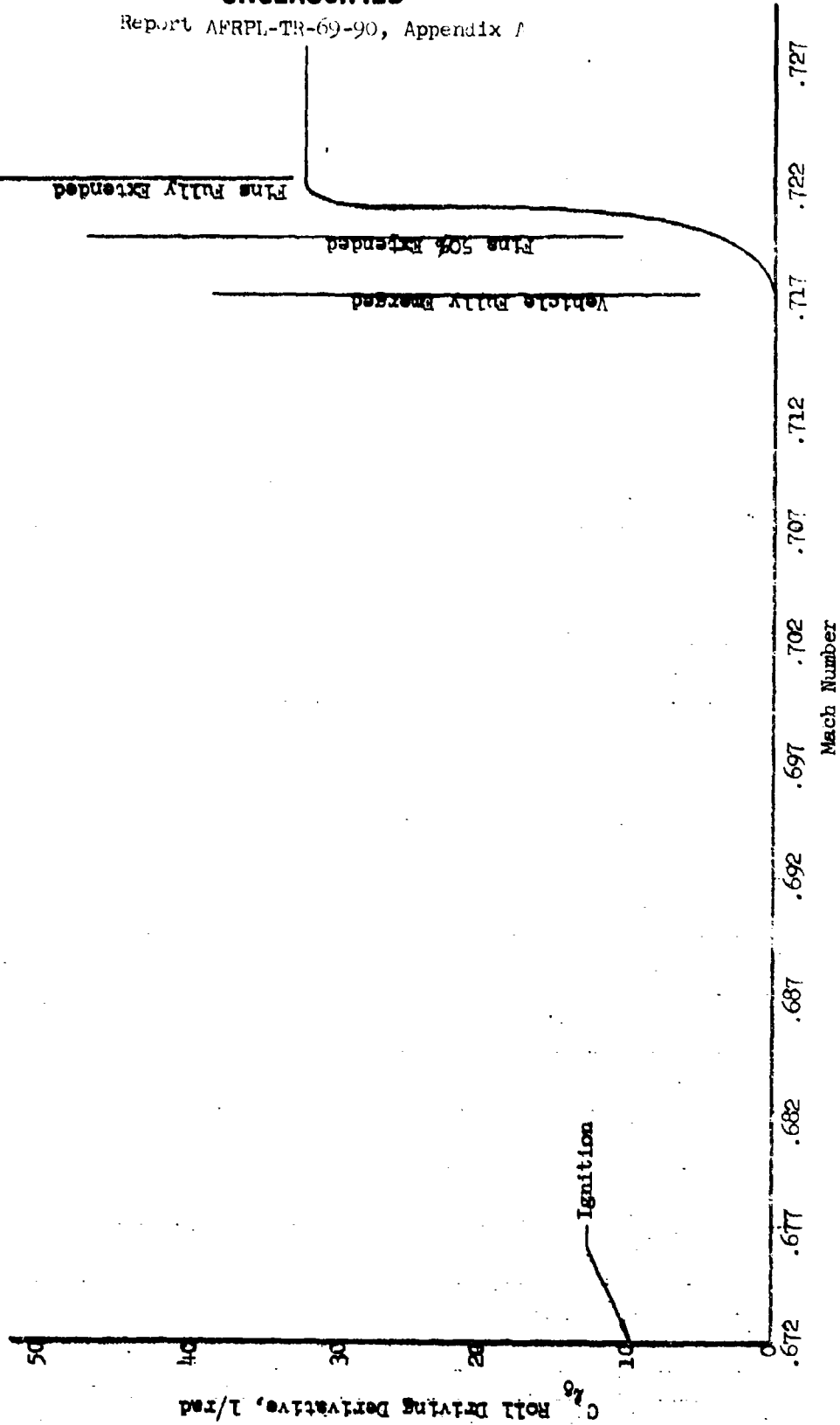


UNCLASSIFIED

UNCLASSIFIED

Report AFRPL-TR-69-90, Appendix A

Figure 5.1.1-13  
2.75 FFAR Vehicle  
Transient  $C_{L_0}$  as a Function  
of Mach Number

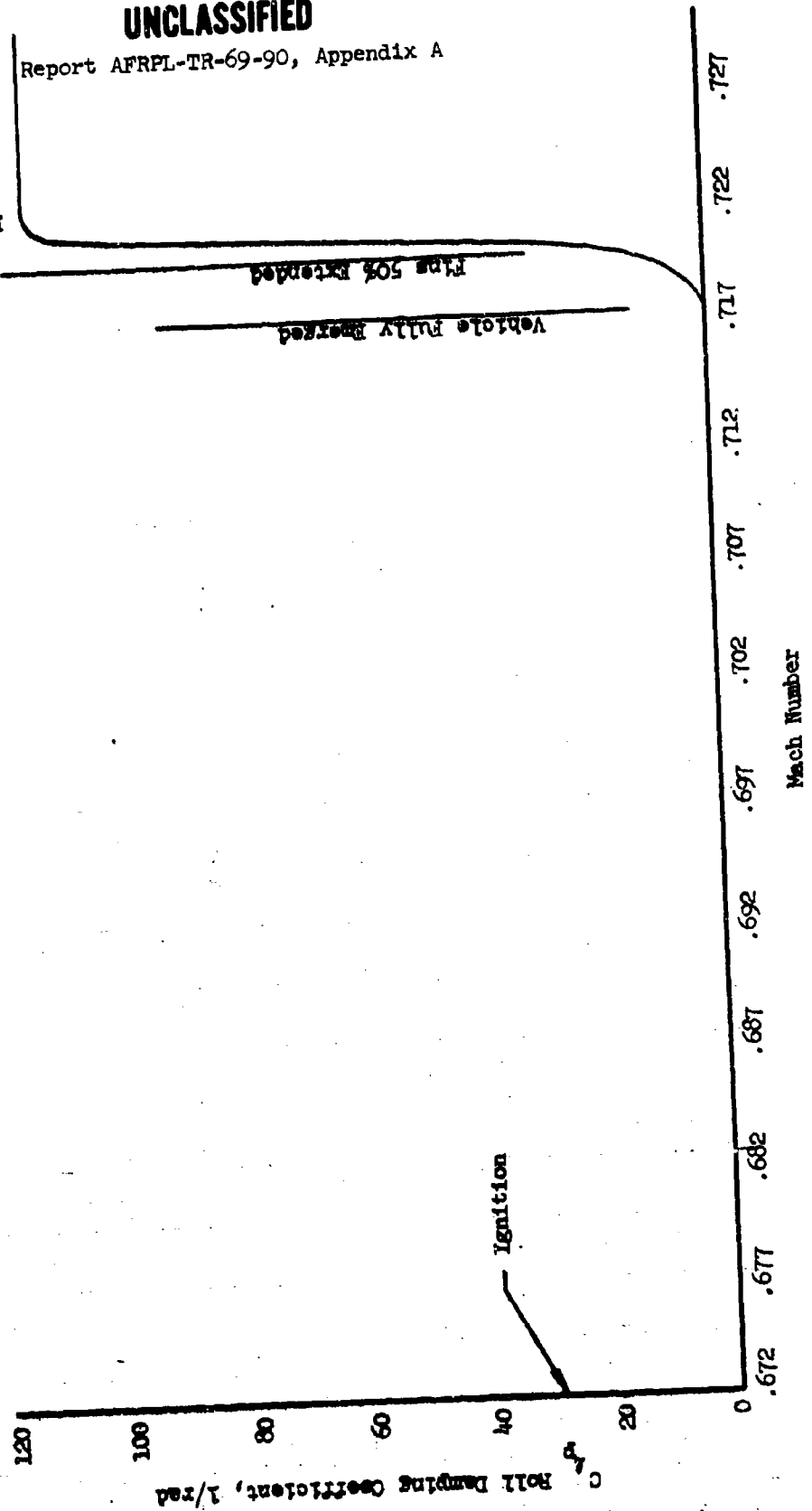


UNCLASSIFIED

UNCLASSIFIED

Report AFRPL-TR-69-90, Appendix A

Figure 5.1.1-14  
2.75 FFAR Vehicle  
Transient  $C_{Lp}$  as a Function  
of Mach Number



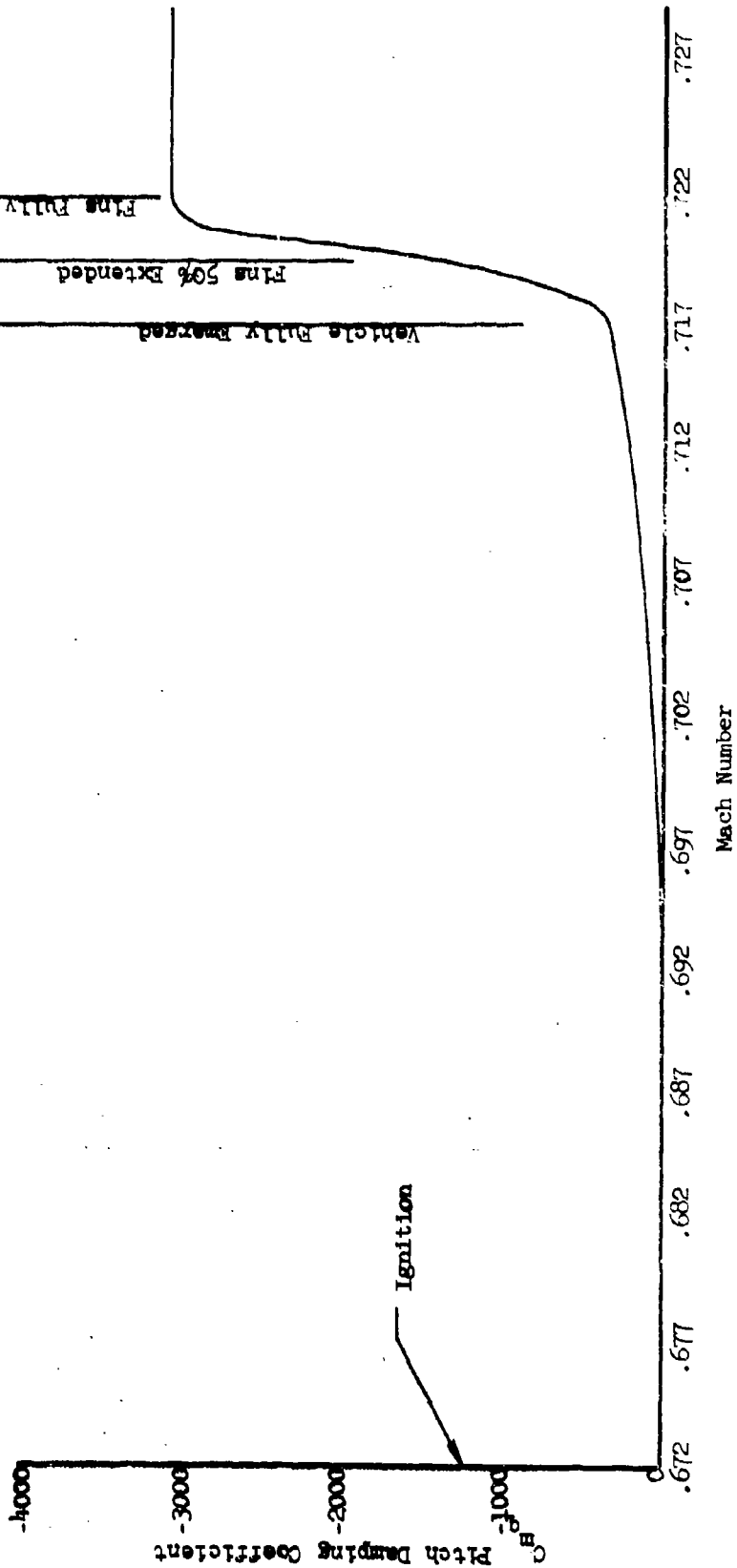
UNCLASSIFIED



UNCLASSIFIED

Report AFRPL-TR-69-90, Appendix A

Figure 5.1.1.15  
2.75 FFAR Vehicle  
Transient  $C_{m,q}$  as a Function  
of Mach Number



UNCLASSIFIED

## UNCLASSIFIED

Report AFRPL-TR-69-90, Appendix A

### 5.1.2 PRELIMINARY AEROELASTICITY

A preliminary aeroelastic analysis was conducted to assess the effects of span and sweep angle on the vehicle static margin. Analysis performed during the proposal phase indicated that aeroelastic effects due to body bending were quite small. Therefore, for this preliminary analysis, only fin elasticity was considered.

Two sweep angles were considered in the analysis. These were  $30^\circ$  and  $45^\circ$ . Three spans were considered. These were 100%, 77.7% and 55.3% of the exposed span. The flight condition considered was at maximum dynamic pressure where aeroelastic effects are a maximum.

The analysis was performed according to the methods presented in Section 4.3.2.2.1. The structural influence coefficients used were those discussed in Section 4.3.3.2.1.

The aeroelastic fin analysis provided elasticized tail  $C_{N_\alpha}$ 's. These were then combined with the rigid body lift and center of pressure to determine the vehicle static stability margin.

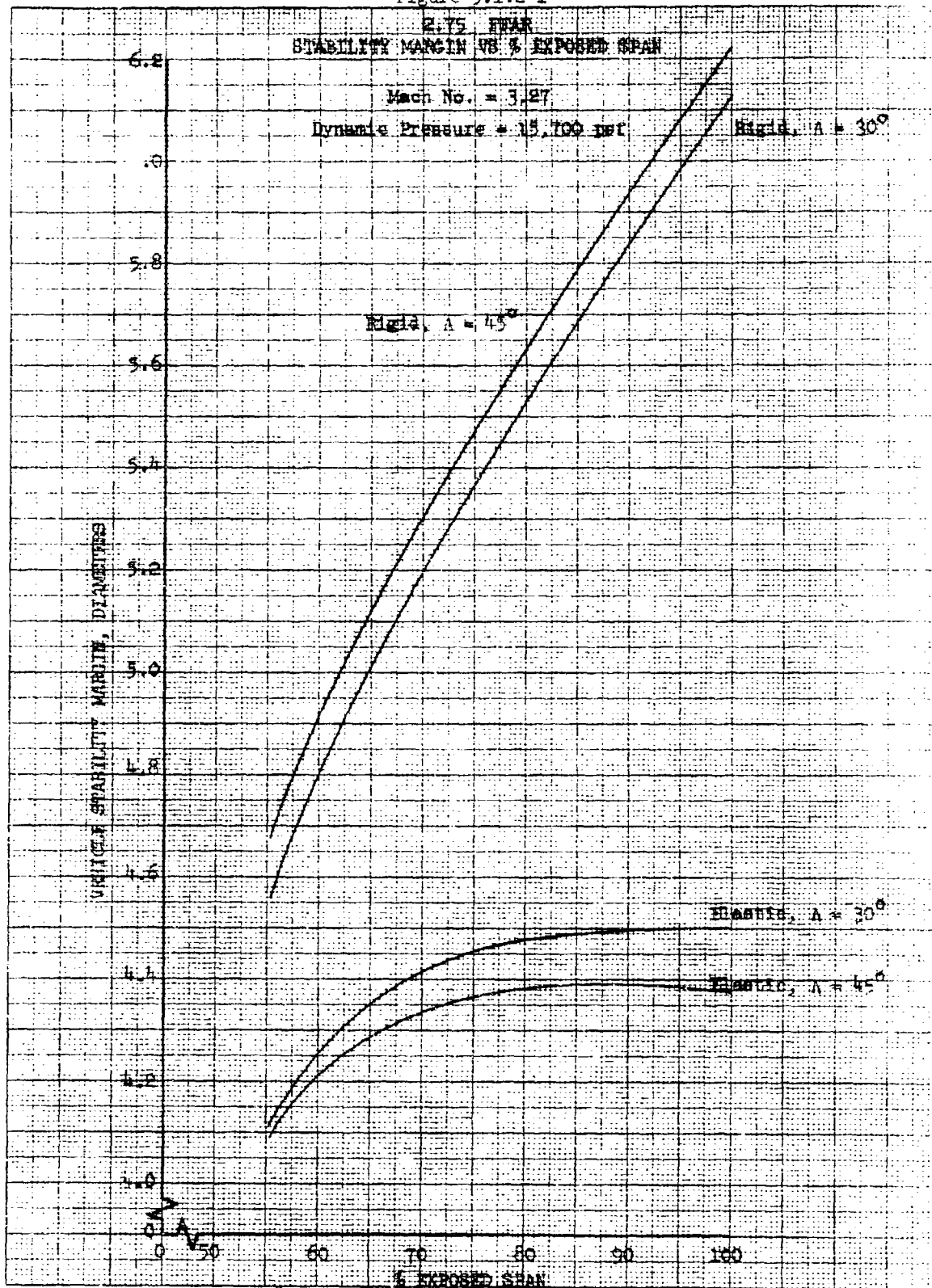
The results of this analysis are presented in Figure 5.1.2-1, where the various stability margins are plotted vs percent exposed span. A comparison is shown between elastic and rigid stability margins for various sweeps. It can be seen that by reducing the span by as much as 30% in the elastic case that the vehicle static stability margin is only changed slightly. Also the effects of fin sweep seem to have little effect on the static margin.

UNCLASSIFIED

UNCLASSIFIED

Report AFRL-TR-69-90, Appendix A

Figure 5.1.2-1



UNCLASSIFIED

# UNCLASSIFIED

Report AFRPL-TR-69-90, Appendix A

## 5.2 WIND TUNNEL TEST

### 5.2.1 SUMMARY

The wind tunnel test of a flight hardware (full scale) model of the 2.75 FFAR has been performed and the resulting data reduced and analyzed. Two items were changed in this test as compared to similar data from scale model tests. These were the center of pressure of the body alone component, and the zero lift drag coefficient. The uncorrected zero lift drag data was increased some 15.4% and the body alone center of pressure was moved forward 1.8 body diameters. These values are the changes in comparison to the previous tests. The remaining force and moment coefficients and their derivatives were essentially unchanged from the values obtained from the previous tests.

The triangular creased fin tips tested produced a rolling moment coefficient comparable to that produced by 1/8 degree fin cant.

### 5.2.2 INTRODUCTION

The available wind tunnel data at the beginning of the Improved 2.75 FFAR Program consisted of two scale model tests. It was anticipated that the tail design would be changed and so the full scale test was scheduled. The results of the program indicated little tail design change would be required and the present test serves as verification for the scale model tests.

The objective of the test was to determine the stability and drag characteristics of the 2.75 FFAR Improved configuration. The following are a presentation of the test preparation, performance, data reduction and data analysis of the full scale test.

### 5.2.3 SYMBOLS AND NOMENCLATURE

#### Model

- B - Body assembly, consisting of the nose (see Figure 5.2.1), centerbody and adaptor.

# UNCLASSIFIED

Report AFRPL-TR-69-90, Appendix A

- $T_1$  - Tail assembly consisting of four fins (see Figure 5.2.1), which have a leading edge sweep of  $45^\circ$ , have a modified double wedge cross-section and have a panel span of 4.68 inches. Each of the fins have a differential cant of  $1/2$  degree such as to produce a clockwise rolling moment.
- $T_2$  - Tail assembly identical (see Figure 5.2.1) to  $T_1$  except tail fin tip is bent  $4^\circ$  in a spanwise plane.

## Data

The wind tunnel data were reduced in both aeroballistic and body axis systems. In addition, the axial force data are to be corrected to zero base drag, i.e.,  $p_b = p_\infty$ .

The axis system to be presented in this report (aeroballistic) is described in the following paragraphs.

## Aeroballistic Axis

This axis system is known colloquially as tunnel axes. In this axis system the X axis (longitudinal axis) is coincident with the body longitudinal axis and remains coincident with the body as angle of attack changes. The Z axis remains normal to the body longitudinal axis as the angle of attack is changed. The Z axis remains in the tunnel vertical plane regardless of the vehicle roll position. The Y axis remains orthogonal to the other two axes and remains in the tunnel horizontal plane.

In the selected system, the origin of the axis system is coincident with the center of the strain gage balance. In all configurations, B,  $BT_1$ , and  $BT_2$  the center of the balance will be located 27.488 inches aft of the nose on the body longitudinal axis of symmetry.

The following designations are associated with the conditions in the wind tunnel test section and with the aerodynamic inputs.

UNCLASSIFIED

# UNCLASSIFIED

Report AFRPL-TR-69-90, Appendix A

- A = axial force, force along X axis, positive (+) direction is aft, lb
- $C_A$  = axial force coefficient, ( $C_A = A/qS$ )
- $C_l$  = rolling moment coefficient ( $C_l = RM/qSd$ )
- $C_m$  = pitching moment coefficient ( $C_m = PM/qSd$ )
- $C_n$  = yawing moment coefficient ( $C_n = YM/qSd$ )
- $C_N$  = normal force coefficient ( $C_N = N/qS$ )
- $C_Y$  = sideforce coefficient, ( $C_Y = Y/qS$ )
- $C_{D_0}$  = zero lift drag coefficient ( $C_{D_0} = \frac{D_0}{qS}$ )
- $C_{l_\delta}$  = change in rolling moment coefficient due to differential deflection of four tail fins, per radian
- $C_{N_\alpha}$  = normal force coefficient slope, per radian
- $C_{N_\delta}$  = change in normal force coefficient due to deflection of two tail fins in pitch plane, per radian
- $C_{p_b}$  = base pressure coefficient ( $C_{p_b} = (p_b - p)/q$ )
- d = body diameter, to be used as the reference length for data reduction (d = 2.75 in.)
- M = free stream Mach number
- N = normal force, force along the Z axis, positive (+) direction is up, lb
- p = free stream static pressure, (lb/in<sup>2</sup>)
- $p_b$  = model base pressure, (lb/in<sup>2</sup>)
- $p_t$  = free stream total pressure, (lb/in<sup>2</sup>)
- PM = pitching moment, moment about the y axis, a positive (+) moment is one tending to raise the model nose, inch-lb
- q = dynamic pressure, (lb/in<sup>2</sup>) ( $q = \frac{\gamma}{2} \rho V^2$ )
- RM = rolling moment, moment about the X axis, a positive (+) moment is clockwise when viewed from the rear, inch-lb
- RN = Reynold's number
- S = body cross-sectional area, to be used as the reference area for data reduction, (S = 5.94 in<sup>2</sup>)
- u = velocity component along the x axis ( $u = V \cos \alpha$ ), ft/sec
- v = velocity component along the y axis ( $v = 0$  aeroballistic axis)
- V = freestream velocity, ft/sec
- w = velocity component along the z axis ( $w = V \sin \alpha$  aeroballistic axis), ft/sec

UNCLASSIFIED

# UNCLASSIFIED

Report AFRPL-TR-69-90, Appendix A

$(x/d)_{cp_N}$  Normal force longitudinal center of pressure location  
(diameters aft of nose)

$$\left[ \left( \frac{x}{d} \right)_{cp_N} = \left( \frac{x}{d} \right)_{cg} - \left( \frac{C_m}{C_N} \right) \right]$$

$(x/d)_{cp_Y}$  Side force longitudinal center of pressure location  
(diameters aft of nose)

$$\left[ \left( \frac{x}{d} \right)_{cp_Y} = \left( \frac{x}{d} \right)_{cg} - \left( \frac{C_n}{C_Y} \right) \right]$$

Y = sideforce, force along y axis, positive (+) direction  
is to right, lb

YM = yawing moment, moment about the Z axis, a moment tending  
to rotate the model clockwise when viewed from above is  
positive (+), inch-lb

$\alpha$  = angle of attack in the aeroballistic axis system ( $\alpha = \tan^{-1} \frac{w}{u}$ ).  
 $\alpha$  is positive (+) when the model nose is above the  
horizontal, degrees.

$\delta$  = tail fin cant angle, deg.

$\Delta\Omega$  = tail fin tip bend angle, deg.

$\gamma$  = ratio of specific heats of fluid

$\phi$  = roll position angle, it will be designated as the angle  
between fin 1 and the tunnel vertical plane,  $\phi = 0^\circ$  when  
fin 1 is in the vertical plane on top the body. A  
positive (+)  $\phi$  is in the clockwise direction when the  
model is viewed from the rear, degrees.

## 5.2.4 MODEL DESCRIPTION

The wind tunnel model used for this test was fabricated from flight hardware. The resulting configuration is shown in Figures 5.2-1 and 5.2-2. Figure 5.2-1 presents the major dimensions of the basic configuration and the two tail panels. Figure 5.2-2 presents the detail model drawing used in fabricating the model. The complete model nose was made of plastic, consists of two parts, and is threaded into the main body assembly. The

# UNCLASSIFIED

Report AFRPL-TR-69-90, Appendix A

front piece of the nose is a conical section made of a molded plastic and is held to the rest of the plastic nose by three Allen head bolts. The tail panel used in the  $T_1$  tail assembly is identical to that used in past 2.75 FFAR applications. The tail panels in tail assembly  $T_2$  are similar except that the fin tips have been bent  $4^\circ$  in a counterclockwise direction (looking forward). This is shown in Figures 5.2-1 and 5.2-2. The wind tunnel model body shell and tail panels were made of an aluminum alloy. The nose was made of a plastic material. The aft tail nozzle block was fabricated of 17-7 PH stainless steel. The flight hardware was not used in this instance because the tail cant angles were machined into this item. The projecting parts of the tail attaching bolts shown in Figure 5.2-2 were removed by machining. This was performed on both tail assemblies.

As can be seen, in Figure 5.2-2, the angular tolerances on the fabricated wind tunnel vehicle were designated as  $\pm 0.1$  degrees. The desired cant angles on both tail assemblies were  $\delta = 0.5 \pm 0.1^\circ$ . The model tail assemblies were fabricated to these values. After fabrication, the tail panels were measured with an indicator and the averages from 24 readings (6 per tail panel) are given below.

Table I  
TAIL ASSEMBLY CANT VALUES

<u>Configuration</u>	<u><math>\delta</math> Ave.</u>	<u><math>\sigma</math></u>
BT <sub>1</sub>	.5882 deg	.2391 deg
BT <sub>2</sub>	.5377 deg	.2872 deg

As can be seen, the average tail cants are very near the desired  $\delta_c = 0.5$  degrees. However, the standard deviations from the mean are approximately half the cant value, indicating some very large excursions from the given values.

In addition, the bent tail fins were measured with an indicator. The average tail fin bend angle was  $\Delta\eta = 3.725^\circ$ . This was the average of eight readings (2 per tail panel). This was somewhat lower than the  $4^\circ$  desired,

UNCLASSIFIED



# UNCLASSIFIED

Report AFRPL-TR-69-90, Appendix A

but was considered to be acceptable. The standard deviation from this value was  $\sigma = .6136^\circ$  which was 16% of the mean. This indicates a reasonable accuracy.

## 5.2.5 RUN SCHEDULE

The following is a tabular itemization of all the runs which were performed in the wind tunnel test at Tunnel A, AEDC.

Run	Group	Config.	Mach	$\alpha$ Deg.	$\phi$ Deg.	Data
1	1	B	3.49	-4 $\rightarrow$ +10	0	6 Comp. + Base Press.
1	2	B	3.5			
2	3	B	2.5			
	4	B	2.5			
	5	B	3.0			
	6	B	2.25			
3	7	BT <sub>1</sub>	2.5		0	
	8				5	
	9				10	
	10				15	
	11				30	
	12				30	
	13				45	
	14		3.0		0	
	15				5	
	16				10	
	17				15	
	18				30	
	19				45	
	20				22.5	

UNCLASSIFIED

# UNCLASSIFIED

Report AFRPL-TR-69-90, Appendix A

Run	Group	Config.	Mach	$\alpha$ Deg.	$\phi$ Deg.	Data
4	21	BT <sub>1</sub>	3.5	-4 - +10	0	6 Comp. + Base Press.
	22				5	
	23				10	
	24				15	
	25				30	
	26				45	
	27				22.5	
5	28	BT <sub>2</sub>	3.5		0	
	29				5	
	30				10	
	31				15	
	32				22.5	
	33				30	
	34				45	
6	35		2.5		0	
	36				5	
	37				10	
	38				15	
	39				22.5	
	40				30	
	41				45	
	42		3.0		0	
	43				5	
	44				10	
	45				15	
	46				22.5	
	47				30	
	48				45	
	49		2.00		0	

UNCLASSIFIED

# UNCLASSIFIED

Report AFRPL-TR-69-90, Appendix A

Run	Group	Config.	Mach	$\alpha$ Deg.	$\phi$ Deg.	Data
7	50	BT <sub>2</sub>	4.03	-4 to +10	0	6 Comp. Base Press.
	51				5	
	52				10	
	53				15	
	54				22.5	
	55				30	
	56				45	

## 5.2.6 BASIC DATA PRESENTATION

The basic data gathered during the wind tunnel test are presented graphically in this section. The run schedule in Section 5.2-5 indicates that approximately 50 runs were performed on three configurations at 4 Mach numbers. These data are presented tabularly in Reference 1. A presentation of the basic data in a clear concise graphical form is given in this section. Figure 5.2-3 presents the Reynold's number per inch as a function of Mach number for this test.

The first group of data plots are presented in Figure 5.2-4. These data are for the body alone and the data are presented in polar form. Presented is  $C_N$  as a function of  $C_A$ ,  $\alpha$ , and  $C_{m_{27.488}}$  for Mach numbers 2.25, 2.50, 3.0, and 3.50. The data behavior is as predicted in References 2 and 3 in general. One exception is that the center of pressure at low angles of attack is some 1.8 diameters forward of that predicted in Reference 2 for a scale model. This difference is attributed to the gap (approximately 1/16 inch) at the juncture of the conical nose and the remainder (cylindrical) of the nose. The second item is a 16% increase in the axial force coefficient. The remaining data exhibit conventional characteristics. That is, there is a decrease in drag coefficient with increasing Mach number, there is no significant change in normal force coefficient slope with Mach number, and the center of pressure moves aft with increasing Mach number and increasing angle of attack.

UNCLASSIFIED

# UNCLASSIFIED

Report AFRPL-TR-69-90, Appendix A

The next series of plots, Figures 5.2-5, 5.2-6, and 5.2-7 present similar data, i.e.,  $C_N$  as a function of  $C_A$ ,  $\alpha$ , and  $C_{m27.488}$ , but with the roll angle,  $\phi$ , as a parameter. Each of the plots are for a different Mach number, in this instance,  $M_\infty = 2.5, 3.0$ , and  $3.5$ . These data are for a body tail combination, designated as BT<sub>1</sub> (Configuration 2 in Reference 1). As can be seen, there is virtually no difference in the drag coefficient and normal force coefficient due to roll position angle. There are some differences in pitching moment coefficient due to roll position angle. As can be seen in Figure 5.2-5, the most stable (most aft center of pressure) configuration results when  $\phi = 45^\circ$ . The least stable when  $\phi = 0^\circ$ . This is borne out in the data at higher Mach numbers also. The difference in center of pressure due to roll position is of the order of  $1/4$  diameter. Since this is near the expected accuracy of the data an average center of pressure through these values was used in subsequent computations.

Figures 5.2-8, 5.2-9 and 5.2-10 present the lateral data for the same configuration as in the previous three plots. Presented are  $C_l$ ,  $C_y$ , and  $C_{n27.488}$  as a function of roll position angle  $\phi$  with angle of attack as a parameter. These data are for Configuration BT<sub>1</sub> in Figure 5.2-1. This is designated as Configuration 2 in Reference 1. In the rolling moment data, it may be noted that the rolling moment coefficient is not zero at zero angle of attack. This is due to the cant angle incorporated into the tail assembly. In this instance,  $\delta = 0.5882^\circ$  (average). The rolling moment at  $\alpha = 0^\circ$  is all due to the cant. Note the small variation in  $C_l$  at  $\alpha = 0^\circ$ . At the larger angles of attack, there is a more significant variation with roll position; this is due to the various fins becoming effective and since their average cant angles are different, the rolling moment changes. Comparing the rolling moment coefficient for the three Mach numbers, it is seen that  $C_l$  decreases with increasing Mach number. Also, at constant  $\alpha$ ,  $C_l$  varies sinusoidally with roll position angle  $\phi$ . The  $C_y$  and  $C_m$  behave similarly to  $C_l$  except their values are small at  $\alpha = 0^\circ$ . They both decrease with increasing Mach number and vary in a sinusoidal fashion with  $\phi$ .

UNCLASSIFIED

# UNCLASSIFIED

Report AFRPL-TR-69-90, Appendix A

Figures 5.2-11, 5.2-12, 5.2-13, and 5.2-14 present the longitudinal stability and drag data for Configuration 3 (BT<sub>2</sub> in Figure 5.2-1). This is the configuration in which the triangular tail fin tips have been creased to an angle of 4° relative to the tail chord plane in a plane normal to the vehicle axial centerline. Data are presented for Mach numbers, M = 2.5, 3, 3.5, and 4. Essentially, these data are identical with the data for Configuration 2 (BT<sub>2</sub>, Figure 5.2-1). The bent tips were expected to have little or no effect on the longitudinal characteristics. The one item different in this series is that there are data for M = 4. These data agree very well with the data from lower Mach numbers.

The lateral coefficients for the BT<sub>2</sub> configuration are presented in Figures 5.2-15, 5.2-16, 5.2-17, and 5.2-18. Presented are C<sub>l</sub>, C<sub>y</sub>, and C<sub>n</sub> as a function of roll position angle  $\phi$ , with  $\alpha$  as a parameter. In these data the bent tail fin tip does make a difference. At Mach number, M = 2.50, and zero angle of attack, the rolling moment coefficient for the configuration with the creased tips is C<sub>l</sub> = .128. The comparable value for the unmodified tips is C<sub>l</sub> = .114. Since the cant angles are comparable, (BT<sub>2</sub>  $\delta$  = .5377°, BT<sub>1</sub>  $\delta$  = .5882°), the difference in rolling moment coefficient may be attributed to the creased tip. As such, the present creased fin is equivalent to a cant angle of  $\delta_{\text{equivalent}}$  = .125 degrees. Essentially, the creased tail fin behaves like a curved tail fin. That is, a compressive flow field is set up on the concave surface and an expansive flow field on the convex surface. The difference in pressure due to these two fields generates the rolling moment coefficient. The remainder of the coefficients, C<sub>y</sub>, C<sub>n</sub>, behave just like the configuration without the creased tips. The data are sinusoidal in  $\phi$  and increase with  $\alpha$ . Also, they decrease with increasing Mach number.

These figures, 5.2-4 through 5.2-18, constitute the presentation of the basic data.

## 5.2.7 ESTIMATED ACCURACY

The estimated accuracy of the reduced data was obtained from References 2 and 3. The resulting values are tabulated below. These are

UNCLASSIFIED

# UNCLASSIFIED

Report AFRPL-TR-69-90, Appendix A

considered to be preliminary and the values published in the AEDC wind tunnel report will be considered to be final.

## ESTIMATED ACCURACY TEST DATA

<u>Item</u>	<u>Accuracy</u>
$C_N$	$\pm .01$
$\left(\frac{x}{d}\right)_{pitch}$	$\pm .10$
$C_A$	$\pm .01$
$C_d$	$\pm .008$
$C_y$	$\pm .01$
$\left(\frac{x}{d}\right)_{yaw}$	$\pm .20$
$C_{P_b}$	$\pm .01$
$\alpha$	$\pm .1^\circ$
$\phi$	$\pm .1^\circ$
$M$	$\pm .02$

These values are from previous AEDC tests on a scale model of the 2.75 FFAR and are accepted as being appropriate for this test also.

### 5.2.8 RESULTS AND DISCUSSION

The test was satisfactorily performed and the results corroborated the data from tests in References 2 and 3. The two items which are different in the results of the present test are the drag coefficient is higher by 8 to 23%. The average value is 15.4%. This is attributed to the more realistic model and an increase in parasite drag was not expected. The details of the scale model in References 2 and 3 were unavailable. This means the roughness and parasite drag details may not have been adequately reproduced.

UNCLASSIFIED

## UNCLASSIFIED

Report AFRPL-TR-69-90, Appendix A

These drag values are for the raw uncorrected drag coefficient data. The second item is the center of pressure of the body alone component. The body alone center of pressure in the present test is 1.8 diameters forward of the location in the previous test. This is attributed to the 1/16 inch gap between the nose cone and the following cylinder in the flight hardware model.

Another source of some discrepancy is the incorrect moment reference point used in the data reduction of Reference 2. This amounted to an error of approximately 1/2 diameter.

In summary, it is believed the present test is completely valid and these data should be used in all subsequent performance and stability computations.

### 5.2.9 PROCESSED DATA PRESENTATION AND DISCUSSION

The test data from Reference 1 were processed to obtain data suitable for use in a Space-General Six-Degree-of-Freedom Digital Computer Program.

The initial processing was performed on the axial force data to obtain a new drag coefficient curve as a function of Mach number. The resulting data are presented in Figure 5.2-19. These data are for the power-on full scale flight between sea level and 5000 ft altitude. The data in Figure 5.2-19 were obtained by correcting the test data from Reference 1 for Reynold's number with painted surface roughness (data from Reference 7), correcting for base drag, power on, (again Reference 7), and correcting for the removal of 18 Allen head screws, 2 body joints, and the drag due to the fin cant. Since the experimental data were for the Mach numbers,  $M = 2.5$ , 3.0, 3.5, and 4, it was necessary to obtain appropriate data for the transonic and subsonic regimes. This was accomplished using the data from Reference 1 and applying an incremental correction. In addition, an independent value of drag was computed for this configuration at  $M = 1$  using Reference 7. This corroborated the incrementally corrected data from Reference 1. It may be noted that these values are a 20% increase in drag over the processed data from previous tests. This is due to an increase in parasite drag, (full scale test), and a reduced Reynold's number correction (using curves with roughness

UNCLASSIFIED

# UNCLASSIFIED

Report AFRPL-TR-69-90, Appendix A

Reference 7, page 5-1). The roughness used was .001 inches - which is for painted surfaces.

Figure 5.2-20 presents the normal force coefficient slope (body alone and body tail) as a function of Mach number for low angles of attack. These data from this test are essentially identical with normal force coefficient slope data from References 2 and 3.

Figure 5.2-21 presents the center of pressure (body alone and body tail) as a function of Mach number for low angles of attack. The body-tail center of pressure is identical to that from References 2 and 3. The body alone center of pressure is approximately 1.8 diameters forward of the body alone center of pressure from References 2 and 3. This is attributed to the use of flight hardware in the full scale model of the latest test, and a 1/2 diameter error in data reduction of Reference 2. The latest test data are considered to be the most correct and will be used in any subsequent computations.

Figure 5.2-22 presents the rolling moment coefficient at zero angle of attack for both tail configurations tested in Reference 1. As can be seen, the tail configuration ( $T_2$ ) with the creased tip has a larger rolling moment. This is attributed to the crease acting like a curved tail fin. Using the data in Figure 5.2-22 for configuration  $BT_1$  and its cant angle,  $\delta = .5882^\circ$ , the  $C_{l_\delta}$  derivative was computed. These data are shown in Figure 5.2-23. Presented is  $C_{l_\delta}$  as a function of Mach number for low angles of attack. It may be noted that these data substantiate the estimates made using the breakdown force data from References 2 and 3. The test data are 15% lower than the values computed using breakdown data.

The data in Figures 5.2-22 and 5.2-23 were used to isolate the rolling moment coefficient due to creased tail fin tips. This was done in the following fashion:

$$\Delta C_{l_{\text{Fin Tips}}} = C_{l_{BT_2}} - C_{l_\delta} \delta_{T_2}$$

UNCLASSIFIED



## UNCLASSIFIED

Report AFRPL-TR-69-90, Appendix A

The assumption was made that  $C_{L\delta}$  was the same for both tail configurations. The resulting data are presented in Figure 5.2-24. Presented is the rolling moment due to tail fin creased tip as a function of Mach number. It may be noted that this fin tip crease is equivalent to a fin cant,  $\delta = .125$  deg in the supersonic Mach number range.

### 5.2.10 RECOMMENDATIONS AND CONCLUSIONS

Examination of the wind tunnel data resulting from the present test indicates that the data are correct and valid and should be used in all aerodynamic computations.

It is recommended that a test to obtain some full scale transonic test data be initiated at some future date.

### 5.2.11 REFERENCES

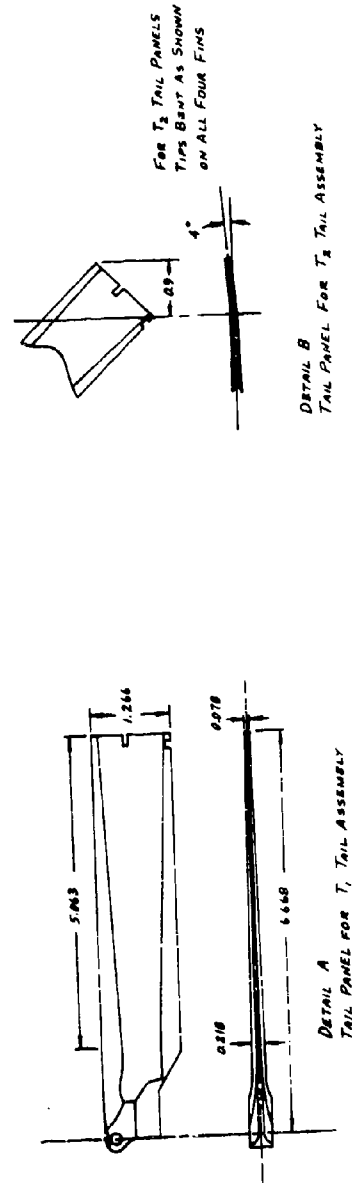
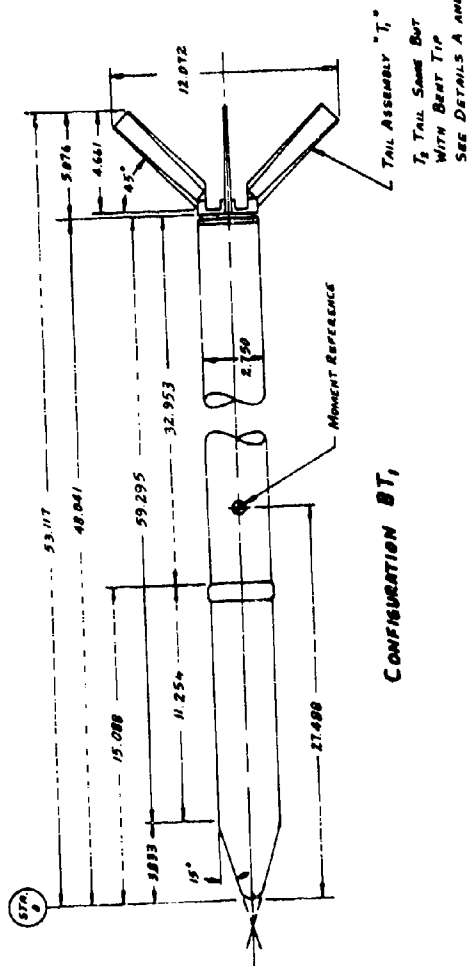
1. AFRLP Aerojet 2.75 in. Rockets Project No. VA 0706, Tunnel 40-Inch Supersonic Tunnel Type Data, Tabulated Data Test Completion Date, Dec. 12, 1967, AEDC Tullahoma, Tennessee.
2. AEDC TR-65-267, "Wind Tunnel Tests of a 2.75 FFAR,  $M = 1.50$  to 5".
3. AEDC TR-65-248, "Wind Tunnel Tests of a 2.75 FFAR,  $M = 0.60$  to 1.50".
4. Test Facilities Handbook (6th Edition) Arnold Engineering Development Center, Arnold Air Force Station, Tennessee, 1966.
5. SG Dwg. No. 13655 1117634, Wind Tunnel Model 2.75 in. Folding Fin Aircraft Rocket.
6. "2.75 FFAR Wind Tunnel Pretest Data", Aerojet-General Corporation, Space-General Plant, El Monte, California, 1967.
7. "Fluid Dynamic Drag", by Sighard Hoerner, 1958.

UNCLASSIFIED

UNCLASSIFIED

Report AFRPL-TR-69-90, Appendix A

FIGURE 3.2-1  
2.75 FFAR CONFIGURATION DEFINITION  
AEDC WIND TUNNEL TEST VAO706



UNCLASSIFIED

UNCLASSIFIED

Report AFRPL-TR-69-90, Appendix A

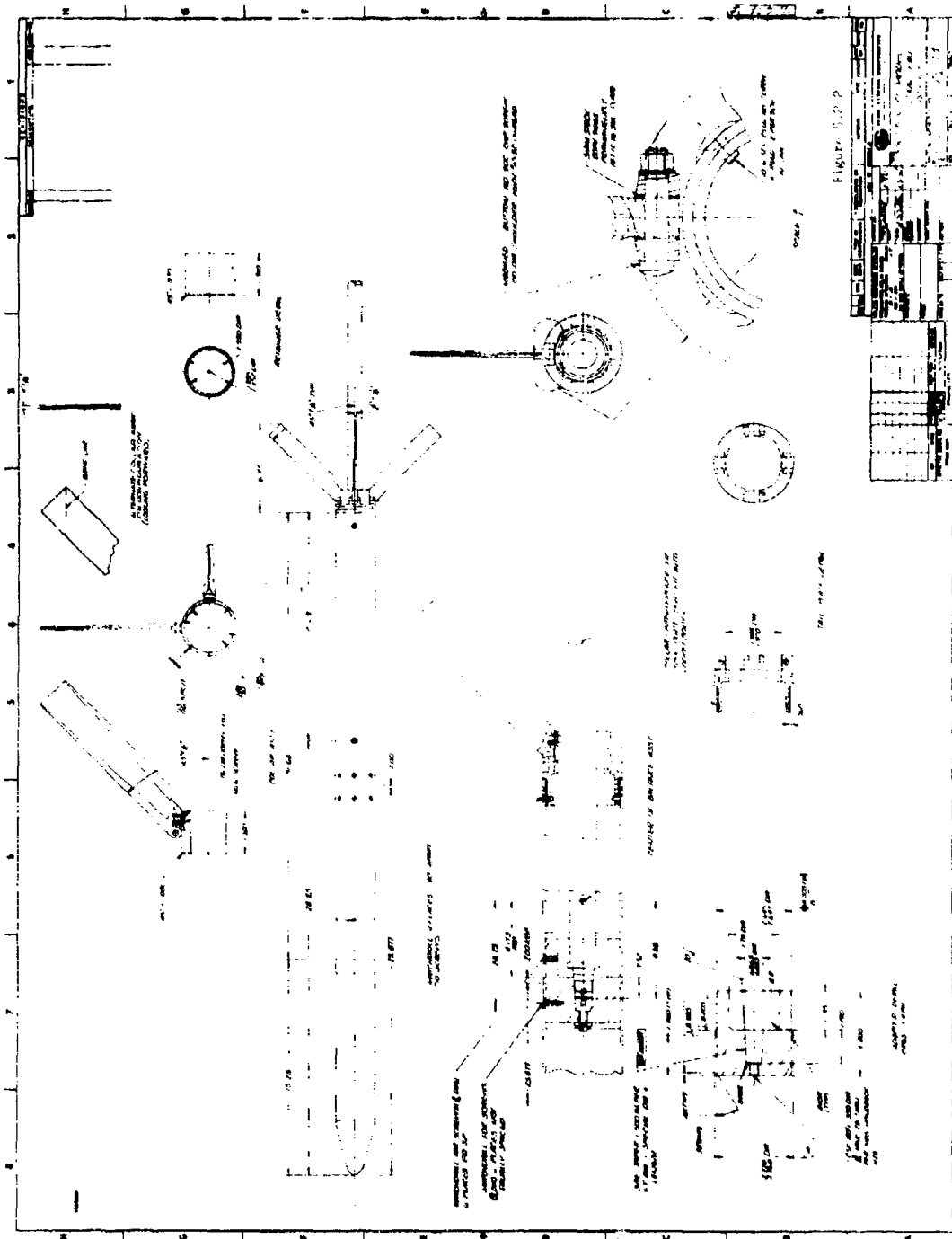


Figure 3.2.2

UNCLASSIFIED

UNCLASSIFIED

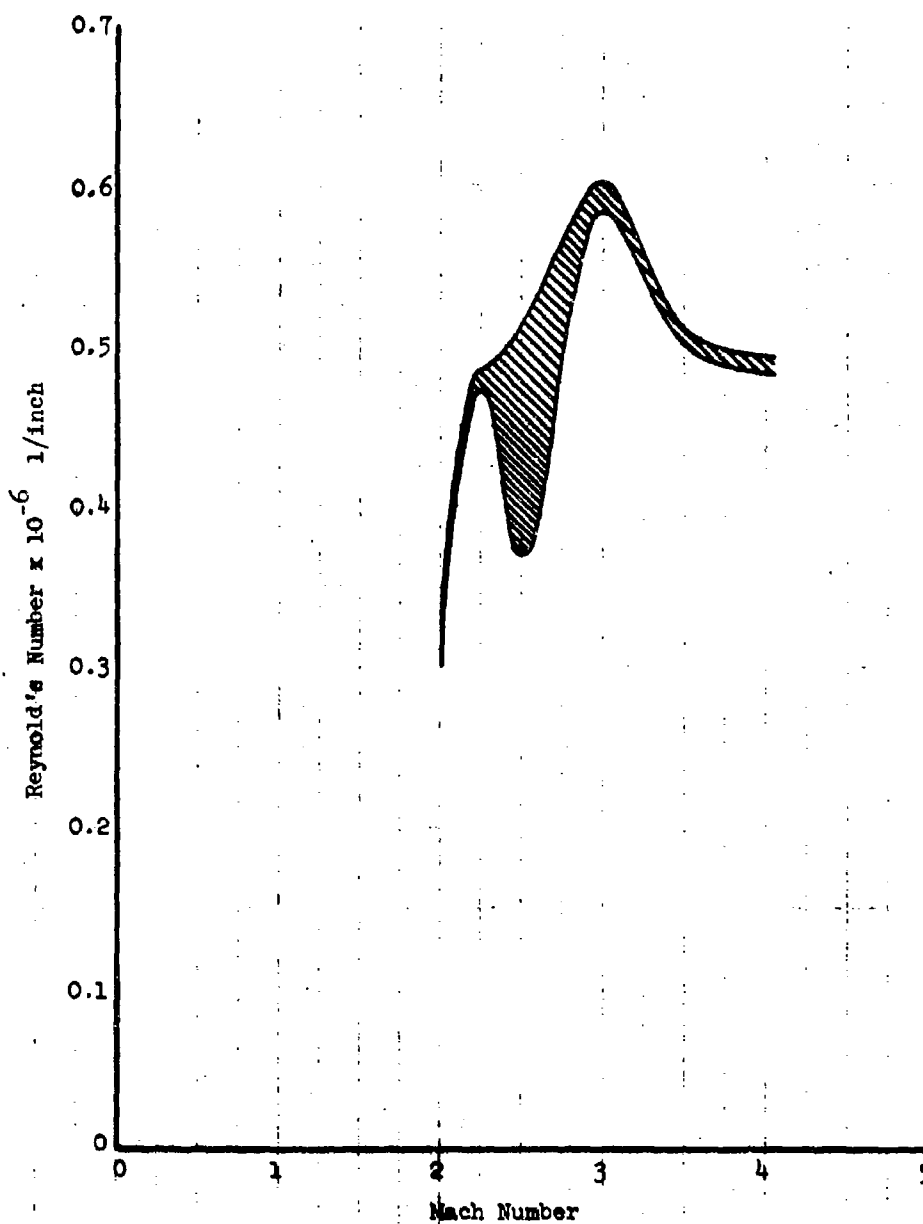
Report AFRPL-TR-69-90, Appendix A

Figure 5.2-3

2.75 FTAR Vehicle

AEDC Wind Tunnel Test VA 0706

Test Reynold's Number as a Function of Mach Number



UNCLASSIFIED

# UNCLASSIFIED

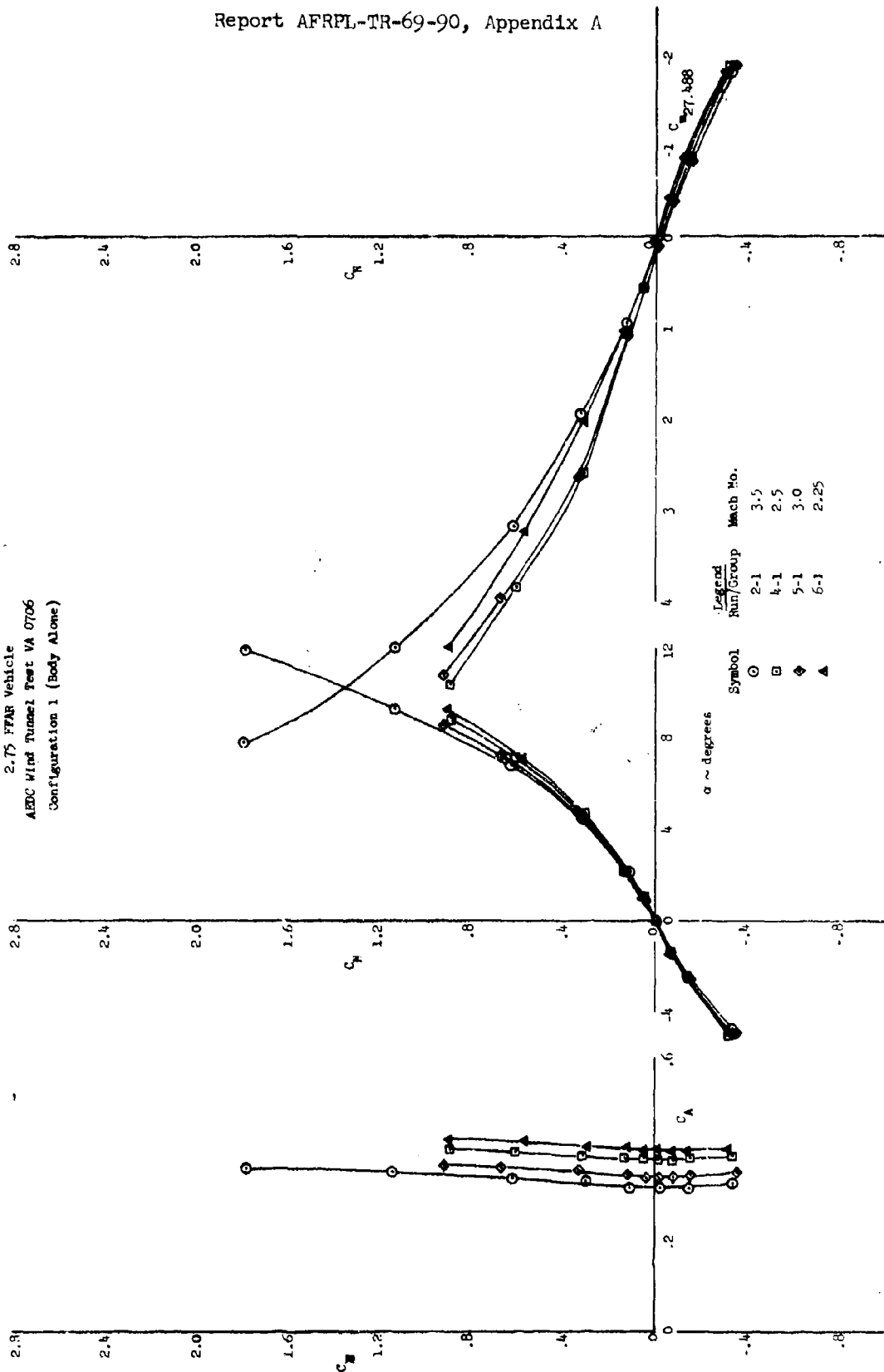
Report AFRPL-TR-69-90, Appendix A

Figure 5.2-4

2.75 FPAR Vehicle

AEDC Wind Tunnel Test VA 0706

Configuration 1 (Body Alone)

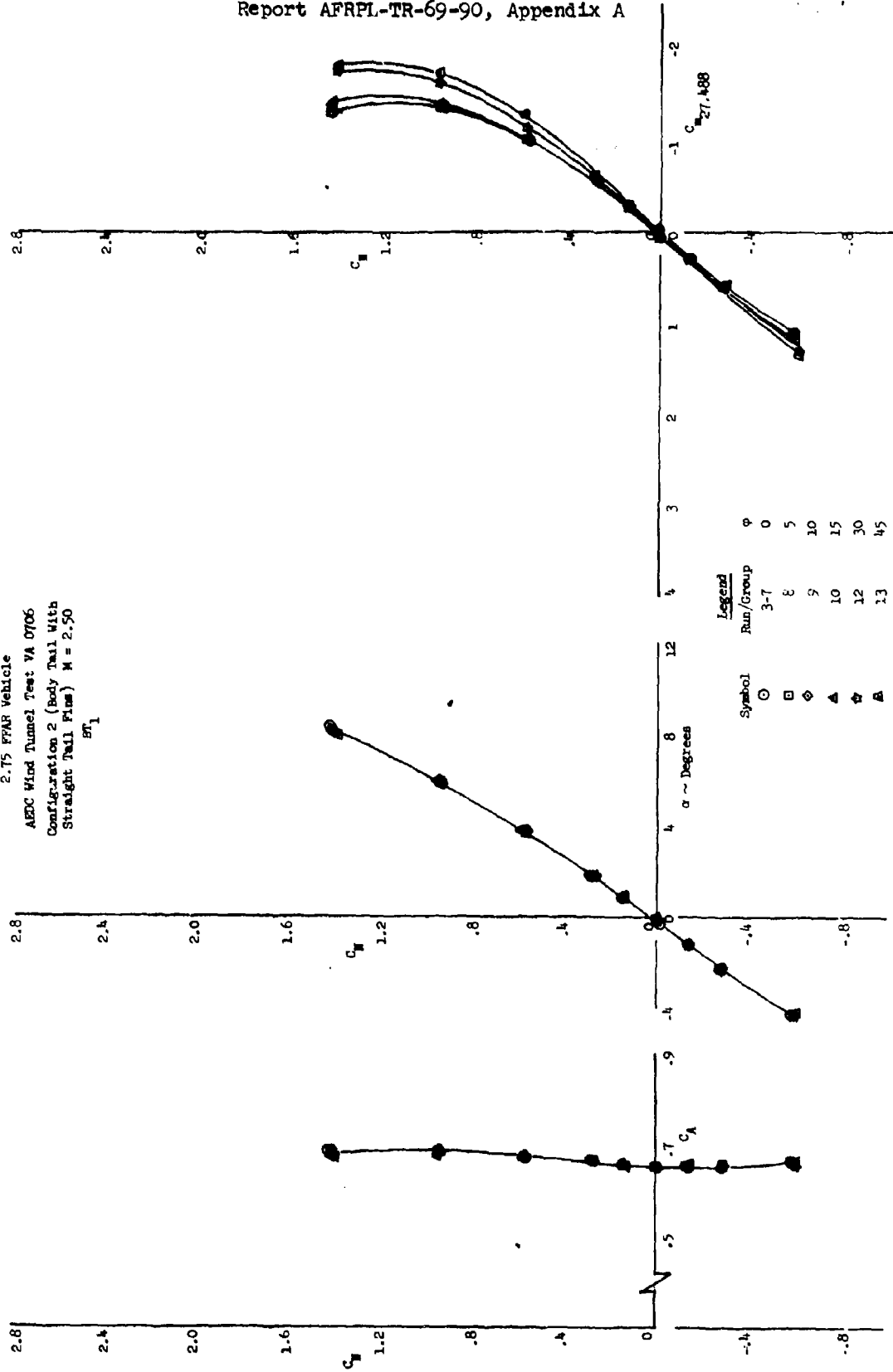


UNCLASSIFIED

UNCLASSIFIED

Report AFRPL-TR-69-90, Appendix A

Figure 5.2-5  
2.75 FPAF Vehicle  
AEDC Wind Tunnel Test VA 0706  
Configuration 2 (Body Tail With  
Straight Tail Fin)  $M = 2.50$   
 $BT_1$

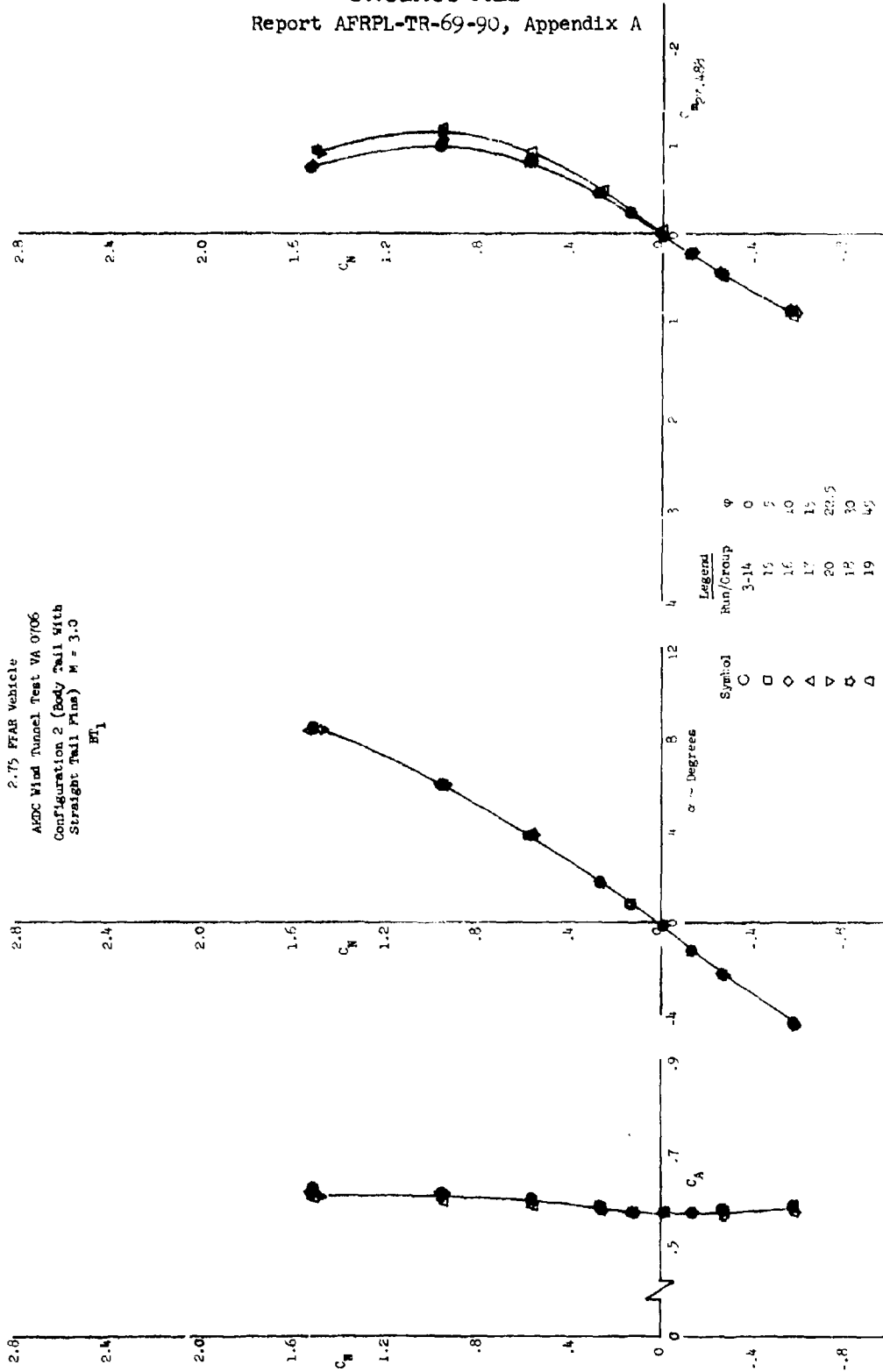


UNCLASSIFIED

UNCLASSIFIED

Report AFRPL-TR-69-90, Appendix A

Figure 5.2-6  
2.75 FFAB Vehicle  
AMDC Wind Tunnel Test VA 0706  
Configuration 2 (Body Tail With  
Straight Tail Fins)  $M = 3.0$   
 $BT_1$

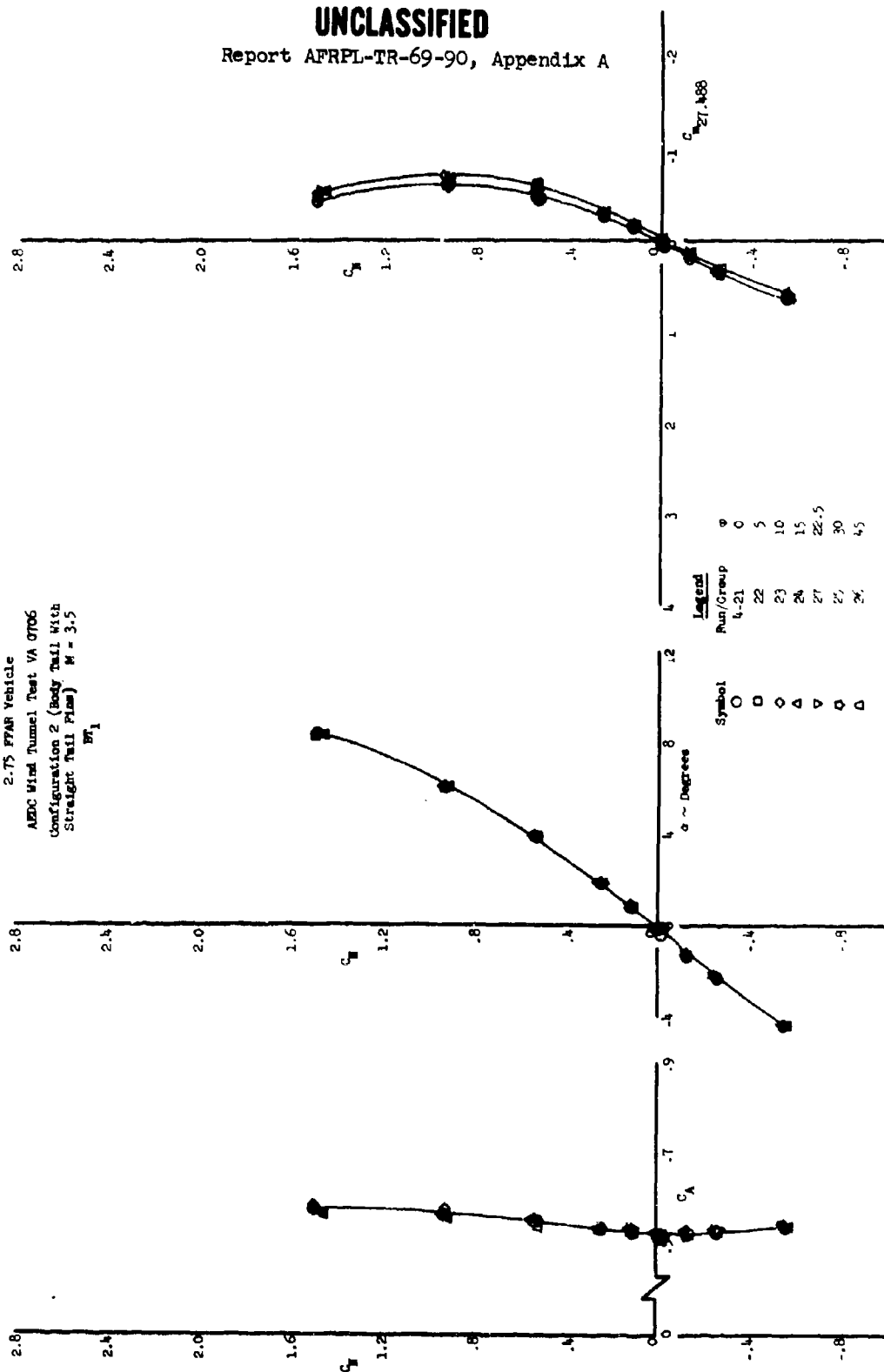


UNCLASSIFIED

UNCLASSIFIED

Report AFRPL-TR-69-90, Appendix A

Figure 5.2-7  
2.75 F7AR Vehicle  
AEDC Wind Tunnel Test VA 0706  
Configuration 2 (Body Tail With  
Straight Tail Plane)  $M = 3.5$   
 $DT_1$



UNCLASSIFIED

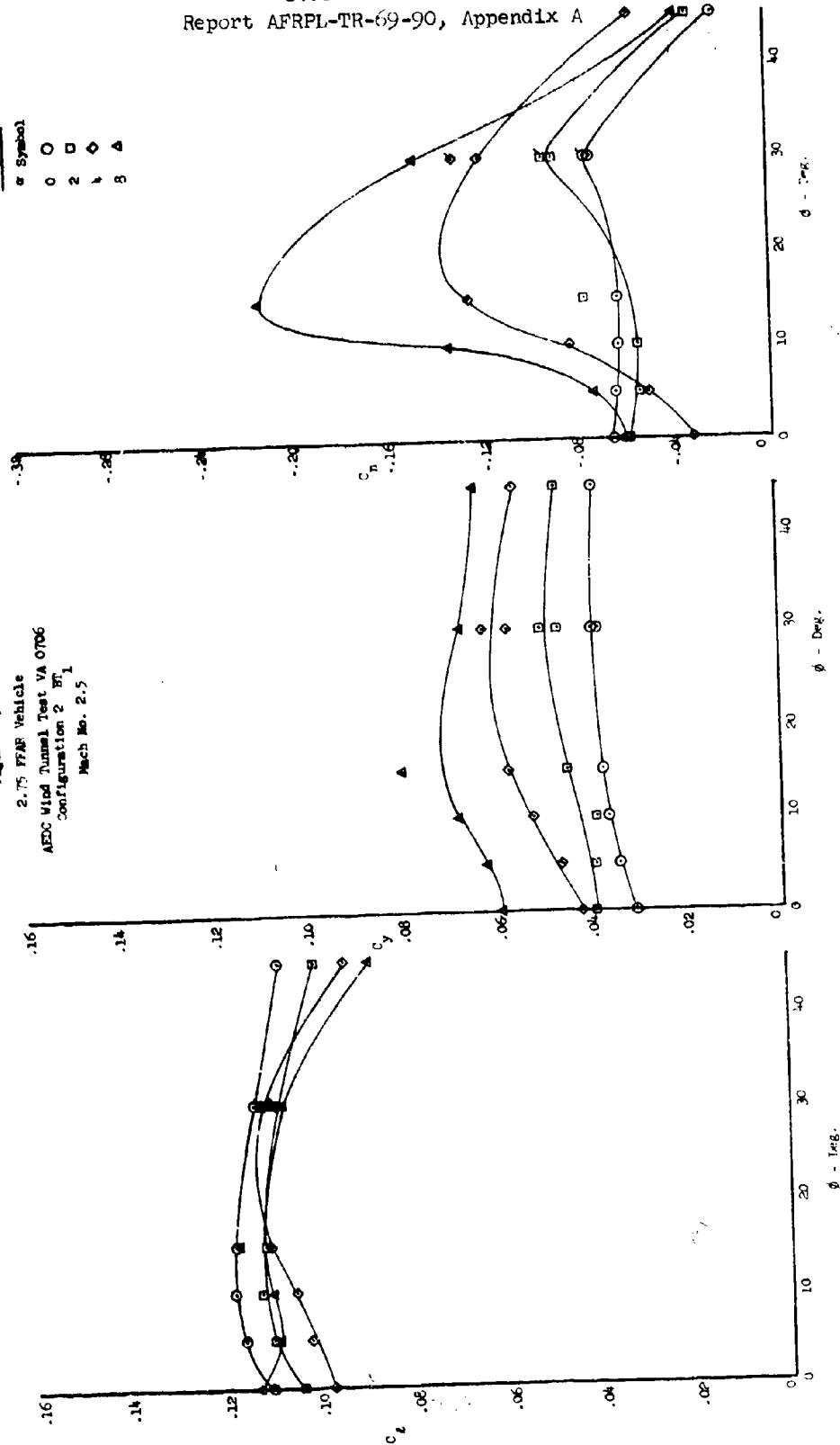


UNCLASSIFIED

Report AFRPL-TR-69-90, Appendix A

Legend  
 $\alpha$  Symbol  
 0  $\circ$   
 2  $\square$   
 4  $\diamond$   
 8  $\triangle$

Figure 2.5-8  
 2.75 FFAR Vehicle  
 AEDC Wind Tunnel Test VA 0706  
 Configuration 2 BT  
 Mach No. 2.5



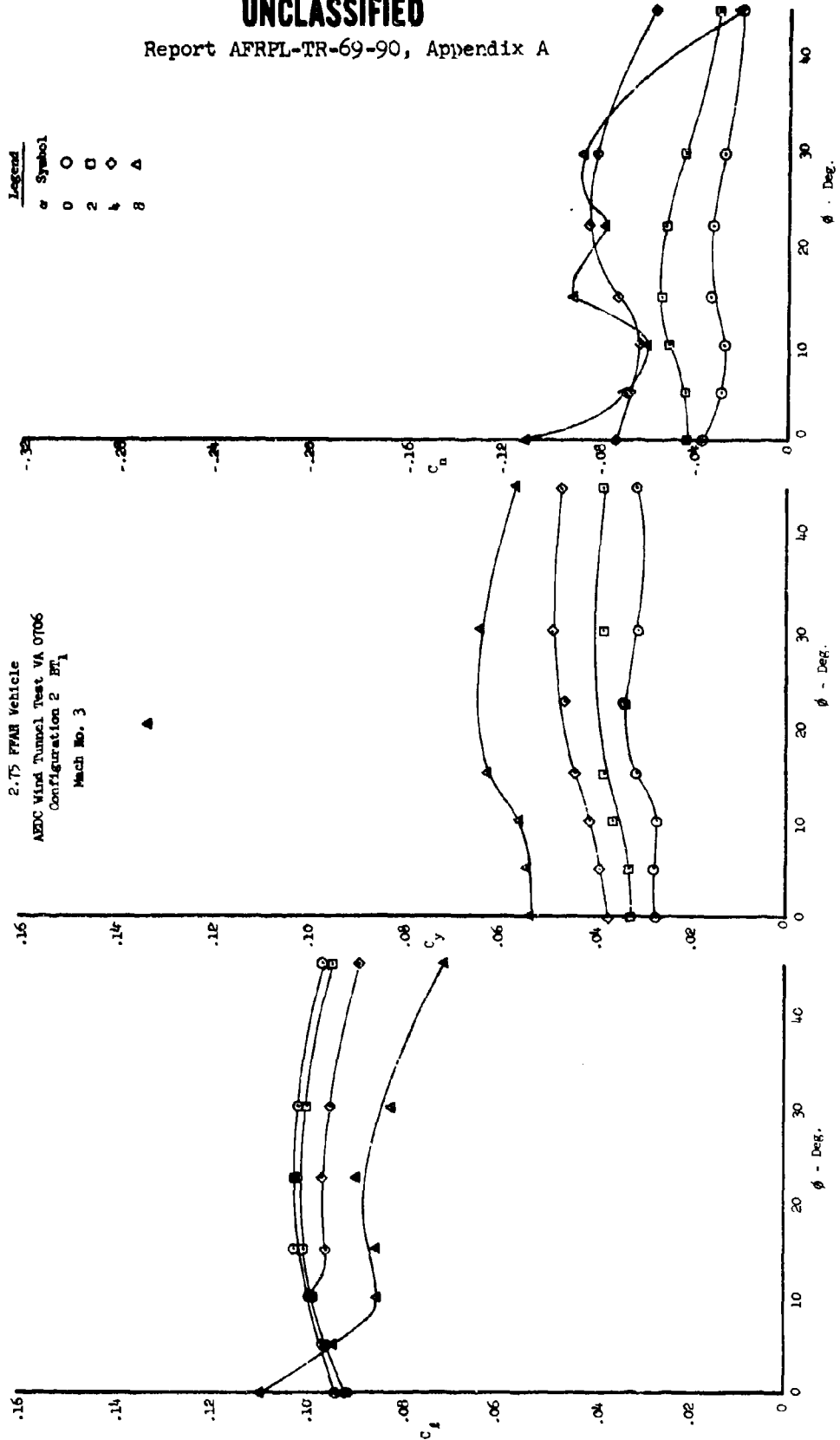
UNCLASSIFIED

UNCLASSIFIED

Report AFRPL-TR-69-90, Appendix A

Legend	$\alpha$	Symbol
0	0	○
2	2	□
4	4	◇
8	8	△

Figure 5.2-9  
2.75 FTAB Vehicle  
AEDC Wind Tunnel Test VA 0706  
Configuration 2 BT<sub>1</sub>  
Mach No. 3



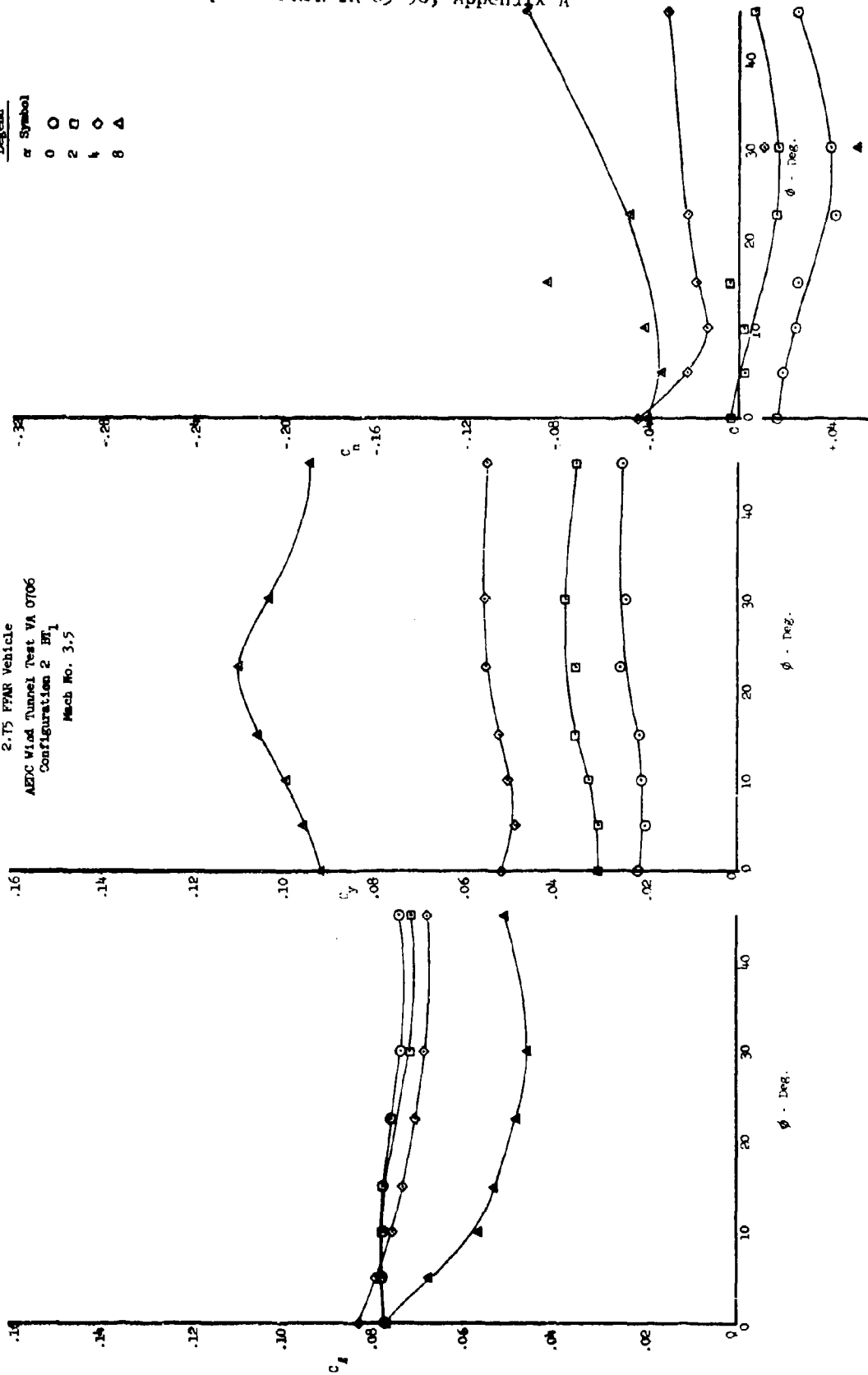
UNCLASSIFIED

UNCLASSIFIED

Report AFRPI-TR-69-90, Appendix A

Legend	$\alpha$	Symbol
0	0	○
2	2	□
4	4	◇
8	8	△

Figure 5.2-10  
2.75 FPAR Vehicle  
AEDC Wind Tunnel Test VA 0706  
Configuration 2 BT<sub>1</sub>  
Mach No. 3.5



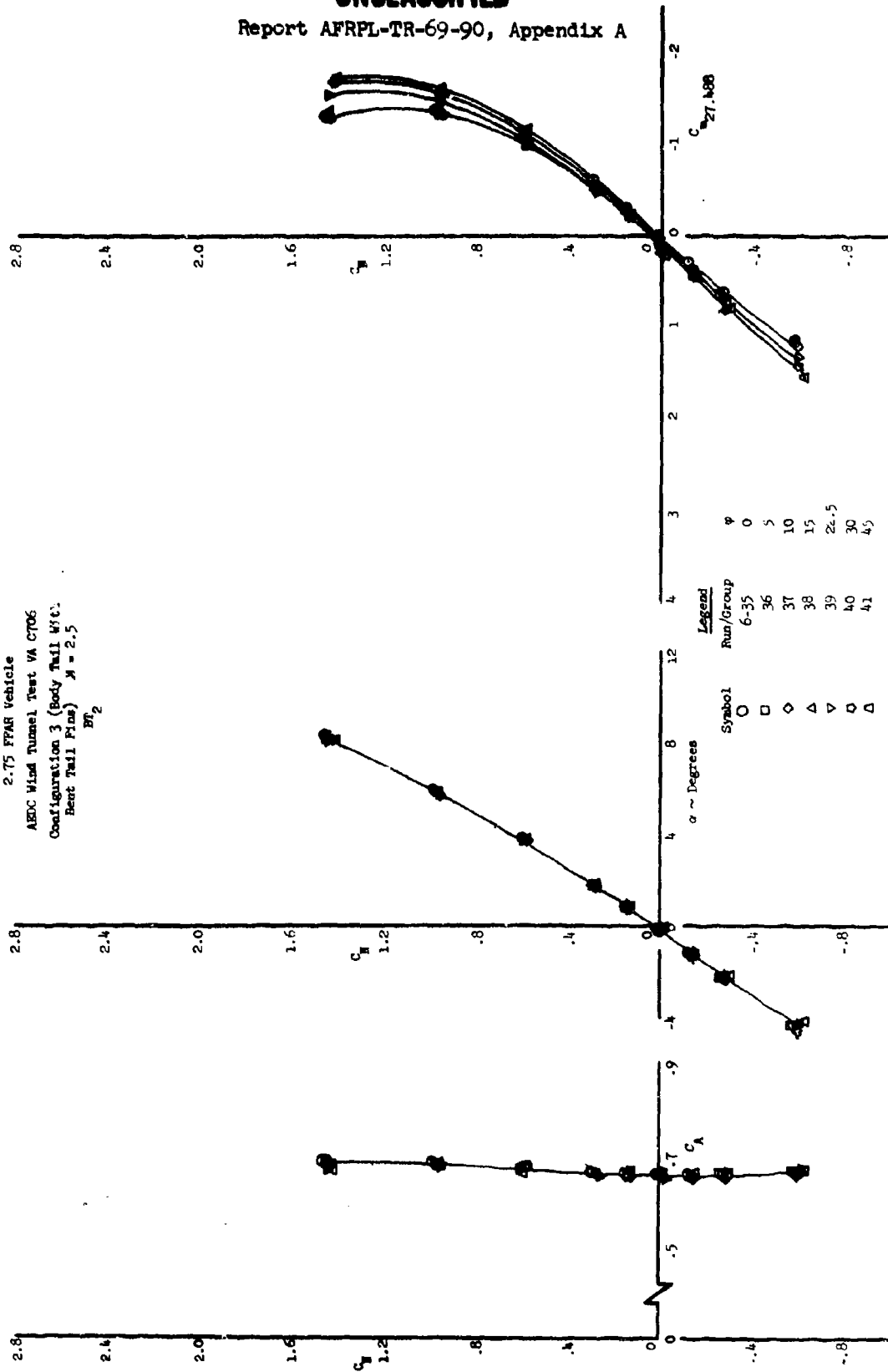
UNCLASSIFIED

UNCLASSIFIED

Report AFRPL-TR-69-90, Appendix A

Figure 5.2-11  
2.75 FPAR Vehicle

AEDC Wind Tunnel Test VA C706  
Configuration 3 (Body Tail Wt.  
Bent Tail Fins)  $M = 2.5$   
 $Re_2$

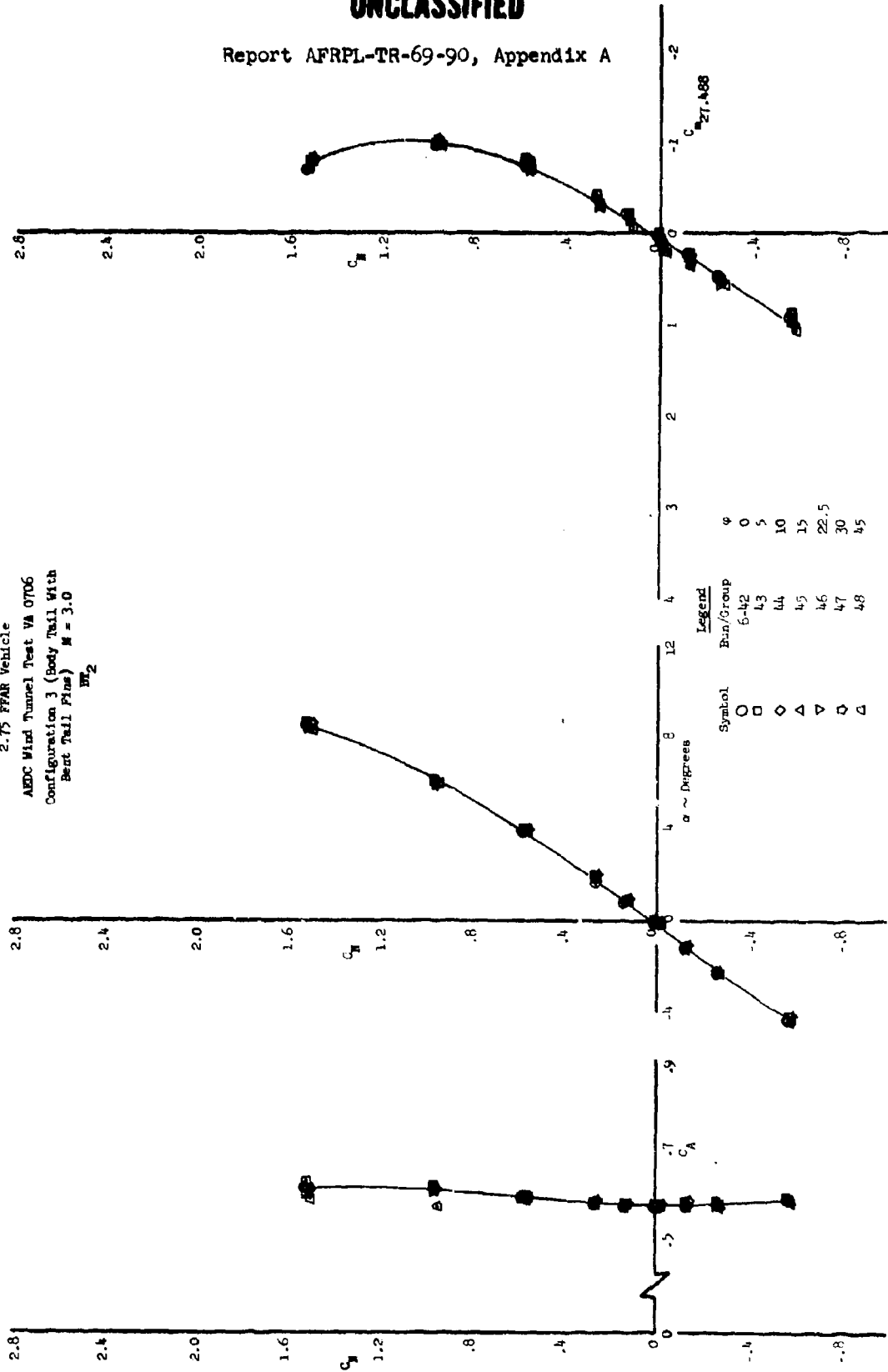


UNCLASSIFIED

UNCLASSIFIED

Report AFRPL-TR-69-90, Appendix A

Figure 5.2-12  
2.75 FEAR Vehicle  
ABDC Wind Tunnel Test VA 0706  
Configuration 3 (Body Tail With  
Bent Tail Fins)  $M = 3.0$

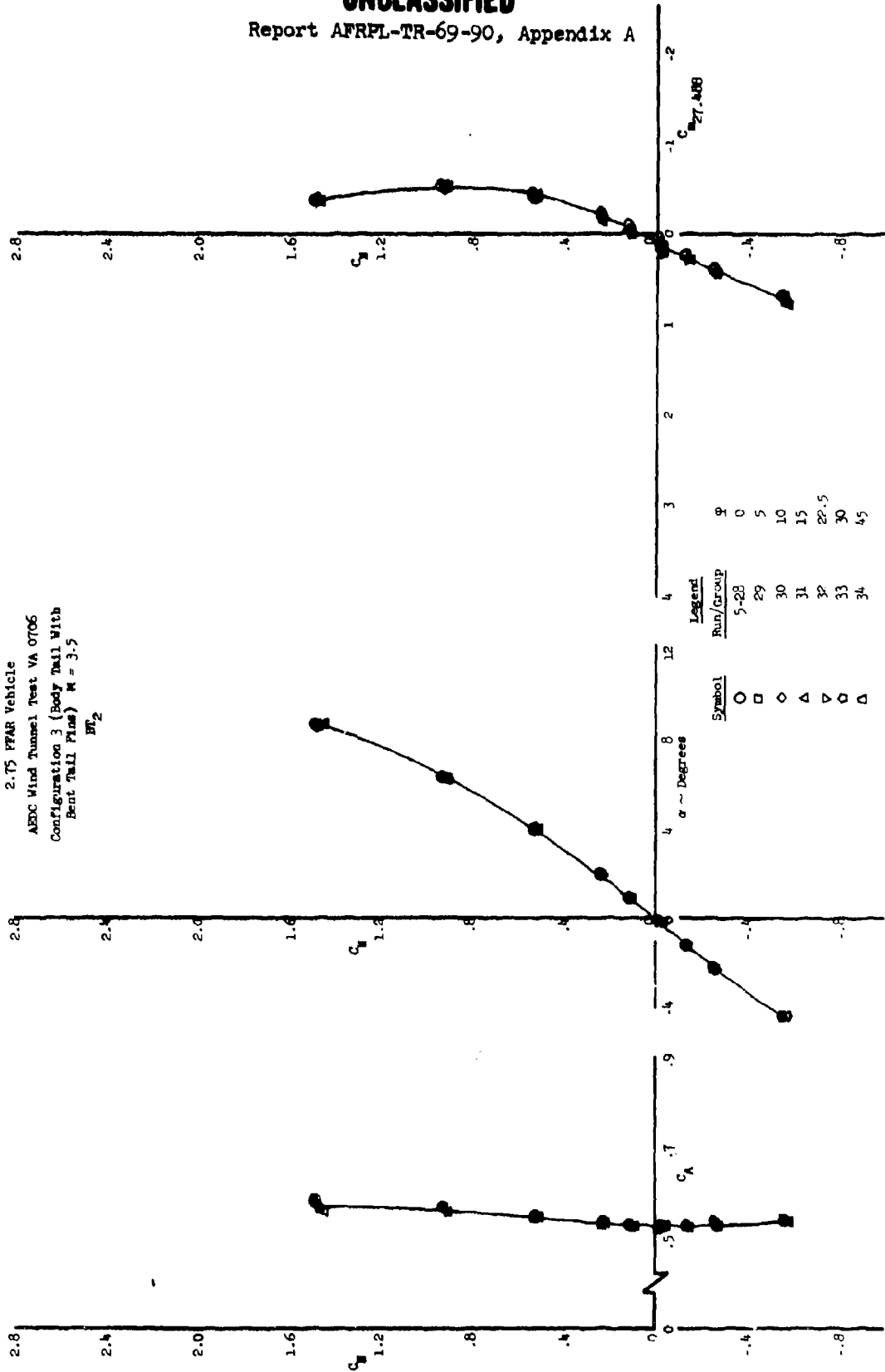


UNCLASSIFIED

UNCLASSIFIED

Report AFRPL-TR-69-90, Appendix A

Figure 5.2-13  
2.75 PFAR Vehicle  
AEDC Wind Tunnel Test VA 0706  
Configuration 3 (Body Tail With  
Bent Tail Fins)  $M = 3.5$   
 $W_2$

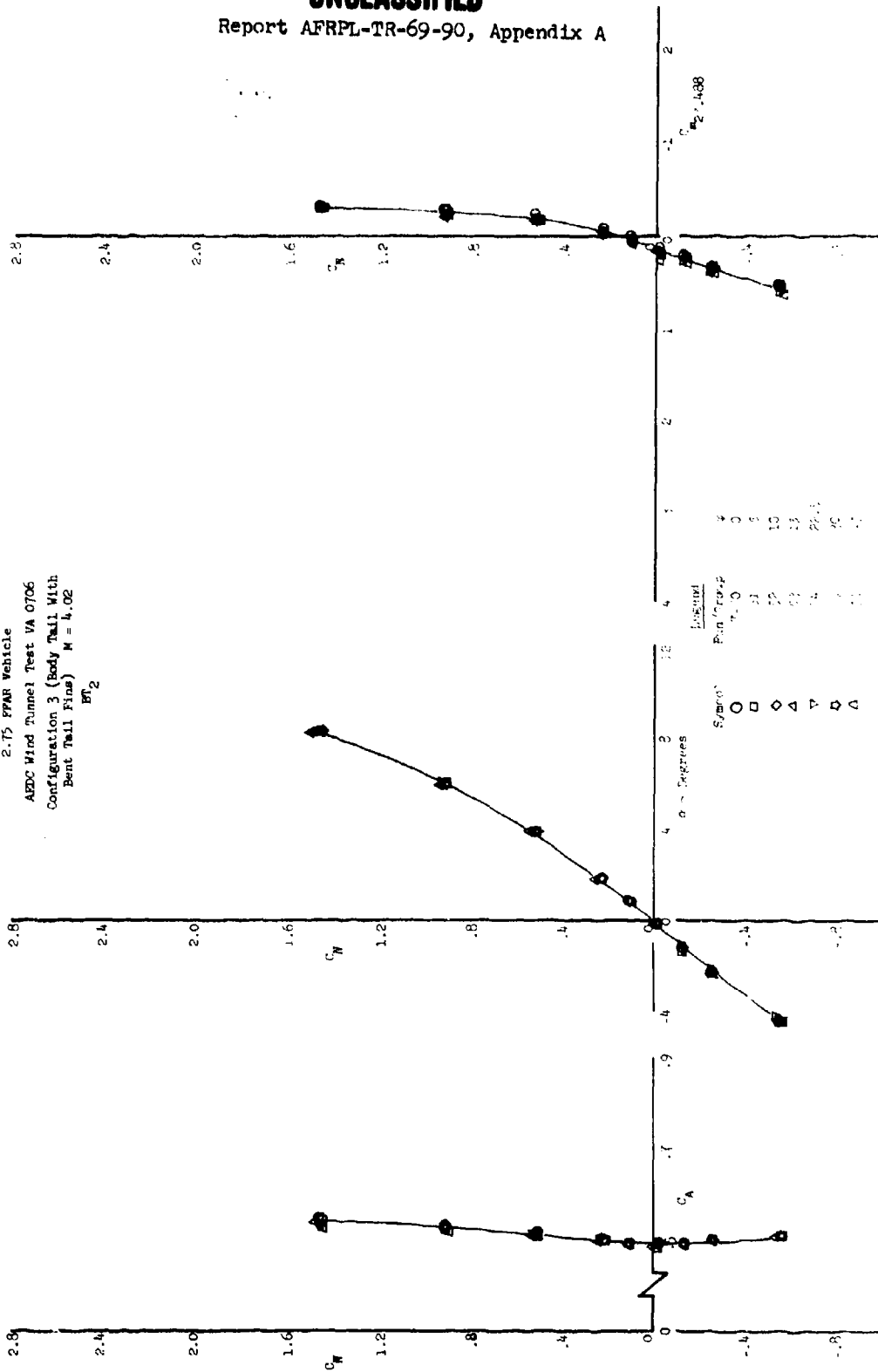


UNCLASSIFIED

UNCLASSIFIED

Report AFRPL-TR-69-90, Appendix A

Figure 5.2-14  
2-T5 PFAR Vehicle  
AUSC Wind Tunnel Test VA 0706  
Configuration 3 (Body Tail With  
Bent Tail Fin)  $M = 4.02$   
 $Re_2$

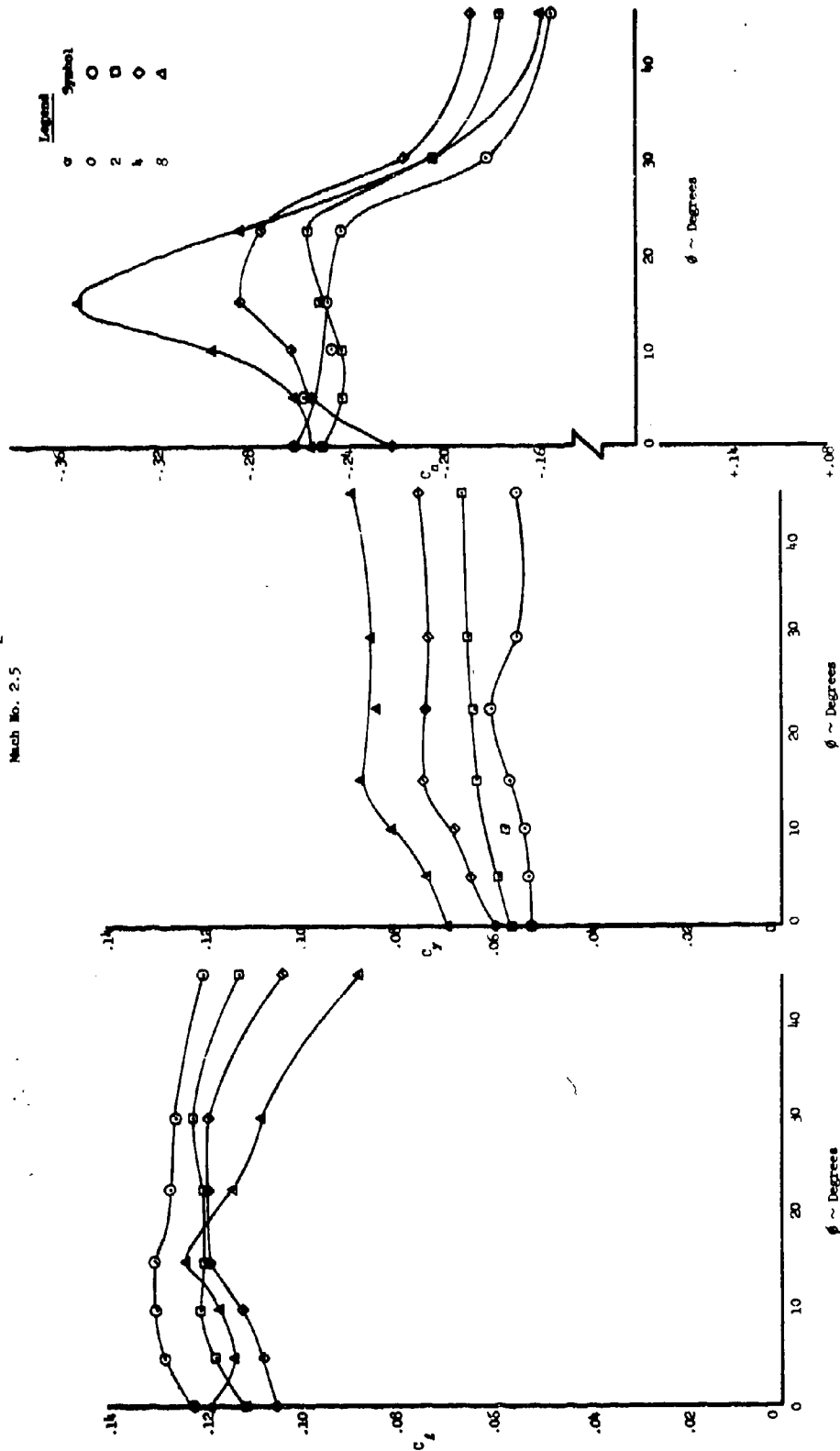


UNCLASSIFIED

UNCLASSIFIED

Report AFRPL-TR-69-90, Appendix A

Figure 5.2-15  
2.5 PFAR Vehicle  
ABDC Wind Tunnel Test VA 0706  
Configuration 3 BF<sub>2</sub>  
Mach No. 2.5



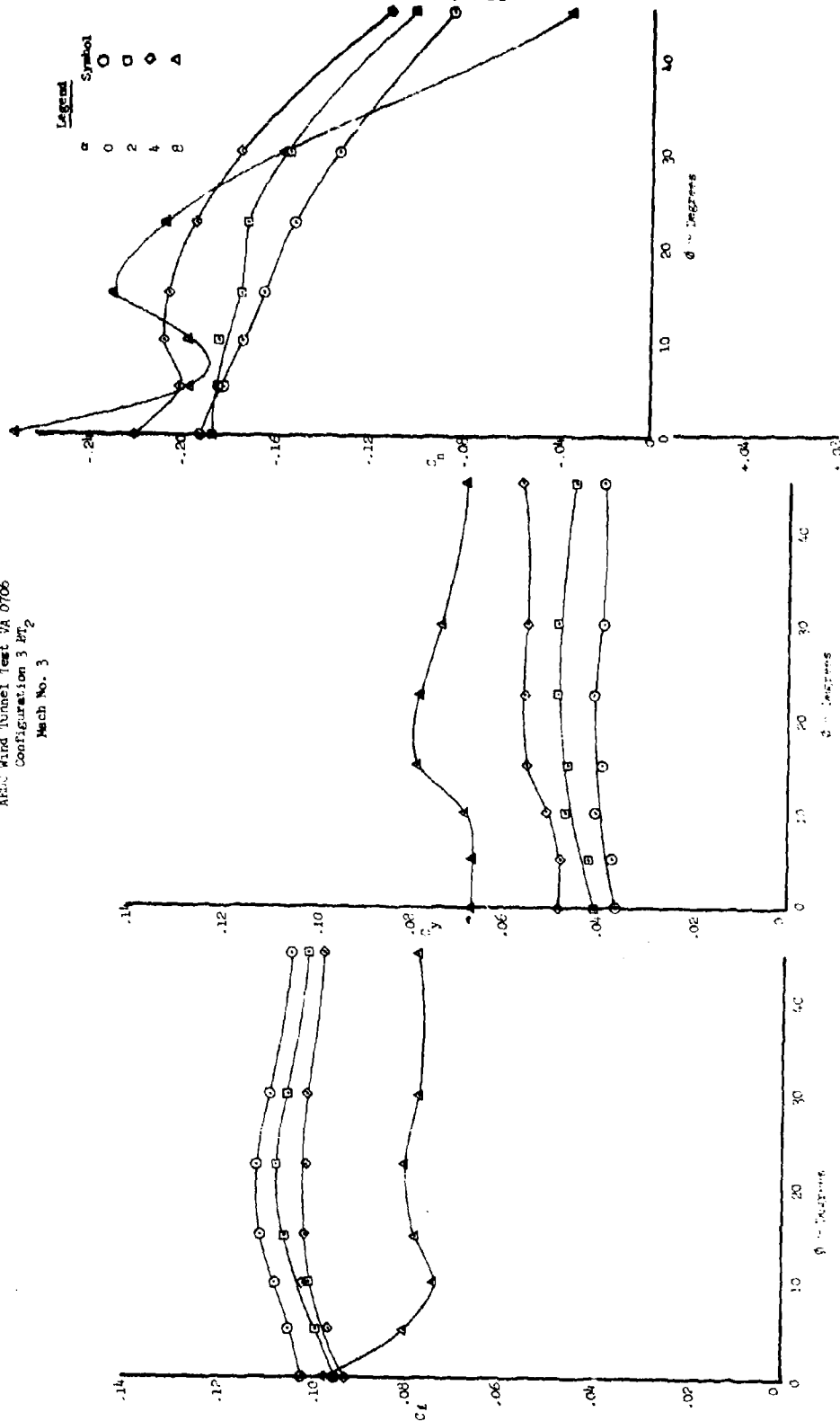
UNCLASSIFIED



UNCLASSIFIED

Report AFRPL-TR-69-90, Appendix A

Figure 5.2-16  
2.75 FFAR Vehicle  
AFRC Wind Tunnel Test VA 0706  
Configuration 3 BT2  
Mach No. 3

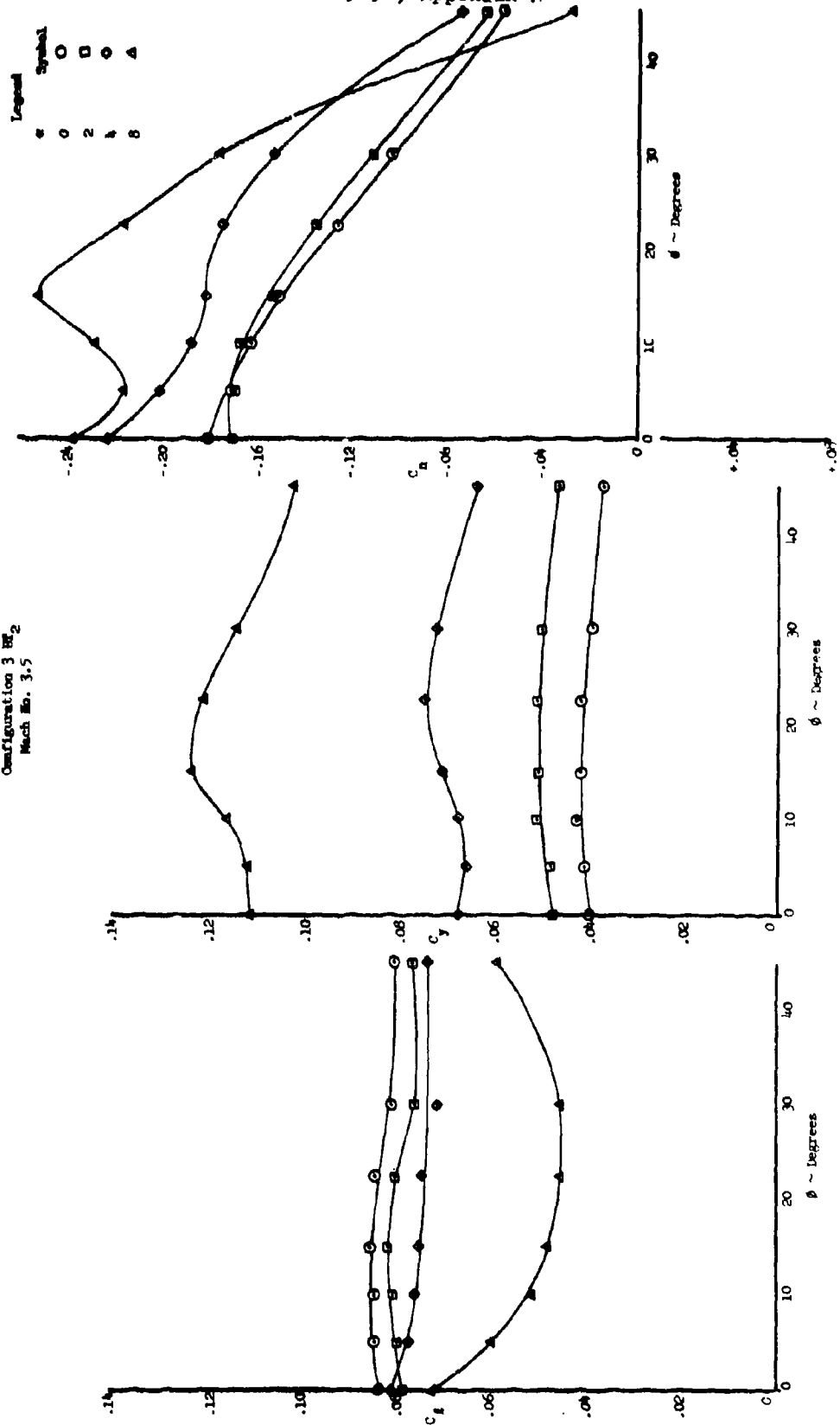


UNCLASSIFIED

UNCLASSIFIED

Report AFRPL-TR-69-90, Appendix A

Figure 5.2-17  
2.75 TFAR Vehicle  
AEDC Wind Tunnel Test VA 0706  
Configuration 3 RZ<sub>2</sub>  
Mach No. 3.5

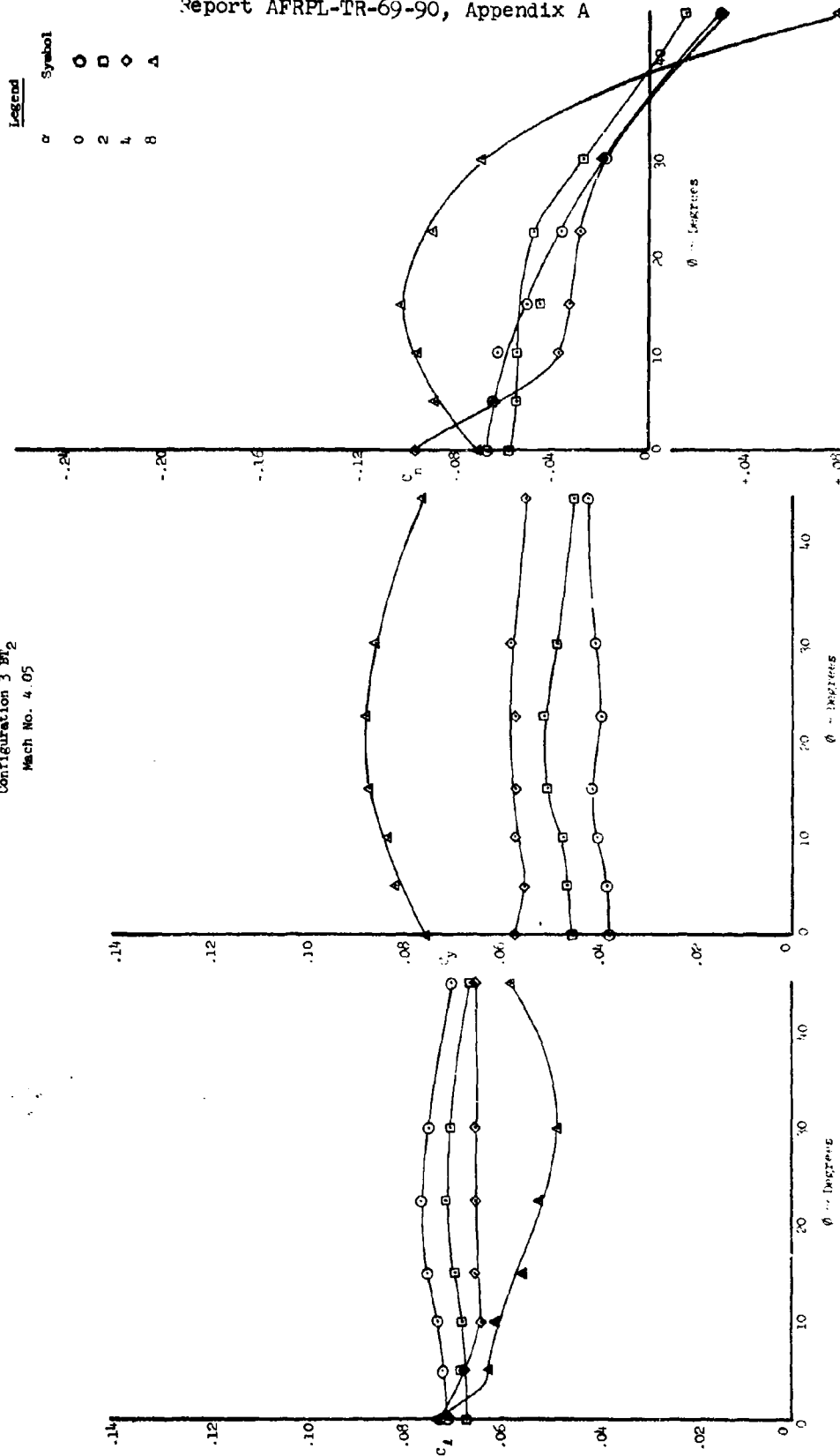


UNCLASSIFIED

UNCLASSIFIED

Report AFRPL-TR-69-90, Appendix A

Figure 5.2-18  
2.75 FPAR Vehicle  
AEDC Wind Tunnel Test VA 0706  
Configuration 3 BF<sub>2</sub>  
Mach No. 4.05

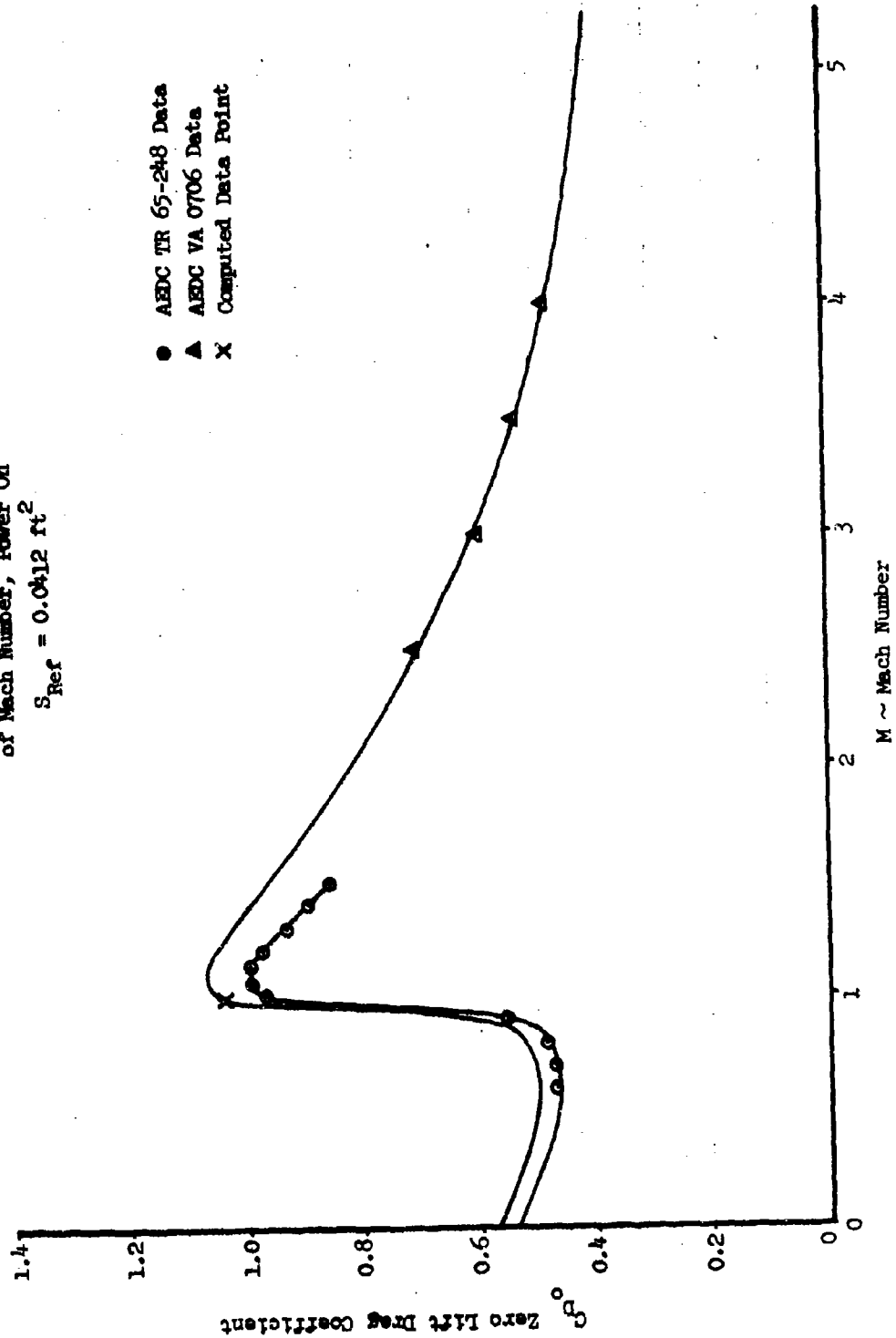


UNCLASSIFIED

UNCLASSIFIED

Report AFRL-TR-69-90, Appendix A

Figure 5.2-19  
AEDC VA 0706 Wind Tunnel Test  
Drag Coefficient as a Function  
of Mach Number, Power On  
 $S_{Ref} = 0.0412 \text{ ft}^2$

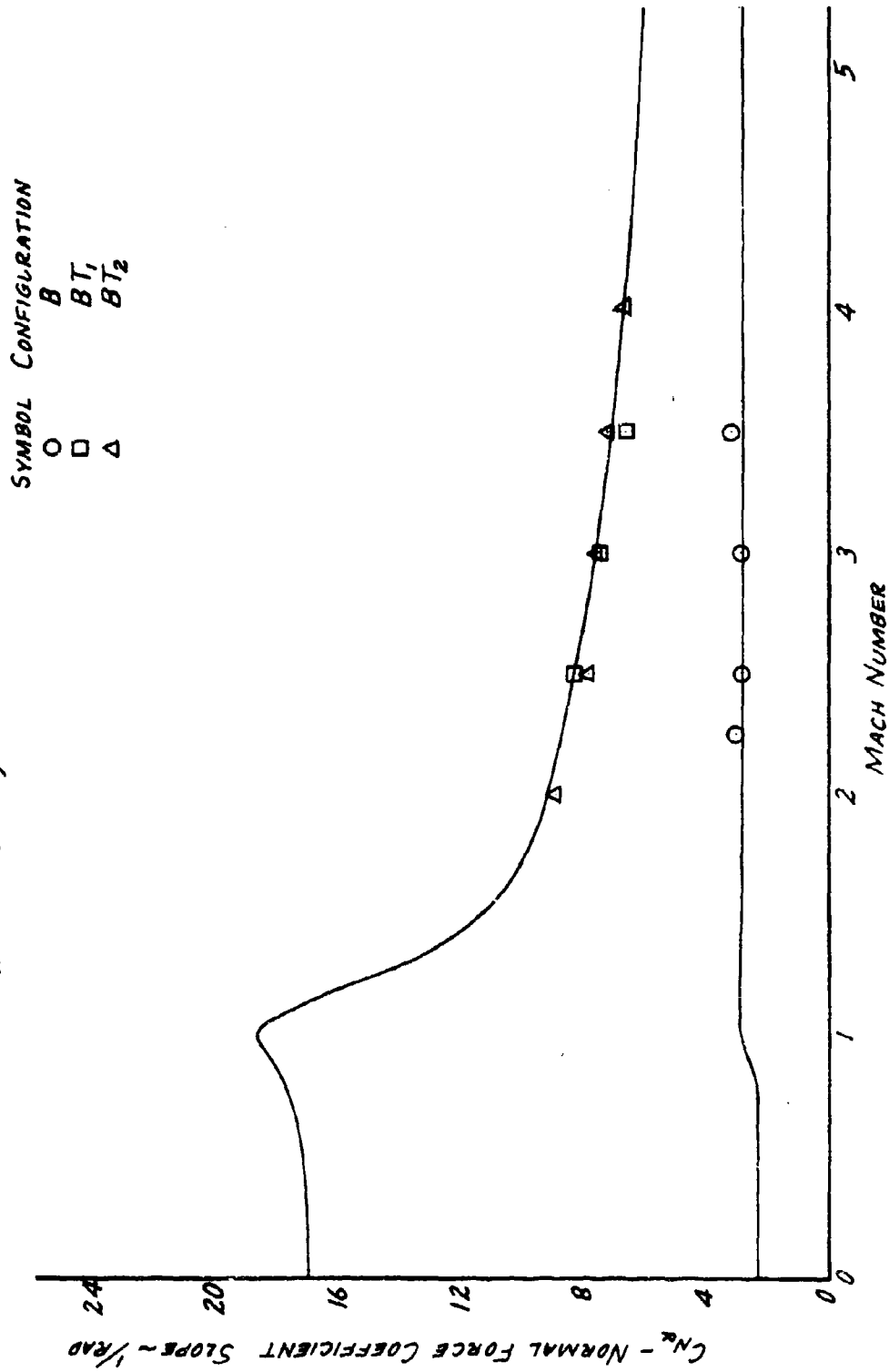


UNCLASSIFIED

UNCLASSIFIED

Report AFRPL-TR-69-90, Appendix A

FIGURE 5.2-20  
AEDC VA0706 WIND TUNNEL TEST  
NORMAL FORCE SLOPE AS A FUNCTION  
OF MACH NUMBER  
 $\alpha = -4^\circ$  TO  $+4^\circ$ ,  $\phi = 0^\circ$



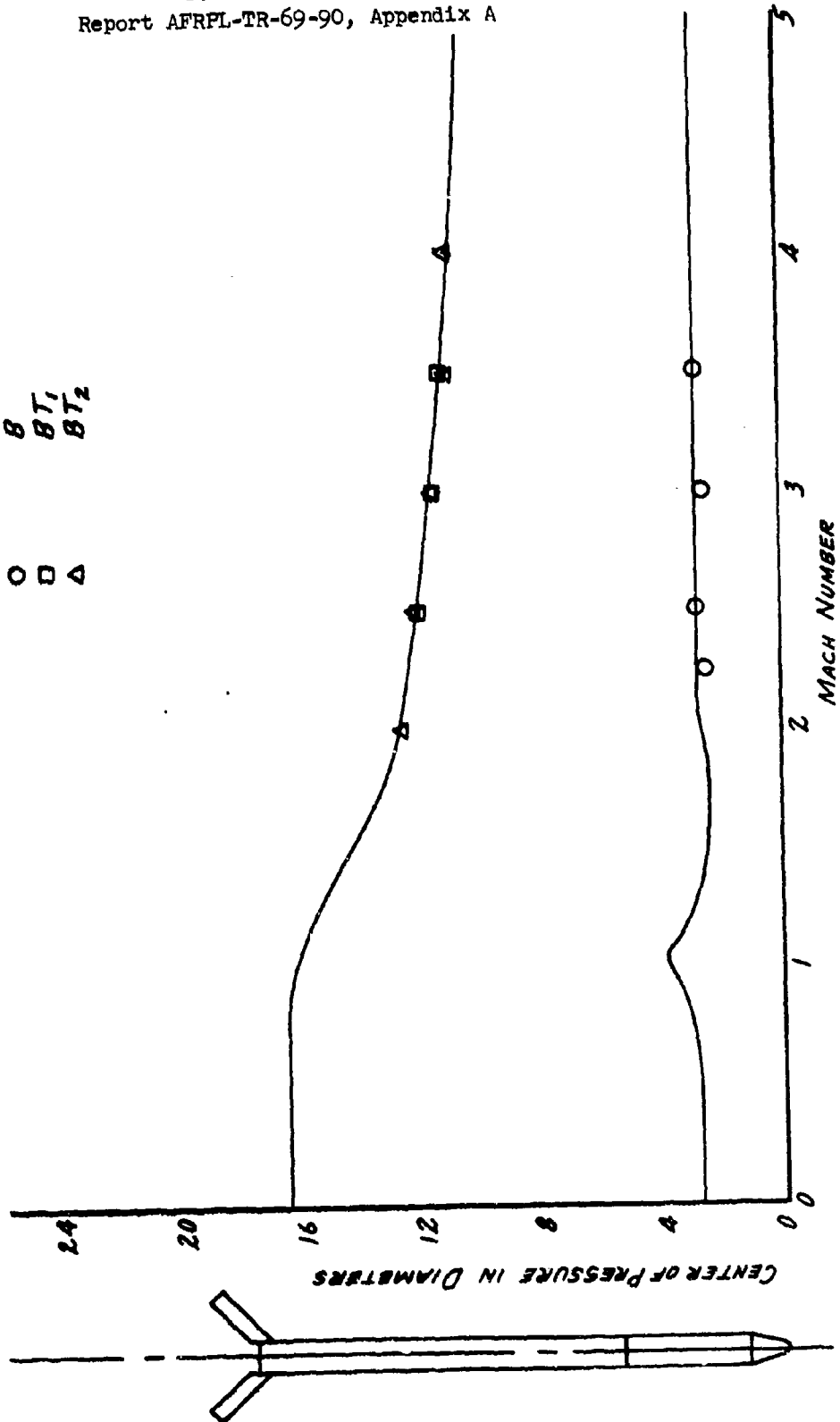
UNCLASSIFIED

UNCLASSIFIED

Report AFRPL-TR-69-90, Appendix A

FIGURE 5.2-21  
AEDC VA0706 WIND TUNNEL TEST  
CENTER OF PRESSURE AS A FUNCTION  
OF MACH NUMBER  
 $\alpha = -4^\circ$  TO  $+4^\circ$ ,  $\phi = 0^\circ$

SYMBOL CONFIGURATION	
○	B
□	BT <sub>1</sub>
△	BT <sub>2</sub>

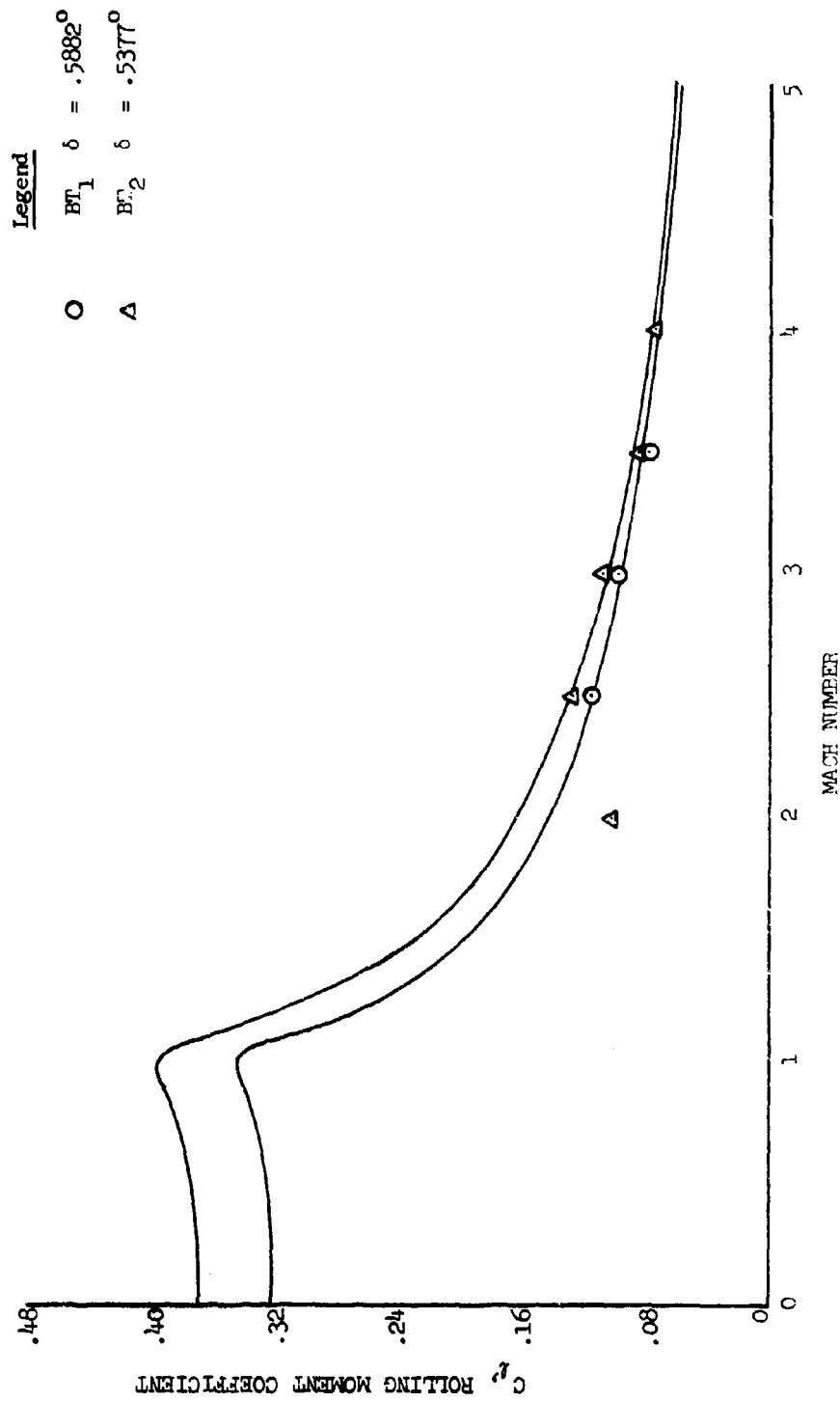


UNCLASSIFIED

UNCLASSIFIED

Report AFRPL-TR-69-90, Appendix A

Figure 5.2-22  
2.75 FFAR Vehicle  
Rolling Moment as a Function of Mach  
Number at Zero Angle of Attack  
AEDC Test VA 0706

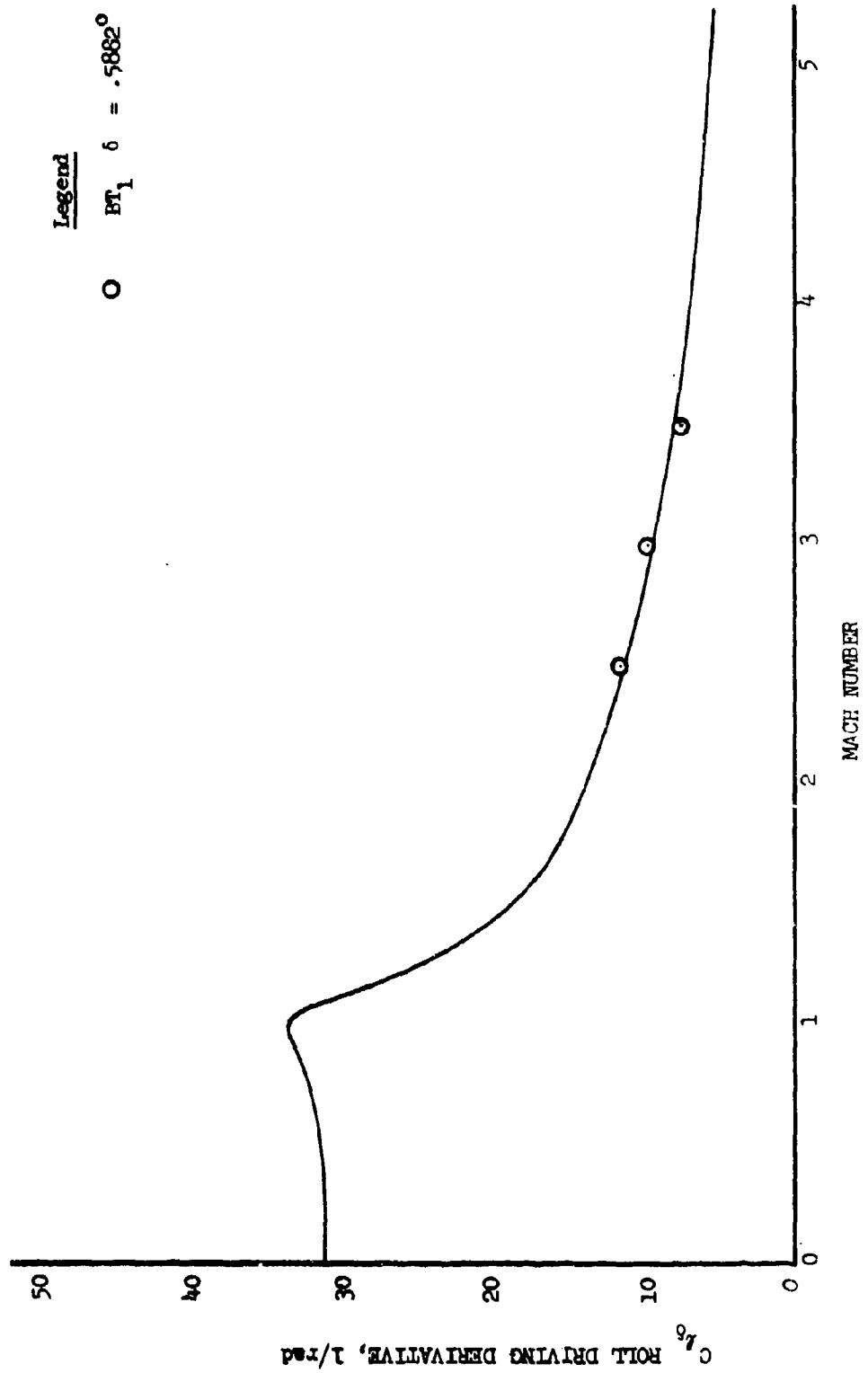


UNCLASSIFIED

UNCLASSIFIED

Report AFRPL-TR-69-90, Appendix A

Figure 5.2-23  
2.75 FFAR Vehicle  
Roll Driving Derivative as a Function  
of Mach Number,  $\alpha = 0$   
AEDC VA 0706



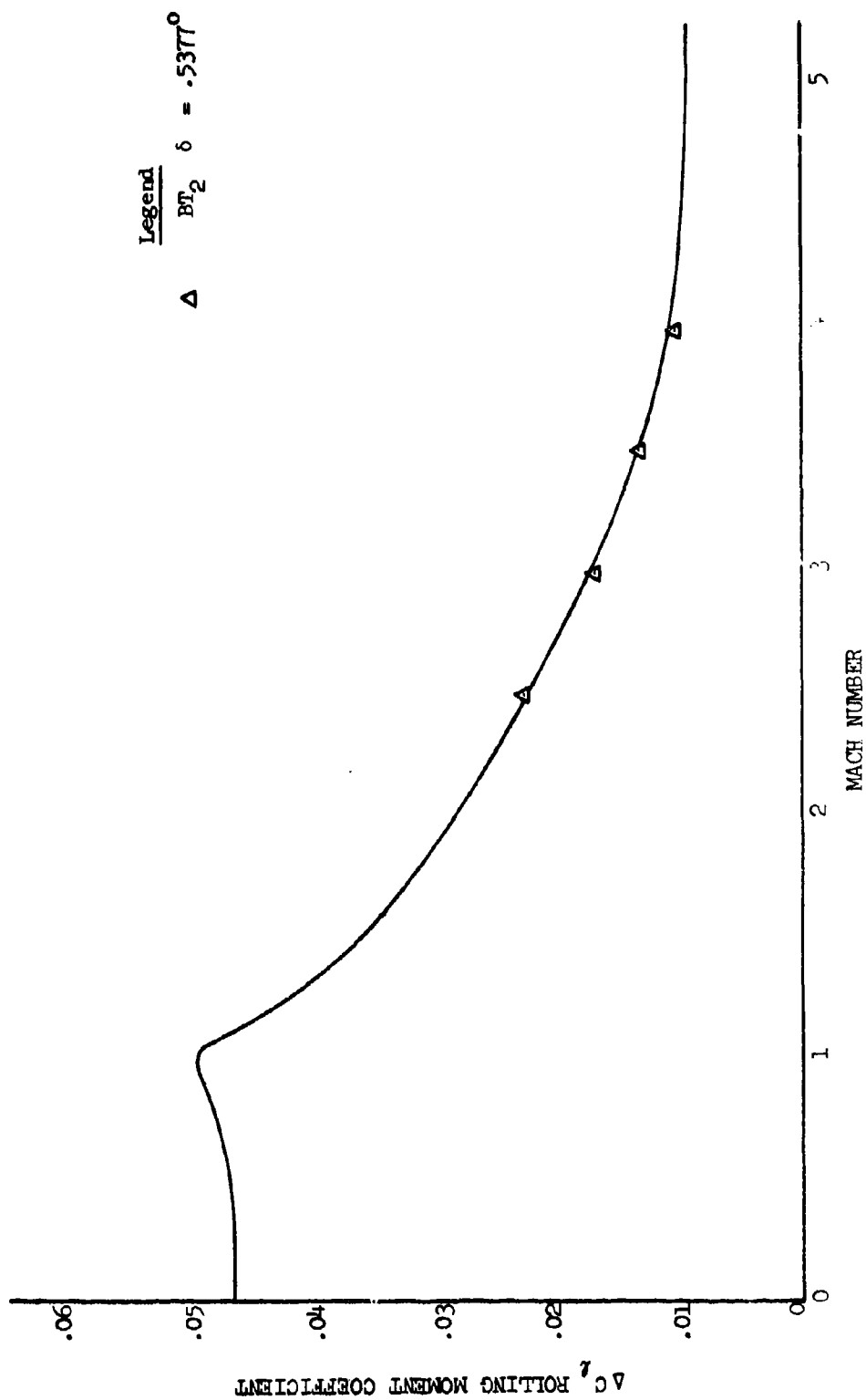
UNCLASSIFIED



UNCLASSIFIED

Report AFRPL-TR-69-90, Appendix A

Figure 5.2-24  
2.75 FFAR Vehicle  
Rolling Moment Coefficient due to Folded Tail  
Fin Tips as a Function of Mach Number,  $\alpha = 0^\circ$   
AEDC VA 0706



UNCLASSIFIED

**UNCLASSIFIED**

Report AFRPL-TR-69-90, Appendix A

Improved 2.75" FFAR  
STABILITY AND CONTROL REPORT  
Volume II

March 8, 1968

*P. A. Sollow*

P. A. Sollow

Approved:

**ORIGINAL SIGNED BY**

A.W. Ernest, Manager  
Aerothermodynamics Dept.

SPACE DIVISION  
Aerojet-General Corporation

**UNCLASSIFIED**

# UNCLASSIFIED

Report AFRPL-TR-69-90, Appendix A

## TABLE OF CONTENTS

<u>Section</u>	<u>Page No.</u>
1.0 INTRODUCTION . . . . .	1
2.0 SUMMARY . . . . .	2
3.0 SYMBOLS AND NOMENCLATURE . . . . .	3
4.0 CONCLUSIONS . . . . .	5
5.0 ANALYSIS AND DISCUSSION OF RESULTS . . . . .	6
5.1 INPUT DATA . . . . .	8
5.1.1 Nominal Vehicle Characteristics . . . . .	8
5.1.2 Perturbation Input Parameters . . . . .	12
5.2 PRELIMINARY DISPERSION ANALYSIS AND CONFIGURATION SELECTION . . . . .	20
5.2.1 Outline of the Preliminary Dispersion Study . . . . .	22
5.2.2 Method of Analysis . . . . .	24
5.2.3 Results . . . . .	27
5.2.4 Interpretation of Results . . . . .	38
5.3 FINAL CONFIGURATION . . . . .	41
5.3.1 Method of Analysis . . . . .	41
5.3.2 Input Parameters . . . . .	42
5.3.3 Trajectory Computations and Results . . . . .	43
5.4 AIRCRAFT SAFETY . . . . .	49
5.4.1 Input Parameters . . . . .	50
5.4.2 Results . . . . .	51
6.0 REFERENCES . . . . .	53

UNCLASSIFIED

# UNCLASSIFIED

Report AFRPL-TR-69-90, Appendix A

## TABLE OF CONTENTS - Cont'd.

<u>Section</u>	<u>Page No.</u>
7.0 APPENDICES . . . . .	54
7.1 THE EFFECT OF ROLL PROGRAM DISPERSION ON THE BURST POINT DISPERSIONS . . . . .	55
7.1.1 Derivation of Equations . . . . .	55
7.1.2 Determination of $V_x(\gamma, \zeta)$ . . . . .	58
7.1.3 Evaluation of Dispersions . . . . .	66
7.2 EQUATIONS OF MOTION FOR AIRCRAFT SAFETY ANALYSIS . . . . .	70

### APPENDIX TABLES

#### Table No.

7.1-1 Dispersion Due to $1^\circ$ Thrust Misalignment . . . . .	60
7.1-2 Results of Curve Fits . . . . .	61
7.1-3 Dispersion Due to $1^\circ$ Fin Misalignment . . . . .	61
7.1-4 Results of Curve Fits . . . . .	62
7.1-5 Results of Equivalence Coefficient Fits, $a_1$ . . . . .	64
7.1-6 Results of Equivalence Coefficient Fits, $a_2$ . . . . .	64
7.1-7 Resultant $1\sigma$ Dispersions Due To Thrust and Fin Misalignments . . . . .	68

### TABLES

#### Table No.

1 Case List of Six Degree of Freedom Trajectories . . . . .	75 - 80
---	---------

UNCLASSIFIED

# UNCLASSIFIED

Report AFRPL-TR-69-90, Appendix A

## ILLUSTRATIONS

<u>Figure No.</u>		<u>Page No.</u>
1	Inertial Characteristics, Preliminary Configurations . . . . .	81
2	Inertial Characteristics, Final Configuration . . . . .	82
3	Vacuum Thrust, Preliminary Configurations . . . . .	83
4	Sea Level Thrust, Final Configuration . . . . .	84
5	Turbulent Wind Power Spectrum . . . . .	85
6	Dispersion Response to Cyclical Winds . . . . .	86
7	Dispersion due to 1 $\sigma$ Thrust Misalignment as a Function of Differential Nozzle Cant . . . . .	87
8	Roll Rate per Degree of Differential Nozzle Cant vs Time 440 Knot Launch Velocity . . . . .	88
9	Dispersion due to 1 $\sigma$ Thrust Misalignment as a Function of Differential Fin Cant and Initial Spin Rate, Configuration I . . . . .	89
10	Dispersion due to 1 $\sigma$ Thrust Misalignment as a Function of Differential Fin Cant and Initial Spin Rate, Configuration II . . . . .	90
11	Variation of Dispersion due to 1 $\sigma$ Fin Misalignment with Differential Nozzle Cant . . . . .	91
12	Dispersion due to 1 $\sigma$ Fin Misalignment as a Function of Differential Fin Cant and Initial Spin Rate, Configuration I . . . . .	92
13	Dispersion due to 1 $\sigma$ Fin Misalignment as a Function of Differential Fin Cant and Initial Spin Rate, Configuration II . . . . .	93
14	Rigid Body Aerodynamic Natural Frequency vs Time 440 Knot Launch Velocity . . . . .	94
15	Roll Rate per Degree of Differential Fin Cant vs Time 440 Knot Launch Velocity . . . . .	95
16	Amplitude of 3 $\sigma$ Roll Rate Variability 440 Knot Launch Velocity . . . . .	96
17	Difference Between Rigid Body Aerodynamic Natural Frequency and Positive 3 $\sigma$ Spin Due to Fin and Nozzle Misalignments 440 Knot Launch Velocity . . . . .	97
18	Comparison of Roll Histories Due to Preliminary and Final Rigid Body Aerodynamic Rolling Moment Coefficients, Configuration II . . . . .	98

UNCLASSIFIED

# UNCLASSIFIED

Report AFRPL-TR-69-90, Appendix A

## ILLUSTRATIONS - Cont'd.

<u>Figure No.</u>		<u>Page No.</u>
19	Dispersion due to 1 $\sigma$ Roll-Dependent Perturbations as a Function of Differential Nozzle Cant . . . . .	99
20	Dispersions due to 1 $\sigma$ Roll-Dependent Perturbations as a Function of Initial Spin Rate and Differential Fin Cant .	100
21	Total 1 $\sigma$ Dispersion as a Function of Differential Nozzle Cant . . . . .	101
22	Total 1 $\sigma$ Dispersion as a Function of Initial Spin Rate and Differential Fin Cant . . . . .	102
23	Dispersion due to 1 $\sigma$ Fin and Thrust Misalignments as a Function of Differential Fin Cant, Configuration I . . . . .	103
24	Dispersion due to Combined 1 $\sigma$ Roll-Dependent Perturbations as a Function of Differential Fin Cant, Configuration I . .	104
25	Final Configuration, Aerodynamic Natural Frequency and Roll Rate vs Time for 200 Knot Launch . . . . .	105
26	Final Configuration, Aerodynamic Natural Frequency and Roll Rate vs Time for 440 Knot Launch . . . . .	106
27	Final Configuration, Aerodynamic Natural Frequency and Roll Rate vs Time for 600 Knot Launch . . . . .	107
28	Variation of Dispersion due to 1 $\sigma$ Thrust Misalignment with Differential Fin Cant, Final Configuration . . . . .	108
29	Variation of Dispersion due to 1 $\sigma$ Thrust Misalignment with Differential Nozzle Cant, Final Configuration . . . . .	109
30	Variation of Dispersion due to 1 $\sigma$ Fin Misalignment with Differential Fin Cant, Final Configuration . . . . .	110
31	Variation of Dispersion due to 1 $\sigma$ Fin Misalignment with Differential Nozzle Cant, Final Configuration . . . . .	111
32	2.75 FFAR Lateral and Vertical Position Relative to Airplane, Launch Airplane Speed = 200 Kt. . . . .	112
33	2.75 FFAR Lateral and Vertical Position Relative to Airplane, Launch Airplane Speed = 440 Kt. . . . .	113
34	2.75 FFAR Lateral and Vertical Position Relative to Airplane, Launch Airplane Speed = 600 Kt. . . . .	114
35	2.75 FFAR Angular Position Relative to Launch Position Launch Airplane Speed = 200 Kt. . . . .	115
36	2.75 FFAR Angular Position Relative to Launch Position Launch Airplane Speed = 440 Kt. . . . .	116
37	2.75 FFAR Angular Position Relative to Launch Position Launch Airplane Speed = 600 Kt. . . . .	117

Page v

UNCLASSIFIED

# UNCLASSIFIED

Report AFRPL-TR-69-90, Appendix A

## 1.0 INTRODUCTION

The Stability and Control Report for the Improved 2.75 in. FFAR is written in two volumes. The basic purpose of these volumes is to document and substantiate stability and general aerodynamic characteristics of the vehicle together with the flight dynamic behavior. Of specific interest are the burst point dispersion characteristics and an evaluation of aircraft safety from the standpoint of the possibility of the rocket flight path intersecting the launching aircraft; establishment of acceptable behavior in these areas is tantamount to establishing satisfactory stability characteristics of the rocket.

In the present volume, Volume II, the dispersion and aircraft safety studies are described. These studies used as input the basic aerodynamic characteristics of the vehicle and the aeroelastic corrections to these parameters which are reported in Volume I.

Reported herein are not only the results pertinent to the final flight configuration selected (essentially unchanged in exterior geometry from the extant 2.75 in. FFAR configuration), but also the dispersions which were derived for a number of variant configurations prior to the selection of the final design configuration.

UNCLASSIFIED

# UNCLASSIFIED

Report AFRPL-TR-69-90, Appendix A

## 2.0 SUMMARY

The dispersion characteristics of a number of preliminary rocket configurations are presented. These configurations are defined as having exposed fin spans of 40%, 70%, and 100% of the span of the present 2.75 FFAR configuration. The aerodynamics of the 40% and 70% spans were calculated by approximate methods, but the dispersion results are valid for some set of configurations which approximate the assumed aerodynamic characteristics. These preliminary dispersions are calculated for a 440 knot launch velocity and include the assumption of rigid body aerodynamics and a preliminary thrust curve.

On the basis of the results of the preliminary dispersion computations, it was determined that the geometry of the present vehicle would adequately meet the dispersion requirements while necessitating the minimum change in existing tooling and no change in existing launchers. The only external alterations in the configuration which are necessary from the dispersion standpoint are the addition of a  $0.11^\circ$  differential fin cant, to induce roll, and a tightening of the fin alignment tolerances.

The dispersion characteristics of the final configuration were determined using the latest wind tunnel-derived aerodynamic data reported in Volume II corrected for aeroelastic effects as noted in that volume. Additionally a finalized thrust curve was employed in the determination. The dispersion was determined for launch velocities of 200, 440, and 600 knots.

The possibility of a rocket making contact with the launch aircraft, due to the effects of the flow field of the aircraft, was investigated at the three launch velocities cited above with nominal axial performance and at 440 knots with a  $3\sigma$  low thrust curve.

The  $3\sigma$  variation of the roll history was determined and the final configuration was checked to determine whether this magnitude of roll rate variability could lead to pitch-roll resonance. The effect on dispersions of these roll rate variations was evaluated.

UNCLASSIFIED



# UNCLASSIFIED

Report AFRPL-TR-69-90, Appendix A

## 3.0 SYMBOLS AND NOMENCLATURE

Note: Symbols which are defined in the text of the Appendices (Section 7.0) are not presented here.

$C_{l\delta}$	Aerodynamic roll driving coefficient slope (1/radians)
$C_{mI}$	Induced aerodynamic pitching moment coefficient (---)
$C_{NI}$	Induced aerodynamic normal force coefficient (---)
$C_{N\delta}$	Tail normal force coefficient slope (1/radians)
$C_{nI}$	Induced aerodynamic yawing moment coefficient (---)
$C_{YI}$	Induced aerodynamic side force coefficient (---)
c.g.	Center of gravity station (feet)
c.p.	Center of pressure station (feet)
d	Aerodynamic reference length (feet)
Q	Dynamic pressure (lb/ft <sup>2</sup> )
R	Radial distance from vehicle spin axis to nozzle throat centerline (feet)
S	Aerodynamic reference area (ft <sup>2</sup> )
T	Thrust (pounds)
$\alpha$	Angle of attack (radians)
$\delta$	Tail incidence angle (radians)
$\delta'$	Mean differential fin cant (radians)
$\Theta_i$	Standard deviation of single nozzle axis alignment relative to nozzle plate (radians)
$\theta$	Angular deflection of a nozzle about R, causing a rolling torque (radians)

UNCLASSIFIED

# UNCLASSIFIED

Report AFRPL-TR-69-90, Appendix A

- $\theta_n$  Standard deviation, in one plane, of single nozzle axis alignment relative to nozzle plate (radians)
- $\sigma$  Standard deviation (units are those of parameter described)
- $\sigma_F$  Standard deviation of single panel fin incidence angle (radians)
- ( $\dot{\phantom{x}}$ ) A dot above a variable indicates the time derivative of that variable.

UNCLASSIFIED

# UNCLASSIFIED

Report AFRPL-TR-69-90, Appendix A

## 4.0 CONCLUSIONS

Investigation of three candidate configurations which differed in fin area showed that the optimum configuration for the Improved 2.75 FFAR (from the standpoint of simultaneously achieving a  $1\sigma$  dispersion less than 9.5 mils, minimal probability of pitch-roll resonance, minimum change in existing tooling, and no alteration of existing launchers) is identical to the present 2.75 FFAR in external configuration, except for the addition of a  $0.11^\circ$  differential fin cant.

The dispersion of the selected configuration, at the  $1\sigma$  probability level, varies between 1.35 mils for a 600 knot launch aircraft velocity and 6.85 mils for a 200 knot launch aircraft velocity. The effect of changes in launch elevation angle are negligible.

It was found that the maximum excursions, due to the launch aircraft flow field, of an Improved 2.75 FFAR from the flight line defined by the launcher axis is on the order of 1 foot prior to the rocket clearing the nose of the launch aircraft. It was determined that the perturbations which cause a  $1\sigma$  dispersion would cause deflections of the flight path, before the rockets clear the nose of the launch aircraft, of less than 2 feet. It may be concluded that, to a high probability level, no contact between the rockets and the aircraft will occur.

It was found that pitch-roll resonance would not occur, at any launch velocity, at least to the  $3\sigma$  probability level.

UNCLASSIFIED

# UNCLASSIFIED

Report AFRPL-TR-69-90, Appendix A

## 5.0 ANALYSIS AND DISCUSSION OF RESULTS

Reference 1 sets forth design specifications for the Improved 2.75 in. FFAR. Several of these constitute direct performance requirements in the area of flight dynamics, more specifically in the dispersion and aircraft safety areas. The principal requirements are as follows:

- a. The angular dispersion at the warhead dispersal or burst point, i.e., the angle whose tangent is the normal dispersion divided by the flight path length) shall be 9.5 milliradians or less. This limit is understood to mean the limiting value of the standard deviation of the dispersal point.
- b. Pitch-roll resonance shall not occur during the flight of the rocket. This is interpreted to mean that there will be at least a 3 $\sigma$  probability that it will not occur. That is, the probability of occurrence will be less than .0028, assuming a normal distribution of all perturbations. The necessity that the avoidance of pitch-roll resonance be considered on a probabilistic rather than an absolute basis is due to the unavoidable variation of the spin history from its nominal value due to manufacturing tolerances. Thus, even if the nominal spin history is chosen so that it will remain well separated from the natural frequency throughout the flight, some small percentage of a large number of rounds might theoretically be expected to have spin rates far enough removed from the nominal value to allow resonance.
- c. The rocket shall not produce a hazard to the aircraft in terms of danger of colliding with the aircraft. The evaluation of this hazard is to be made using the GFE aircraft-induced flow field data for a typical aircraft.

The analyses and results presented in this section are directed at assuring that the above specifications are met. Section 5.2 presents a preliminary dispersion analysis wherein various configurations and means of achieving spin, etc., were considered. Included in the dispersion analysis is the determination of roll rate variability in response to specification b, above. The purpose of this portion of the study is to permit selection of a configuration best meeting the performance specifications, a and b, above, and

UNCLASSIFIED

## UNCLASSIFIED

Report AFRPL-TR-69-90, Appendix A

to determine whether expected manufacturing tolerances would produce acceptable results and, if not, where they need to be tightened. It should be mentioned here that, in addition to the performance requirements already stated, ancillary requirements from Reference 1 that maximum use of extant tooling be made and that no alterations to the launcher be made must be considered in the configuration selection.

Section 5.3 presents the results of a final dispersion analysis using the configuration selected as a result of the studies reported in Section 5.2.

Section 5.4 presents the evaluation of the aircraft safety problem (requirement c, above), again using the configuration selected in Section 5.2.

Section 5.1 presents a discussion of the input data used in both Sections 5.2 and 5.3 since much of the data are common to both sections. Included in Section 5.1 is a discussion of the perturbations employed in the dispersion studies.

UNCLASSIFIED

# UNCLASSIFIED

Report AFRPL-TR-69-90, Appendix A

## 5.1 INPUT DATA

In order to compute the 6-D trajectories, the characteristics of the vehicle must be completely defined insofar as they affect the motion of the vehicle. These pertinent characteristics include the aerodynamic coefficients, the inertial characteristics (weight, center of gravity location, moments of inertia), the thrust history, geometric asymmetries, and the initial conditions of the flight (the linear and angular rates, and the orientation and position relative to a reference point fixed to the ground). In addition, any external perturbations, such as wind, must be represented.

The data presented in this section are used in the analyses discussed in Sections 5.2 and 5.3 and, where applicable, in Section 5.4. Section 5.1.1 presents the characteristics of the nominal vehicles investigated and Section 5.1.2 presents the data and discussions pertinent to parameters causing dispersion of the vehicle and/or variations in the roll rate histories.

### 5.1.1 NOMINAL VEHICLE CHARACTERISTICS

#### 5.1.1.1 AERODYNAMIC CHARACTERISTICS

For the preliminary dispersion studies, the aerodynamic characteristics for Configuration I (see Section 5.2) were taken from 5.1.1 of Volume I of this report. For Configurations II and III, which differ from Configuration I by having shorter fins, the aerodynamic characteristics were obtained from those for Configuration I by correcting for fin span on the basis of strip theory. Such corrections are not especially accurate, but a configuration with slightly different fin span would produce equivalent characteristics for practical purposes, so the objective of studying fin variations is satisfied and the equivalent tail can be found after the desired characteristics are selected. Rigid vehicle characteristics are employed with aeroelastic corrections being reserved for the final dispersion analyses.

UNCLASSIFIED

# UNCLASSIFIED

Report AFRPL-TR-69-90, Appendix A

For the final dispersion analyses (Section 5.3) the revised aerodynamic characteristics obtained from wind tunnel tests conducted as part of this program were employed. These are presented in Volume I. Also given in Volume I are ratios of elastic to rigid values of those aerodynamic parameters affected by aeroelasticity. These aeroelastic corrections, based on the dynamic pressure time history of the nominal trajectory, were incorporated into the aerodynamic representations of the final configurations.

## 5.1.1.2 INERTIAL CHARACTERISTICS

The inertial characteristics employed in the preliminary dispersion analyses are shown in Figure 1. Since the mass removed in shortening the fins for configuration variations is small, these characteristics were used for all three configurations.

Figure 2 presents the revised and updated data employed for the final configuration analyses.

## 5.1.1.3 THRUST CURVES

The preliminary and final configuration thrust curves employed are presented, respectively in Figures 3 and 4.

## 5.1.1.4 INITIAL CONDITIONS

Reference (1) requires the assessment of the dispersion for all combinations of three initial flight path angles ( $15^{\circ}$ ,  $30^{\circ}$  and  $45^{\circ}$  below the horizontal) and three launch aircraft velocities (200, 440, and 600 knots). Preliminary investigations and experience with other vehicles, however, indicated the effect of flight path angles on dispersions to be negligible within the range specified. Therefore, all subsequent preliminary studies were confined to the  $30^{\circ}$  depression and the dispersion results will apply to all depression angles. The depression angle used for the final dispersion studies was altered to  $20^{\circ}$  to avoid impacting the ground without altering

UNCLASSIFIED

## UNCLASSIFIED

Report AFRPL-TR-69-90, Appendix A

too many input initial conditions. The preliminary dispersion studies were also confined primarily to the 440 kn launch velocity with some check runs at 200 kn.

The 6-D trajectories are started at the time the trailing ends of the folded fins leave the launch tube. Thus, the initial velocity of the rocket is somewhat greater than the launch airplane speed. The acceleration of the rocket inside the launcher was integrated numerically to provide both an initial velocity and an initial time for the beginning of the 6-D trajectories. The aerodynamic drag on the vehicle as it is emerging from the launcher tube is not accurately known. However, for the purposes of calculating the initial conditions, it was assumed that the drag would be equal to the free flight drag at the same Mach Number. An average value of this drag was assumed to act on the vehicle between ignition and full emergence from the tube. For the  $-30^{\circ}$  flight path angle and the 440 knot aircraft velocity, a rocket velocity of 862 feet/second was calculated at tube emergence, which occurred 0.081 seconds after ignition. It was assumed that ignition occurred at an altitude of 3000 feet and an initial altitude of 2770 feet (at 0.081 seconds after ignition) was input to the 6-D program.

In consequence of the change in the thrust curve from the preliminary form, it was necessary to recompute the flight conditions at launcher exit for the final configuration. When it became apparent that the new thrust curve was going to produce a longer flight path between ignition and payload deployment than did the preliminary thrust curve, the flight path angle at launch was changed from  $-30^{\circ}$  to  $-20^{\circ}$ , to insure that payload deployment occurred before ground impact. This allowed the ignition altitude to be kept at its previous value of 3000 feet, so that the speed of sound at launcher exit remained unchanged. By the time the necessity for changing either the launch altitude or the flight path angle became known, considerable work had been done on tailoring the aerodynamic coefficients to the fin opening characteristics. Since the coefficients are functions of Mach Number in the 6-D program, considerable additional effort would have been necessary if the speed of sound during the fin opening sequence had been changed.

Page 10

UNCLASSIFIED



## UNCLASSIFIED

Report AFRPL-TR-69-90, Appendix A

A new launcher exit time was computed for the final configuration, using the same method as in the case of the preliminary trajectories. The launcher exit time was calculated to be 0.102 seconds after ignition. Three launcher exit velocities were calculated to correspond to the three launch aircraft velocities. These are:

Airplane Velocity (knots)	Rocket Speed at Launcher Exit (feet/second)
200	428
440	840
600	1102

### 5.1.1.5 FIN OPENING TRANSIENTS

Since the aerodynamic characteristics vary considerably with fin position, it is necessary to simulate the fin opening transient, at least roughly, in the flight dynamic computations.

Two different fin opening times were used in computing the preliminary trajectories. In Cases 1001 through 1141 (all of the 440 knot launch trajectories), an opening time (from launcher exit to fully open fins) of 0.029 seconds was used. This was based on an assumed mean opening distance of 3 feet for the rocket configurations reported in Reference 8, and the use of the 88 ft/second muzzle velocity reported there to evaluate the acceleration in the neighborhood of launcher exit. When a new opening time had been evaluated based on the actual forces on the fins, and including the use of the thrust curve in Figure 3, it was input to the program. This new time was calculated to be 0.043 seconds.

For the final configuration, the chamber pressure at launcher exit is lower than it was for the preliminary thrust curve and, since the fins are opened by means of a piston driven by the chamber pressure, the time for the fins to open is increased. Volume I shows the fin opening time for the final configuration to be 0.054 seconds.

UNCLASSIFIED

# UNCLASSIFIED

Report AFRPL-TR-69-90, Appendix A

## 5.1.1.6 WARHEAD DISPERSAL POINTS

For the preliminary configuration the payload deployment and burnout were taken to be simultaneous at 2.15 seconds. The payload deployment of the final configuration occurs during tailoff at 2.57 seconds while the motor continues burning until 2.75 seconds, with some tailoff thrust after this time.

## 5.1.2 PERTURBATION INPUT PARAMETERS

In this section, the parameters tending to affect the flight path of the rocket are presented. In accordance with our definition of dispersion (see the first paragraph of Section 5.2), we exclude those perturbations which affect each rocket in a volley in the same way and therefore do not affect the scatter pattern of the burst points. Also included in this section are the parameters causing variability in the roll rate histories.

Note that in general, manufacturing alignment tolerances are treated as  $2\sigma$  values, or more precisely, the standard deviations were taken to be one-half the prescribed manufacturing tolerances. The actual relationship of standard deviations to manufacturing tolerances is not known due to lack of data and of knowledge of the probability density functions and, in any case, probably varies considerably depending on the item being manufactured.

### 5.1.2.1 THRUST MISALIGNMENTS CAUSING PITCHING MOMENTS

The pitching moments due to thrust misalignment may be resolved into two components. Those due to angular nozzle misalignment and those due to lateral offset of the resultant thrust vector from the vehicle centerline (spin axis). These two misalignments are assumed statistically independent and are treated separately.

There are four statistically independent sources of angular thrust misalignment. These sources, together with the design tolerances (assumed  $2\sigma$  probability level) are:

UNCLASSIFIED

# UNCLASSIFIED

Report AFRPL-TR-69-90, Appendix A

	<u>Tolerance (deg)</u>
1) Alignment of nozzle plate to motor centerline	+ .132
2) Normality of nozzle holes in nozzle plate	+ .407
3) Nozzle shell outside diameter parallelism with nozzle hole in nozzle plate	+ .567
4) Nozzle shell outside diameter parallelism with expansion section	+ .175

The last three of the above misalignments are statistically independent between nozzles. For any one nozzle, the RSS value of the misalignment angle due to these three misalignments is  $0.720^{\circ}$ . Combining the contribution of 4 independently misaligned nozzles yield an effective misalignment of the total (4 nozzles) thrust vector of  $0.360^{\circ}$  due to the three misalignments thus far considered. This angle may be combined with the first item, the misalignment of the nozzle plate, as a root-sum-square, since the two are statistically independent. The resultant misalignment angle is  $0.383^{\circ}$ . Since the design tolerances are considered to represent the  $2\sigma$  probability level, the 1 $\sigma$  angular thrust misalignment is  $0.192^{\circ}$ .

There are four statistically independent sources of lateral thrust vector offset. These sources and the associated design tolerances (limits of lateral offset from nominal position) are:

	<u>Tolerance (in.)</u>
1) Concentricity of nozzle plate with motor centerline	.0065
2) Location of nozzle holes in nozzle plate	.0025
3) Nozzle shell outside diameter concentricity with nozzle hole	.0050
4) Nozzle shell outside diameter concentricity with expansion section	.0025

The last three items are statistically independent between nozzles so that the resultant lateral offset of any one nozzle is the RSS of these three offsets, or .0061 inches. The effective lateral offset of the total

UNCLASSIFIED

# UNCLASSIFIED

Report AFRPL-TR-69-90, Appendix A

thrust vector due to these three offsets is then .00305 inches. The total lateral thrust offset tolerance is the RSS of this offset and the concentricity tolerance between the nozzle plate and the motor centerline. This gives a total tolerance of the lateral thrust offset of .0072 inches or, at the  $1\sigma$  probability level, .0036 inches. The pitching/yawing moment, at launcher exit, due to this misalignment is equal to the moment due to a  $0.00875^\circ$  angular thrust misalignment.

## 5.1.2.2 THRUST MISALIGNMENT CAUSING ROLLING MOMENTS

If one of the four nozzles, each of which is nominally at a distance  $R$  from the vehicle spin axis, and parallel with this axis, is rotated about  $R$  through a small angle  $\theta$ , (i.e., a tangential deflection) it will cause a torque about the spin axis of  $\frac{RT}{4} \theta$ , where  $T$  is the total vehicle thrust. Considering  $\theta_n$  to be the standard deviation of the alignment of the nozzle at  $\theta$ , the variance of the torque due to the nozzle is  $R^2 T^2 \theta_n^2 / 16$ , and the variance of four of these nozzles would be  $R^2 T^2 \theta_n^2 / 4$ . Thus, the standard deviation of the torque would be  $R T \theta_n / 2$ , which is the torque due to setting each of the four nozzles at  $\theta_n / 2$ . If the standard deviation of the total misalignment angle of the nozzle axis is  $\theta_i$ , and the distribution is circular normal (equal misalignment distributions in the radial and tangential directions), then  $\theta_n$  will be equal to  $\theta_i / \sqrt{2}$ .

Since the nozzle plate alignment does not affect the roll torque the appropriate value of  $\theta_i$  is  $0.36^\circ$  (see Section 5.1.2.1). Thus, the effective  $1\sigma$  differential nozzle cant is  $0.127^\circ$ .

## 5.1.2.3 FIN MISALIGNMENT CAUSING PITCHING MOMENTS

There are three sources of fin misalignment which combine to cause an aerodynamic pitching or yawing moment at zero angle of attack. One source, misalignment of the nozzle plate, to which the fins are attached, will cause a rotation of all four of the vehicle fins. Within the limits of accuracy of linear aerodynamics, the aerodynamic moment due to unit deflection of the tail

UNCLASSIFIED

# UNCLASSIFIED

Report AFRPL-TR-69-90, Appendix A

assembly is isotropic with the roll orientation of the axis of the rotation. The other two sources of misalignment may be expected to be mutually statistically independent and independent of the nozzle plate misalignment, as well as randomly distributed between the fins. These two misalignment sources are errors in aligning the fins to the nozzle plate, and twist, waviness, or other surface irregularities of the fins themselves. The alignment of the fins to the nozzle plate has been specified to have a design tolerance of  $\pm .125^\circ$ . Interpreting this design tolerance as the  $2\sigma$  value, the standard deviation of the alignment of any one fin is  $\pm .063^\circ$ . It is estimated that fin irregularities will have the effect of about doubling the effective misalignment. Thus, the  $1\sigma$  misalignment of a single fin relative to the nozzle plate is estimated to be  $\pm .125^\circ$ . Each fin has a normal force coefficient of  $C_{N\delta} \delta/2$ , where  $C_{N\delta}$  is the fin normal force coefficient slope for two panels, and  $\delta$  is the incidence angle of the panel. Letting the mean value of  $\delta$  be zero and the standard deviation of  $\delta$  be the standard deviation of the fin alignment,  $\sigma_F$ , the standard deviation of the normal force coefficient of two panels is  $C_{N\delta} \sigma_F/\sqrt{2}$ . There are two orthogonal sets of two panels, each with the same standard deviation of the normal force coefficient. Thus, the standard deviation of the normal force coefficient for all four fins is  $C_{N\delta} \sigma_F$ , and the effective  $1\sigma$  fin misalignment, due to fin to nozzle plate alignment tolerances and fin irregularities, is equal to the single fin standard deviation, or for the present case,  $0.125^\circ$ . The total  $1\sigma$  fin misalignment is the RSS of this angle with the nozzle plate to motor  $1\sigma$  misalignment which is shown in Section 5.1.2.1 to be  $0.066^\circ$ . The total  $1\sigma$  fin misalignment is therefore  $0.141^\circ$ .

## 5.1.2.4 FIN MISALIGNMENTS CAUSING ROLLING MOMENTS

The roll driving torque due to the fins is  $C_{l\delta} \delta' q S d$ , where  $\delta'$  is the mean differential fin cant. The standard deviation of the torque due to one fin is  $C_{l\delta} \sigma_F q S d/4$ , where  $\sigma_F$  is the standard deviation of the angle of cant (i.e., the standard deviation of the rotation of the fin about an axis in the plane of the fin and normal to the spin axis). For four fins, the standard

UNCLASSIFIED

## UNCLASSIFIED

Report AFRPL-TR-69-90, Appendix A

deviation of the roll torque is the square root of four times the variance of the torque due to one fin, or  $CA_8 \sigma_F QSd/2$ . Thus, the standard deviation of the torque is equal to the torque due to setting all four fins at one-half of the standard deviation of the differential cant.

Since the nozzle plate alignment does not affect the roll torque, the appropriate standard deviation for a single fin (see Section 5.1.2.4) is  $0.125^\circ$  and the  $1\sigma$  differential fin cant is  $0.063^\circ$ .

### 5.1.2.5 LAUNCHER TUBE ALIGNMENT

Reference 2 gives the results of alignment measurements made on the tubes of two XM-159 Launcher Pods. For each tube, the misalignments in elevation and azimuth relative to the centerline of the pods were presented. Thus, there are a total of 76 tube angular misalignment components presented. It was assumed that this was a representative sampling. The standard deviation of the sample was found to be 0.475 mils. This represents a rotation about one of the two orthogonal axes (azimuth and elevation) and, assuming a circular normal distribution of misalignment, the total  $1\sigma$  misalignment of a tube was calculated to be 0.673 mils.

### 5.1.2.6 TIPOFF

The tipoff rate is defined as the angular rate of the vehicle, about an axis normal to the spin axis, at the time the vehicle leaves the constraint of the launcher and becomes a free body. The angle which the spin axis of the rocket makes with the axis of the launcher tube at this same time is termed the tipoff angle. Some part of both the tipoff rate and the tipoff angle must be considered nominal since all rockets will exhibit the same magnitude of each of these parameters for launch at a given launch aircraft speed and flight path declination. These nominal rates and angles may be compensated during the calibration of the aiming system. Another part of both the tipoff rate and angle will result in an equal perturbation of all the flight paths of a salvo or ripple fire string and, although they change all of the flight paths from

UNCLASSIFIED

# UNCLASSIFIED

Report AFRPL-TR-69-90, Appendix A

their nominal value, do not contribute to the dispersion. Finally, there will be some portions of the tipoff rate and angle which vary randomly from vehicle to vehicle. These perturbations will cause dispersion.

It is difficult to assess the magnitude of the portions of the tipoff rate and angle which contribute to the dispersion. This is due to the fact that the rocket is constrained, with small clearances, to remain within the geometric confines of the launcher tube. The vehicle may be expected to bounce around the inside of the tube with various points on the rocket being the point of impact at different times. These collisions may be expected to be neither wholly elastic nor wholly inelastic. Additionally, the folded cruciform fins fit inside the tube like the proverbial square peg in a round hole so that the clearance between the rocket and the tube is not roll symmetrical. Additionally, a change in the mean tipoff rate and angle affecting all the rockets will cause a variation in the independent portion of the tipoff of each round by changing the rocket/launcher tube impact history. It is apparent that the best which may be done is the evaluation of a tipoff which appears to be a conservative limit value.

A reasonable approach to the evaluation of a conservative value of the  $1\sigma$  tipoff rate is to assume that, from the time the front bourolette leaves the launcher tube, the vehicle is rotated, about its center of gravity, by the moment due to a  $1\sigma$  thrust misalignment. This approach is conservative since it is probable that some point on the vehicle, such as the fin tips or the aft bourolette will contact the tube so that rotation would be constrained to be about some point far removed from the center of gravity. The ratio of the disturbing moment (due to the thrust misalignment) to the moment of inertia about this point would be considerably lower than for motions about the center of gravity. Thus, the angular acceleration and the tipoff rate and angle would be lower than those computed.

The distance between the bourolettes is approximately 33 inches and the clearance between the bourolettes and the launcher tube wall (based on the measured tube diameter in Reference 3) is .035 inches diametral difference.

Page 17

UNCLASSIFIED

# UNCLASSIFIED

Report AFRPL-TR-69-90, Appendix A

The limiting angular displacement while both bouriolettes are in the tube is thus  $0.061^\circ$ . For the thrust curve employed with the preliminary configuration, the moment due to angular thrust misalignment is 31.2 ft-lb/degree. Section 5.1.2.1 shows the  $1\sigma$  angular thrust misalignment to be  $0.192^\circ$ . The front bouriolette clears the launcher tube at 0.043 seconds and between this time and the time the tips of the fins leave the tube (.081 seconds), the  $1\sigma$  thrust misalignment moment could accelerate the rocket to an angular rate of  $13.7^\circ/\text{sec}$  and an angular displacement of  $0.26^\circ$ . This displacement angle may be added to the  $0.061^\circ$  deflection which the vehicle may attain prior to 0.043 seconds to give a  $1\sigma$  magnitude of the dispersion component of the tipoff angle of  $0.32^\circ$ .

## 5.1.2.7 TURBULENT WINDS

The wind perturbations of interest here are only those portions of the winds which tend to affect different rounds in the same volley in a different manner. It is customary in such cases to separate the total wind power spectrum into so-called steady and turbulent wind spectra. The steady wind spectrum is composed primarily of rather long wavelength winds and is relatively invariant with respect to temporal and horizontal spatial displacements of sizeable magnitudes, i.e., if a wind profile were measured at two different times not differing by greater than a specified increment, the Fourier transforms of these profiles obtained for these discrete times would be expected to be nearly the same for the longer wavelengths. The remainder of the spectrum, called the turbulent wind spectrum, then represents that portion of the winds (shorter wavelengths) expected to appear random in the temporally or spatially separated measurements. It should be apparent that the portion of the total spectrum assignable to the turbulent category is dependant on the separation of the measurements and tends to decrease as the separation interval is decreased and vanishes completely for coincident

UNCLASSIFIED



## UNCLASSIFIED

Report AFRPL-TR-69-90, Appendix A

measurements. Available correlations of this type, such as those of Reference 4 using wind profiles measured above Cape Kennedy, are applicable to intervals of many minutes. On the other hand, the maximum temporal separation of the rockets in a single volley is on the order of tenths of seconds, so the data would appear to be highly unapplicable. The maximum spatial separation of the individual trajectories of the various rockets is on the order of 100 ft indicating that wind components with wavelengths over 400 ft or so would certainly not contribute significantly to dispersion. The turbulent spectrum taken from Reference 4, and shown in Figure 5, however, peaks at around a 600 ft wavelength. This indicates that the spectrum shown contains much longer wavelengths than really should be considered variable here, but, on the other hand, the spectrum is not so inapplicable as purely temporal considerations would indicate; this is primarily due to migration of the launching aircraft during the firing of the volley.

In any case, it is clear that the spectrum in Figure 5 will yield a highly conservative estimate of dispersion due to winds. As will be shown in Section 5.2 and 5.3, this portion of the dispersion is not large, so this situation can be tolerated. Also, it will be permissible to use an approximate method of computing the effects of winds.

UNCLASSIFIED

# UNCLASSIFIED

Report AFRPL-TR-69-90, Appendix A

## 5.2 PRELIMINARY DISPERSION ANALYSIS AND CONFIGURATION SELECTION

The purpose of the dispersion studies presented herein is the determination of the  $1\sigma$  radius of the scatter pattern of the burst points of the rockets fired in a ripple fire volley from a single rocket pod. Whenever the term "dispersion" is used herein it refers to this scatter-pattern dispersion. The dispersions treated do not include any effects which merely change the midpoint of this pattern, i.e., that affect all rockets in a single volley in a similar manner. Therefore such effects as steady winds, aiming errors, etc., are not considered. Lateral displacements only are considered and no perturbations in burning range are included. Also it should be noted that the launching aircraft is assumed to travel at a constant velocity in a perfectly straight line with no angular rates. Effects of aerodynamic or mechanical interference between the various rockets in a volley have been excluded from consideration.

The dispersion characteristics of the Improved 2.75 FFAR were evaluated through the use of a 6-Degree-of-Freedom trajectory simulation program. The program is described in Reference 5. This program was run on an IBM 709<sup>4</sup> digital computer. The program, which was developed by the Aerojet-General Corporation, allows the complete simulation of the trajectory and attitude history of an unguided vehicle relative to a spherical rotating earth. A 1962 U.S. Standard Atmosphere (Reference 6) is employed by this program. The program allows the inflight initiation of trajectories, and, for the present study, all trajectories commenced at the point where the aft end of the vehicle (the tips of the folded fins) leaves the launcher tube.

In order to determine the dispersion due to various perturbations, such as winds, fin misalignment, and thrust misalignment, trajectories were computed with each of these perturbations and in the absence of any perturbations (i.e., nominal trajectories). Comparison of the perturbed trajectories with the nominal cases allowed the determination of the displacement (dispersion) of the point of warhead dispersal due to each of the perturbations. (For the preliminary configurations, dispersal was assumed coincident with thrust termination.)

UNCLASSIFIED

# UNCLASSIFIED

## Report AFRPL-TR-69-90, Appendix A

The specific purpose of the preliminary dispersion studies discussed in this section was to investigate the effects of configuration changes (more specifically modifications in the tail configurations) on dispersion, and to investigate various means of reducing the dispersions to meet or exceed the specifications given in Section 5.0. Primarily, the dispersion reducing methods investigated for fixed configurations were various means of achieving spin and variations in the amount of spin induced, the use of configurations producing spin prior to exit from the launcher tube, and tightening tolerances producing dispersion perturbations. The end result is a specification of vehicle configuration, spin program (and means to produce it), and allowable tolerances to be used in the final configuration analysis and as vehicle manufacturing specifications.

Due to the large number of six-degree-of-freedom trajectories run and the attendant large mass of data to be presented, it is inconvenient to present these data in the order actually occurring in the study, discuss each step, and enumerate the conclusions leading to the next group of runs. Instead, we will present first a brief description of the actual course of the study in order to provide some understanding of why the various individual component investigations were conducted. Then the over-all results are presented in a more integrated form in order to derive the greatest understanding of the results and the phenomena involved. Lastly, the significance of the over-all results are discussed.

Previous dispersion investigations, performed for artillery rockets and sounding rockets, support the assumptions that the normal dispersions of the Improved 2.75 FFAR measured at burnout, are rotationally isotropic and linearly proportional to the magnitudes of the perturbations, and may, for a fixed spin program, be combined by linear superposition. Therefore, in order to determine the  $1\sigma$  dispersion, i.e., the standard deviation of the position of the point of warhead dispersal of a given configurations, the  $1\sigma$  value of each of the dispersion sources is estimated and the dispersions due to each of these are combined as a root-sum-square. The dispersion due to each of the perturbations will differ

UNCLASSIFIED

## UNCLASSIFIED

Report AFRPL-TR-69-90, Appendix A

as the launch velocity and the configuration of the nominal vehicle are altered and the dispersions due to the body fixed perturbations will change with the spin program. For all practical values of spin rate, the gyroscopic moments on the Improved 2.75 FFAR are negligible in comparison to the aerodynamic moments. Thus, the nominal trajectories and the dispersions due to perturbations which are not fixed to the vehicle are independent of spin history. This was borne out by several comparison trajectories.

As will be seen, the dispersions are a function of the spin program employed. Since the spin program itself is subject to statistical variations due to fin and nozzle cant variations, the over-all dispersion must take these statistics into account. This will be done for the final configuration dispersion analysis (Section 5.3). For these preliminary studies, we merely present dispersions for various fixed spin programs.

### 5.2.1 OUTLINE OF THE PRELIMINARY DISPERSION STUDY

Based primarily on experience with previous vehicles (mostly ground launched) and on rather sparse results obtained during the proposal effort, it was initially expected that inducing spin by canting the nozzles was probably more effective in reducing dispersion than the use of fin cant. This is due to the more rapid spin-up obtained with canted nozzles as well as possible spinning in the launch tube though this latter is not certain to occur due to the flow-straightening effect of the folded fins when in the tube.

Therefore the initial effort was concentrated on examining the effects of nozzle cant on vehicles with various amounts of tail span. The spans examined were equal to or smaller than the extant fin spans since it was known that the stability margins with the current tails were considerably larger than required for good stability and dispersion characteristics.

The studies of the canted nozzle configurations were well along when independent studies of manufacturing procedures indicated canting nozzles to be undesirable in comparison to canting the fins. Attention was therefore redirected

UNCLASSIFIED

## UNCLASSIFIED

Report AFRPL-TR-69-90, Appendix A

to examine the dispersions obtained with spin induced by fin cant rather than nozzle cant. It was found that, for these aircraft launches, spin-up with fin cant was sufficiently rapid that canted nozzles offered no particular advantage over this method. Also, due to the sizeable initial dynamic pressures for aircraft launches, investigation of the effects of spinning in the tube (accomplished by skewing the fin tips, see Vol. I) showed that initial spin was not particularly effective and therefore unnecessary.

During the preliminary investigations of dispersions, it was noted that rather small values of fin and/or nozzle cants were required to produce sizeable burnout roll rates. Therefore it became evident that variations in the roll rate histories due to accidental fin and nozzle misalignments presented a problem in terms of both avoiding roll-pitch coupling and keeping a low probability of having low roll rates and the attendant high dispersions. In particular, it was found that the short (40% span) tails, which did provide adequate stability, did not produce sufficient damping in roll to permit maintaining the roll rate below the pitch frequency curve (i.e., avoiding roll-pitch resonance). Some studies were made of the possibility of rolling above the resonant conditions, but not enough spread was available between the pitch frequency curve and roll rate limits on the motor grain (20 or 25 rev/sec). Therefore the 40% fins were eliminated from further consideration.

For the longer (70% and 100% span) fins, damping in roll was found to be adequate to handle nozzle cant tolerances, but it was found that the tolerances on fin alignment had to be tightened to maintain the roll rates within a reasonable range. These were tightened to produce (see Section 5.1.2.4) an effective  $1\sigma$  fin cant variation of  $0.063^\circ$  thus allowing the fins to be set nominally to avoid roll-pitch resonance at the  $3\sigma$  level and still maintain dispersions at an acceptable level. It might be noted here that the extant fins, due primarily to free-play in the mountings have misalignments on the order of  $1^\circ$ .

With the tightened fin alignment tolerances, either the 70% or the 100% span fins produced acceptable dispersions. The shorter fins would present

UNCLASSIFIED

# UNCLASSIFIED

Report AFRPL-TR-69-90, Appendix A

somewhat less risk of the fins of one rocket striking another rocket as they spin up in a volley. However, it was decided that the small advantage of the shorter fins did not warrant shortening the fins from their present length due to the electrical interface problems introduced by the constraint to maintain the present launch tube unmodified and due to the desire to use current tooling.

## 5.2.2 METHOD OF ANALYSIS

The preliminary phase of this investigation encompassed the determination of the dispersions of each of three rocket configurations, with a number of different spin programs, and the selection of a final configuration to be analyzed in detail in the second phase of the study. The three aerodynamic configurations considered in this preliminary phase are referred to as:

- Configuration I: Identical to the present operational vehicle.
- Configuration II: Identical to Configuration I except that the fins are shortened to 70% of the present exposed semi-span.
- Configuration III: Identical to Configuration I except that the fins are shortened to 40% of the present exposed semi-span.

Table I presents a summary of all of the 6-D trajectories run during this Improved 2.75 FFAR program. Cases 1001 through 1155 were run for this preliminary phase of the study and represent flights of Configurations I, II, and III.

To assess the dispersion due to a given perturbation, a trajectory is computed which includes this perturbation, and the position of the payload deployment point is compared with the position of the nominal payload deployment point obtained from a nominal trajectory. The effect of spin on the nominal trajectory is negligible, so that non-spinning nominal trajectories were used for comparison with all the perturbed trajectories with the various spin histories. Cases 1001, 1002, and 1003 are the nominal trajectories for Configurations I, II, and III respectively, with a 440 knot launch velocity. The accuracy of the output of the trajectory program is on the order of  $\pm 1$  ft, or about  $1/4$  mil at the payload deployment point. This is the accuracy with which the program reports the

UNCLASSIFIED

## UNCLASSIFIED

Report AFRPL-TR-69-90, Appendix A

position of the vehicle as calculated from the input data, and not the accuracy with which the data represents the actual vehicle! To check the assumption that the nominal trajectory was independent of the spin history, Case 1007 was calculated. This case includes a  $2^\circ$  differential nozzle cant and is otherwise identical to Case 1002, the non-spinning nominal trajectory for Configuration II. Comparison of these two trajectories showed the positions of the payload deployment points to be identical within 0.18 mils, which is within the accuracy limits of the trajectory program.

Most of the preliminary trajectories were calculated for the 440 knot launch velocity. However, Cases 1142 through 1154 were computed using Configuration I with a 200 knot launch velocity to check the degradation of dispersion performance with decreasing launch velocity.

The dispersion of a particular trajectory is a function of the magnitude and type of perturbation, the vehicle configuration, the launch velocity, and in some cases the spin program. The dispersion sources which are included in the present study are angular thrust misalignment, lateral thrust offset, fin misalignment, atmospheric turbulence, tipoff rate, tipoff angle, and launcher tube misalignment. The dispersions due to each of these perturbations may be calculated by determining, from trajectories, the dispersions due to unit magnitude perturbations of the following types: angular thrust misalignment, fin misalignment, initial pitch rate, initial angle of attack, and a ballistic (constant velocity) crosswind. Only the body fixed misalignments (angular thrust misalignment, lateral thrust offset, and fin misalignment) cause dispersions which vary as the spin program is varied. Thus, only the angular thrust misalignment and fin misalignment trajectories had to be computed for a variety of spin programs.

The spin history of any of the configurations will vary from the nominal due to fin and nozzle misalignments which cause rolling moments. This variation of the spin history from the nominal will cause an alteration in the magnitudes of the dispersions due to the body-fixed misalignments. Additionally, it is required that the vehicle not enter roll-pitch resonance anywhere in the flight.

UNCLASSIFIED

# UNCLASSIFIED

Report AFRPL-TR-69-90, Appendix A

This requirement has been interpreted here as meaning that resonance will not occur at least to the  $3\sigma$  probability level. Since a number of different spin programs were tested in the course of determining the appropriate program for the final design, sufficient data was generated during the preliminary phase of the study to define these roll variability effects to the extent needed to choose the final vehicle configuration.

The following section presents the dispersions calculated for each of the perturbations defined in Section 5.1.2. These dispersions are presented for each of the configurations considered and, where applicable, as a function of the roll program. For purposes of clarity, the dispersions due to the vehicle component misalignments are presented as if the misalignment magnitudes were known a priori. In actuality, the alignment tolerances were selected during the course of the preliminary dispersion calculations and in light of them. Since the chosen tolerances are considered practical minimums for large scale production, there is at least not complete arbitrariness in the selection of the perturbation magnitudes or in the calculated dispersion magnitudes.

The dispersions due to a fixed magnitude fin or thrust misalignment will vary with the roll history selected. Thus, in order to define the final configuration, it is necessary to determine the dispersion due to these perturbations with a variety of roll histories, and to choose the roll history and vehicle configuration which yield acceptable dispersion magnitude while best satisfying the other design objectives: minimum cost, minimum change in existing tooling, no required changes in the launcher, and no pitch-roll resonance to at least a  $3\sigma$  probability level. It will be shown in Section 5.2.3.3 that Configuration III does not satisfy this last requirement. When this became apparent, the configuration was dropped from further consideration and the dispersion of this configuration is consequently rather incompletely defined.

UNCLASSIFIED



# UNCLASSIFIED

Report AFRPL-TR-69-90, Appendix A

## 5.2.3 RESULTS

In this section, the results of the 6-D trajectory determination of the dispersion due to each individual perturbation is reported first. Next, the spin history variability due to fin and nozzle misalignments is discussed; then the dispersion due to the combined perturbations is assessed; and finally, sources of variation of the dispersion magnitude are indicated.

### 5.2.3.1 DISPERSION DUE TO ROLL INSENSITIVE PERTURBATIONS

Figure 5 presents a log turbulent wind power spectrum which was calculated from a number of wind spectrum measurements made above Cape Kennedy by NASA, George C. Marshall Space Flight Center. These measurements are reported in Reference 4. Additionally, shown in Reference 7 is the normalized dispersion response of a small artillery rocket to cyclical winds. This response is the square of the dispersion distance per unit wind amplitude for sinusoidal winds of a given Wave Number (inversely proportional to wavelength). The burning distance of the small artillery rocket for which the curve was calculated is similar to the burning distance of the 2.75 FFAR. Although this similarity does not imply equality, the dispersion calculated here will be conservative in any case and the extensive work required to calculate the exact response would be unwarranted. Therefore it was assumed that the available curve could be used as a reference to construct a similar curve for the present vehicle. The dispersion response magnitude in the reference is somewhat oscillatory with increasing Wave Number. However, these oscillations represent characteristics of the particular vehicle, and a smoothed curve fitted through the mean of these oscillations was considered to be a better generalization of the data. Figure 6 shows this fitted curve. It may be seen that the dispersion response has been normalized so that, at any Wave Number, the parameter presented is the ratio of the dispersion response at that Wave Number to the dispersion response at zero Wave Number (a Ballistic Wind).

UNCLASSIFIED

# UNCLASSIFIED

Report AFRPL-TR-69-90, Appendix A

Reference 7 shows that, if the product of the dispersion response ( $\text{dispersion}^2/\text{unit amplitude wind}^2$ ) at a given Wave Number and the turbulent wind spectral density ( $\text{velocity}^2/\text{Wave Number}$ ) is integrated over Wave Number, the resultant value is the square of the dispersion due to wind variability at the probability level associated with the turbulent wind spectrum. Since the spectrum shown in Figure 5 is the  $1\sigma$  spectrum, the square root of the resultant of the integration is the  $1\sigma$  dispersion due to atmospheric turbulence. If the normalized dispersion response replaces the dispersion response in the integration, then the square root of the integral become the  $1\sigma$  dispersion per unit response to a unit ballistic wind. The integration was performed, using the normalized wind response, and it was found that the turbulent wind spectrum would cause a 1.2 mil dispersion per mil dispersion per ft/second ballistic wind.

The dispersion due to wind turbulence calculated by the above method may be quite conservative since the temporal and spatial separation of the rockets in a ripple fire sequence is extremely small. Although turbulence is sometimes defined as instantaneous wind deviations from some mean value, the use of the term "instantaneous" is relative, and in the portion of the turbulent spectrum where there is any significant energy, the implied "instant" is on the order of seconds or minutes (for a fixed point in space) rather than the 20 milliseconds separating the rocket firings in the ripple fire mode.

A trajectory was calculated, for each of the three preliminary configurations, with a 10 ft/second crosswind, and a 440 knot launch velocity. The following table summarizes the results of these cases and of the subsequent dispersion calculations:

<u>Configuration</u>	<u>Dispersion due to 10 ft/sec ballistic crosswind (mils)</u>	<u><math>1\sigma</math> Dispersion due to atmospheric turbulence (mils)</u>
I	6.70	0.80
II	6.64	0.80
III	6.30	0.76

UNCLASSIFIED

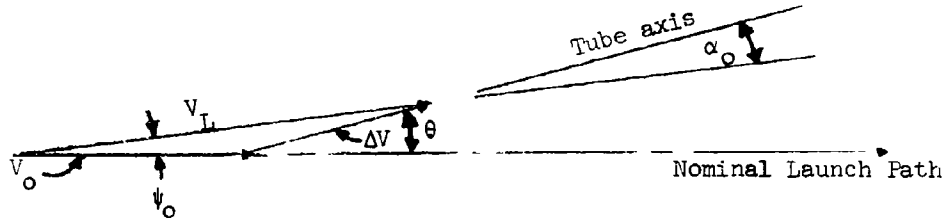
# UNCLASSIFIED

Report AFRPL-TR-69-90, Appendix A

It is interesting to note that despite the large variation in fin areas between configurations, all three are so aerodynamically stable as to produce negligible differences in the dispersions due to winds.

Section 5.1.2.5 gives the  $1\sigma$  launcher tube misalignment as 0.673 mils. The dispersion due to this misalignment may be calculated using the 6-D trajectory data which gives the dispersion per unit initial angle of attack. However, the launcher misalignment is not numerically equal to the initial angle of attack since the velocity increment developed during the launch portion of the trajectory (i.e., from ignition to tube exit) is parallel to the misaligned tube axis rather than to the nominal aiming direction. Thus, the following form must be used to relate the two:

The sketch shows a misalignment of a launcher tube of  $\theta$ .  $V_o$  is the airplane velocity,  $\Delta V$  is the velocity increment during launch, and  $V_L \approx V_o + \Delta V$ .



If the vehicle launched from the tube followed a point mass trajectory, it would have a dispersion of  $\psi_o$ , where:

$$\psi_o = \Delta V \sin \theta / V_L \quad (5.2-1)$$

UNCLASSIFIED

# UNCLASSIFIED

Report AFRPL-TR-69-90, Appendix A

However, for the actual case, the vehicle will have an additional dispersion due to the angle of attack  $\alpha_0$ , where:

$$\alpha_0 = \theta - \psi_0 = \theta (1 - \Delta V/V_L) \quad (5.2-2)$$

The dispersion due to  $\alpha_0$  is  $\alpha_0 (d\psi/d\alpha)$ , where  $d\psi/d\alpha$  is the dispersion per unit initial angle of attack calculated from the 6-D trajectories. Combining the two dispersion contributions yields the dispersion due to tube misalignment,  $\Delta\psi_T$ :

$$\Delta\psi_T = \theta \{ (d\psi/d\alpha)(1 - \Delta V/V_L) + \Delta V/V_L \} \quad (5.2-3)$$

where the small angle approximation  $\theta = \sin \theta$  has been used. The following table summarizes the results of the application of this equation to the preliminary configurations. It may be seen that, in all cases, the dispersions are negligible compared to those from other sources.

Configuration	$d\psi/d\alpha$ (mils/mil)	$\Delta V/V_L$ (---)	Dispersion due to 0.673 mil 1 $\sigma$ launcher tube misalign- ment (mils)
I	.0424	0.13	0.112
II	.0424	0.13	0.112
III	.0315	0.13	0.106

The dispersion due to tube misalignment is independent of the spin history.

Section 5.1.2.6 shows that a conservative estimate of the 1 $\sigma$  dispersion due to tipoff may be made using the maximum possible tipoff rate and angle due to a 1 $\sigma$  thrust misalignment. These have been calculated to be, respectively, 13.7°/second and 0.32°. Trajectories with a 440 knot launch velocity have been computed, for each of the three preliminary cases, which included either a 1° initial angle of attack, or a 10°/second initial pitch rate. Multiplying the dispersions per unit pitch rate and unit angle of attack, respectively, by the 1 $\sigma$

# UNCLASSIFIED

Report AFRPL-TR-69-90, Appendix A

tipoff pitch rate and tipoff angle and summing the results yields the  $1\sigma$  dispersion due to tipoff. The following table summarizes the results of both the trajectories and the tipoff dispersion computations:

<u>Configuration</u>	<u><math>10^\circ</math>/Second Initial Rate</u>		<u><math>1^\circ</math> Initial Angle of Attack</u>		<u><math>1\sigma</math> Tipoff Dispersion</u>
	<u>Case No.</u>	<u>Dispersion(Mils)</u>	<u>Case No.</u>	<u>Dispersion(Mils)</u>	<u>(Mils)</u>
I	1031	0.36	1025	0.55	0.67
II	1029	0.55	1015	0.74	0.99
III	1030	0.74	1020	0.74	1.25

## 5.2.3.2 ROLL DEPENDENT DISPERSIONS

There are two thrust misalignments which may cause a pitching/yawing moment; these are the angular thrust misalignment and the lateral thrust offset. It has been found, in previous dispersion studies, that the dispersions due to each of these are in the same ratio as the moments due to each at launcher exit. It was shown in Section 5.1.2 that the  $1\sigma$  angular thrust misalignment is  $0.192^\circ$  while the  $1\sigma$  lateral offset yields a moment at launcher exit which is equivalent to a  $0.00875^\circ$  angular thrust misalignment. These two misalignments are statistically independent and thus may be combined as an RSS to yield the total  $1\sigma$  thrust misalignment. The lateral offset contributes negligibly to the dispersion and the effective  $1\sigma$  thrust misalignment is  $0.192^\circ$ .

A number of trajectories were computed with a  $0.125^\circ$  angular thrust misalignment and various differential nozzle cants between  $0^\circ$  and  $2^\circ$ . Cases were computed both with zero spin rate at launcher exit and with a spin rate at that point which would result if the thrust torque were fully effective during the launch phase. All three preliminary configurations were investigated. Figure 7 shows the results of these trajectories with the dispersions scaled up linearly to the expected values with a  $0.192^\circ$  effective angular thrust misalignment. It may be seen that for any spin rate at launcher exit between zero and the value calculated

UNCLASSIFIED

## UNCLASSIFIED

Report AFRPL-TR-69-90, Appendix A

from the thrust torque, there is little variation in the dispersion. Comparing the dispersions shown for zero differential cant, it is seen that, as expected, the dispersion increases as the fin area, and hence the aerodynamic restoring moment, is reduced. This variation is not as apparent at the higher differential nozzle cants, but it should be borne in mind (see Figure 8) that the roll rate per unit differential nozzle cant increases rapidly with decreasing span. Thus, the maximum roll rate of Configuration III is 19 times as high as the maximum roll rate of Configuration I with the same differential nozzle cant.

For both Configuration I and Configuration II, a number of thrust misalignment cases have been computed with various combinations of differential fin cant and roll rate at launcher exit. The trajectories were computed with a  $0.125^\circ$  thrust misalignment, but the resultant dispersions have been scaled up to a  $0.192^\circ$  misalignment, and the resultant  $1\sigma$  dispersions plotted as Figures 9 and 10. Comparing these two figures shows that Configuration II is much more sensitive to an initial spin rate than Configuration I. This lack of sensitivity of Configuration I is particularly apparent when it is noted that, for a fixed direction of the initial spin rate, positive and negative fin cants yield essentially the same dispersion. On the other hand, the dispersion of Configuration II is significantly lower when the sense of the differential fin cant is such as to cause spin in the same direction as the initial spin. This difference becomes more marked as the initial spin rate is increased. It is interesting to note that, for zero differential cant, the dispersion does not always decrease as the initial spin rate is increased.

A number of trajectories were computed, for all three configurations, which included a  $1/4^\circ$  fin misalignment and various differential nozzle cants. These trajectories all included a spin rate at launcher exit which was the value that would exist if the torque due to the differential nozzle cant were fully effective. Section 5.1.2.3 shows that the  $1\sigma$  fin misalignment is  $0.141^\circ$ . The dispersions calculated from the computed cases were ratioed to yield the dispersion due to the  $1\sigma$  fin misalignment and the resultant  $1\sigma$  dispersions are shown in Figure 11 as a function of differential nozzle cant. It may be seen, by comparing

UNCLASSIFIED

# UNCLASSIFIED

Report AFRPL-TR-69-90, Appendix A

the zero spin rate dispersions, that the dispersion due to fin misalignment varies little between configurations. This is due to the fact that reducing the fin area reduces the upsetting moment due to a given misalignment angle, as well as the restoring moment.

Figures 12 and 13 show the  $1\sigma$  dispersions of, respectively, Configuration I and Configuration II due to fin misalignment, as a function of differential fin cant and initial spin rate (at launcher exit). These figures were prepared from data gathered from a number of trajectories computed with a  $1/4^\circ$  fin misalignment. Comparison of the figures shows that, with no initial spin rate, there is little difference in the dispersion of the two configurations. As in the case of the thrust misalignment, the magnitude of the initial spin rate in general has little effect on the dispersion of Configuration I, but does effect Configuration II. It may be seen that, for Configuration II, initial spin in the same direction as the spin produced by the canted fins reduces dispersion while counter-rotation increases it. Shown on Figure 13 as a broken line is the dispersion calculated using the later aerodynamic rolling moment coefficients (the rigid body coefficients calculated for the final configuration but reduced, using strip theory, to apply to Configuration II). It may be seen that, except for the case of counter-rotation, the dispersion is reduced from the values calculated with the earlier roll aerodynamics. This indicates that, for practical configurations, the previously calculated results are conservative.

## 5.2.3.3 ROLL HISTORY VARIABILITY

In the previous sections, it was shown that the magnitudes of the dispersions due to fin and thrust misalignment could be varied greatly by the employment of various spin programs. Additionally, it was shown that the dispersions due to all sources could be varied by changes in vehicle configuration. In this investigation these configuration variations were limited to fin span variations though the implication is, of course, that other configuration variations might conceivably be used to supply the aerodynamic properties of the selected

UNCLASSIFIED

## UNCLASSIFIED

Report AFRPL-TR-69-90, Appendix A

configuration. On the other hand, the requirement that maximum use be made of existing tooling probably does make span variation the most suitable means of varying the configuration.

The dispersions so far computed have been presented in terms of different combinations of configuration and spin history, but the efficacy of the different combinations from viewpoints other than dispersion control has not yet been discussed. The most significant of these other points is the selection of a design which minimizes the possibility of pitch-roll resonance. Figure 14 presents the history of the aerodynamic natural frequency of each of the three preliminary configurations. These histories are for a 440 knot launch velocity and include the preliminary rigid body aerodynamics. In Figure 8, the spin rate due to a  $1^\circ$  differential thrust cant is shown as a function of time for the same three configurations and a 440 knot launch velocity. The standard deviation of the differential nozzle cant is given in Section 5.1.2.2 as  $0.127^\circ$ . Thus, the  $3\sigma$  variability of the differential nozzle cant is  $\pm 0.381^\circ$ . Using the data of Figure 8, the spin rate of Configuration III, due to the  $3\sigma$  differential nozzle cant is found to be  $\pm 8.78$  cps at 2.0 seconds after ignition. The rigid body natural frequency at this time (from Figure 14) is only 8.5 cps. Thus, for any design spin rate below the natural frequency, resonance will occur below the  $3\sigma$  probability level, and this configuration is unsuitable for use. The high spin rates required to stay above the natural frequency at a  $3\sigma$  level are not considered compatible with the propellant environmental requirements. It should be mentioned that the stated nozzle alignment tolerances, as well as the fin alignment tolerances, are considered minimums for a practical design, so the elimination of Configuration III is not arbitrary.

Besides the spin variability due to nozzle misalignments, there is also a component due to fin misalignments which give an effective differential fin cant. Figure 15 shows the spin history of Configuration I and II for a  $1^\circ$  differential fin cant and a 440 knot launch velocity. Section 5.1.2.4 gives a standard deviation of the differential fin cant of  $0.063^\circ$ , so that the  $3\sigma$

UNCLASSIFIED



## UNCLASSIFIED

Report AFRPL-TR-69-90, Appendix A

variability of this cant is  $0.189^\circ$ . The spin rate, at any point along a given trajectory, due to differential fin cant is directly proportional to the magnitude of the cant, so the data of Figure 15 may be used to determine the  $3\sigma$  variability of the spin histories due to differential fin cant variability.

The  $3\sigma$  spin histories due to differential nozzle cant variability and differential fin cant variability may be combined by the RSS method to yield the total  $3\sigma$  spin history variability. This computation has been performed and the results are presented in Figure 16 for Configurations I and II. The variability is greater for Configuration II, while the aerodynamic natural frequency (Figure 14) is lower, thus showing this to be the more critical configuration in regard to pitch-roll resonance. However, some margin is present for both configurations, although it might be expected that, using elasticized aerodynamic coefficients, Configuration II may become quite critical. The consequence of having to avoid pitch-roll resonance in a vehicle which may have a spin history which is quite a bit different from the nominal is that the allowable spin histories which may be built into the vehicle are much more limited than they would be if it were only necessary to avoid resonance between the aerodynamic natural frequency and the nominal spin rate. Figure 17 shows the allowable spin history envelope for Configurations I and II. These envelopes are based on rigid body aerodynamics and may be expected to be considerably smaller for the aeroelastic vehicle. Comparing this figure with Figure 8, it may be seen that Configuration II is limited to differential nozzle cants below about  $1^\circ$ , to avoid resonance, while cants up to about  $6^\circ$  could be used with Configuration I. Referring to Figure 15, it may be seen that differential fin cant is limited to about  $0.43^\circ$  with Configuration I, while only about a  $0.17^\circ$  cant would be possible with Configuration II. It will be seen in Section 5.3 that the allowable cants are, in fact, much more limited for the aeroelastic vehicle.

As mentioned earlier, revised rigid body roll aerodynamics were employed starting with Case 1139. Figure 18 shows a comparison of the roll histories of Configuration II with both the earlier and the later roll aerodynamics. It may be seen that the two differ but little.

UNCLASSIFIED

## UNCLASSIFIED

Report AFRPL-TR-69-90, Appendix A

### 5.2.3.4 DISPERSION DUE TO COMBINED PERTURBATIONS

The dispersion sources being considered are statistically independent. Therefore, the dispersion due to the combined effects of all the perturbations may be determined, at the 1 $\sigma$  probability level, as the square root of the sum of the squares (RSS) of the 1 $\sigma$  component dispersions. The dispersions may be conveniently considered in two parts (which may be combined by the RSS method): the roll insensitive dispersions and the roll dependent dispersions.

There are three dispersion sources which are independent of the roll history: atmospheric turbulence, launcher tube misalignment, and tipoff. Section 5.2.3.1 reports the component dispersions for all three preliminary configurations, and a launch velocity of 440 knots. The following table summarizes the combined dispersion due to these perturbations:

<u>Configuration</u>	<u>1<math>\sigma</math> Dispersion due to Roll- Insensitive Perturbations (Mils)</u>
I	1.05
II	1.28
III	1.47

The roll dependent dispersions include fin misalignment and thrust misalignment, with the latter being a combination of the angular thrust misalignment and the lateral thrust offset. Figure 19 shows the roll dependent dispersions as a function of differential nozzle cant, while Figure 20 shows them as a function of both initial roll rate and differential fin cant. Both of these figures show the results for Configurations I and II and a 440 knot launch velocity.

The total dispersion, at the 1 $\sigma$  level, of the Configurations I and II vehicles, when launched from an aircraft travelling at 440 knots, is depicted in Figures 21 and 22 for a variety of spin programs. The most significant point apparent from these results is that both configurations yield smaller dispersions than are required for the design for all spin histories investigated, including the non-spinning cases.

UNCLASSIFIED

# UNCLASSIFIED

Report AFRPL-TR-69-90, Appendix A

In comparing the results for the two configurations, it may be seen that, if they are not to be spun, Configuration I will produce only 78% of the dispersion of Configuration II. If the vehicles are spun by means of canted nozzles, then Configuration II will produce a lower dispersion up to about a  $0.7^\circ$  differential nozzle cant while Configuration I is superior above this cant. If the vehicle is to be spun by means of differentially canted fins, then Configuration I will provide lower dispersion with initial spin rates below about 2 cps while Configuration II will provide the lower dispersion for higher initial spin rates.

## 5.2.3.5 VARIATION OF DISPERSION WITH LAUNCH VELOCITY

In order to assess the degradation of dispersion with decreased launch velocity, a number of trajectories were computed with a launch aircraft velocity of 200 knots, the minimum velocity for which the vehicle is to be designed. Trajectories were computed both with and without differential fin cant and with and without initial spin. Only Configuration I was investigated and the perturbations considered were limited to fin misalignment and thrust misalignment. Figure 23 displays the dispersion due to the individual contributions while Figure 24 shows the combined effect, i.e., the  $1\sigma$  dispersion due to the roll dependent perturbations. Since these dispersion data have been calculated using the preliminary rigid body aerodynamics, it must be expected that an actual aeroelastic vehicle of otherwise similar configuration would display even higher dispersion, as, of course, Configuration II would. It may be concluded that, since the  $1\sigma$  dispersion of Configuration I due to the roll dependent perturbations is 8.25 mils for no initial spin and no differential fin cant, neither vehicle configuration would be satisfactory as a non-spinning vehicle. It may be seen from the zero initial spin curve of Figure 24 that a  $0.15^\circ$  fin cant reduced the dispersion by only 43% from the non-spinning case, in comparison to the approximately 80% reduction possible with a 440 knot launch velocity (Figure 20). The indication of this is that the vehicle will probably require as high a spin rate as possible within the pitch-roll resonance restrictions.

UNCLASSIFIED

## UNCLASSIFIED

Report AFRPL-TR-69-90, Appendix A

### 5.2.3.6 DISPERSION CONTRIBUTION OF ROLL HISTORY VARIABILITY

The spin rate variability affects the dispersion of the vehicle in two ways, each of which has been mentioned earlier. First, it reduces the range within which a nominal spin history may be chosen; and second it causes a  $1\sigma$  dispersion which will be different from that computed from the  $1\sigma$  dispersion-causing perturbations and the nominal spin history. This is due to the fact that the actual spin histories will be distributed about a mean (the nominal spin history) so that the  $1\sigma$  dispersion will be some integrated function of the  $1\sigma$  dispersions at all the spin histories which may occur. Since, for both differential fin cant and differential nozzle cant, the  $1\sigma$  dispersion as a function of cant is concave upward with decreasing cant, it may be expected that the dispersion calculated with the spin history variability included will exceed that calculated for the nominal spin history. It is apparent that this integration of the dispersion distribution must be carried out to assess the actual dispersion magnitude for the vehicle. Section 7.1 develops the necessary mathematics to perform this integration and it is applied in the evaluation of the dispersion of the final configuration.

### 5.2.4 INTERPRETATION OF RESULTS

It was shown in the preceding analysis that Configuration III was unsuitable for use due to the extreme roll rate variability inherent in the short fin design. Both Configurations I and II produce  $1\sigma$  dispersions well within the required limits, with or without spin, with a 440 knot launch. However, with a 200 knot launch velocity, the dispersion of Configuration I was shown to be excessive without spin, and the dispersion of Configuration II may be expected to be even more so.

The necessity for avoiding pitch-roll resonance plus the large variability of the roll history from its nominal value limits the range of nominal spin histories which may be employed. This limitation is more severe in the case of Configuration II. It is apparent that the limits on the allowable roll

UNCLASSIFIED

## UNCLASSIFIED

Report AFRPL-TR-69-90, Appendix A

history will become even more stringent in the case of the actual aeroelastic vehicle, and very little margin for design may be left in the case of Configuration II.

Both differential fin cant and differential nozzle cant are effective in reducing dispersion, but an initial spin rate makes little contribution.

It may be seen that a suitable configuration could probably be found almost anywhere in the range between 70% (Configuration II) and 100% (Configuration I) of the present vehicle's span. Also, spin may be provided either by differential fin cant or differential nozzle cant, within the required dispersion limit and without the occurrence of pitch-roll resonance. Thus, it is necessary to choose a final configuration at least partly on the basis of considerations other than dispersion magnitude and resonance sensitivity.

The ripple fire launching interval is short enough that the rockets will be overlapped at launch. Since the spacing of the launcher tubes is small compared to the fin span, it is possible that there will be some contact between rockets immediately following launch. It may be presumed that if the rockets are spinning at launch, this contact could lead to more erratic behavior of the rockets than if there were no spin. Since initial spin contributes little to reducing dispersion in any case, there seems to be no valid argument against dispensing with it. As mentioned above, either differential fin cant or differential nozzle cant may be used to provide the spin necessary to satisfy the dispersion requirements. However, it is the opinion of the vehicle designers that the differential nozzle cant would be more costly to implement. In any case, the nozzle cant causes a higher spin rate early in the flight and would thus be less desirable from the standpoint of minimizing the adverse effects of contact between the rocket immediately following launch. Thus, it may be concluded that differential fin cant is the most satisfactory means of achieving the necessary roll history.

It has been stated earlier that, in order to meet the dispersion requirements at the lowest launch velocity (200 knots) a high spin rate would probably be necessary. Since it is probable that the allowable spin rate of

UNCLASSIFIED

# UNCLASSIFIED

Report AFRPL-TR-69-90, Appendix A

Configuration II would be severely limited due to spin variability, Configuration I becomes the preferred candidate for the final configuration. This choice allows the greatest use of existing tooling and no modification of the launcher and is thus most suitable from all aspects.

It should be pointed out that although the chosen configuration appears identical to the present design in external configuration, there are several significant differences: The motor performance has been increased to improve range and velocity capability. This normally would lead to increased dispersion. However, reducing fin alignment tolerances to the practical minimum, and incorporating differential fin cant will result in a vehicle with excellent dispersion characteristics and an extremely low probability of experiencing pitch-roll resonance.

UNCLASSIFIED

# UNCLASSIFIED

Report AFRPL-TR-69-90, Appendix A

## 5.3 FINAL CONFIGURATION

In Section 5.2 the performances of several configurations were evaluated and a final configuration chosen. The preliminary configurations were studied using rigid body aerodynamics and a preliminary thrust curve. In the present section, the dispersion of the selected configuration will be evaluated using the latest wind tunnel values of the vehicle's aerodynamics with aeroelastic corrections applied (both the wind tunnel data and the aeroelastic corrections are reported in Volume I), and the finalized thrust curve. Additionally, the effect of roll history variability on dispersion will be numerically evaluated in the Appendix (Section 7.1) and the results presented here.

It has been found from numerous studies that the dispersion, measured normal to the nominal flight path, of a rocket of high acceleration and short flight path length is independent of flight path elevation angle at launch. Thus, the dispersions given here are appropriate to all initial elevation angles.

### 5.3.1 METHOD OF ANALYSIS

As in the case of the preliminary configurations discussed in Section 5.2, the dispersion characteristics of the final configuration were evaluated through the use of 6-D trajectories. Both nominal trajectories and trajectories which included the various perturbations which will cause dispersion were computed. By comparing the calculated payload deployment points of the perturbed trajectories with those computed for the nominal trajectories, the dispersion due to each of the perturbations was evaluated. In addition to the perturbations which cause dispersion directly, there are two perturbations which, while they do not cause dispersion of themselves, will change the magnitude of the dispersions caused by other perturbations. The two perturbations which have this indirect effect are fin and nozzle misalignments which induce variations in the spin history from its nominal value. A number of trajectories were computed which included each of these effects in combination with each of the perturbations which cause dispersions that vary with the roll history. These trajectories provided data

UNCLASSIFIED

## UNCLASSIFIED

Report AFRPL-TR-69-90, Appendix A

describing the variation of the dispersion of the vehicle with variations in the spin history. Using the assumption that the spin histories would be normally distributed about a mean represented by the design spin history, the method developed in Section 7.1 was used to determine the actual  $1\sigma$  dispersion of the vehicle with roll history variability included.

### 5.3.2 INPUT PARAMETERS

The final configuration which was chosen is geometrically identical to Configuration I of the preliminary phase of this study. However, the aerodynamic characteristics and the thrust curve both differ from Configuration I. Due to the change in the thrust curve, there are alterations both in the initial conditions at launcher exit and in the fin opening time (see Section 5.1.1).

#### 5.3.2.1 VEHICLE CHARACTERISTICS

Figure 4 shows the finalized thrust characteristics of the rocket motor developed for the Improved 2.75 FFAR. This thrust curve is considerably different from the curve assumed for the preliminary configurations (Figure 3).

Volume I gives the final rigid body aerodynamic coefficients as determined from wind tunnel tests. Also presented in Volume I are the ratios of the aeroelastic aerodynamic coefficients to their rigid body equivalents, and the aeroelastic change in center of pressure. These aeroelastic corrections were applied to the rigid body data, and the resultant aeroelastic coefficients input to the 6-D Program.

Once the aeroelastic coefficients were known, it was possible to make an estimate of the natural frequency at payload deployment and of the spin rate per unit differential fin cant at this same time. Although the burnout velocity (for the same launch velocity) proved to be lower for the final configuration than for the preliminary configurations, the ratio of spin rate per unit differential fin cant to the aerodynamic natural frequency was little affected. Since the roll rate variability, at payload deployment, due to misalignments was essentially equal to the variability due to differential fin

UNCLASSIFIED



## UNCLASSIFIED

Report AFRPL-TR-69-90, Appendix A

cant variability alone, sufficient data were available to allow the determination of the maximum allowable nominal differential fin cant which would preclude pitch-roll resonance below the  $3\sigma$  probability level. This differential fin cant was calculated to be  $0.11^\circ$  and since the preliminary work had shown that it would probably be necessary to use as much cant as possible, this value was chosen for the final configuration.

### 5.3.2.2 PERTURBATIONS TO FLIGHT

Section 5.1.2 presents the magnitudes of the various perturbations which may cause dispersion and describes the derivations of these values. These data were used, unchanged, in the calculation of the dispersion of the final configuration. Additionally, the effect on dispersion of the roll perturbations discussed in Section 5.2.3.3 was numerically evaluated. These roll perturbations are, at the  $1\sigma$  probability level, a differential nozzle cant variability of  $0.127^\circ$ , and a differential fin cant variability of  $0.063^\circ$ . Section 7.1 discusses the technique by which these secondary effects are incorporated in the dispersion analysis.

### 5.3.3 TRAJECTORY COMPUTATIONS AND RESULTS

Table I summarizes the trajectories computed for this study. Cases 1156 through 1197 were computed for the final configuration. Cases 1156 through 1173 were used to evaluate the dispersion, at the three launch velocities, when the roll history was that due to the nominal differential fin cant. The balance of the trajectories include either a variation in differential fin cant or a differential nozzle cant, as well as the various dispersion inducing perturbations.

#### 5.3.3.1 NOMINAL TRAJECTORIES AND ROLL HISTORY

Cases 1156, 1157 and 1158 reproduce the nominal trajectories of the final configuration with launch aircraft velocities of 200, 440, and 600 knots, respectively. Figures 25, 26, and 27 show the aerodynamic natural frequency,

UNCLASSIFIED

## UNCLASSIFIED

Report AFRPL-TR-69-90, Appendix A

nominal roll rate, and  $3\sigma$  high roll rate for each of the three launch aircraft velocities. It may be seen that the variation in aerodynamics, the reduced velocity at payload deployment, and the incorporation of aeroelasticity have all contributed to a major reduction in aerodynamic natural frequency. Comparing Figures 14 and 26, both computed for a 440 knot launch aircraft velocity, it may be seen that the natural frequency of preliminary Configuration I was calculated to be 1.6 times as high as the frequency computed for the final configuration. However, Figures 25 through 27 show that the aerodynamic natural frequency remains slightly above the  $3\sigma$  high roll rate, proving the selected differential fin cant of  $0.11^\circ$  to be suitable from the standpoint of avoiding resonance. Also, it may be seen from Figure 27 that this is as high a cant as could be used. Thus, the choice of a  $0.11^\circ$  fin cant was justified.

### 5.2.3.2 DISPERSIONS DUE TO INDIVIDUAL CONTRIBUTIONS

The dispersions presented here are evaluated from the 6-D trajectory results, and represent 1 $\sigma$  probability level magnitudes. Except for the dispersions due to fin misalignment and the thrust angular misalignments and offset, the magnitudes of the dispersions are independent of the roll history used.

It is shown in Section 5.2.3.1 that the dispersion due to wind variability may be conservatively calculated as the dispersion due to the total turbulent wind spectrum. It is also shown that this dispersion is directly proportional to the dispersion due to a unit ballistic crosswind and that the constant of proportionality is 1.2 mile of dispersion per mil dispersion per ft/second ballistic wind. The following table summarizes the dispersion of the final configuration due to atmospheric turbulence, as calculated from the results of 6-D trajectories which included a 10 ft/second crosswind:

Page 44

UNCLASSIFIED

# UNCLASSIFIED

Report AFRPL-TR-69-90, Appendix A

Launch Aircraft Velocity (knots)	Dispersion per ft/sec Ballistic Wind (mils)	1 $\sigma$ Dispersion due to Atmospheric Turbulence (mils)
200	1.42	1.71
440	0.63	0.76
600	0.42	0.50

Section 5.2.3.1 presents the method by which the dispersion due to launcher tube misalignment is calculated. The dispersions of the three preliminary configurations are calculated there and shown to be negligible compared to the dispersions due to other perturbations. The following table summarizes the results of applying Eqr. 5.2-3 from Section 5.2.3.1 to the final configuration, and includes the significant terms used in that equation.

Airplane Velocity $V_o$ (knots)	$d\psi/d\alpha$ (-----)	$\Delta V/V_L$ (-----)	Dispersion due to 0.673 mil 1 $\sigma$ launcher tube misalignment (mils)
200	0.110	0.210	0.20
440	0.0417	0.107	0.10
600	0.0343	0.0815	0.08

It is shown in Section 5.1.2.6 that a conservative estimate of the 1 $\sigma$  dispersion due to tipoff may be made using the maximum possible tipoff rate and angle due to a 1 $\sigma$  thrust misalignment (combined angular misalignment and lateral thrust offset). The tipoff rate calculated there for this condition is 13.7°/sec while the tipoff angle is 0.32°. For this worst case condition, the dispersions due to the tipoff rate and angle are assumed to be in the same direction so that the component dispersions are additive. Trajectories were computed for all three launch velocities both with a 10°/second initial pitch rate and a 1° initial angle of attack. The dispersions due to tipoff were calculated from the results of these trajectories. The following table summarizes the component and total dispersions due to tipoff.

UNCLASSIFIED

# UNCLASSIFIED

Report AFRPL-TR-69-90, Appendix A

Launch Aircraft Velocity (knots)	Dispersion Due to 13.7°/Second Tipoff Rate (mils)	Dispersion Due to 0.32° Tipoff Angle (mils)	1σ Dispersion Due to Tipoff (mils)
100	2.36	0.62	2.98
400	0.51	0.23	0.74
600	0.45	0.21	0.66

There are two dispersion components attributable to thrust misalignment: That due to the angular thrust misalignment and that due to a lateral offset of the thrust vector. However, it is shown in Section 5.1.2 that the latter is so small in comparison to the former as to be completely negligible. The 1σ dispersion due to thrust misalignment may therefore be computed as the dispersion due to a 0.192° angular thrust misalignment. It was shown in the investigation of the preliminary configurations that the dispersion due to a fixed magnitude thrust misalignment varies significantly with changes in the roll program. Since the roll history of the Improved 2.7 SPAR will vary widely from the nominal, it is necessary to integrate the dispersion over the entire roll history distribution to determine a statistically correct value of 1σ dispersion. Section 7.1 develops the methodology of this integration and contains the numerical evaluation of the dispersion. In order to provide the necessary data for that evaluation, it was necessary to compute a series of roll histories which included not only a thrust misalignment and each of the three launch velocities, but also a variety of roll programs. These roll histories included, in addition to the nominal (due to a 0.11° differential fin cant), a differential fin cant of 0.01°, non-spinning cases, and four positive and negative 1σ (0.127°) differential nozzle cant, in combination with the nominal differential fin cant. Figure 28 shows the dispersion due to thrust misalignment as a function of differential fin cant, while Figure 29 presents the dispersion as a function of differential nozzle cant with the nominal fin cant. The following table summarizes the dispersion due to the 1σ thrust misalignment when the roll history is not allowed to vary from its nominal

# UNCLASSIFIED

Report AFRPL-TR-69-90, Appendix A

Launch Aircraft Velocity (knots)	Dispersion Due to 1σ Thrust Misalignment (mils) (Roll History Held to Nominal Value)
200	5.40
440	0.92
600	0.50

As in the case of the thrust misalignment, the magnitude of the dispersion due to a given magnitude of fin misalignment will vary greatly with changes in the roll program. Thus it is necessary to evaluate the 1σ dispersion due to fin misalignment in terms of a distribution of roll histories about the nominal. An array of 6-D trajectories, paralleling those computed for the thrust misalignment case, were determined to allow the computation of the correct 1σ dispersion due to fin misalignment. This computation is performed in Section 7.1. The following table summarizes the dispersion due to the 1σ fin misalignment ( $0.141^\circ$ ) with the roll history held to its nominal value.

Launch Aircraft Velocity (knots)	Dispersion Due to 1σ Fin Misalignment (mils) (Roll History Held to Nominal Value)
200	0.95
440	0.43
600	0.40

Figure 30 shows the dispersion due to fin misalignment as a function of differential fin cant while Figure 31 shows it as a function of differential nozzle cant in combination with the nominal fin cant.

## 5.3.3.3 DISPERSION DUE TO COMBINED PERTURBATIONS

The dispersion sources which have been considered here are statistically independent. In addition, these dispersions are small enough that the dispersion magnitudes may be considered to be linearly proportional to the perturbation

UNCLASSIFIED

# UNCLASSIFIED

Report AFRPL-TR-69-90, Appendix A

magnitudes. Thus, the total dispersion at a  $1\sigma$  level may be calculated as the square root of the sum of the squares of the component  $1\sigma$  dispersions. The roll rate variability adds some non-linearity to the solution in that the dispersions due to fin and thrust misalignments do not vary linearly with variations in differential fin or nozzle cant. However, despite this, the dispersions due to these misalignments are still linearly proportional to the magnitude of the misalignments for any fixed spin history. The effective  $1\sigma$  dispersions due to fin and thrust misalignment are calculated in Section 7.1, including the effect of roll history variability. The following table summarizes the  $1\sigma$  dispersion of the Improved 2.75 FFAR both with and without the inclusion of the roll variability effect.

Launch Aircraft Velocity (knots)	Dispersion Due to $1\sigma$ Perturbations (mils) (Roll Variability Effect not Included)	$1\sigma$ Dispersion (mils)
200	6.56	6.85
440	1.49	1.87
600	1.05	1.35

UNCLASSIFIED

# UNCLASSIFIED

Report AFRPL-TR-69-90, Appendix A

## 5.4 AIRCRAFT SAFETY

A paramount consideration in the design of a rocket to be launched from a manned aircraft is to assure that the rocket cannot make physical contact with the aircraft after launch. This is effected here by determining that neither the perturbations which cause dispersion nor the aircraft flow field will deflect the rocket enough to cause contact.

In order to determine whether any of the perturbations which contribute to misalignment could cause a safety hazard, the flight paths computed by the 6-D trajectory program for the cases of the final configuration which included these perturbations were compared with the nominal trajectories over the first 0.6 seconds of the flight. This time corresponds to a separation distance between the rocket and the aircraft of almost 100 feet. Except for the case of an initial pitch rate of  $10^{\circ}$ /second, the perturbations used in the trajectories were several times as large as the calculated  $1\sigma$  perturbations. Despite this, the separations of the perturbed trajectories from the nominals were always well within 2 feet, and usually substantially less. Thus, it was apparent that these perturbations presented no problem of launch aircraft safety. It should be mentioned that the trajectory with a  $10^{\circ}$ /second initial pitch rate remained within about 1/2 foot of the nominal, so that an initial rate several times as large as the conservative  $13.7^{\circ}$ /second estimated for the  $1\sigma$  tipoff would not present a hazard.

The more detailed portion of the aircraft safety evaluation involved the calculation of the trajectory of the rocket in the presence of the flow field of the launch aircraft. The equations of motion defining this trajectory are developed in Section 7.2. These equations were numerically integrated for all three launch velocities (200, 440, 600 knots) and followed the rocket to a point about 50 feet ahead of the nose of the launch aircraft. Besides the three nominal trajectories, one trajectory was computed with a  $3\sigma$  low thrust (about 75% of nominal thrust) and a 440 knot launch velocity.

UNCLASSIFIED

## UNCLASSIFIED

Report AFRPL-TR-69-90, Appendix A

### 5.4.1 INPUT PARAMETERS

The required input to allow the integration of the equations of motion defining the aircraft safety trajectories may be divided into two parts: those parameters defining the rocket itself, and those defining the flow field of the launch aircraft.

#### 5.4.1.1 ROCKET CHARACTERISTICS

The axial velocity history of the rocket is taken directly from the 6-D nominal trajectories and the vehicle is assumed not to roll. Thus, only the side and normal forces and the pitching and yawing moments on the rocket need be defined. The aerodynamic terms which are necessary to define these are the normal force coefficient, the pitch damping coefficient and the center of pressure. All of these are functions of Mach Number and were taken directly from the 6-D trajectory input. The inertial and geometric description of the vehicle is also identical to the 6-D input. These data include the diameter, reference area, weight, pitch moment of inertia, and center of gravity location.

#### 5.4.1.2 LAUNCH AIRCRAFT FLOW FIELD

Reference 9 gives the estimated induced aerodynamic coefficients acting on a typical anti-tank rocket due to the flow field of an F-4C/D aircraft. The reference indicates that these data are considered applicable to the present study. The airplane diagram included with the reference gives the carrying position of the rocket c.g. as:

Fuselage Station 265 inches (positive aft of Station 0.0, where the aircraft nose tip is F.S. -27.1)

Water Line -26 inches to -35 inches, where the underside of the fuselage is W.L.O.

Lateral Position: 81.5 inches outboard of the centerline.

A mean W.L. of -30.5 was assumed for the trajectories. The rocket free-flight was assumed to commence when the tips of the fins cleared the launcher, i.e., when it had travelled its own length.

UNCLASSIFIED



## UNCLASSIFIED

Report AFRPL-TR-69-90, Appendix A

The induced aerodynamic coefficients taken from the reference and employed in the range safety trajectories were the normal force ( $C_{N_I}$ ), pitching moment ( $C_{m_I}$ ), side force ( $C_{Y_I}$ ) and yawing moment ( $C_{n_I}$ ) coefficients. These coefficients are presented in the reference as a function of distance ahead of the rocket carrying position for aircraft Mach Numbers of 0.6, 0.9, and 0.96. A second order fit, of each of the coefficients, was made with Mach Number to provide data at the three launch velocities considered.

### 5.4.2 RESULTS

It was found that for none of the cases considered did the rocket deviate from the flight line at launch by more than a foot before it had passed the nose of the aircraft. At all launch velocities, and with both the nominal and the 3 $\sigma$  low thrust, the rocket dropped away from the aircraft in the vertical plane. The lateral motion was outboard for the 200 knot launch and inboard for the others. Figures 32 through 34 depict the translational position of the vehicle as a function of distance forward of the aircraft Fuselage Station 0.0. Comparing the lateral tracks at the different launch velocities, it is apparent that the aiming point of the rocket will vary appreciably with launch velocity.

Figures 35 through 37 present the angular orientations calculated for the four cases. It may be seen that the greatest angular deflections are exhibited by the case with a 200 knot launch velocity. The rocket in this instance showed a maximum pitch up angle of 2.7° and a maximum outboard yaw angle of 3.25°.

Although the rocket launched at 200 knots showed the greatest flight path perturbations due to the aircraft flow field, the 440 knot launch case was considered the most critical of the nominal cases since it exhibited the largest inboard deflection. Thus, this launch velocity was chosen to test the effect of a 3 $\sigma$  low thrust curve. The flight path with the low thrust is compared with the flight path with the nominal thrust on Figure 33. The angular displacements are

UNCLASSIFIED

# UNCLASSIFIED

Report AFRPL-TR-69-90, Appendix A

compared on Figure 36. It may be seen that the change in flight path due to the approximately 25% low thrust is minimal, with the lateral deflection of the rocket toward the launch aircraft only increasing by about 0.1 feet up to the time when the rocket passes ahead of the nose of the launch aircraft.

It may be concluded that there is no possibility of the Improved 2.75 FFAR contacting the launch aircraft after launch due to the combined effect of the launch aircraft flow field and realizable vehicle anomalies (discussed in Section 5.4). This, of course, presumes that the flow field of any launch aircraft used is substantially similar to the flow field of the F4C aircraft, as given in Reference 9.

UNCLASSIFIED

# UNCLASSIFIED

Report AFRPL-TR-69-90, Appendix A

## 6.0 REFERENCES

1. Air Force Contract No. FO4611-67-C-0114; "Development and Demonstration of an Improved Rocket for the Flechette Warhead"; 2 June 1967.
2. W.M. Hadaway, "Accuracy Comparison of Modified and Unmodified 2.75-inch (FFAR) Rockets Fired From an Airborne Armed Chinook Helicopter"; Report No. RD-TR-66-19; U.S. Army Missile Command, Redstone Arsenal, Alabama; July 1966.
3. J.L. Childers, "Improved 2.75-inch FFAR Program"; Report No. RT-TM-65-60; U.S. Army Missile Command, Redstone Arsenal, Alabama; December 1965.
4. J.R. Scoggins; "Preliminary Study of Atmospheric Turbulence Above Cape Canaveral, Florida"; MTP-AERO-63-10; George C. Marshall Space Flight Center; 1 February 1963.
5. P.A. Sollow; "Six-Degree-of-Freedom Trajectory Program Users' Manual"; Report No. 1042-RI; Space-General Corporation, El Monte, Calif; Dec. 1966.
6. "U.S. Standard Atmosphere, 1962; U.S. Government Printing Office, Washington, D.C.; December 1962.
7. P.A. Sollow; "Computer Applications to Wind Weighting and Their Limitations"; Preprint of Paper to be Presented at the Unguided Rocket Ballistics Meteorology Conference; 31 October - 2 November 1967, New Mexico State University.
8. W.M. Hadaway, I.H. Shokes; "2.75-inch Rocket (FFAR) Accuracy Improvement Study"; U.S. Army Missile Command, Redstone Arsenal, Alabama, Report No. RD-TR-66-2; January 1966.
9. L.W. Rucker, "Aircraft Flow Field Data, Contract FO4611-67-C-0114"; Letter to Tom Bowden, Aerojet-General Corp.; 10 July, 1967; Dept. of the Air Force, Headquarters, Air Force Flight Test Center, Edwards Air Force Base; Ref. FTMKR-1 (L.W. Rucker/277-2610).

UNCLASSIFIED

# UNCLASSIFIED

Report AFRPL-TR-69-90, Appendix A

## 7.0 APPENDICES

The following appendices contain the mathematical development necessary to evaluate the effects of roll program variability on dispersion (Section 7.1) and the development of the equations of motion for the aircraft safety analysis (Section 7.2). These analyses are separated from the Analysis and Discussion of Results (Section 5.0) to avoid unnecessarily cluttering that section with detailed mathematical derivations.

UNCLASSIFIED

# UNCLASSIFIED

Report AFRPL-TR-69-90, Appendix A

## 7.1 THE EFFECT OF ROLL PROGRAM DISPERSION ON THE BURST POINT DISPERSIONS

### 7.1.1 DERIVATION OF EQUATIONS

Denoting the various dispersion producing perturbations (thrust misalignments, fin misalignments, winds, aiming errors, etc.) by  $y_n$ ,  $n = 1, 2, \dots$ , and the dispersions due to individual unit values of the  $y_n$ 's by  $a_n$ , we assume the dispersion,  $x$ , to be a linear function of the perturbations and write

$$x = \sum_{n=1}^N a_n y_n. \quad 7.1-1$$

In the normal dispersion problem, the  $y_n$ 's are all taken to be linearly independent and the  $a_n$ 's are constants. Then the variance of  $x$  is found simply as

$$\sigma_x^2 = \sum_{n=1}^N a_n^2 \sigma_{y_n}^2.$$

In the present instance, however, two of the  $a_n$ 's (those pertaining to dispersion due to thrust and fin misalignments) are dependent on two additional statistical variables, the random portions of the roll-producing parts of the nozzle and fin misalignments. Selecting  $a_1$  and  $a_2$  to be the affected coefficients and the additional variables denoted  $w$  and  $z$ , we have

$$x = a_1(w, z) y_1 + a_2(w, z) y_2 + \sum_{n=3}^N a_n y_n \quad 7.1-2$$

and

$$\sigma_x^2 = \langle a_1^2(w, z) y_1^2 + a_2^2(w, z) y_2^2 \rangle + \sum_{n=3}^N a_n^2 \sigma_{y_n}^2 \quad 7.1-3$$

where the notation  $\langle \rangle$  indicates an ensemble average over many vehicles.

Letting  $p_{a_n, y_n}(\alpha, \beta)$  be the joint probability density function of  $a_n$  and  $y_n$ , then

$$\langle a_n^2 y_n^2 \rangle = \int_{-\infty}^{\infty} \int_{-\infty}^{\infty} \alpha^2 \beta^2 p_{a_n, y_n}(\alpha, \beta) d\alpha d\beta \quad 7.1-4$$

# UNCLASSIFIED

Report AFRPL-TR-69-90, Appendix A

Now  $p_{a_n, y_n}$  is the joint density function as affected by all variations.

Let  $p_{a_n, y_n | w, z}(\alpha, \beta | \gamma, \zeta)$  be the corresponding conditional density function, i.e., the joint probability density function which would result if  $w$  and  $z$  were held fixed at the values  $\gamma$  and  $\zeta$ , respectively. Then,

$$p_{a_n, y_n}(\alpha, \beta) = \int_{-\infty}^{\infty} \int_{-\infty}^{\infty} p_{a_n, y_n | w, z}(\alpha, \beta | \gamma, \zeta) p_w(\gamma) p_z(\zeta) d\gamma d\zeta \quad 7.1-5$$

where  $p_w$  and  $p_z$  are the density functions for  $w$  and  $z$  and where we have assumed  $w$  and  $z$  to be statistically independent. Furthermore, with  $w$  and  $z$  fixed,  $a_n(w, z)$  is not random at all but has a specific value. Therefore

$$\begin{aligned} p_{a_n, y_n | w, z}(\alpha, \beta | \gamma, \zeta) &= p_{a_n | w, z}(\alpha | \gamma, \zeta) p_{y_n | w, z}(\beta | \gamma, \zeta) \\ &= \delta(f_n(\gamma, \zeta) - \alpha) p_{y_n | w, z}(\beta | \gamma, \zeta) \end{aligned} \quad 7.1-6$$

where  $\delta$  is the Dirac delta function and we have used  $f_n(\gamma, \zeta)$  to denote  $a_n$  evaluated at  $w = \gamma$  and  $z = \zeta$ . Inserting (7.1-6) into (7.1-5) and the result into (7.1-4) yields

$$\langle a_n^2 y_n^2 \rangle = \int_{-\infty}^{\infty} \int_{-\infty}^{\infty} \alpha^2 \beta^2 \int_{-\infty}^{\infty} \int_{-\infty}^{\infty} \delta(f_n(\gamma, \zeta) - \alpha) p_{y_n | w, z}(\beta | \gamma, \zeta) p_w(\gamma) p_z(\zeta) d\gamma d\zeta \quad 7.1-7$$

Carrying out the integration over  $\alpha$ ,

$$\begin{aligned} \langle a_n^2 y_n^2 \rangle &= \int_{-\infty}^{\infty} \beta^2 d\beta \int_{-\infty}^{\infty} p_w(\gamma) d\gamma \int_{-\infty}^{\infty} f_n^2(\gamma, \zeta) p_{y_n | w, z}(\beta | \gamma, \zeta) p_z(\zeta) d\zeta \\ &= \int_{-\infty}^{\infty} p_w(\gamma) d\gamma \int_{-\infty}^{\infty} f_n^2(\gamma, \zeta) y_{y_n}(\gamma, \zeta) p_z(\zeta) d\zeta \end{aligned} \quad 7.1-8$$

UNCLASSIFIED

# UNCLASSIFIED

Report AFRPL-TR-69-90, Appendix A

where  $V_{y_n}(\gamma, \zeta)$  is the variance that  $y_n$  would have if  $w$  and  $z$  were fixed at  $\gamma$  and  $\zeta$ .

Substituting (7.1-8) into (7.1-3)

$$\begin{aligned} \sigma_x^2 = & \int_{-\infty}^{\infty} p_w(\gamma) d\gamma \int_{-\infty}^{\infty} p_z(\zeta) [r^2(\gamma, \zeta) V_{y_1}(\gamma, \zeta) \\ & + r_2^2(\gamma, \zeta) V_{y_2}(\gamma, \zeta)] d\zeta \\ & + \sum_{n=3}^N a_n^2 \sigma_{y_n}^2 \end{aligned}$$

or

$$\sigma_x^2 = \int_{-\infty}^{\infty} p_w(\gamma) d\gamma \int_{-\infty}^{\infty} p_z(\zeta) V_x(\gamma, \zeta) d\zeta + \sum_{n=3}^N a_n^2 \sigma_{y_n}^2 \quad 7.1-9$$

where  $V_x(\gamma, \zeta)$  is the variance that would result in  $x$  due to  $y_1$  and  $y_2$  if the roll program were fixed by setting  $w = \gamma$  and  $z = \zeta$ . Eqn. (7.1-9) shows that we may compute dispersions in the usual way for different values of nozzle and fin cant and then combine the results by integrating over the probabilities of having those values.  $V_x(\gamma, \zeta)$  is evaluated by means of six-degree-of-freedom computer runs.

This does not, however, provide a completely satisfactory solution to our problem since a prohibitive number of runs would be required to evaluate  $V_x(\gamma, \zeta)$  over even the area of appreciable dispersion. Also, the infinite limits on the integrals in Equation (7.1-9) could leave considerable question about the utility of normal numerical integration schemes. In the next section we therefore seek an analytical form for  $V_x$  to seek to circumvent some of these problems.

UNCLASSIFIED

# UNCLASSIFIED

Report AFRPL-TR-69-90, Appendix A

## 7.1.2 DETERMINATION OF $V_x(\gamma, \zeta)$

In order to utilize computer runs for the determination of  $V_x(\gamma, \zeta)$ , it is necessary to assume some functional form to permit evaluation of the integrals in Eqn. (7.1-9). In order to simplify the problem of choosing an appropriate function, we first restrict attention to the single variable case,  $V_x(0, \zeta)$ . To begin with, it is known from past experience and from the results of preliminary analyses under this study, that  $V_x(0, \zeta)$  is symmetrical with respect to  $\zeta = 0$ , is monotonic decreasing with increasing  $|\zeta|$ ,\* and is asymptotic to zero for large  $|\zeta|$ . Therefore it is natural to attempt to fit  $V_x(0, \zeta)$  with exponential functions such as

$$(a + b \zeta) e^{-c \zeta^2}$$

or

$$\frac{a}{1 + b \zeta} e^{-c \zeta^2}$$

or

$$a e^{-b(\zeta^2 + c \zeta^4)}$$

All these forms were tried, but the results were deemed unsatisfactory due to resultant negative values at high  $\zeta$  or to divergently large results at large  $\zeta$ . A more suitable form was found to be

$$V_x(0, \zeta) \approx \frac{k_o^2 \sigma_z^2}{[1 + k_1 \zeta^2]^{2n}} \quad 7.1-10$$

or

$$a_n(0, \zeta) \approx \frac{k_o}{[1 + k_1 \zeta^2]^n} \quad 7.1-11$$

where  $k_o$ ,  $k_1$  and  $n$  are determined to match the data.

\* It should be noted here that no "bump" in the  $V_x(0, \zeta)$  curve was found when roll-yaw resonance was encountered late in the  $x$  flight. There may be such a bump for roll-yaw resonance very early in the flight, but this is at such a low probability level that results would not be significantly affected.



# UNCLASSIFIED

Report AFRPL-TR-69-90, Appendix A

At each of the launch velocities of interest, computer runs were made to evaluate  $a_n(0, \zeta)$  at  $\zeta = 0, 0.05, 0.11$  (where  $\zeta$  here represents differential fin cant in degrees). The results are shown for the case of dispersion due to a  $1^\circ$  thrust misalignment in Table 7.1-1, below. Also shown are the results for combinations of  $\zeta = 0.11$  and  $\gamma = \pm 0.127$  ( $\gamma$  is differential nozzle cant in degrees). The function (7.1-11) was fitted to these data as follows.

$$k_0 = a_n(0,0) \quad 7.1-12$$

$n$  was determined by trial and error from

$$\zeta_2^2 \left( \frac{a_n(0,0)}{a_n(0,\zeta_1)} \right)^{1/n} - \zeta_1^2 \left( \frac{a_n(0,0)}{a_n(0,\zeta_2)} \right)^{1/n} = \zeta_2^2 - \zeta_1^2 \quad 7.1-13$$

where  $\zeta_1$  and  $\zeta_2$  are any two values for which data are available.  $n$  is given to a good approximation (for  $1/n$  large) by

$$\frac{1}{n} \approx \frac{2 \ln \left( \frac{\zeta_1}{\zeta_2} \right)}{\ln \left( \frac{a_n(0,\zeta_2)}{a_n(0,\zeta_1)} \right)} \quad 7.1-14$$

and this was used for an initial guess. Finally,  $k_1$  is found as

$$k_1 = \frac{\left[ \frac{a_n(0,0)}{a_n(0,\zeta)} \right]^{1/n} - 1}{\zeta^2} \quad 7.1-15$$

for any  $\zeta$ .

Using Eqns. (7.1-12) through (7.1-15) and the data of Table 7.1-1, the results shown in Table 7.1-2, below, were obtained.

# UNCLASSIFIED

Report AFRPL-TR-69-90, Appendix A

Table 7.1-1  
DISPERSION DUE TO 1° THRUST MISALIGNMENT

Launch Velocity (m/s)	Differential Fin Cant (deg)	Differential Nozzle Cant (deg)	Dispersion (mils)
200	0	0	52.44
	0.05	0	31.34
	0.11	0	28.06
	0.11	0.127	24.22
	0.11	-0.127	32.02
440	0	0	27.34
	0.05	0	6.68
	0.11	0	4.74
	0.11	0.127	4.33
	0.11	-0.127	5.48
600	0	0	24.94
	0.05	0	4.42
	0.11	0	2.58
	0.11	0.127	2.42
	0.11	-0.127	3.12

UNCLASSIFIED

# UNCLASSIFIED

Report AFRPL-TR-69-90, Appendix A

Table 7.1-2

## RESULTS OF CURVE FITS

$$\epsilon_1(0, \epsilon) \approx \frac{k_0}{[1 + k_1 \epsilon^2]^n}$$

Launch Velocity (kn)	$k_0$ (mils/deg)	$k_1$ (deg <sup>-2</sup> )	n (--)
200	52.44	$4.51 \cdot 10^5$	0.0731
440	27.34	$2.60 \cdot 10^5$	0.217
600	24.94	$6.11 \cdot 10^4$	0.344

Applying the same techniques to the fin misalignment case, see Table 7.1-3, yields the results shown in Table 7.1-4.

Table 7.1-3

## DISPERSION DUE TO 1° FIN MISALIGNMENT

Launch Velocity (kn)	Differential Fin Cant (deg)	Differential Nozzle Cant (deg)	Dispersion (mils)
200	0	0	30.73
	0.05	0	10.17
	0.11	0	6.75
	0.11	0.127	5.20
	0.11	-0.127	9.51
440	0	0	29.75
	0.05	0	5.77
	0.11	0	3.41
	0.11	0.127	2.94
	0.11	-0.127	4.32
600	0	0	30.59
	0.05	0	4.94
	0.11	0	2.84
	0.11	0.127	2.32
	0.11	-0.127	3.48

UNCLASSIFIED

# UNCLASSIFIED

Report AFRPL-TR-69-90, Appendix A

Table 7.1-4

## RESULTS OF CURVE FITS

$$a_2(0, \zeta) \approx \frac{k_0}{[1 + k_1 \zeta^2]^n}$$

Launch Velocity (kn)	$k_0$ (mils/deg)	$k_1$ (deg <sup>-2</sup> )	$n$ (--)
200	30.73	$3.16 \cdot 10^4$	0.252
440	29.75	$5.24 \cdot 10^4$	0.336
600	30.59	$7.12 \cdot 10^4$	0.351

Returning to the problem of fitting curves to the two-variable functions  $a_n(\gamma, \zeta)$ , it is immediately apparent that to make a truly general fit to the functions, it would be necessary to assume a form such as

$$a_n(\gamma, \zeta) \approx \frac{k_0(\gamma)}{[1 + k_1(\gamma) \{\zeta - \zeta_0(\gamma)\}^2]^{n(\gamma)}}$$

where  $k_0$ ,  $k_1$ ,  $\zeta_0$ , and  $n$  are all functions of  $\gamma$ . Each of these parameters would then have to be curve-fitted as functions of  $\gamma$ . It is apparent that a prohibitive amount of work is involved including a large matrix of six-degree-of-freedom runs. Even after this effort, the assumed functional forms might be found unsatisfactory. Also, use of such results in Eqn. (7.1-9) would certainly present an almost insurmountable problem in properly evaluating the required improper integrals.

Therefore, instead of attacking this general problem, we attempt a more restricted extension of Eqn. (7.1-11) and seek checks on the adequacy of the assumed form. Noting that in most dispersion problems of this type, the important parameter is reducible to the number of turns about the roll axis

UNCLASSIFIED

# UNCLASSIFIED

Report AFRPL-TR-69-90, Appendix A

in some initial period of time or initial portion of flight path length, it seems reasonable to inquire whether or not there exists some equivalence between thrust cant and nozzle cant angles. It is immediately clear that this would rigorously be the case if both means of inducing spin produced spin histories of the same shape. Since this is not the case, we make the assumption that there is an equivalence and that we may therefore write

$$a_n(\gamma, \zeta) \approx \frac{k_o}{[1 + k_1 (\zeta + k\gamma)^2]^n} \quad 7.1-16$$

where  $k$  is some equivalence factor to be determined.  $k_o$ ,  $k_1$  and  $n$  are to remain the same as shown in Tables 7.1-2 and 7.1-4.

It is clear that Eqn. (7.1-16) is valid for small  $k\gamma$ 's relative to  $\zeta$ 's so that, for  $q_w$  sufficiently small the assumption is adequate. We must, however, check the adequacy of this form in other cases. The equivalence factors,  $k$ , will, of course vary with flight velocity due to variations in the relative effectiveness of thrust and fin cant. Also, it is to be expected that the  $k$ 's will differ for response due to thrust misalignment and response due to fin misalignment since the temporal build-up of these responses are different and therefore changes in the initial rate of spin-up affect them differently.

The procedure employed here to arrive at satisfactory values of  $k$  is to compute, using the data of Tables 7.1-1 and 7.1-3,  $k$ 's satisfying the trajectory data for  $a_n(+0.127, 0.11)$  and  $a_n(-0.127, 0.11)$ , i.e., for one-sigma thrust cant variations about the nominal fin cant condition. If a single value of  $k$  can be found to satisfy the results for both  $\gamma = 0.127$  and  $-0.127$ , within reasonable accuracy, then the fit is considered satisfactory. Tables 7.1-5 and 7.1-6 present the results of such computations. Shown here are the  $k$ 's obtained and comparisons of the values computed from Eqn. 7.1-16 using these  $k$ 's with the actual values from Tables 7.1-1 and 7.1-3.

UNCLASSIFIED

# UNCLASSIFIED

Report AFRPL-TR-69-90, Appendix A

Table 7.1-5

RESULTS OF EQUIVALENCE COEFFICIENT FITS

$$a_1(\gamma, \zeta) = \frac{k_o}{[1 + k_1(\zeta + k\gamma)^2]^n}$$

Launch Velocity (kn)	k (--)	$a_1(.127, .11)$ (mils/deg)			$a_1(-.127, .11)$ (mils/deg)		
		Table 7.1-1	Computed	% Error	Table 7.1-1	Computed	% Error
200	1.324	24.22	24.40	0.74	32.02	31.58	-1.37
440	.2125	4.38	4.34	-0.92	5.48	5.38	-1.82
600	0.149	2.42	2.30	-4.96	3.12	2.92	-6.40

Table 7.1-6

RESULTS OF EQUIVALENCE COEFFICIENT FITS

$$a_2(\gamma, \zeta) = \frac{k_o}{[1 + k_1(\zeta + k\gamma)^2]^n}$$

Launch Velocity (kn)	k (--)	$a_2(.127, .11)$ (mils/deg)			$a_2(-.127, .11)$ (mils/deg)		
		Table 7.1-3	Computed	% Error	Table 7.1-3	Computed	% Error
200	0.525	5.20	5.43	4.43	9.51	10.92	14.8
440	0.2355	2.94	2.90	-1.36	4.32	4.24	-1.85
600	0.253	2.32	2.39	3.02	3.48	3.56	2.30

UNCLASSIFIED

## UNCLASSIFIED

Report AFRPL-TR-69-90, Appendix A

From Table 7.1-5, it is noted that good fits (less than 6.5% errors) are obtained to the dispersion due to thrust misalignment for all cases. Furthermore, these errors are largest at the higher launch velocities where dispersions due to thrust misalignments are less important. It should also be noted that a good fit was obtained even for the 200 kn case where the thrust cant effect is so large as to effectively reverse the direction of the roll rate for  $\gamma = -.127^\circ$ , i.e.,  $\zeta -.127 \text{ k} < 0$ .

Examination of Table 7.1-6 reveals that the assumed form (Eqn. 7.1-16) is less successful in dealing with the dispersion due to fin misalignments since an error of 14.8% is obtained at  $\gamma = -.127^\circ$ ,  $\zeta = .11^\circ$  for a 200 kn. launch. For other cases, the fit was again quite good. For the 200 kn. launch velocity where the fit is worst, the dispersions due to thrust misalignment is considerably larger than that due to fin misalignment. Therefore, when these components are root-sum-squared, the errors in the fit to the fin misalignment portion will not be particularly important. It is therefore concluded that the fits obtained are adequate for our purpose.

UNCLASSIFIED

# UNCLASSIFIED

Report AFRPL-TR-69-90, Appendix A

## 7.1.3 EVALUATION OF DISPERSIONS

Returning to Eqn. 7.1-9 and using Eqn. 7.1-16 for  $V_x = a_n^2 \sigma_{y_n}^2$ , we must evaluate

$$\langle a_n^2 y_n^2 \rangle = k_o^2 \sigma_{y_n}^2 \int_{-\infty}^{\infty} \int_{-\infty}^{\infty} \frac{p_w(\gamma) p_z(\zeta) d\gamma d\zeta}{[1 + k_1 (\zeta + k\gamma)^2]^{2n}} \quad 7.1-17$$

i.e., we must obtain the mean value of the function  $k_o^2 \sigma_{y_n}^2 [1 + k_1 (\zeta + k\gamma)^2]^{-2n}$  given the probability density functions  $p_w(\gamma)$  and  $p_z(\zeta)$ . It was elected to evaluate this integral by Monte Carlo methods rather than direct numerical integration. Regardless of the technique employed, however, it is first necessary to select functional form for  $p_w(\gamma)$  and  $p_z(\zeta)$ .

Inasmuch as the integral in Eqn. 7.1-17 will not be evaluated analytically, there is no longer any particular advantage to choosing normal distributions. Instead we choose distributions which should give more reasonable probabilities for the larger excursions. Recalling (c.f., Section 5.0) that we have consistently and reasonably chosen  $1\sigma$  levels as being one-half of the maximum allowable manufacturing tolerance, we select probability density functions to conform to this assumption. To choose a simple functional form, set

$$p(x-\bar{x}) = c_1 - c_2 x^2, \quad |x| \leq 2\sigma$$

$$= 0, \quad |x| > 2\sigma$$

and require that the integral from  $-2\sigma$  to  $2\sigma$  be unity, i.e., require that  $-1\sigma \leq x \leq 1\sigma$  always. We also require that the variance be

$$\sigma^2 = \int_{-2\sigma}^{2\sigma} p(x) x^2 dx$$

These two conditions are sufficient to evaluate the constants  $c_1$  and  $c_2$  and we obtain



# UNCLASSIFIED

Report AFRPL-TR-69-90, Appendix A

$$p_w(\gamma) = \frac{3}{64\sigma_w} \left[ 7 - \frac{5}{4} \left( \frac{\gamma}{\sigma_w} \right)^2 \right] \quad 7.1-18$$

and

$$p_z(\zeta) = \frac{3}{64\sigma_w} \left[ 7 - \frac{5}{4} \left( \frac{\zeta - \bar{z}}{\sigma_z} \right)^2 \right] \quad 7.1-19$$

where we have selected  $\bar{w}$ , the mean effective nozzle cant angle to be zero.  $\bar{z}$ , of course represents the nominal fin cant. As a matter of interest, the above density functions have values at the  $2\sigma$  limits of 0.348 times the values at nominal, which again appears reasonable and, perhaps, somewhat conservative. In order to apply Monte Carlo techniques, it is necessary to obtain the cumulative frequency functions,

$$P(x) = \int_{-2\sigma}^x p(x) dx$$

and then invert this function to obtain  $x$  in terms of  $P$ . Integrating Eqn. 7.1-18 gives

$$P_w(\gamma) = \frac{21}{64} \left( \frac{\gamma}{\sigma_w} + 2 \right) - \frac{5}{256} \left[ \left( \frac{\gamma}{\sigma_w} \right)^3 + 8 \right]$$

This expression was inverted approximately by means of the curve fit

$$\frac{\gamma}{\sigma_w} \approx b_1(P_w - .5) + b_2(P_w - .5)^3,$$

which has the proper symmetry conditions.  $b_1$  was selected to match the slope in the large linear central region around  $\gamma = 0$  and  $b_2$  was selected to attain  $\gamma = \pm 2\sigma_w$  for  $P_w = 0, 1$ . The result is

$$\frac{\gamma}{\sigma_w} \approx 3.05 (P_w - .5) + 3.80 (P_w - .5)^3 \quad 7.1-20$$

Likewise

$$\frac{\zeta - \bar{z}}{\sigma_w} \approx 3.05 (P_z - .5) + 3.80 (P_z - .5)^3 \quad 7.1-21$$

UNCLASSIFIED

# UNCLASSIFIED

Report AFRPL-TR-69-90, Appendix A

The function, Eqn. 7.1-17, was evaluated by randomly selecting two numbers,  $P_w$  and  $P_z$ , on flat distributions between 0 and 1, obtaining  $\gamma$  and  $\zeta$  from Eqns. 7.1-20 and 7.1-21, and computing

$$\frac{k_o^2 \sigma_{y_n}^2}{[1 + k_1(\zeta + k\gamma)^2]^{2n}}$$

using these values. The average value obtained after a sufficient number of trials is the desired value of the integral, Eqn. 7.1-17. Using the  $k_o$ ,  $k_1$  and  $k$  values from Section 7.1.2 and the  $\sigma_{y_n}$  values appropriate to thrust misalignment and fin misalignments (for  $n = 1$  and 2, respectively) as  $0.192^\circ$  and  $0.141^\circ$  (see Section 5.1), the following table is obtained.

Table 7.1-7

RESULTANT  $1\sigma$  DISPERSIONS DUE TO  
THRUST AND FIN MISALIGNMENTS

Launch Velocity (kn)	$\sqrt{\langle a_1^2 y_1^2 \rangle}$ (mils)	$a_{1 \text{ nom}} \sigma_{y_1}$ (mils)	$\sqrt{\langle a_2^2 y_2^2 \rangle}$ (mils)	$a_{2 \text{ nom}} \sigma_{y_2}$ (mils)
200	5.39	5.39	2.45	0.95
400	1.25	0.91	0.39	0.42
600	0.70	0.50	0.30	0.40

The above table was computed using a relatively small number of samples (35) but, since it is only the average values of the integral that are of interest (rather than the variance of the integral, etc.), the results should be sufficiently accurate for present purposes. This is particularly true of the first entry, the dispersion due to thrust misalignment for the 200 kn launch, due to the relatively slow variation of dispersion with roll rate (see Table 7.1-1). This is fortunate since this result is really the only one which is at all critical with respect to

# UNCLASSIFIED

Report AFRPL-TR-69-90, Appendix A

meeting the dispersion requirements. The accuracy of the computations of other values in the table is likely to be worse, but they are not so significant.

—Also shown in Table 7.1-7 are the dispersions which would have resulted if no nozzle or fin cant variation were allowed. For the dispersion due to thrust misalignment for the 200 kn launch, it is noted that the value is the same with or without nozzle and fin cant variations. This again is reasonable due to the relative insensitivity to roll rate in this case.

For the remaining cases, the peak dispersion (obtained for combinations of nozzle and fin cant resulting in near-zero roll rates early in the trajectory) is much higher than the nominal. Therefore the low dispersion contributions resulting from rolling faster than the nominal case do not compensate the averages nearly so well as for flatter distributions. For these cases, the ratio of actual dispersion to nominal dispersion varies from 1.4 to 2.6. This again appears reasonable as do the trends of the values in Table 7.1-7.

UNCLASSIFIED

# UNCLASSIFIED

Report AFRPL-TR-69-90, Appendix A

## 7.2 EQUATIONS OF MOTION FOR AIRCRAFT SAFETY ANALYSIS

We will define a right-handed coordinate system,  $x'$ ,  $y'$ ,  $z'$  which is fixed to the launch aircraft so that  $x'$  is forward,  $y'$  is to the right, and  $z'$  is down. The unit vectors in this system will be denoted  $i'$ ,  $j'$ ,  $k'$ . A second right-handed system,  $x$ ,  $y$ ,  $z$  will be fixed to the body of the rocket and will have unit vectors  $i$ ,  $j$ ,  $k$ . The two systems will be related by:

$$i = i' \cos a_1 + j' \cos b_1 + k' \cos c_1 \quad 7.2-1$$

$$j = i' \cos a_2 + j' \cos b_2 + k' \cos c_2 \quad 7.2-2$$

$$k = i' \cos a_3 + j' \cos b_3 + k' \cos c_3 \quad 7.2-3$$

The angular rate of the rocket is defined by:

$$\vec{\Omega} = ip + jq + kr \quad 7.2-4$$

in the  $x$ ,  $y$ ,  $z$  system, and

$$\vec{\Omega} = i'\omega_1 + j'\omega_2 + k'\omega_3 \quad 7.2-5$$

in the  $x'$ ,  $y'$ ,  $z'$  system. The  $x'$ ,  $y'$ ,  $z'$  system has been assumed irrotational, i.e., the launch aircraft flies a straight path and does not roll. The velocity of the rocket, relative to the ground, may be written as

$$\vec{V} = iu + jv + kw \quad 7.2-6$$

The launch aircraft has a velocity in the  $x'$  direction of  $iV_a$ . Thus, the velocity of the rocket in the  $x'$ ,  $y'$ ,  $z'$  system will be

$$\vec{V}' = \vec{V} - iV_a \quad 7.2-7$$

Assuming that the pitch and yaw moments of inertia of the rocket ( $I_y$  and  $I_z$ ) are equal, the angular momentum of the rocket is:

UNCLASSIFIED

# UNCLASSIFIED

Report AFRPL-TR-69-90, Appendix A

$$\vec{H} = i I_x \dot{p} + I(j\dot{q} + k\dot{r}) \quad 7.2-8$$

where  $I = I_y = I_z$ .

The equations of motion of the rocket are:

$$\frac{\vec{F}}{m} = \frac{d\vec{V}}{dt} = \dot{\vec{V}} + \vec{\Omega} \times \vec{V} \quad 7.2-9$$

and,

$$\vec{M} = \frac{d\vec{H}}{dt} = \dot{\vec{H}} + \vec{\Omega} \times \vec{H} \quad 7.2-10$$

differentiating yields:

$$\dot{\vec{V}} = i\dot{u} + j\dot{v} + k\dot{w} \quad 7.2-11$$

and,

$$\dot{\vec{H}} = i I_x \dot{\dot{p}} + I(j\dot{\dot{q}} + k\dot{\dot{r}}) + i p \dot{I}_x + \dot{I}(jq + kr) \quad 7.2-12$$

Combining Eqns. 7.2-4, 7.2-6, 7.2-9 and 7.2-11 yields:

$$\frac{\vec{F}}{m} = i\dot{u} + j\dot{v} + k\dot{w} + i(qw - vr) + j(ru - pw) + k(pv - qu) \quad 7.2-13$$

Combining Eqns. 7.2-4, 7.2-8, 7.2-10 and 7.2-12 yields:

$$\vec{M} = i I_x \dot{\dot{p}} + I(j\dot{\dot{q}} + k\dot{\dot{r}}) + i p \dot{I}_x + \dot{I}(jq + kr) + j p r (I_x - I) + k p q (I - I_x) \quad 7.2-14$$

It was determined, from 6-D trajectories, that the nominal flight path of the Improved 2.75 FFAR was not significantly affected by roll rates of the magnitude which will occur in the selected configuration. Thus, a non-rolling vehicle may be assumed. For the non-rolling vehicle,  $p = \dot{p} = 0$ , which allows simplification of Eqns. 7.2-13 and 7.2-14:

$$\frac{\vec{F}}{m} = i(\dot{u} + qw - vr) + j(\dot{v} + ru) + k(\dot{w} - qu) \quad 7.2-15$$

and

$$\vec{M} = j(I\dot{q} + \dot{I}q) + k(I\dot{r} + \dot{I}r) \quad 7.2-16$$

# UNCLASSIFIED

Report AFRPL-TR-69-90, Appendix A

Eqns. 7.2-6 and 7.2-7 may be combined, using the relationship of Eqns. 7.2-1, 7.2-2, 7.2-3, to yield

$$\dot{x}' = u \cos a_1 + v \cos a_2 + w \cos a_3 - V_a \quad 7.2-17$$

$$\dot{y}' = u \cos b_1 + v \cos b_2 + w \cos b_3 \quad 7.2-18$$

$$\dot{z}' = u \cos c_1 + v \cos c_2 + w \cos c_3 \quad 7.2-19$$

Similarly, Eqns. 7.2-4 and 7.2-5 may be combined to yield, for  $p = 0$ ,

$$\omega_1 = q \cos a_2 + r \cos a_3 \quad 7.2-20$$

$$\omega_2 = q \cos b_2 + r \cos b_3 \quad 7.2-21$$

$$\omega_3 = q \cos c_2 + r \cos c_3 \quad 7.2-22$$

For the small deflections of the x-axis of the body from the nominal flight path (i.e., small values of  $a_1$ ) which might be expected from any rocket adjudged satisfactory, the preceding six equations may be considerably simplified to:

$$\dot{x}' = u - V_a \quad 7.2-23$$

$$\dot{y}' = u \cos b_1 + v \quad 7.2-24$$

$$\dot{z}' = u \cos c_1 + w \quad 7.2-25$$

$$\omega_1 = 0 \quad 7.2-26$$

$$\omega_2 = q \quad 7.2-27$$

$$\omega_3 = r \quad 7.2-28$$

UNCLASSIFIED

# UNCLASSIFIED

Report AFRPL-TR-69-90, Appendix A

The variation with time of the variables  $\cos b_1$ ,  $\cos c_1$  may be determined from:

$$\vec{n} \cdot (j' \times i) = (j' \omega_2 + k' \omega_3) \cdot (-k' \cos a_1 + i' \cos c_1) = -\omega_3 \cos a_1 \quad 7.2-29$$

$$\dot{b}_1 = -\omega_3 \cos a_1 / \sin b_1 = -r \cos a_1 / \sin b_1 \quad 7.2-30$$

$$\frac{d}{dt} (\cos b_1) = -\dot{b}_1 \sin b_1 = r \cos a_1 \quad 7.2-31$$

$$\vec{n} \cdot (k' \times i) = (j' \omega_2 + k' \omega_3) \cdot (j \cos a_1 - i \cos b_1) = \omega_2 \cos a_1 \quad 7.2-32$$

$$\dot{c}_1 = \omega_2 \cos a_1 / \sin c_1 = q \cos a_1 / \sin c_1 \quad 7.2-33$$

$$\frac{d}{dt} (\cos c_1) = -\dot{c}_1 \sin c_1 = -q \cos a_1 \quad 7.2-34$$

The assumption of small values of  $a_1$  allow the simplification of Eqns. 7.2-31 and 7.2-34 to

$$\frac{d}{dt} (\cos b_1) = r \quad 7.2-35$$

$$\frac{d}{dt} (\cos c_1) = -q \quad 7.2-36$$

Since the rocket will be considered non-rolling, the  $i$ -component of the driving moment is unnecessary. Additionally,  $u$  is available as a function of time from the nominal 6-D trajectories, so the  $i$ -component of the driving force need not be considered. The remaining forces and moments are all aerodynamic in origin, with the exception of a gravity force in the  $+z$  direction. Inspection of the input data to the 6-D showed that the jet damping moments were insignificant in comparison to the aerodynamic damping moments. Since these jet damping moments conventionally include the  $\dot{I}q$  and  $\dot{I}r$  terms of Eqn. 7.2-16, it is consistent to rewrite that equation as:

$$\vec{M} = j I \dot{q} + k I \dot{r} \quad 7.2-37$$

# UNCLASSIFIED

Report AFRPL-TR-69-90, Appendix A

The induced aerodynamic force and moment coefficients given in Reference 9 are given in the airplane coordinate system, but since a non-rolling rocket will be assumed, they may be inserted directly in the x, y, z system. The force equation, including the induced forces due to aircraft flow field is:

$$\vec{F} = QS [j(C_{y_I} - C_{N_\alpha} v/u) - k(C_{N_I} + C_{N_\alpha} w/u)] + kmg \cos \theta \quad 7.2-38$$

$$\begin{aligned} \vec{M} = QS \{ & j[C_{m_I} d + C_{m_q} (\frac{qd}{2u})d - C_{N_\alpha} (w/u)(c.p.-c.g.)] + k[C_{n_I} d \\ & + C_{m_q} (\frac{rd}{2u})d + C_{N_\alpha} (v/u)(c.p.-c.g.)] \} \end{aligned} \quad 7.2-39$$

The dynamic pressure Q, may be evaluated as

$$Q \approx \frac{\rho}{2} u^2 \quad 7.2-40$$

The translational equations of motion, represented by Eqn. 7.2-15, may be simplified, since the i-component of the motion is defined by the 6-D output, to:

$$\frac{\vec{F}}{m} = j(\dot{v} + ru) + k(\dot{w} - qu) \quad 7.2-41$$

In summary, Eqns. 7.2-37 and 7.2-41 represent the basic equations of motion. Eqns. 7.2-38, 7.2-39, 7.2-40 are the forcing functions, the position of the rocket relative to the aircraft is defined by integrating  $\dot{x}'$ ,  $\dot{y}'$ ,  $\dot{z}'$ , which are defined in Eqns. 7.2-23, 7.2-24, 7.2-25, and the angular orientation is determined by integrating  $\omega_2$  and  $\omega_3$  which are identically q and r, respectively. The terms  $\cos b_1$  and  $\cos c_1$  are determined from integration of Eqns. 7.2-35 and 7.2-36.

UNCLASSIFIED



UNCLASSIFIED

Report AFRPL-TR-69-90, Appendix A

Table I  
CASE LIST OF SIX DEGREE OF FREEDOM TRAJECTORIES

Note: Roll Coeffs: A = Preliminary Rigid Body  
B = Final Rigid Body  
C = Final Aeroelastic

Case No.	Span	V <sub>o</sub> (kts)	Differ.		At Fin Opening (deg)	Thrust Misalgn. (deg)	Fin Misalgn. (deg)	Initial Pitch up Angle (deg)	Initial Pitch up Rate (deg/sec)	Wind from Right (fps)	Roll Coeff. Elastic (mils)	Aero (Rigid or Elastic)	Disper sion (mils)
			Differ. Fin Cant (deg)	Nozzle Cant (deg)									
1001	1	440	0	0	.029	0	0	0	0	0	A	R	-
1002	.7	440	0	0	.029	0	0	0	0	0	A	R	-
1003	.4	440	0	0	.029	0	0	0	0	0	A	R	-
1004	.7	440	0	0	.029	1/8	0	0	0	0	A	R	3.12
1005	.7	440	0	1.0	.029	1/8	0	0	0	0	A	R	0.52
1006	.7	440	0	2.0	.029	1/8	0	0	0	0	A	R	0.64
1007	.7	440	0	2.0	.029	0	0	0	0	0	A	R	0.18
1008	1	440	0	0	.029	1/8	0	0	0	0	A	R	2.20
1009	1	440	0	1.0	.029	1/8	0	0	0	0	A	R	0.54
1010	1	440	0	2.0	.029	1/8	0	0	0	0	A	R	0.48
1011	.4	440	0	0	.029	1/8	0	0	0	0	A	R	6.43
1012	.4	440	0	1.0	.029	1/8	0	0	0	0	A	R	0.74
1013	.4	440	0	2.0	.029	1/8	0	0	0	0	A	R	0.78
1014	.7	440	0	0	.029	0	0	0	0	10	A	R	6.64
1015	.7	440	0	0	.029	0	0	1	0	0	A	R	0.74
1016	.7	440	0	0	.029	0	1/4	0	0	0	A	R	5.34
1017	.7	440	0	1.0	.029	0	1/4	0	0	0	A	R	0.29
1018	.7	440	0	2.0	.029	0	1/4	0	0	0	A	R	0.22
1019	.4	440	0	0	.029	0	0	0	0	10	A	R	6.30
1020	.4	440	0	0	.029	0	0	1	0	0	A	R	0.74
1021	.4	440	0	0	.029	0	1/4	0	0	0	A	R	6.05
1022	.4	440	0	1.0	.029	0	1/4	0	0	0	A	R	0.26
1023	.4	440	0	2.0	.029	0	1/4	0	0	0	A	R	0.10
1024	1	440	0	0	.029	0	0	0	0	10	A	R	6.70
1025	1	440	0	0	.029	0	0	1	0	0	A	R	0.55
1026	1	440	0	0	.029	0	1/4	0	0	0	A	R	4.96
1027	1	440	0	1.0	.029	0	1/4	0	0	0	A	R	0.61
1028	1	440	0	2.0	.029	0	1/4	0	0	0	A	R	0.03
1029	.7	440	0	0	.029	0	0	0	10	0	A	R	0.55
1030	.4	440	0	0	.029	0	0	0	10	0	A	R	0.74

UNCLASSIFIED

UNCLASSIFIED

Report AFRPL-TR-69-90, Appendix A

Table I - continued

Case No.	Span	V <sub>0</sub> (kt.)	Differ. Fin Cent (deg)	Differ. Poz L. Cent (deg)	Δ fin Opening (deg)	Thrust Misalign. (deg)	Fin Misalign. (deg)	Initial Pitch up Angle (deg)	Initial Pitch up Rate (deg/sec)	Wind from Right (fps)	Roll Coeff. Elastic)	Aero (Rigid or Elastic)	Dispersion (mils)
1031	1	440	0	0	.029	0	0	0	10	0	A	R	0.36
1032	.7	440	0	1.0	.029	1/8	0	0	0	0	A	R	0.43
1033	.7	440	0	2.0	.029	1/8	0	0	0	0	A	R	0.27
1034	.7	440	0	2.0	.029	0	0	0	0	0	A	R	0.18
1035	1	440	0	1.0	.029	1/8	0	0	0	0	A	R	0.42
1036	1	440	0	2.0	.029	1/8	0	0	0	0	A	R	0.22
1037	.4	440	0	1.0	.029	1/8	0	0	0	0	A	R	0.66
1038	.4	440	0	2.0	.029	1/8	0	0	0	0	A	R	0.42
1039	1	440	0	0.5	.029	1/8	0	0	0	0	A	R	0.89
1040	.7	440	0	0.5	.029	1/8	0	0	0	0	A	R	0.60
1041	1	440	0	0.5	.029	0	1/4	0	0	0	A	R	1.18
1042	.7	440	0	0.5	.029	0	1/4	0	0	0	A	R	0.52
1043	1	440	.075	0	.029	1/8	0	0	0	0	A	R	0.88
1044	1	440	.15	0	.029	1/8	0	0	0	0	A	R	0.58
1045	1	440	2.25	0	.029	1/8	0	0	0	0	A	R	0.20
1046	1	440	.075	0	.029	1/8	0	0	0	0	A	R	0.59
1047	1	440	.15	0	.029	1/8	0	0	0	0	A	R	0.59
1048	1	440	2.25	0	.029	1/8	0	0	0	0	A	R	0.11
1049	1	440	.075	0	.029	1/8	0	0	0	0	A	R	0.85
1050	1	440	.15	0	.029	1/8	0	0	0	0	A	R	0.54
1051	1	440	2.25	0	.029	1/8	0	0	0	0	A	R	0.12
1052	1	440	.075	0	.029	1/8	0	0	0	0	A	R	0.73
1053	1	440	.15	0	.029	1/8	0	0	0	0	A	R	0.45
1054	1	440	2.25	0	.029	1/8	0	0	0	0	A	R	0.12
1055	1	440	.075	0	.029	0	1/4	0	0	0	A	R	1.62
1056	1	440	.15	0	.029	0	1/4	0	0	0	A	R	0.96
1057	1	440	2.25	0	.029	0	1/4	0	0	0	A	R	0.12
1058	1	440	.075	0	.029	0	1/4	0	0	0	A	R	1.64
1059	1	440	.15	0	.029	0	1/4	0	0	0	A	R	0.95
1060	1	440	2.25	0	.029	0	1/4	0	0	0	A	R	0.12
1061	1	440	.075	0	.029	0	1/4	0	0	0	A	R	1.52
1062	1	440	.15	0	.029	0	1/4	0	0	0	A	R	0.86
1063	1	440	2.25	0	.029	0	1/4	0	0	0	A	R	0.12
1064	1	440	.075	0	.029	0	1/4	0	0	0	A	R	1.27
1065	1	440	.150	0	.029	0	1/4	0	0	0	A	R	0.70
1066	1	440	2.25	0	.029	0	1/4	0	0	0	A	R	0.12

UNCLASSIFIED

UNCLASSIFIED

Report AFRPL-TR-69-90, Appendix A

Table I - continued

Case No.	Span	V <sub>o</sub> (kts)	Differ. Fin Cant (deg)	Differ. Nozzle Cant (deg)	Po (cps)	At Fin Opening (deg)	Thrust Misalign. (deg)	Fin Misalign. (deg)	Initial Pitch up Angle (deg)	Initial Pitch up Rate (deg/sec)	Wind from Right (fps)	Roll Coeff.	Aero (Rigid or Elastic)	Displacement (mils)
1067	.7	440	.075	0	0	.029	1/8	0	0	0	0	A	R	1.25
1068	.7	440	.15	0	0	.029	1/8	0	0	0	0	A	R	0.99
1069	.7	440	2.25	0	0	.029	1/8	0	0	0	0	A	R	0.41
1070	.7	440	.075	0	1.5	.029	1/8	0	0	0	0	A	R	1.02
1071	.7	440	.15	0	1.5	.029	1/8	0	0	0	0	A	R	0.87
1072	.7	440	2.25	0	1.5	.029	1/8	0	0	0	0	A	R	0.31
1073	.7	440	.075	0	3	.029	1/8	0	0	0	0	A	R	0.51
1074	.7	440	.15	0	3	.029	1/8	0	0	0	0	A	R	0.51
1075	.7	440	2.25	0	3	.029	1/8	0	0	0	0	A	R	0.32
1076	.7	440	.075	0	4.5	.029	1/8	0	0	0	0	A	R	0.04
1077	.7	440	.15	0	4.5	.029	1/8	0	0	0	0	A	R	0.28
1078	.7	440	2.25	0	4.5	.029	1/8	0	0	0	0	A	R	0.30
1079	.7	440	.075	0	0	.029	0	1/4	0	0	0	A	R	1.42
1080	.7	440	.15	0	0	.029	0	1/4	0	0	0	A	R	0.97
1081	.7	440	2.25	0	0	.029	0	1/4	0	0	0	A	R	0.26
1082	.7	440	.075	0	1.5	.029	0	1/4	0	0	0	A	R	1.17
1083	.7	440	.15	0	1.5	.029	0	1/4	0	0	0	A	R	0.74
1084	.7	440	2.25	0	1.5	.029	0	1/4	0	0	0	A	R	0.18
1085	.7	440	.075	0	3.0	.029	0	1/4	0	0	0	A	R	0.61
1086	.7	440	.15	0	3.0	.029	0	1/4	0	0	0	A	R	0.37
1087	.7	440	2.25	0	3.0	.029	0	1/4	0	0	0	A	R	0.19
1088	.7	440	.075	0	4.5	.029	0	1/4	0	0	0	A	R	0.36
1089	.7	440	.15	0	4.5	.029	0	1/4	0	0	0	A	R	0.19
1090	.7	440	2.25	0	4.5	.029	0	1/4	0	0	0	A	R	0.15
1091	1	440	0	0	1.5	.029	1/8	0	0	0	0	A	R	2.05
1092	1	440	0	0	3.0	.029	1/8	0	0	0	0	A	R	2.38
1093	1	440	0	0	4.5	.029	1/8	0	0	0	0	A	R	2.51
1094	1	440	0	0	1.5	.029	0	1/4	0	0	0	A	R	5.50
1095	1	440	0	0	3.0	.029	0	1/4	0	0	0	A	R	6.25
1096	1	440	0	0	4.5	.029	0	1/4	0	0	0	A	R	6.70
1097	.7	440	0	0	1.5	.029	1/8	0	0	0	0	A	R	3.63
1098	.7	440	0	0	3.0	.029	1/8	0	0	0	0	A	R	3.29
1099	.7	440	0	0	4.5	.029	1/8	0	0	0	0	A	R	2.20
1100	.7	440	0	0	1.5	.029	0	1/4	0	0	0	A	R	6.50
1101	.7	440	0	0	3.0	.029	0	1/4	0	0	0	A	R	6.10
1102	.7	440	0	0	4.5	.029	0	1/4	0	0	0	A	R	4.72
1103	1	440	-.75	0	1.5	.029	1/8	0	0	0	0	A	R	0.24

UNCLASSIFIED

UNCLASSIFIED

Report AFRPL-TR-69-90, Appendix A

Table I - continued

Case No.	Span	V <sub>o</sub> (kts)	Differ. Fin Cart (deg)	Differ. Nozzle Cart (deg)	P <sub>o</sub> (cps)	At Fin Opening	Thrust Misalign. (deg)	Fin Misalign. (deg)	Initial Pitch up Angle (deg)	Initial Pitch up Rate (deg/sec)	Wind from Right (fps)	Pol. Coeff.	Aero (Rigid or Elastic)	Dispersion (mils)
1104	1	440	-15	0	1.5	.029	1/8	0	0	0	0	A	R	0.65
1105	1	440	-75	0	3	.029	1/8	0	0	0	0	A	R	0.37
1106	1	440	-15	0	3	.029	1/8	0	0	0	0	A	R	0.56
1107	1	440	-75	0	4.5	.029	1/8	0	0	0	0	A	R	0.39
1108	1	440	-15	0	4.5	.029	1/8	0	0	0	0	A	R	0.57
1109	1	440	-75	0	1.5	.029	0	1/4	0	0	0	A	R	0.41
1110	1	440	-15	0	1.5	.029	0	1/4	0	0	0	A	R	0.83
1111	1	440	-75	0	3.0	.029	0	1/4	0	0	0	A	R	0.38
1112	1	440	-15	0	3.0	.029	0	1/4	0	0	0	A	R	0.75
1113	1	440	-75	0	4.5	.029	0	1/4	0	0	0	A	R	0.38
1114	1	440	-15	0	4.5	.029	0	1/4	0	0	0	A	R	0.83
1115	.7	440	-75	0	1.5	.029	1/8	0	0	0	0	A	R	0.56
1116	.7	440	-15	0	1.5	.029	1/8	0	0	0	0	A	R	1.10
1117	.7	440	-75	0	3.0	.029	1/8	0	0	0	0	A	R	0.61
1118	.7	440	-15	0	3.0	.029	1/8	0	0	0	0	A	R	1.20
1119	.7	440	-75	0	4.5	.029	1/8	0	0	0	0	A	R	0.83
1120	.7	440	-15	0	4.5	.029	1/8	0	0	0	0	A	R	1.38
1121	.7	440	-75	0	1.5	.029	0	1/4	0	0	0	A	R	0.40
1122	.7	440	-15	0	1.5	.029	0	1/4	0	0	0	A	R	0.93
1123	.7	440	-75	0	3.0	.029	0	1/4	0	0	0	A	R	0.58
1124	.7	440	-15	0	3.0	.029	0	1/4	0	0	0	A	R	1.33
1125	.7	440	-75	0	4.5	.029	0	1/4	0	0	0	A	R	0.64
1126	.7	440	-15	0	4.5	.029	0	1/4	0	0	0	A	R	1.57
1127	1	440	-075	0	1.5	.029	1/8	0	0	0	0	A	R	0.80
1128	1	440	-075	0	3.0	.029	1/8	0	0	0	0	A	R	0.75
1129	1	440	-075	0	4.5	.029	1/8	0	0	0	0	A	R	0.95
1130	1	440	-075	0	1.5	.029	0	1/4	0	0	0	A	R	1.40
1131	1	440	-075	0	3.0	.029	0	1/4	0	0	0	A	R	1.29
1132	1	440	-075	0	4.5	.029	0	1/4	0	0	0	A	R	1.53
1133	.7	440	-075	0	1.5	.029	1/8	0	0	0	0	A	R	1.30
1134	.7	440	-075	0	3.0	.029	1/8	0	0	0	0	A	R	1.68
1135	.7	440	-075	0	4.5	.029	1/8	0	0	0	0	A	R	1.67
1136	.7	440	-075	0	1.5	.029	0	1/4	0	0	0	A	R	1.47
1137	.7	440	-075	0	3.0	.029	0	1/4	0	0	0	A	R	1.86
1138	.7	440	-075	0	4.5	.029	0	1/4	0	0	0	A	R	2.07
1139	.7	440	0	0	3.0	.029	0	.1	0	0	0	A	E	1.67
1140	.7	440	-15	0	3.0	.029	0	.1	0	0	0	A	E	0.72

UNCLASSIFIED

UNCLASSIFIED

Report AFRPL-TR-69-90, Appendix A

Table I - continued

Case No.	Span	V (kts)	Differ. Fin Cant (deg)	Differ. Nozzle Cant (deg)	Po (cps)	At Fin Opening	Thrust Misalgn. (deg)	Fin Misalgn. (deg)	Initial Pitch up Angle (deg)	Initial Pitch up Rate (deg/sec)	Wind from Right (fps)	Roll Coeff.	Aero (Rigid or Elastic)	Disper- sion (mils)
1141	.7	440	.15	0	3.0	.029	0	.1	0	0	0	B	R	0.08
1142	1	200	0	0	0	.043	0	0	0	0	0	B	R	-
1143	1	200	0	0	0	.043	0	1	0	0	0	B	R	22.80
1144	1	200	.15	0	0	.043	0	1	0	0	0	B	R	6.22
1145	1	200	-.15	0	0	.043	0	1	0	0	0	B	R	6.22
1146	1	200	0	0	0	.043	1/2	0	0	0	0	B	R	19.80
1147	1	200	.15	0	0	.043	1/2	0	0	0	0	B	R	12.05
1148	1	200	-.15	0	0	.043	1/2	0	0	0	0	B	R	12.05
1149	1	200	0	0	3.0	.043	0	1	0	0	0	B	R	24.20
1150	1	200	-.15	0	3.0	.043	0	1	0	0	0	B	R	8.79
1151	1	200	.15	0	3.0	.043	0	1	0	0	0	B	R	2.42
1152	1	200	0	0	3.0	.043	1/2	0	0	0	0	B	R	20.30
1153	1	200	-.15	0	3.0	.043	1/2	0	0	0	0	B	R	15.60
1154	1	200	.15	0	3.0	.043	1/2	0	0	0	0	B	R	8.15
1155	1	600	0	0	0	.043	0	0	0	0	0	A	R	-
1156	1	200	.11	0	0	.054	0	0	0	0	0	C	E	-
1157	1	440	.11	0	0	.054	0	0	0	0	0	C	E	-
1158	1	600	.11	0	0	.054	0	0	0	0	0	C	E	-
1159	1	200	.11	0	0	.054	1/2	0	0	0	0	C	E	14.03
1160	1	200	.11	0	0	.054	0	1	0	0	0	C	E	6.75
1161	1	200	.11	0	0	.054	0	0	0	0	10	C	E	14.19
1162	1	200	.11	0	0	.054	0	0	1	0	0	C	E	1.93
1163	1	200	.11	0	0	.054	0	0	0	10	0	C	E	1.72
1164	1	440	.11	0	0	.054	1/2	0	0	0	0	C	E	2.37
1165	1	440	.11	0	0	.054	0	1	0	0	0	C	E	3.41
1166	1	440	.11	0	0	.054	0	0	0	0	10	C	E	6.26
1167	1	440	.11	0	0	.054	0	0	1	0	0	C	E	0.73
1168	1	440	.11	0	0	.054	0	0	0	10	0	C	E	0.37
1169	1	600	.11	0	0	.054	1/2	0	0	0	0	C	E	1.29
1170	1	600	.11	0	0	.054	0	1	0	0	0	C	E	2.84
1171	1	600	.11	0	0	.054	0	0	0	0	10	C	E	4.17
1172	1	500	.11	0	0	.054	0	0	1	0	0	C	E	0.66
1173	1	600	.11	0	0	.054	0	0	0	10	0	C	E	0.33
1174	1	200	0	0	0	.054	1/2	0	0	0	0	C	E	26.22
1175	1	200	0	0	0	.054	0	1	0	0	0	C	E	30.73
1176	1	200	.05	0	0	.054	1/2	0	0	0	0	C	E	15.67
1177	1	200	.05	0	0	.054	0	1	0	0	0	C	E	10.17

UNCLASSIFIED

Table I - continued

Case No.	Span	V <sub>o</sub> (kts)	Diff. Fin Cant (deg)	Diff. Nozzle Cant (deg)	Po (cps)	Δ Fin Opening	Thrust Misalign. (deg)	Pin Misalign. (deg)	Initial Pitch up Angle (deg)	Initial Pitch up Rate (deg/sec)	Wind from Right (fps)	Pol Coeff.	Aero (Rigid or Elastic)	Disper sion (mils)
1178	1	440	0	0	0	.054	1/2	0	0	0	0	C	E	13.67
1179	1	440	0	0	0	.054	0	1	0	0	0	C	E	29.75
1180	1	440	.05	0	0	.054	1/2	0	0	0	0	C	E	3.34
1181	1	440	.05	0	0	.054	0	1	0	0	0	C	E	5.77
1182	1	600	0	0	0	.054	1/2	0	0	0	0	C	E	12.47
1183	1	600	0	0	0	.054	1/2	1	0	0	0	C	E	30.59
1184	1	600	.05	0	0	.054	1/2	0	0	0	0	C	E	2.21
1185	1	600	.05	0	0	.054	0	1	0	0	0	C	E	4.94
1186	1	200	.11	+0.127	0	.054	1/2	0	0	0	0	C	E	12.11
1187	1	200	.11	-0.127	0	.054	1/2	0	0	0	0	C	E	16.01
1188	1	200	.11	+0.127	0	.054	0	1	0	0	0	C	E	5.20
1189	1	200	.11	-0.127	0	.054	0	1	0	0	0	C	E	9.51
1190	1	440	.11	+0.127	0	.054	1/2	0	0	0	0	C	E	2.19
1191	1	440	.11	-0.127	0	.054	1/2	0	0	0	0	C	E	2.74
1192	1	440	.11	+0.127	0	.054	0	1	0	0	0	C	E	2.94
1193	1	440	.11	-0.127	0	.054	0	1	0	0	0	C	E	4.32
1194	1	600	.11	+0.127	0	.054	1/2	0	0	0	0	C	E	1.21
1195	1	600	.11	-0.127	0	.054	1/2	0	0	0	0	C	E	1.56
1196	1	600	.11	+0.127	0	.054	0	1	0	0	0	C	E	2.32
1197	1	600	.11	-0.127	0	.054	0	1	0	0	0	C	E	3.48

UNCLASSIFIED

UNCLASSIFIED

Report AFRPL-TR-69-90, Appendix A

CONFIDENTIAL

Report AFRPL-TR-69-90, Appendix A

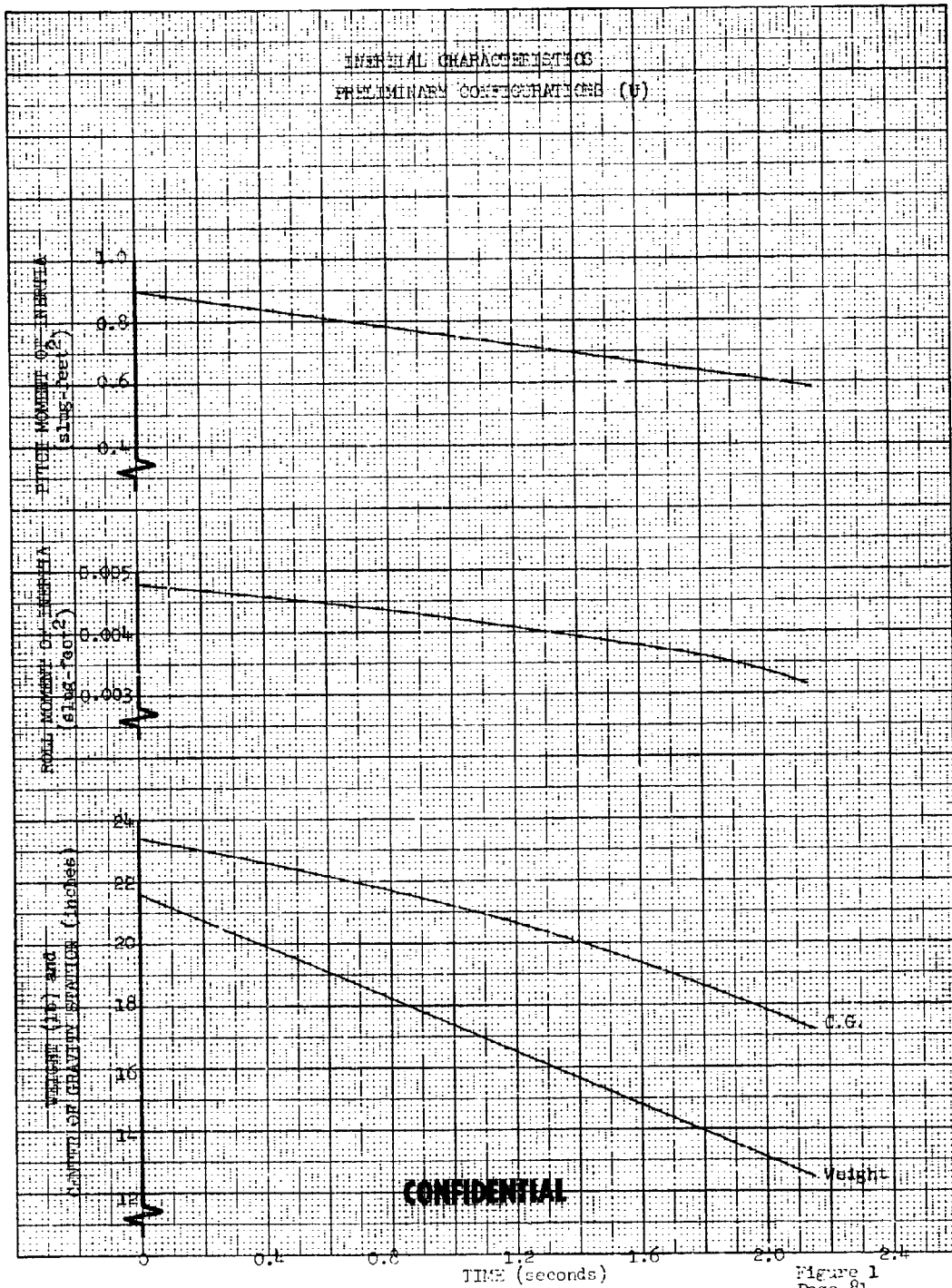


Figure 1  
Page 81

CONFIDENTIAL

CONFIDENTIAL

Report AFRPL-TR-69-90, Appendix A

CONFIDENTIAL

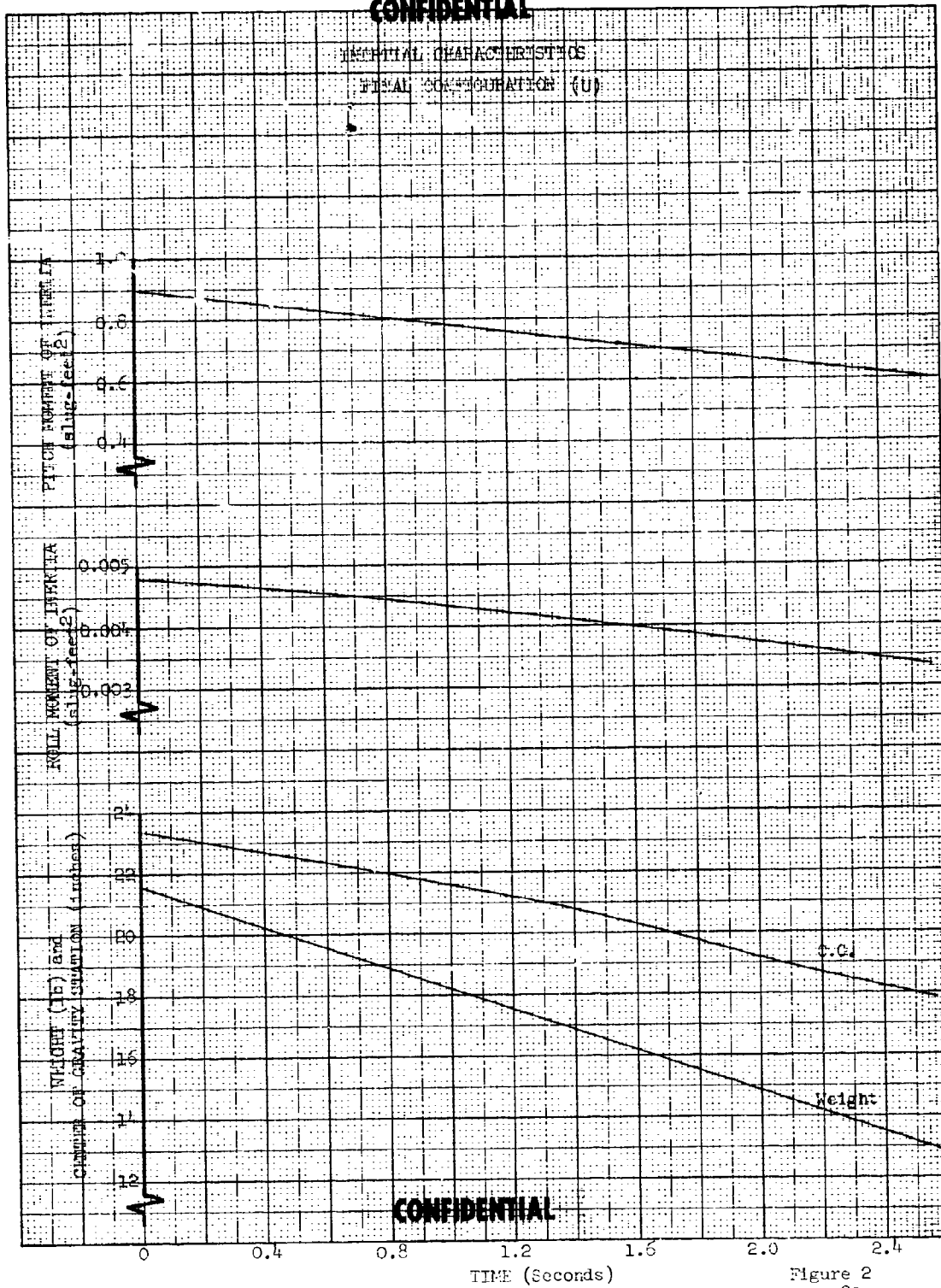


Figure 2  
Page 82

CONFIDENTIAL



# CONFIDENTIAL

Report AFRPL-TR-69-90, Appendix A

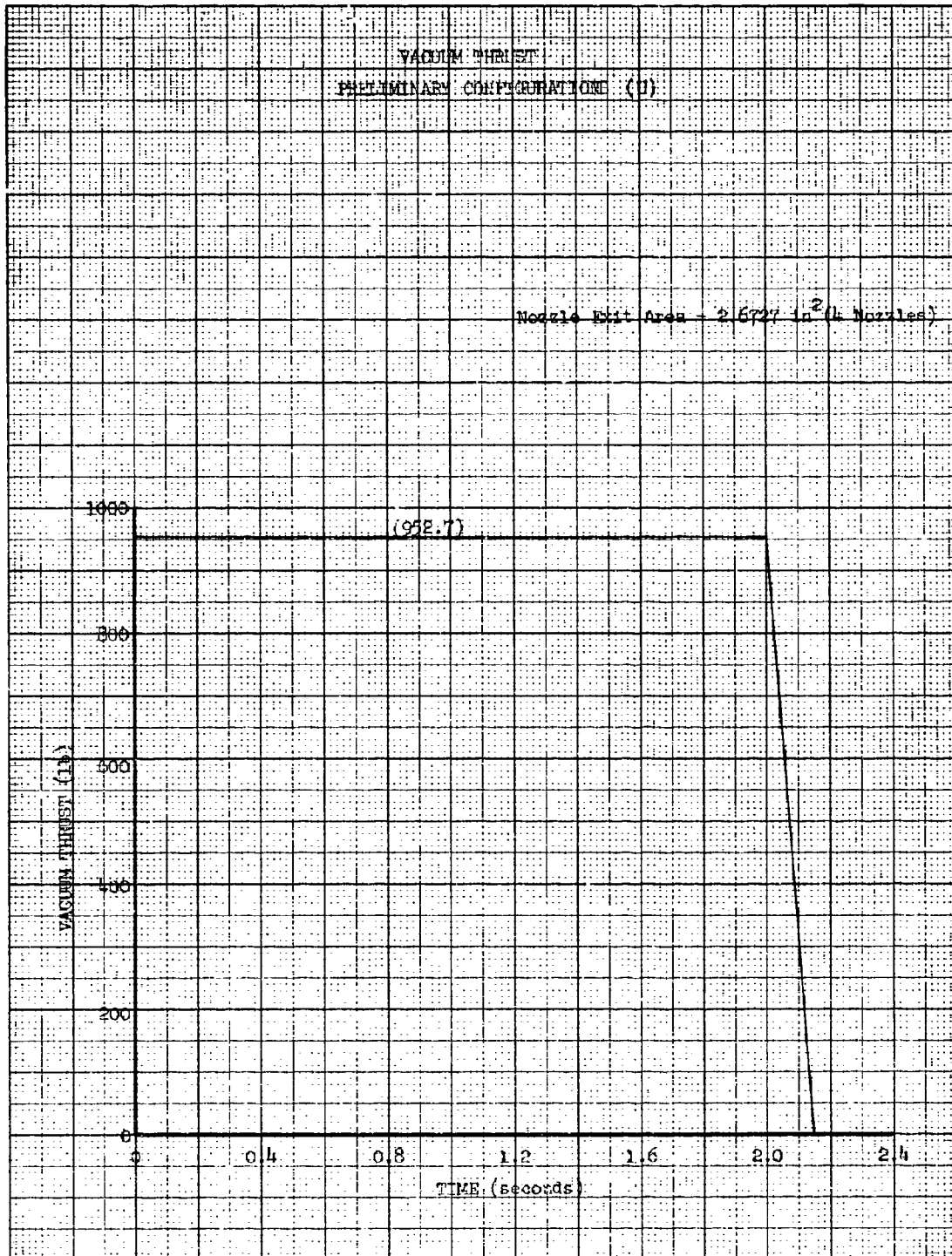


Figure 3  
Page 83

CONFIDENTIAL

# CONFIDENTIAL

Report AFRPL-TR-69-90, Appendix A

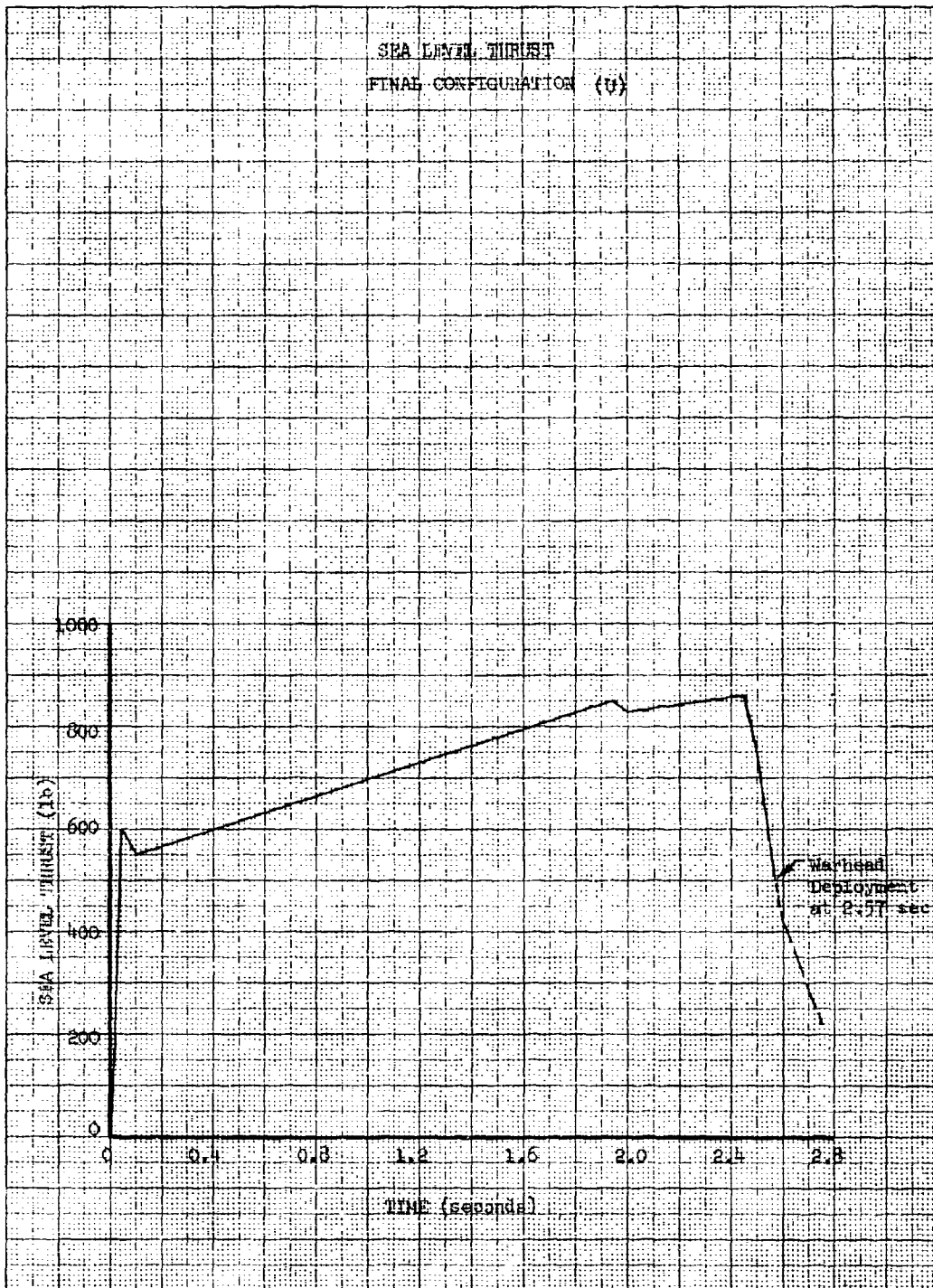


Figure 4  
Page 84

CONFIDENTIAL

UNCLASSIFIED

Report AFRPL-TR-69-90, Appendix A

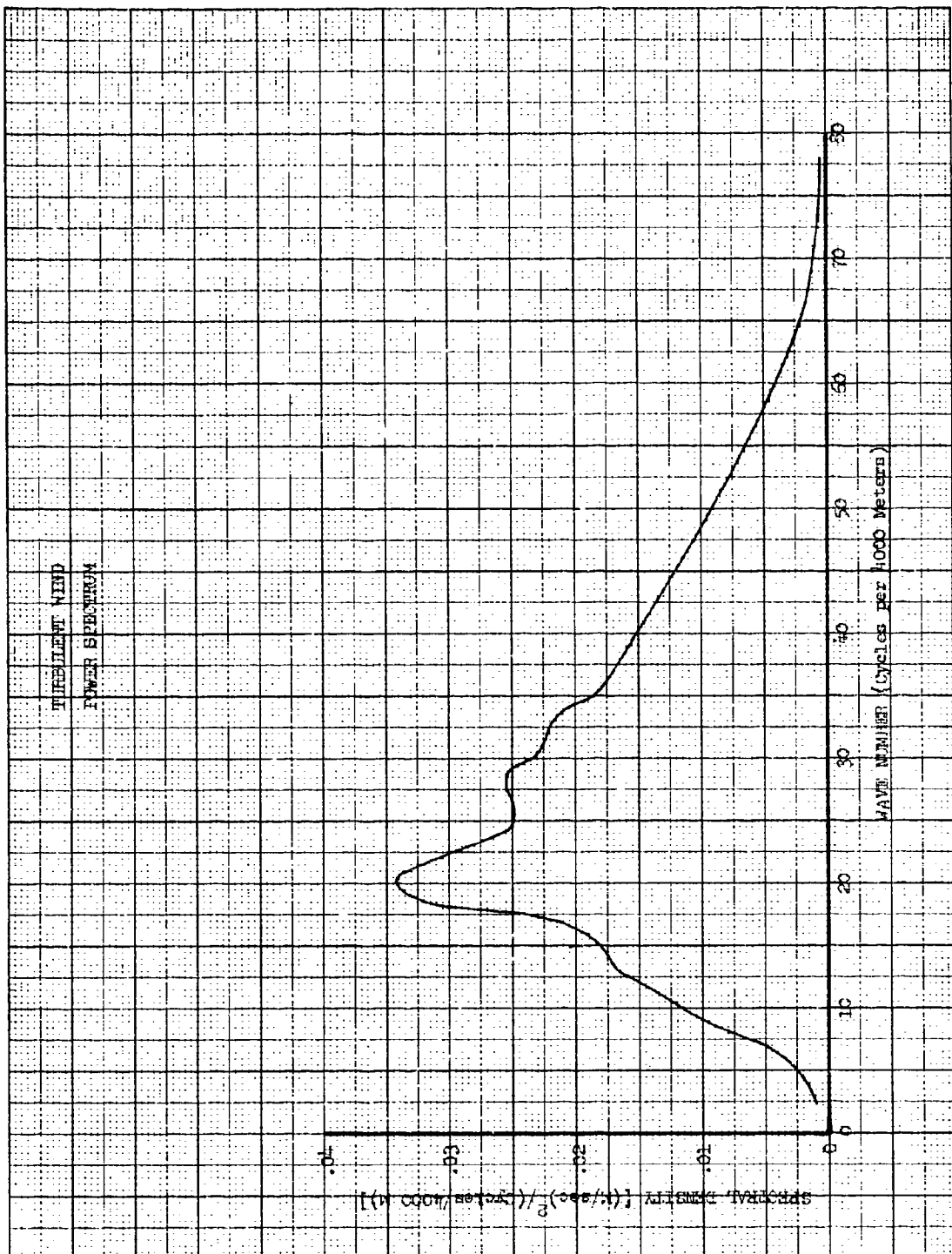


Figure 5  
Page 85

UNCLASSIFIED

UNCLASSIFIED

Report AFRPL-TR-69-90, Appendix A

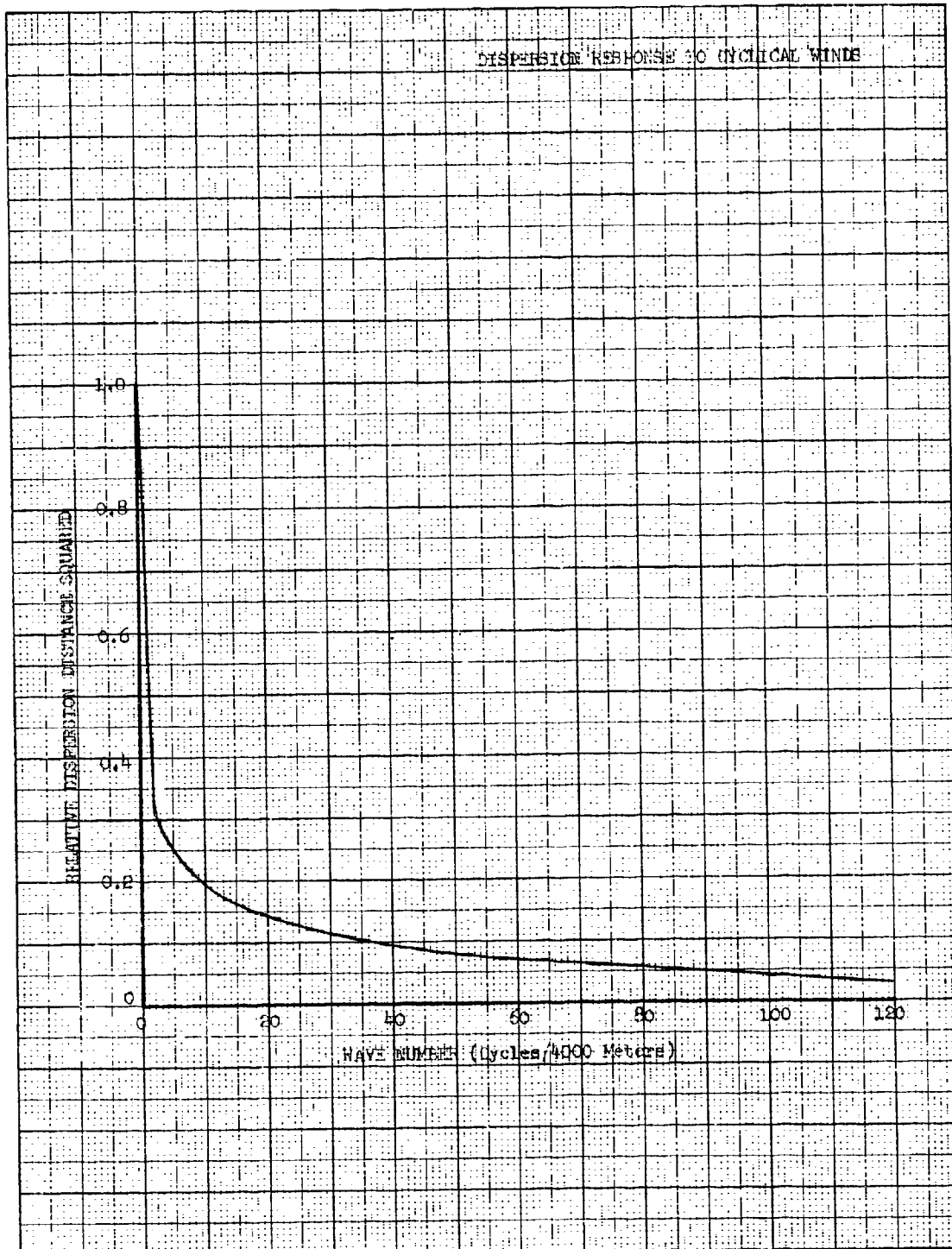


Figure 6  
Page 26

UNCLASSIFIED

# UNCLASSIFIED

Report AFRPL-TR-69-90, Appendix A

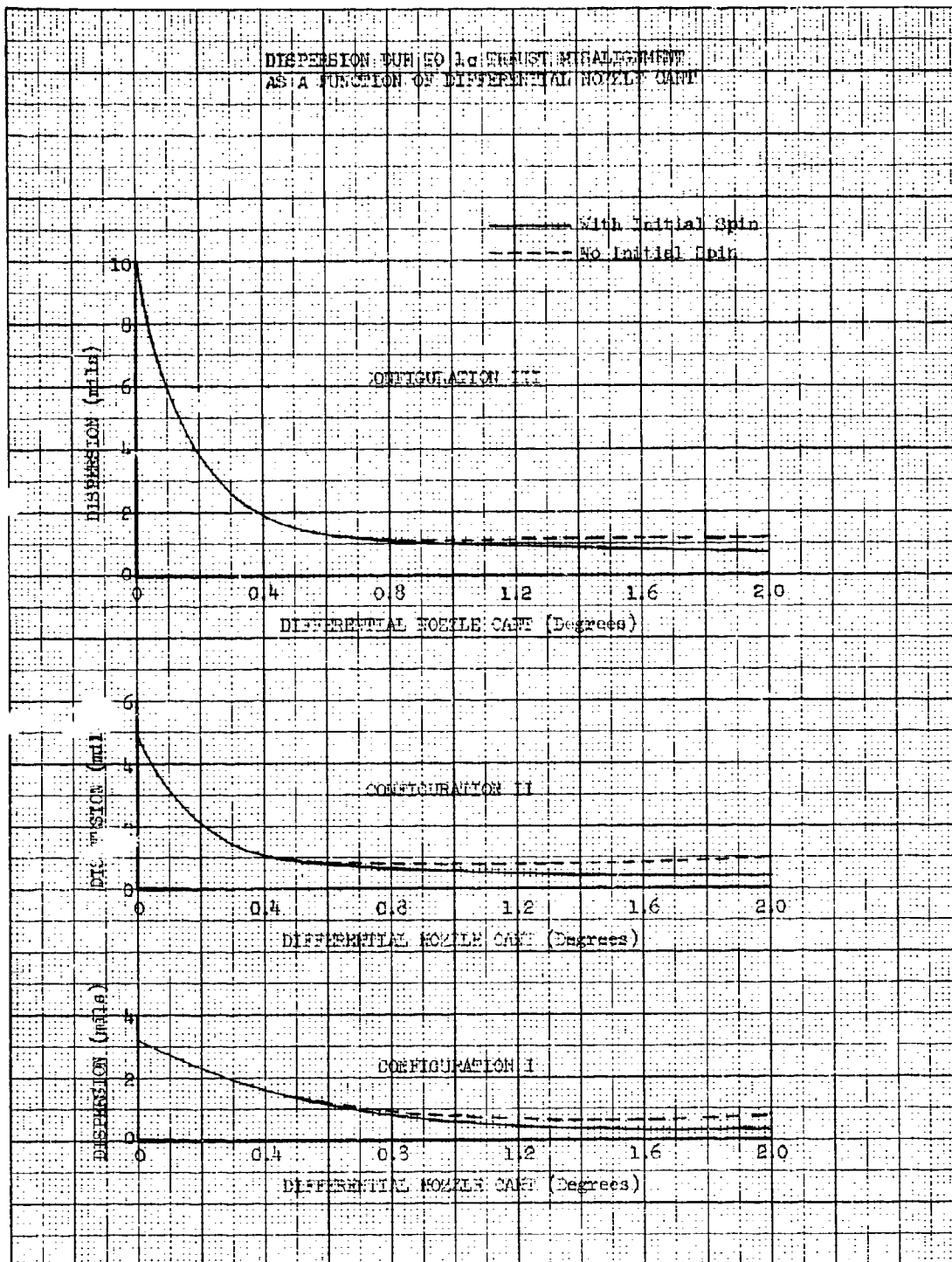


Figure 7  
Page 37

UNCLASSIFIED

UNCLASSIFIED

Report AFRPL-TR-69-90, Appendix A

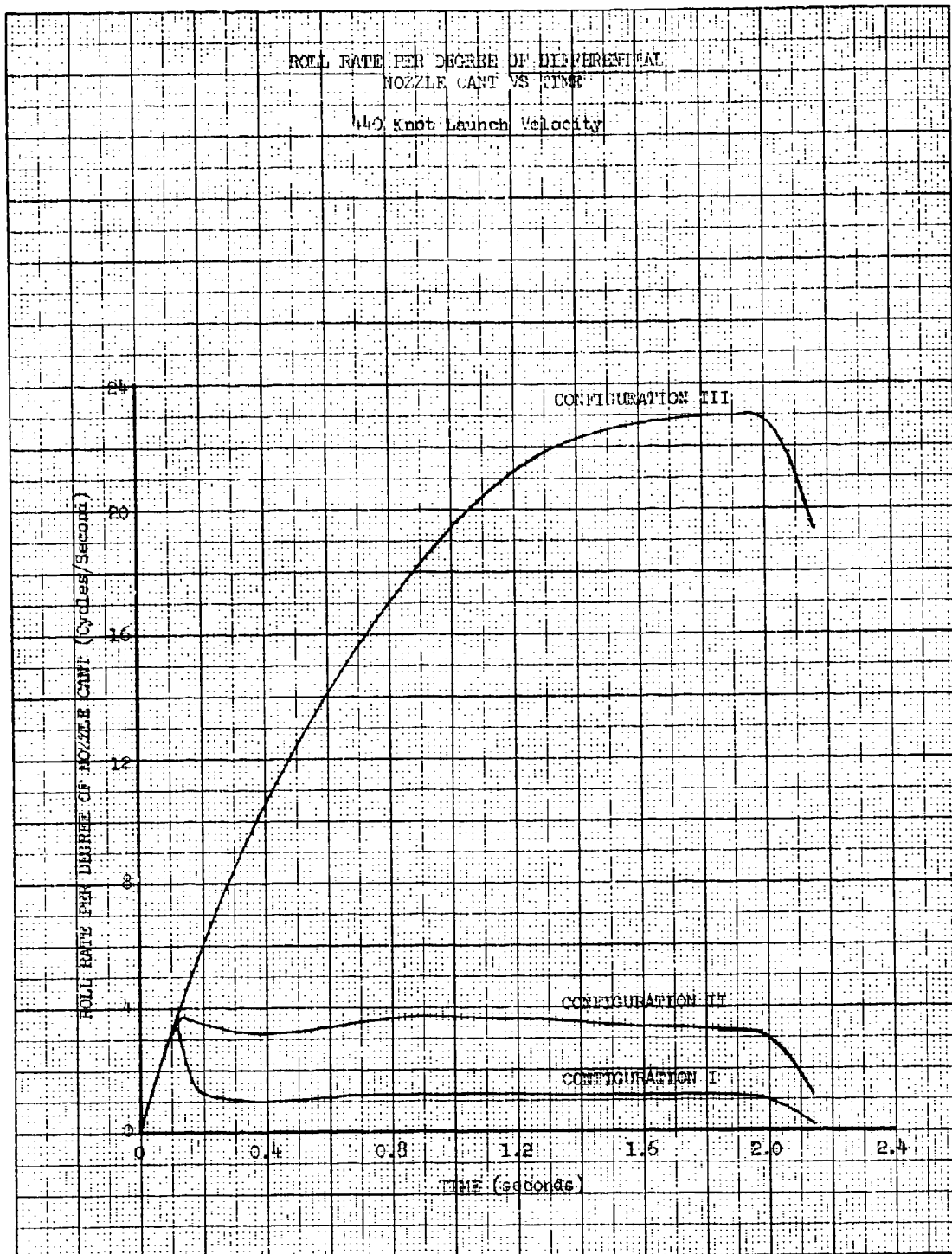


Figure 8  
Page 83

UNCLASSIFIED

UNCLASSIFIED

Report AFRPL-TR-69-90, Appendix A

DISPERSION DUE TO  $1\sigma$  THRUST MISALIGNMENT  
AS A FUNCTION OF DIFFERENTIAL FIN CANT  
AND INITIAL SPIN RATE

CONFIGURATION I

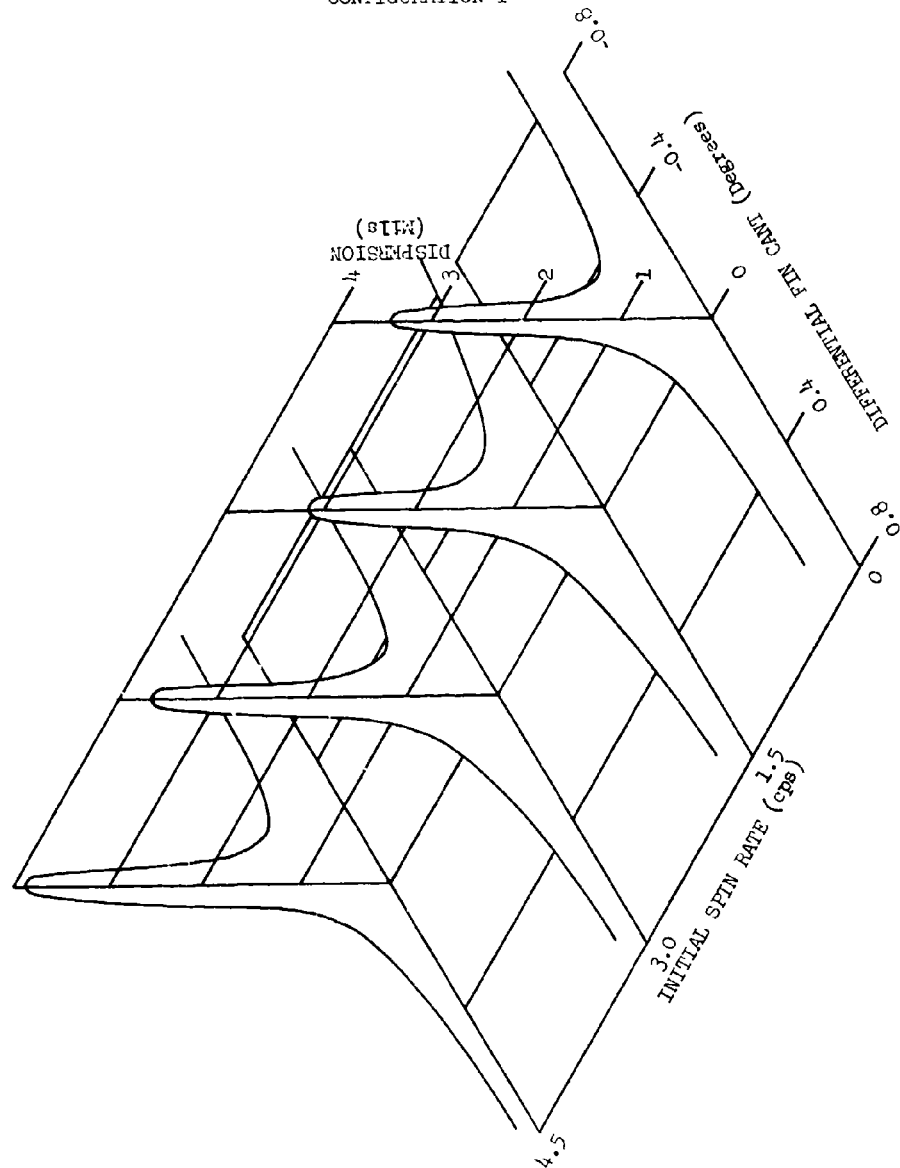


Figure 9  
Page 89

UNCLASSIFIED

UNCLASSIFIED

Report AFRPL-TR-69-90, Appendix A

DISPERSION DUE TO  $1\sigma$  THRUST MISALIGNMENT  
AS A FUNCTION OF DIFFERENTIAL FIN CANT  
AND INITIAL SPIN RATE

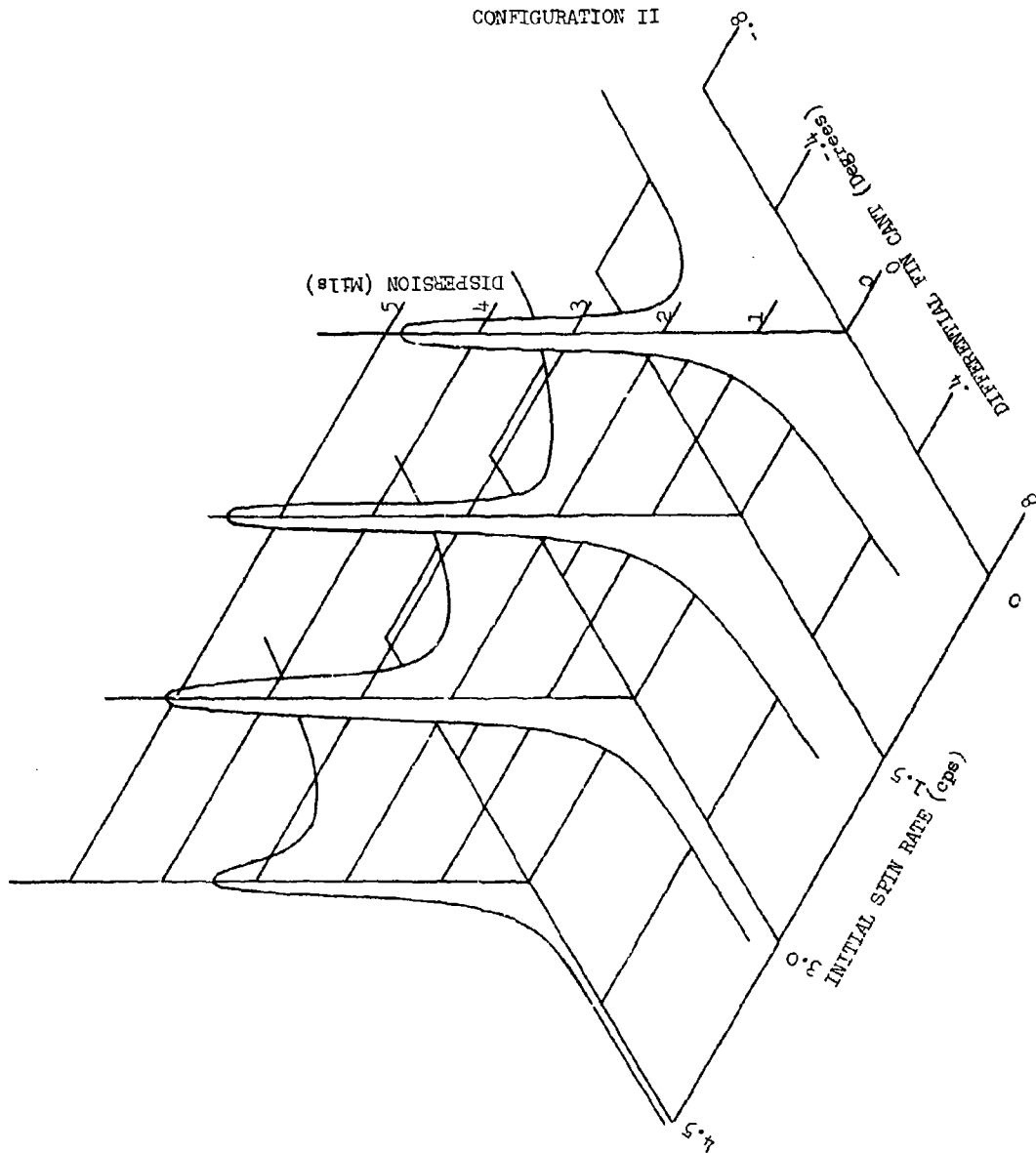


Figure 10  
Page 90

UNCLASSIFIED



# UNCLASSIFIED

Report AFRPL-TR-69-90, Appendix A

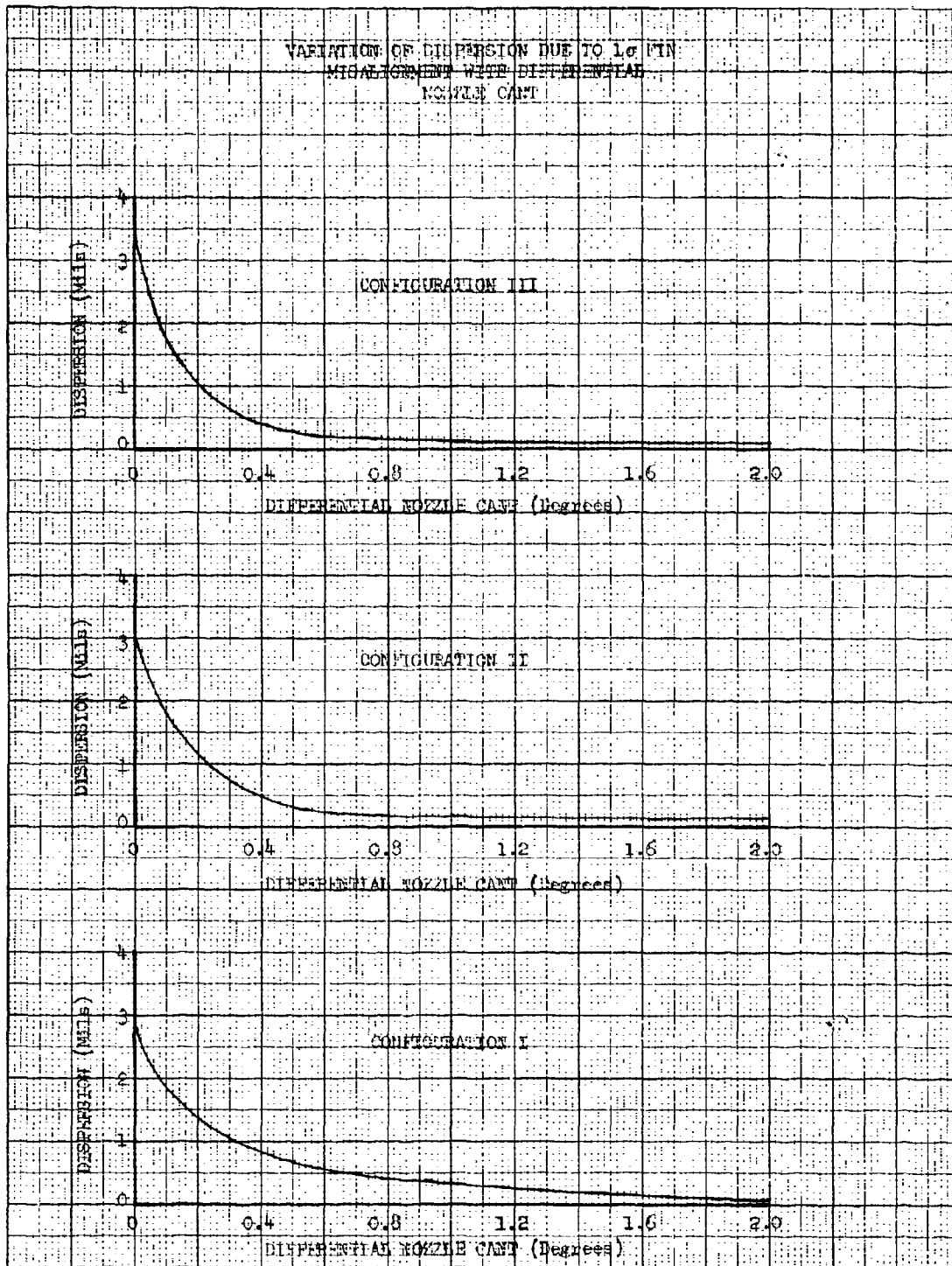


Figure 11  
Page 91

UNCLASSIFIED

UNCLASSIFIED

Report AFRPL-TR-69-90, Appendix A

DISPERSION DUE TO 1σ FIN MISALIGNMENT AS A  
FUNCTION OF DIFFERENTIAL FIN CANT AND  
INITIAL SPIN RATE

CONFIGURATION I

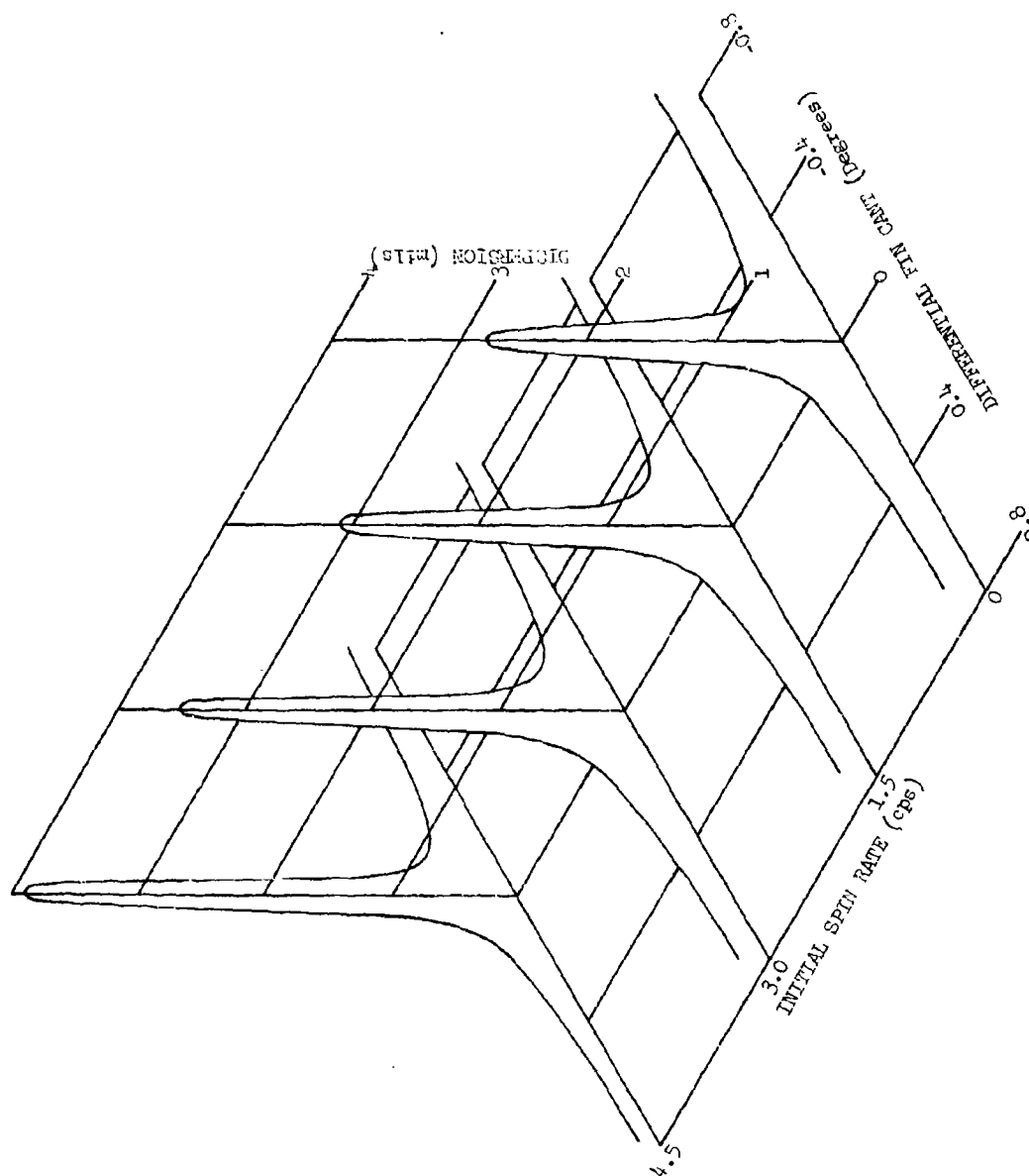


Figure 12  
Page 92

UNCLASSIFIED

UNCLASSIFIED

Report AFRPL-TR-69-90, Appendix A

DISPERSION DUE TO 1° FIN MISALIGNMENT AS A  
FUNCTION OF DIFFERENTIAL FIN CANT AND  
INITIAL SPIN RATE

CONFIGURATION II

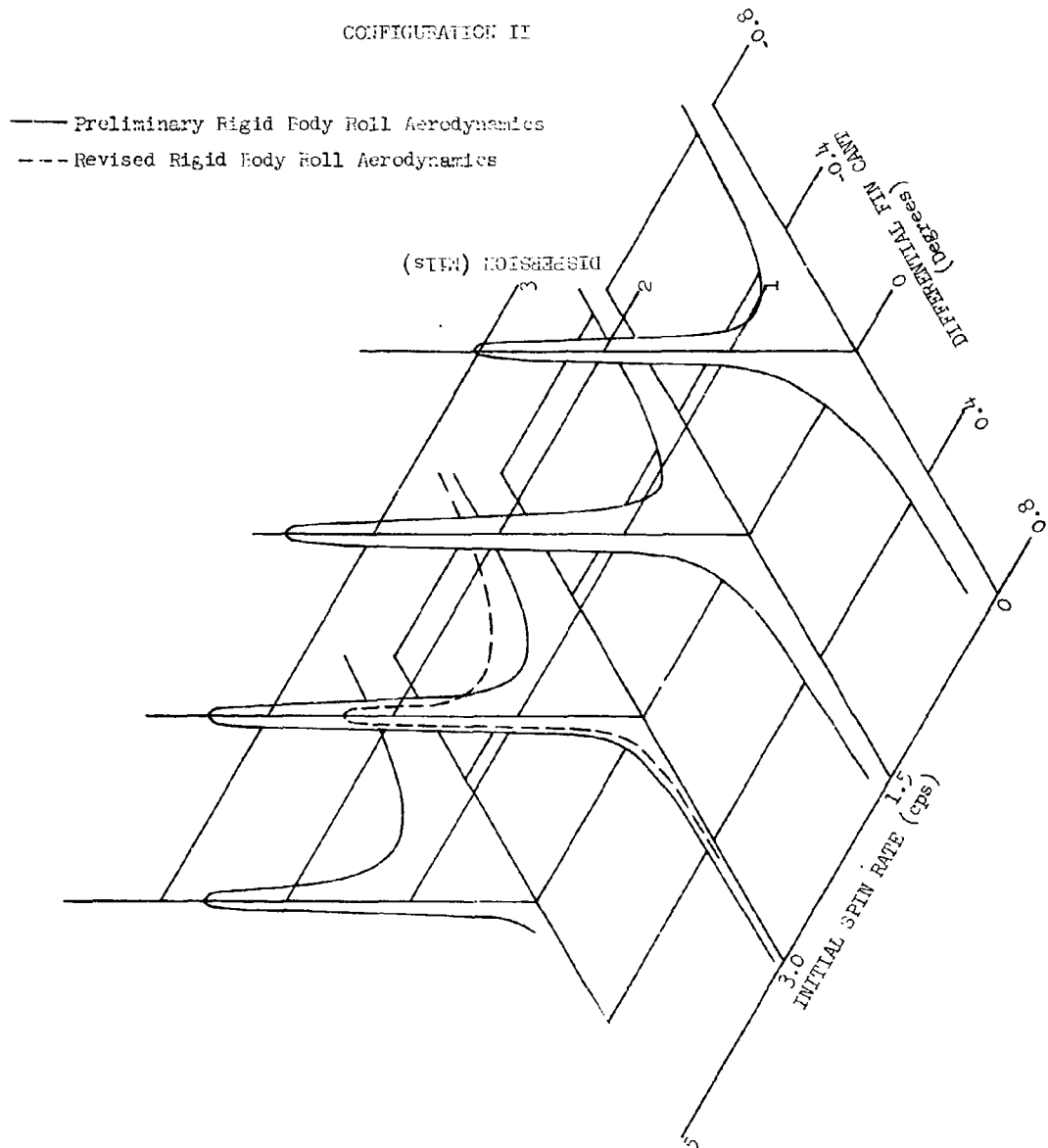


Figure 13  
Page 93

UNCLASSIFIED

UNCLASSIFIED

Report AFRPL-TR-69-90, Appendix A

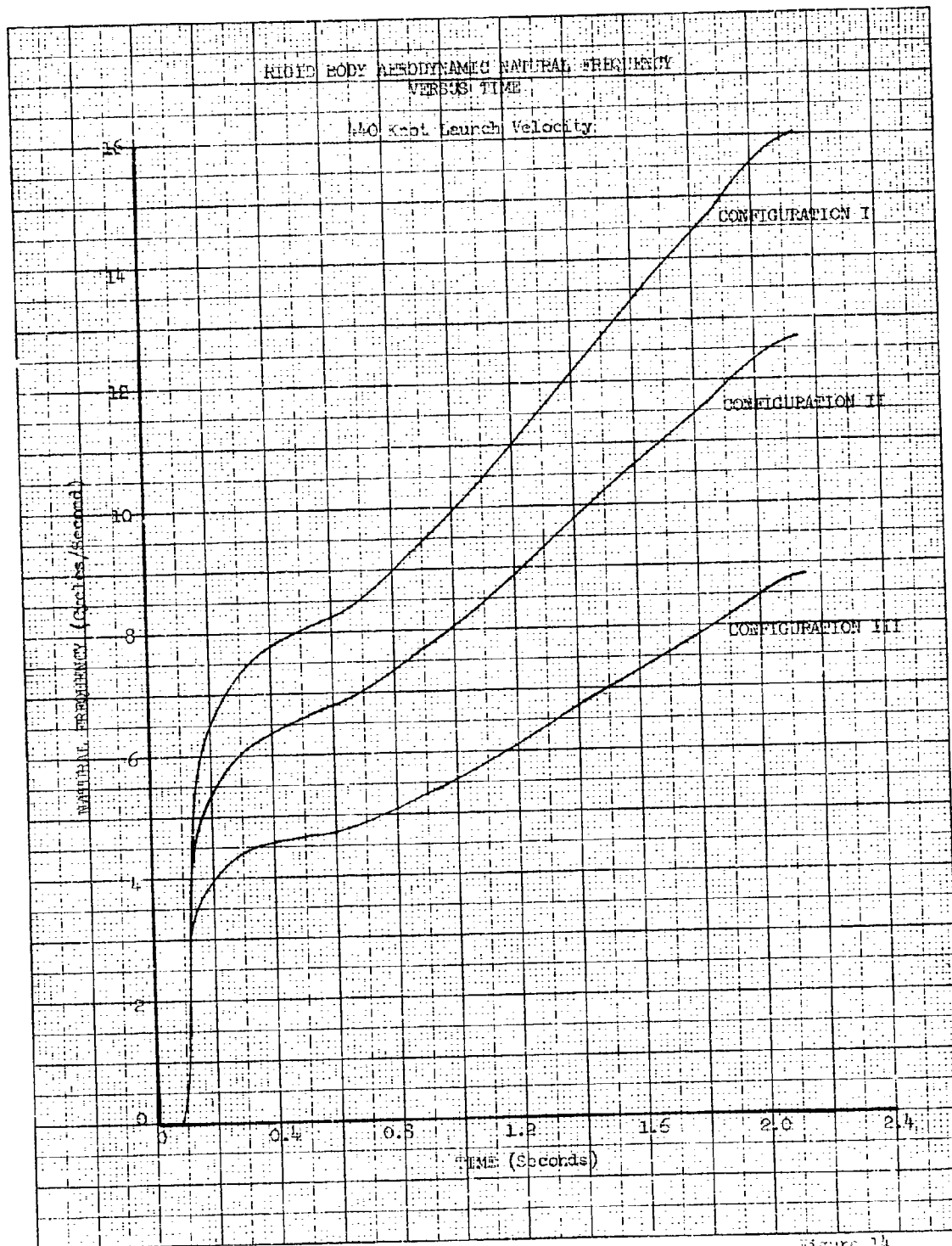


Figure 14

Page 94

UNCLASSIFIED

UNCLASSIFIED

Report AFRPL-TR-69-90, Appendix A

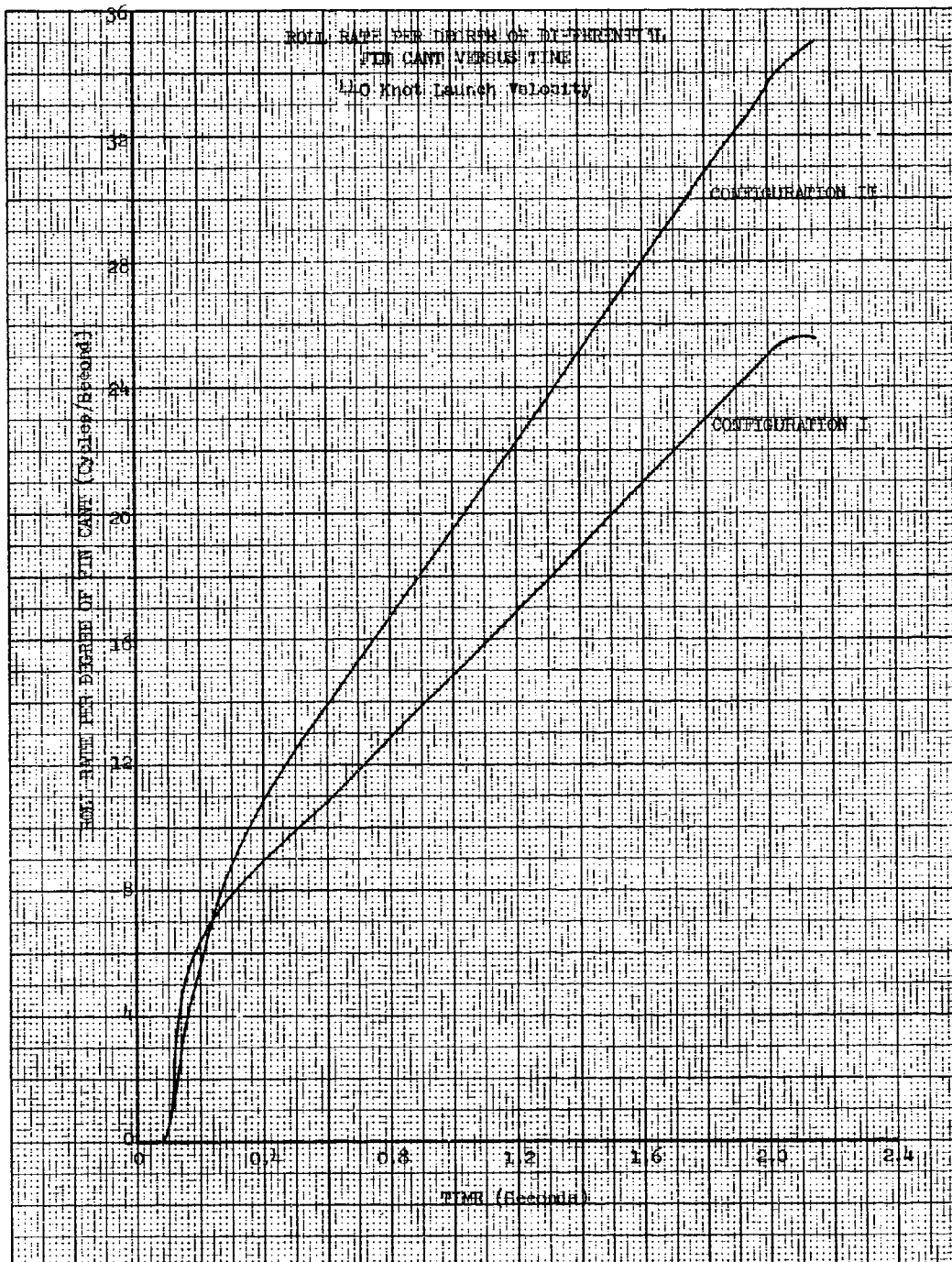


Figure 15  
Page 95

UNCLASSIFIED

UNCLASSIFIED

Report AFRPL-TR-69-90, Appendix A

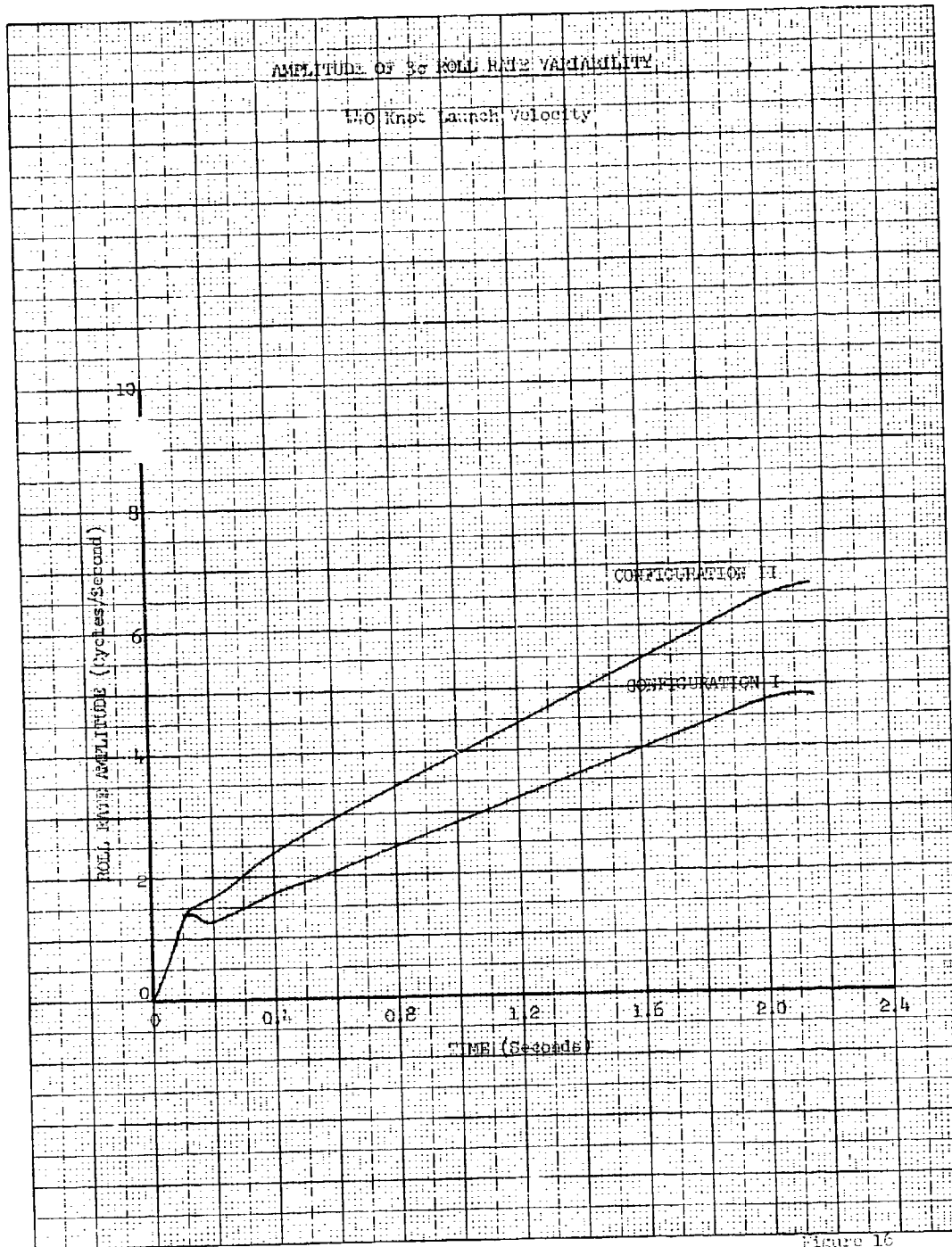


Figure 16  
Page 96

UNCLASSIFIED

# UNCLASSIFIED

Report AFRPL-TR-69-90, Appendix A

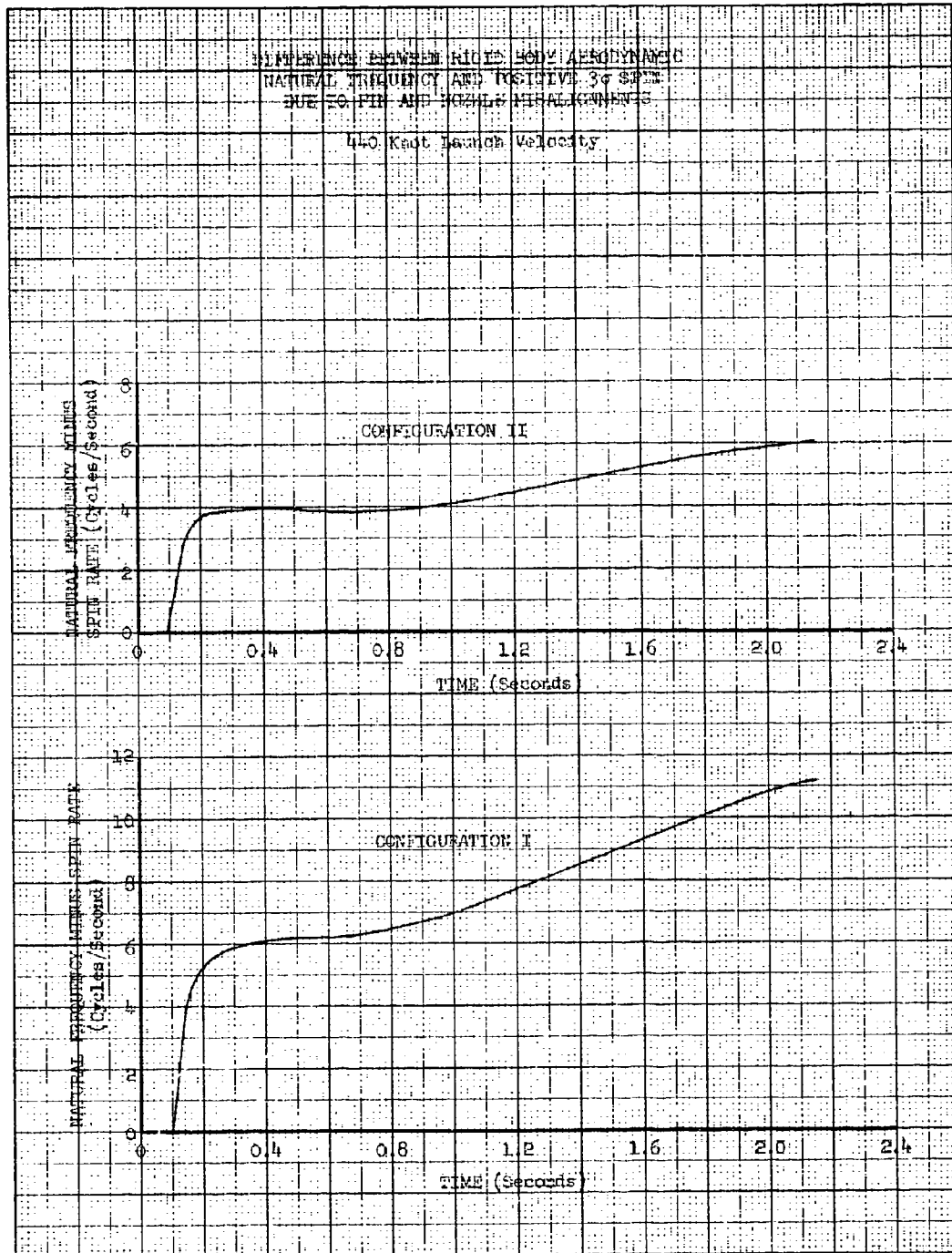


Figure 17  
Page 97

UNCLASSIFIED

UNCLASSIFIED

Report AFRPL-TR-69-90, Appendix A

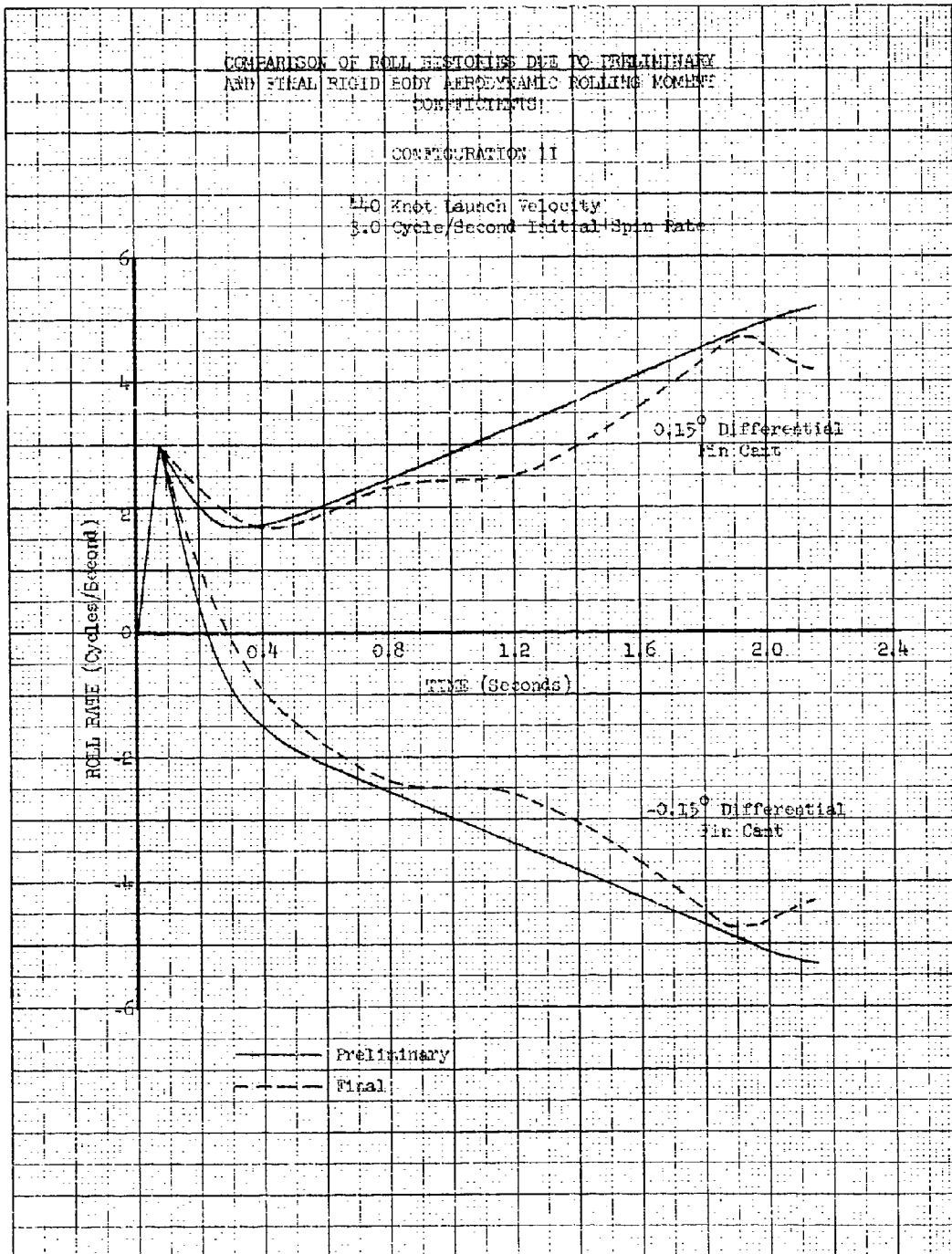


Figure 13  
Page 98

UNCLASSIFIED



# UNCLASSIFIED

Report AFRPL-TR-69-90, Appendix A

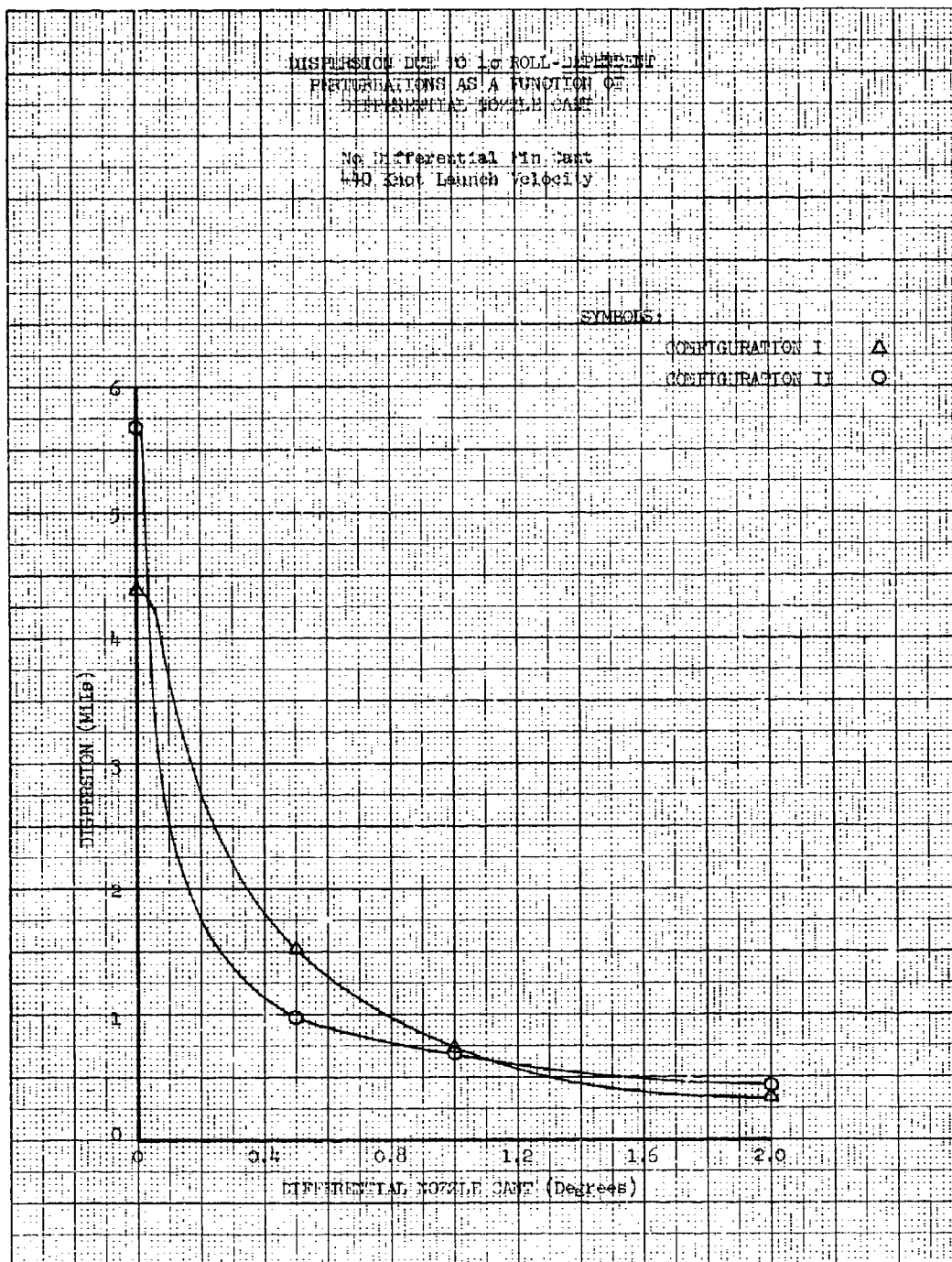


Figure 19  
Page 99

UNCLASSIFIED

UNCLASSIFIED

Report AFRPL-TR-69-90, Appendix A

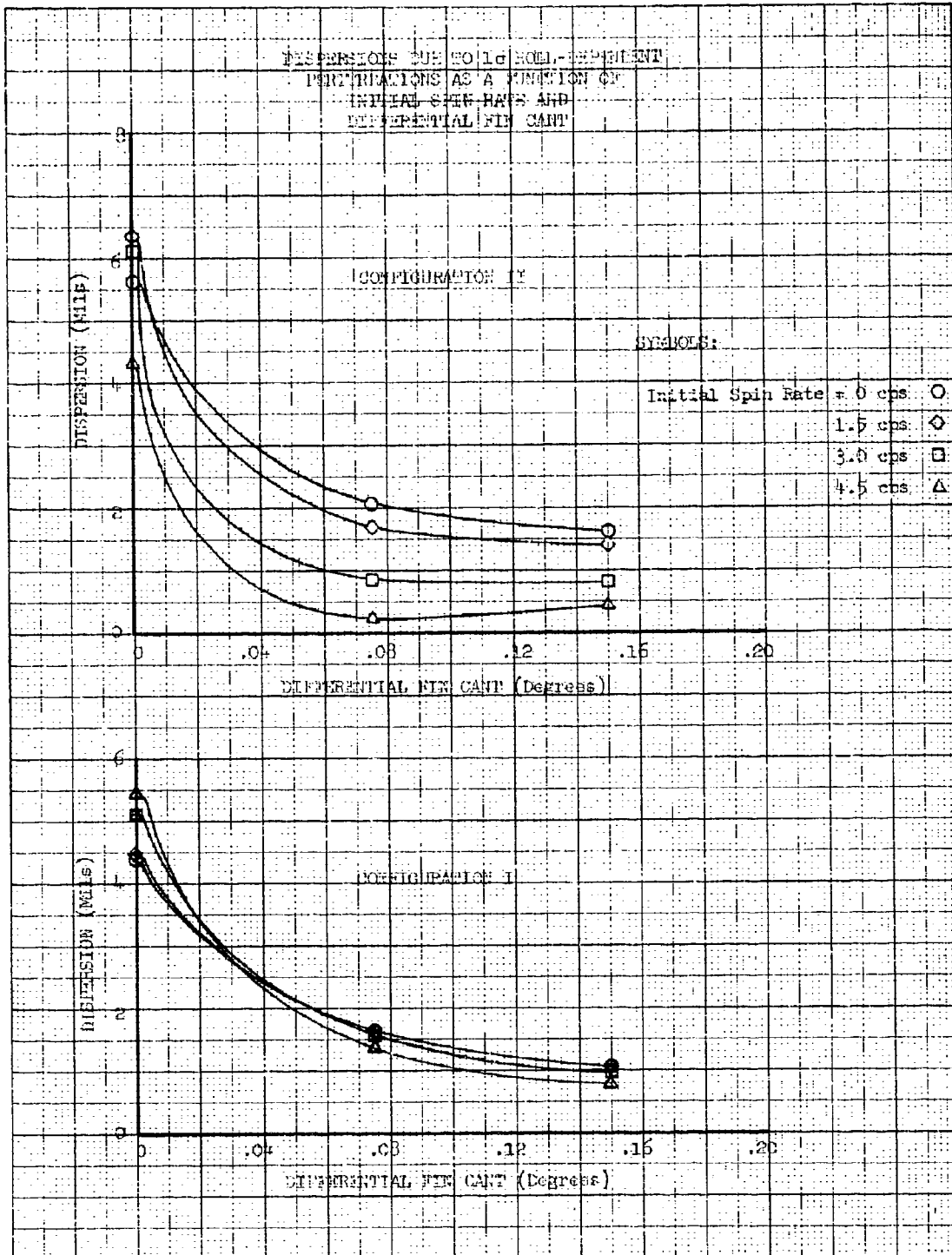


Figure 20  
Page 100

UNCLASSIFIED

UNCLASSIFIED

Report AFKPL-TR-69-90, Appendix A

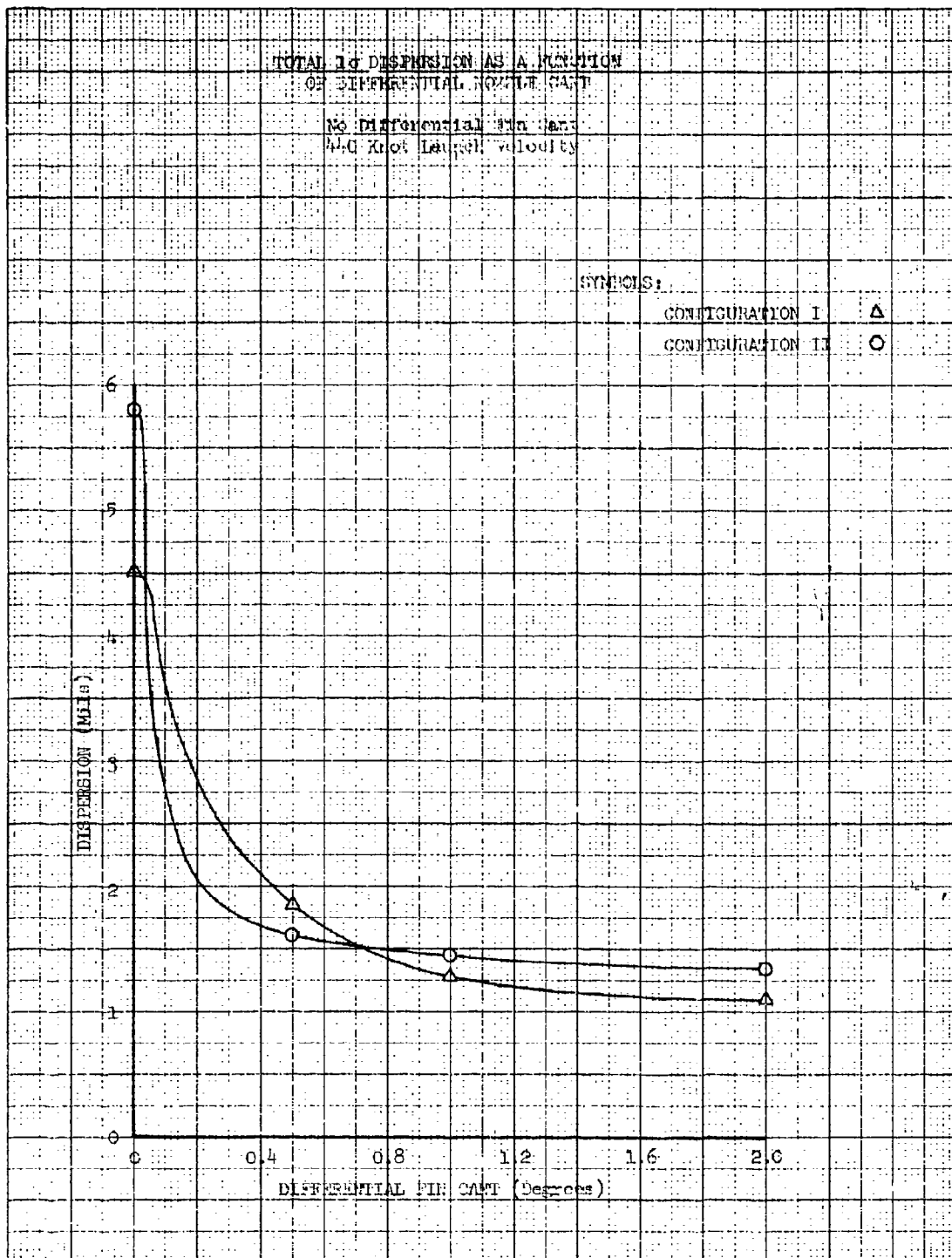


Figure 21  
Page 101

UNCLASSIFIED

# UNCLASSIFIED

Report AFRPL-TR-69-90, Appendix A

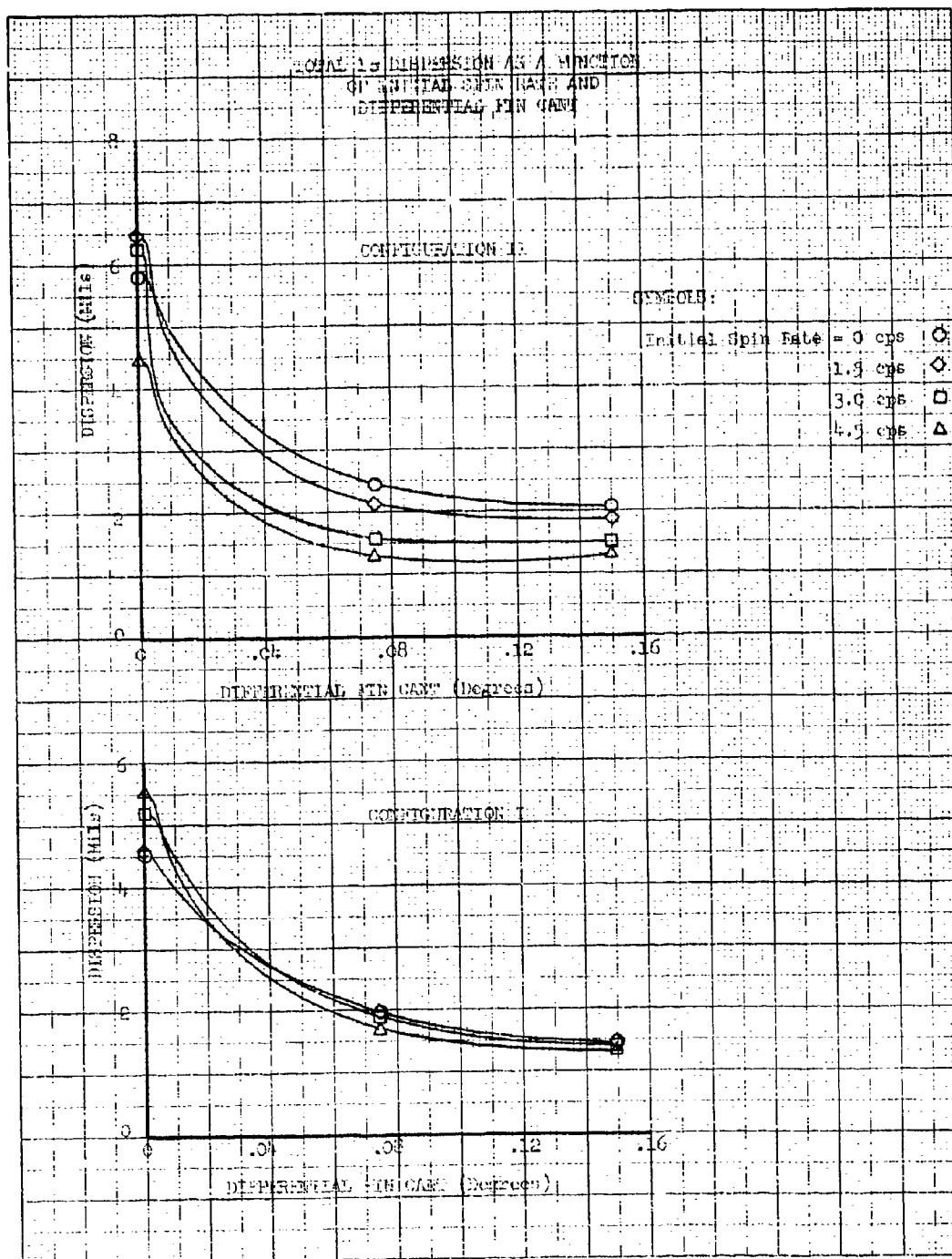


Figure 22  
Page 102

UNCLASSIFIED

# UNCLASSIFIED

Report AFRPL-TR-69-90, Appendix A

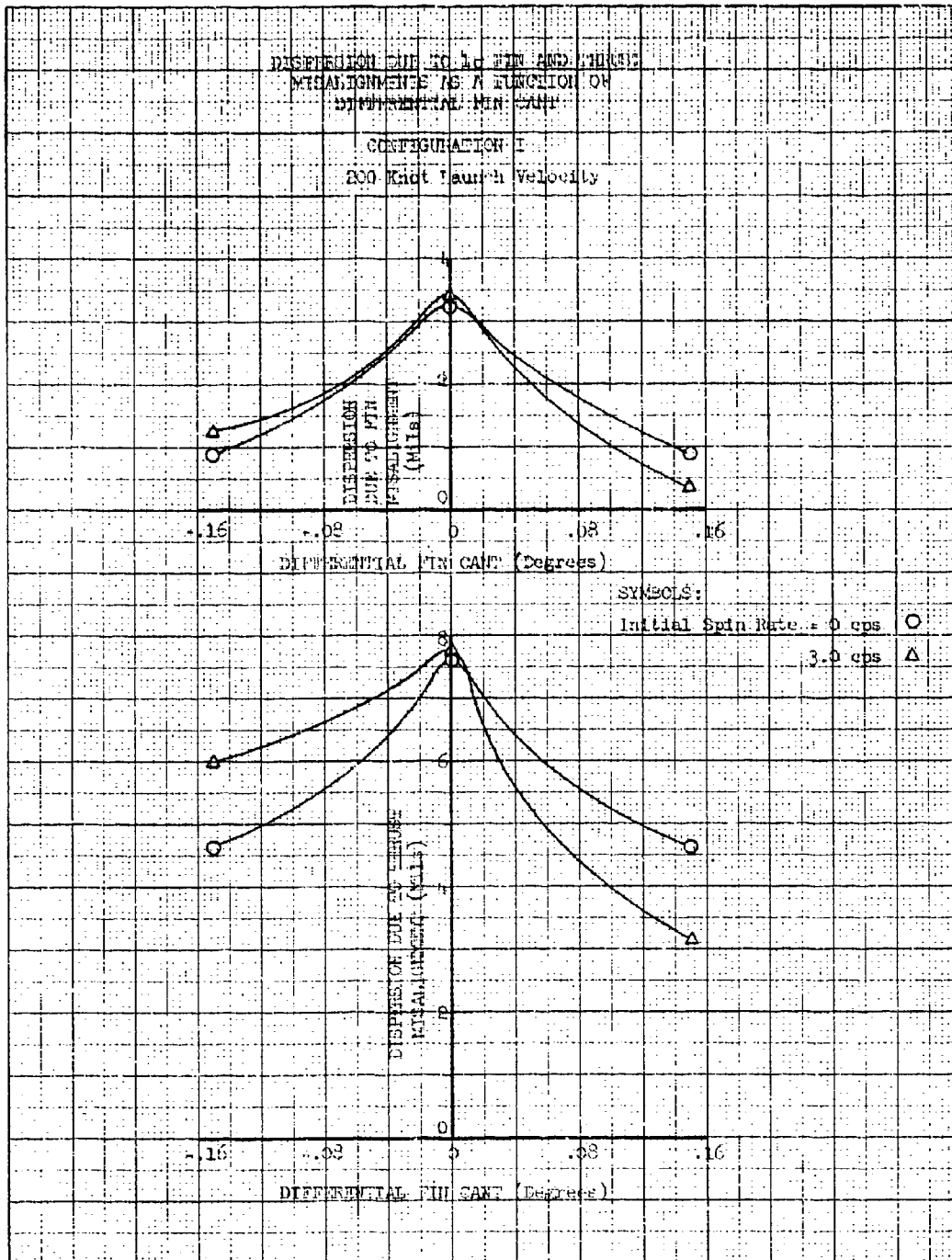


Figure 73  
Page 103

UNCLASSIFIED

UNCLASSIFIED

Report AFRPL-TR-69-90, Appendix A

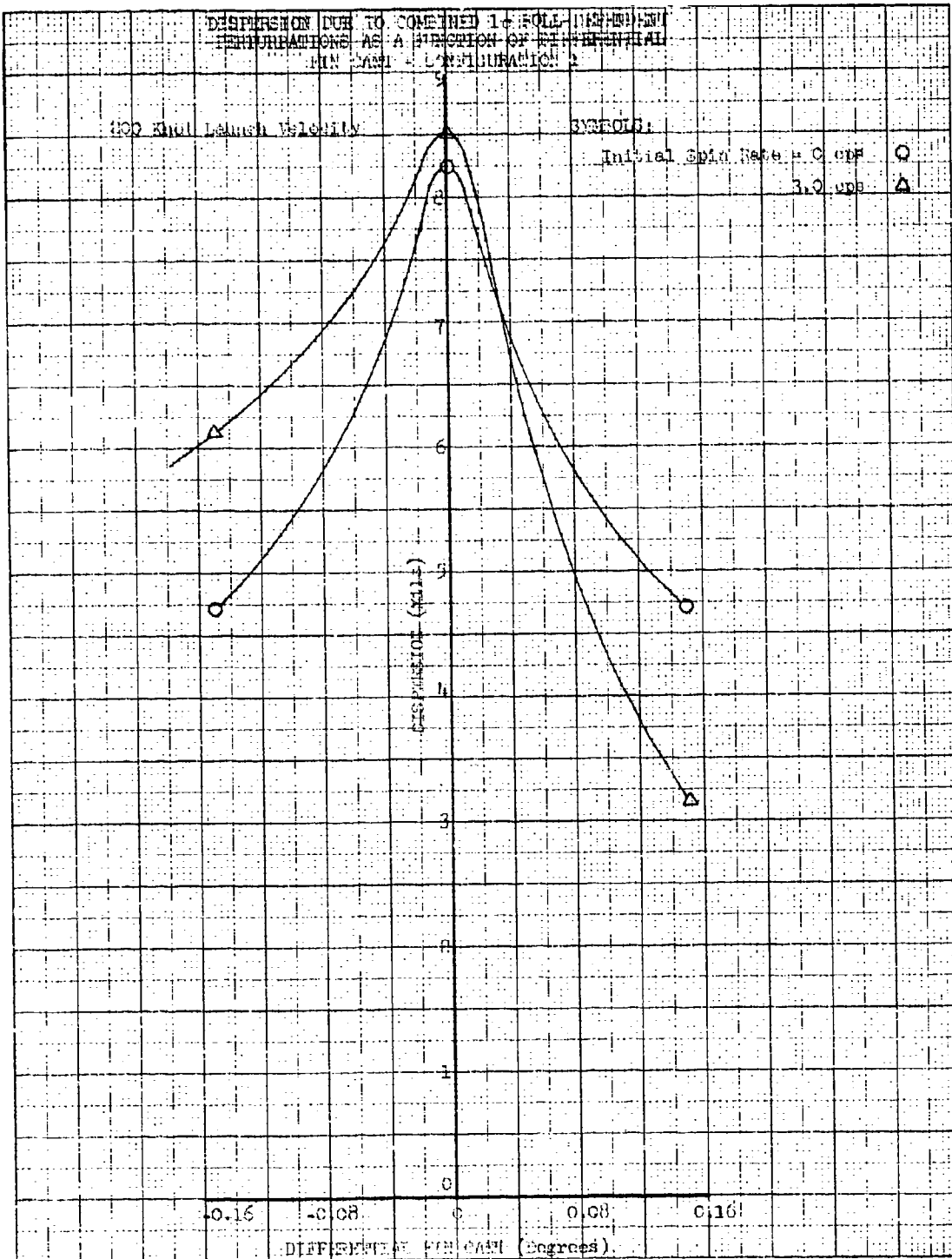


Figure 24.  
Page 104

UNCLASSIFIED

UNCLASSIFIED

Report AFRPL-TR-69-90, Appendix A

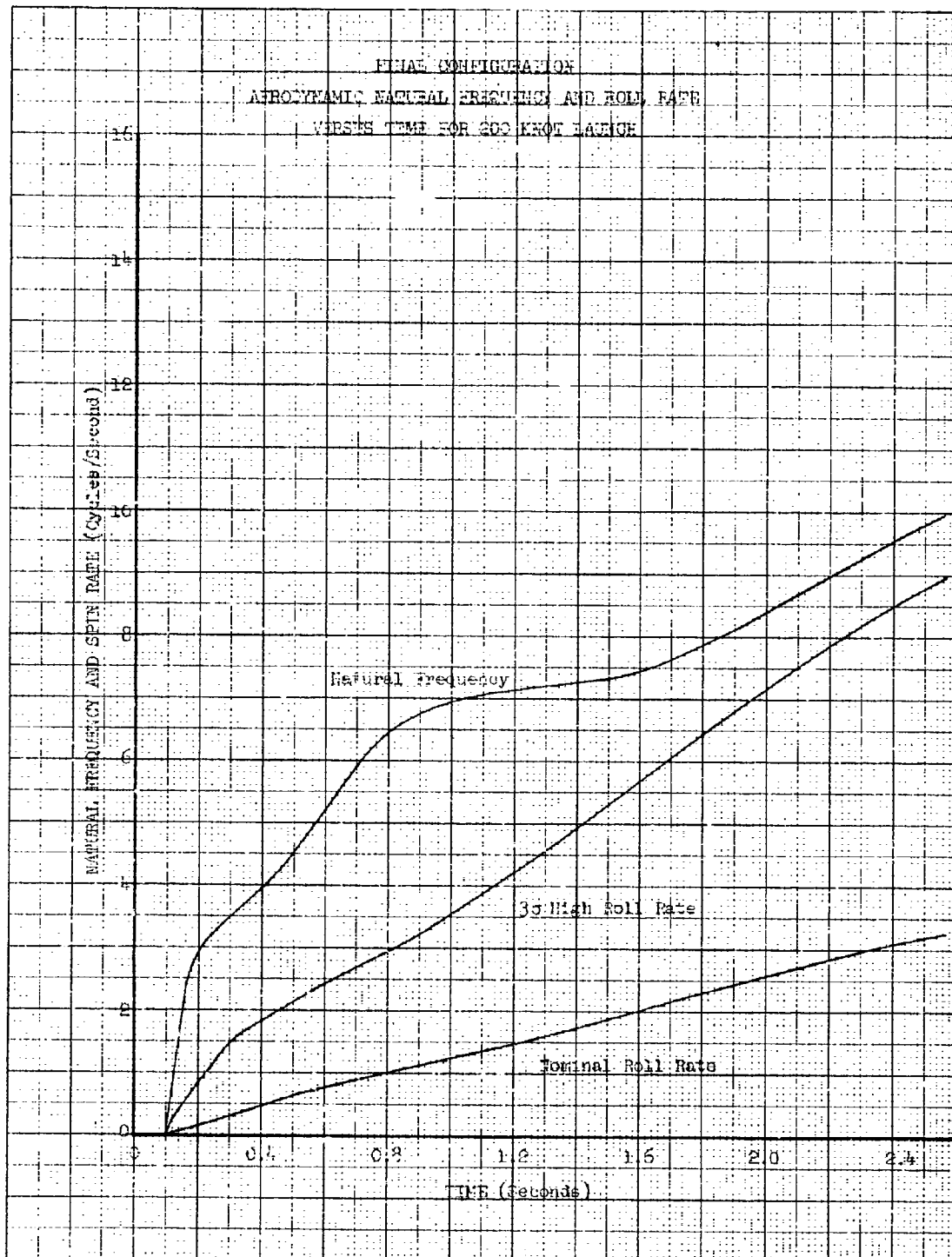


Figure 25  
Page 105

UNCLASSIFIED

UNCLASSIFIED

Report AFRPL-TR-69-90, Appendix A

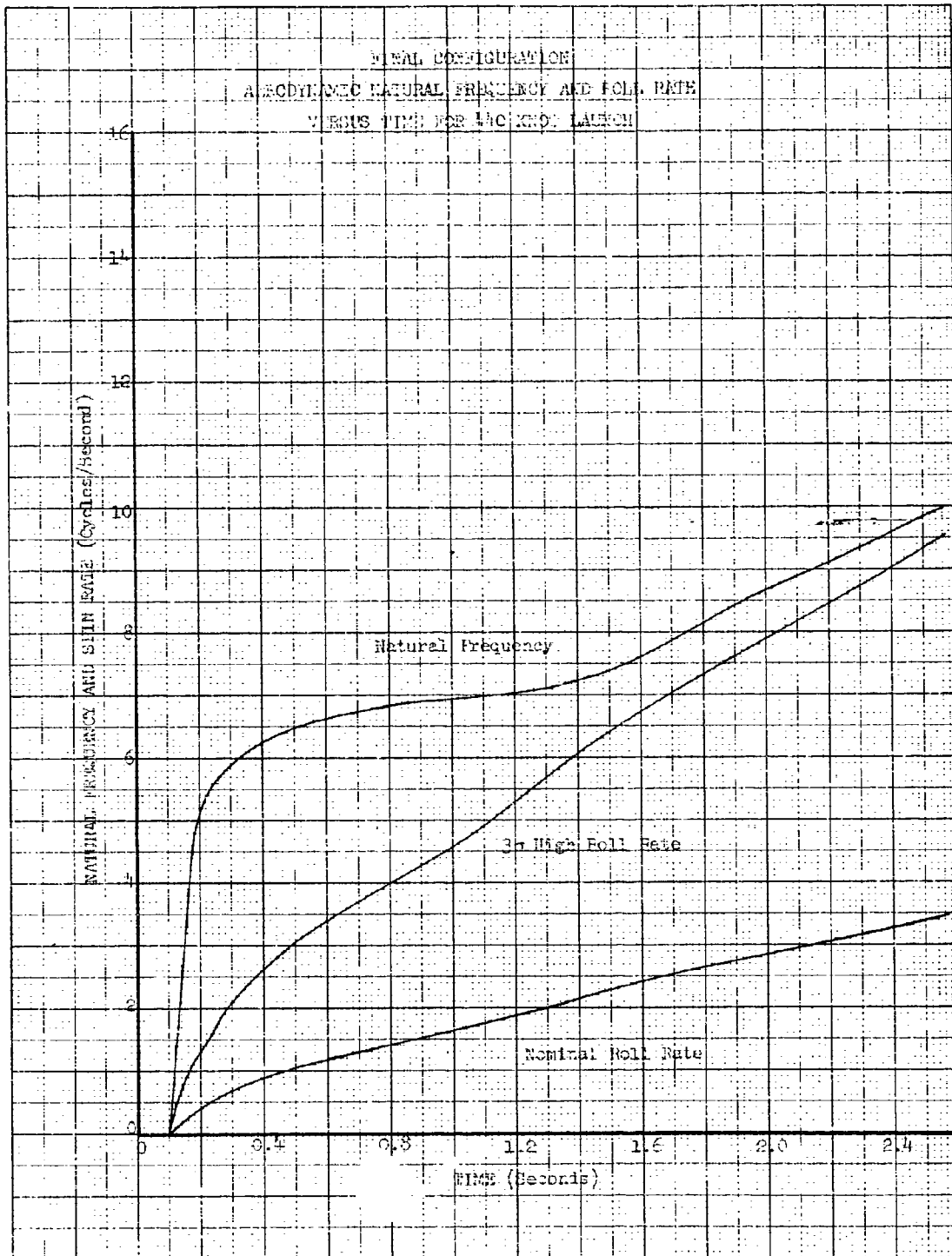


Figure 26  
Page 106

UNCLASSIFIED



# UNCLASSIFIED

Report AFRPL-TR-69-90, Appendix A

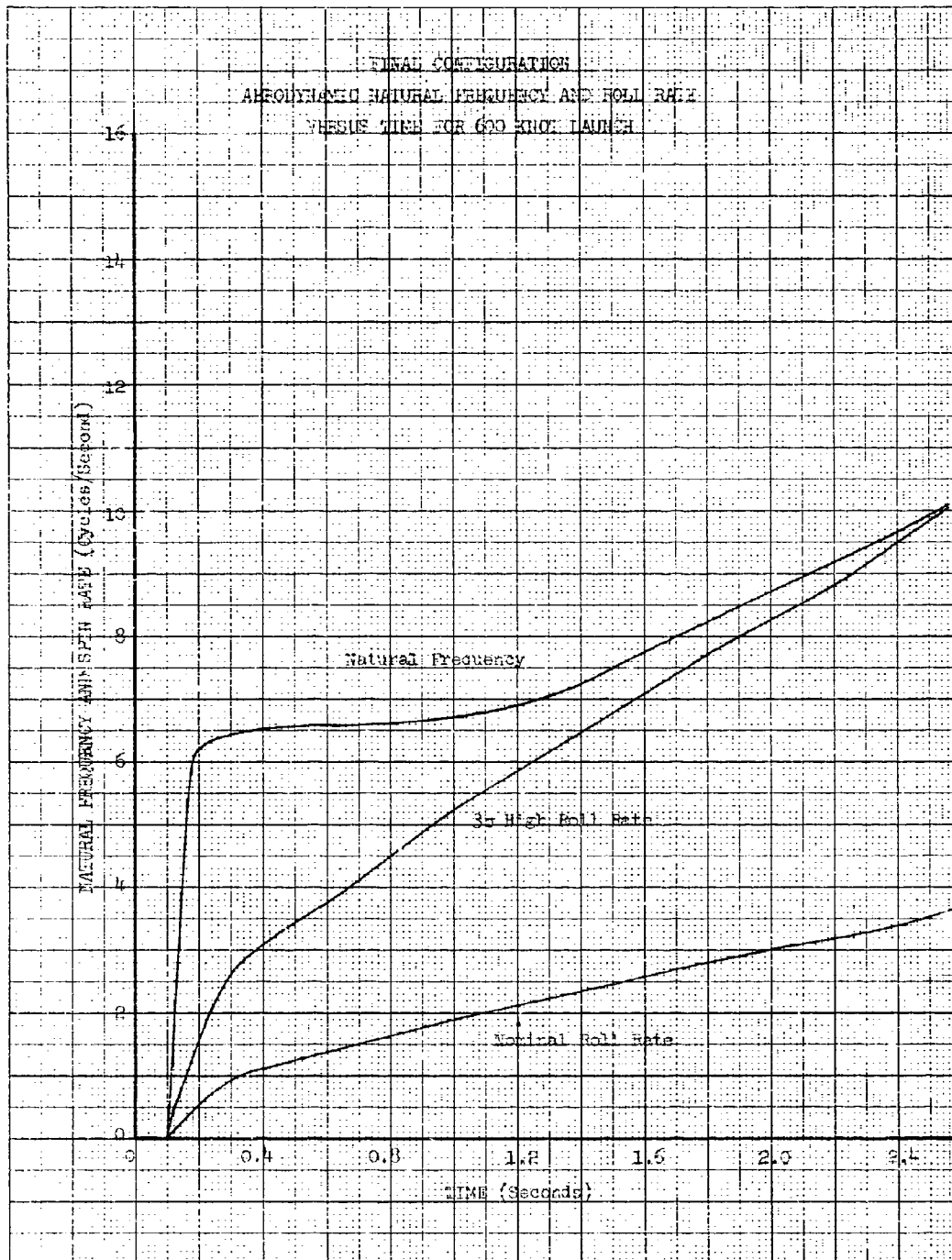


Figure 27  
Page 137

UNCLASSIFIED

# UNCLASSIFIED

Report AFRPL-TR-69-90, Appendix A

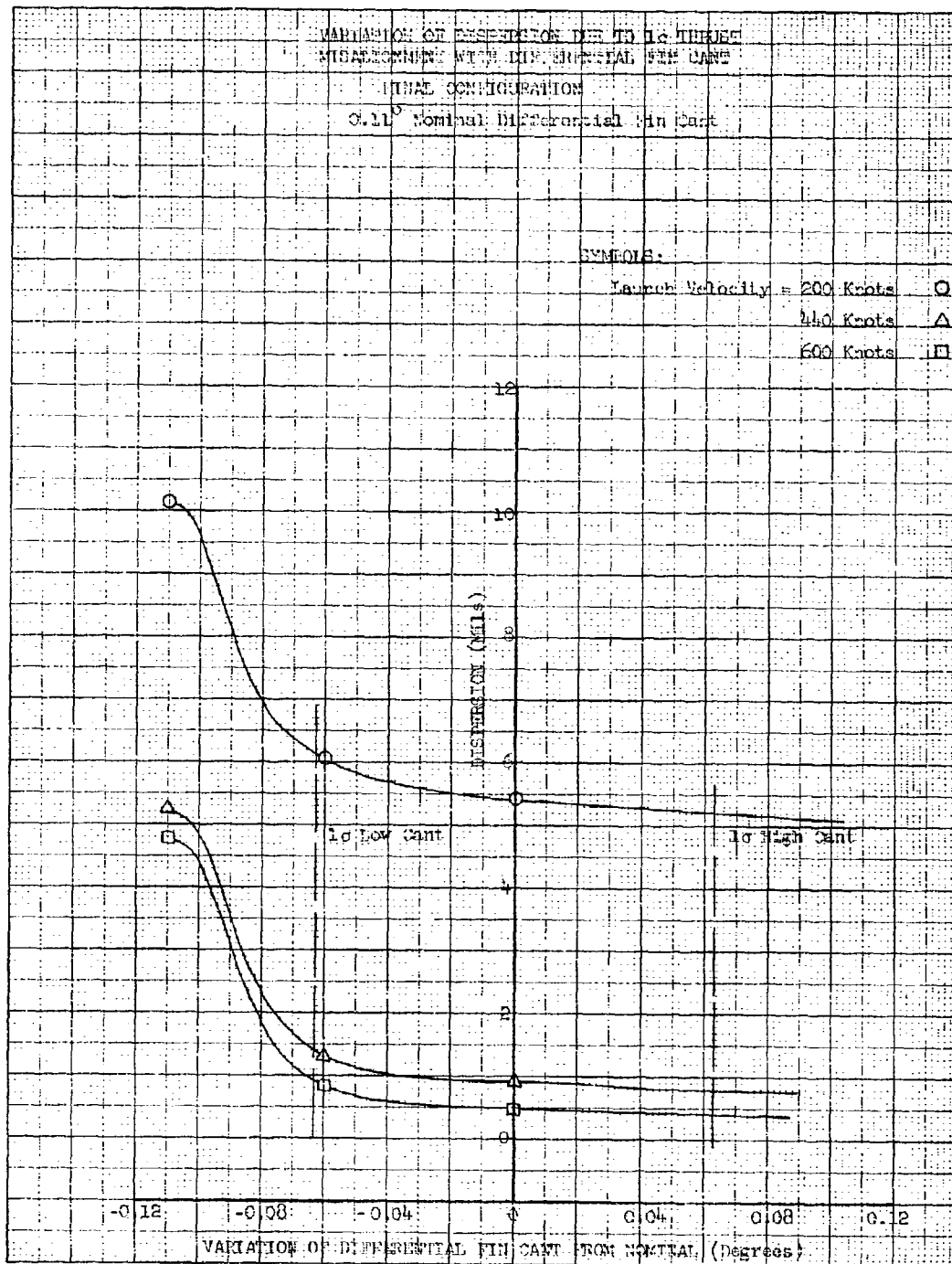


Figure 28  
Page 108

UNCLASSIFIED

UNCLASSIFIED

Report AFRPL-TR-69-90, Appendix A

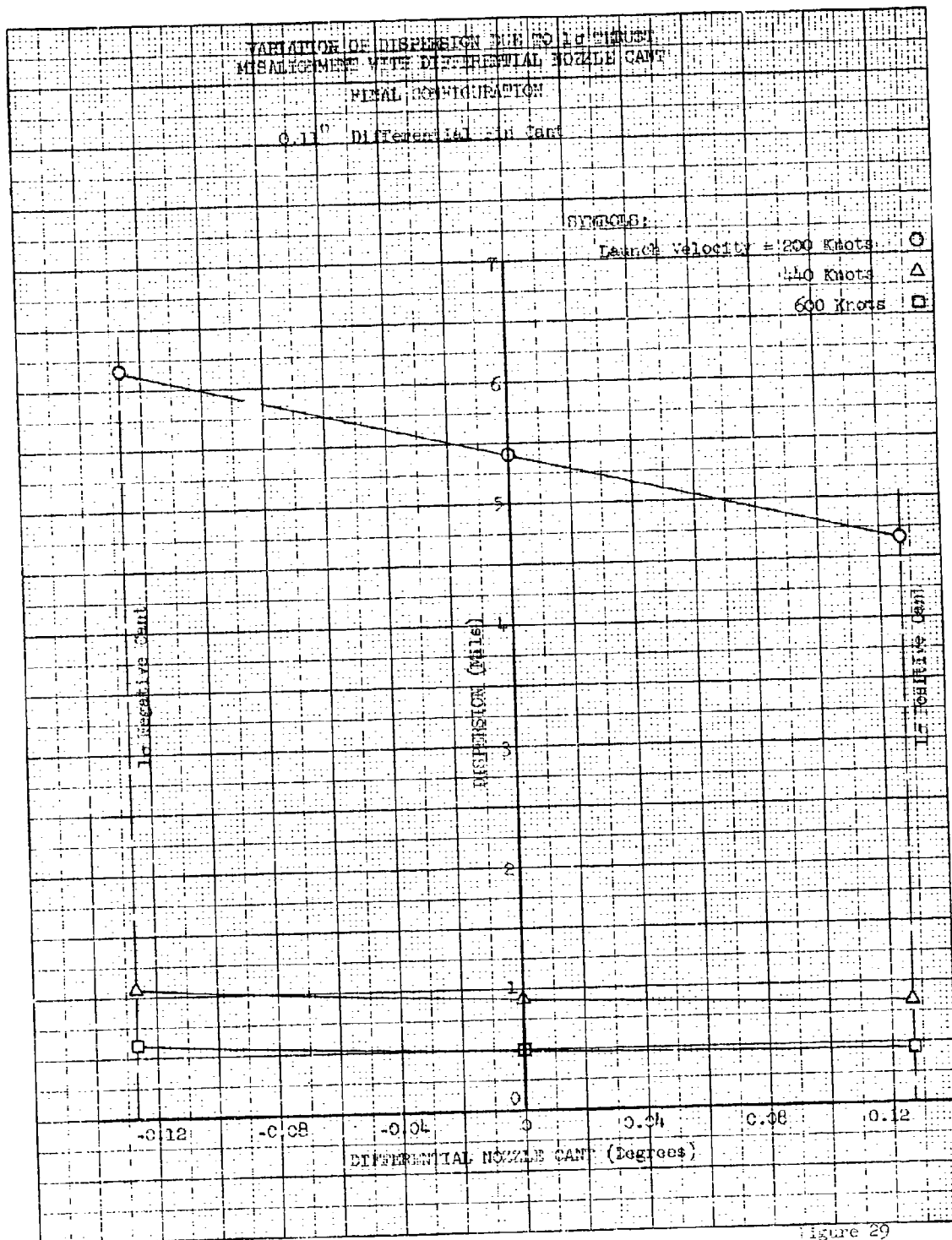


Figure 29  
Page 109

UNCLASSIFIED

# UNCLASSIFIED

Report AFRPL-TR-69-90, Appendix A

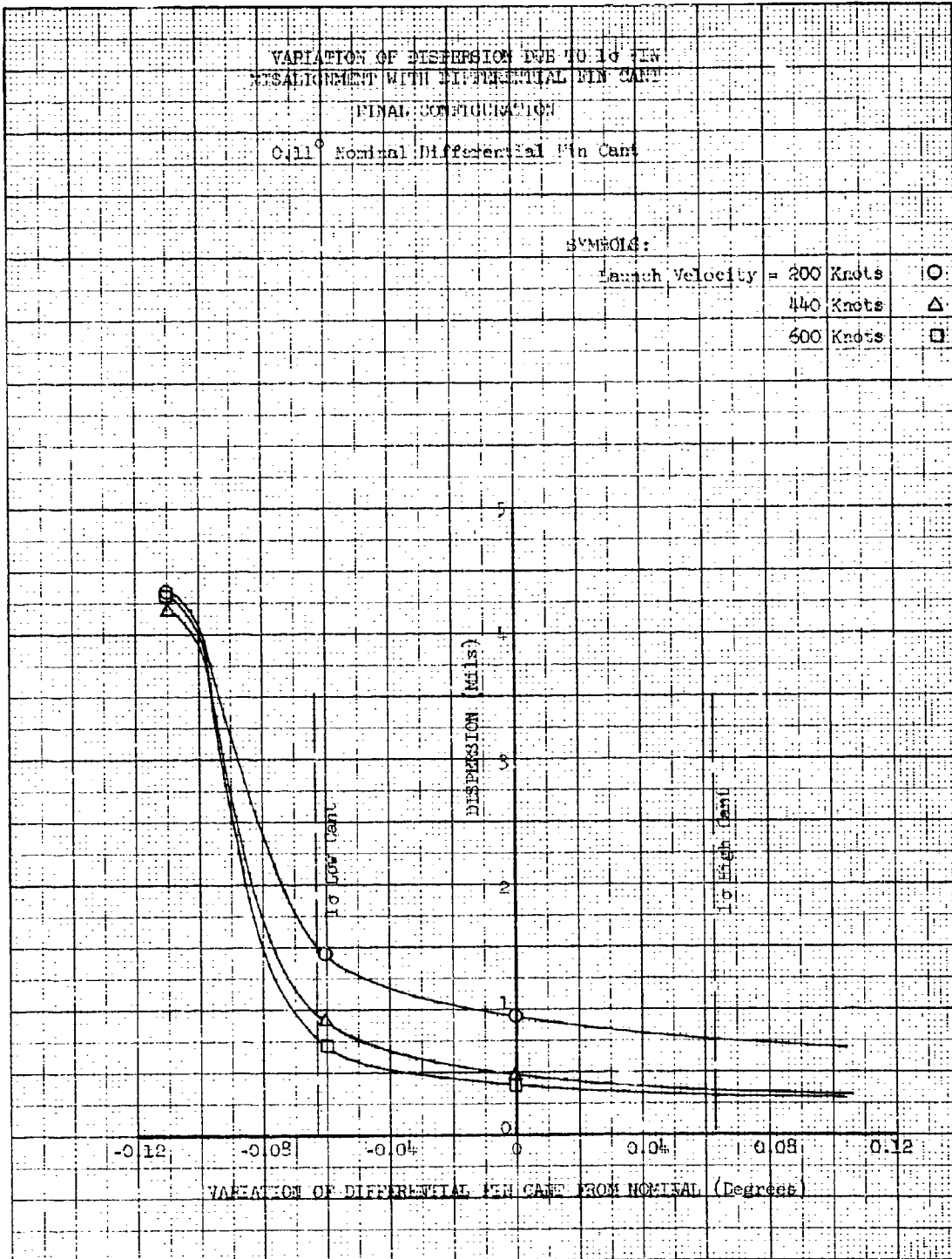


Figure 30  
Page 110

UNCLASSIFIED

UNCLASSIFIED

Report AFRPL-TR-69-90, Appendix A

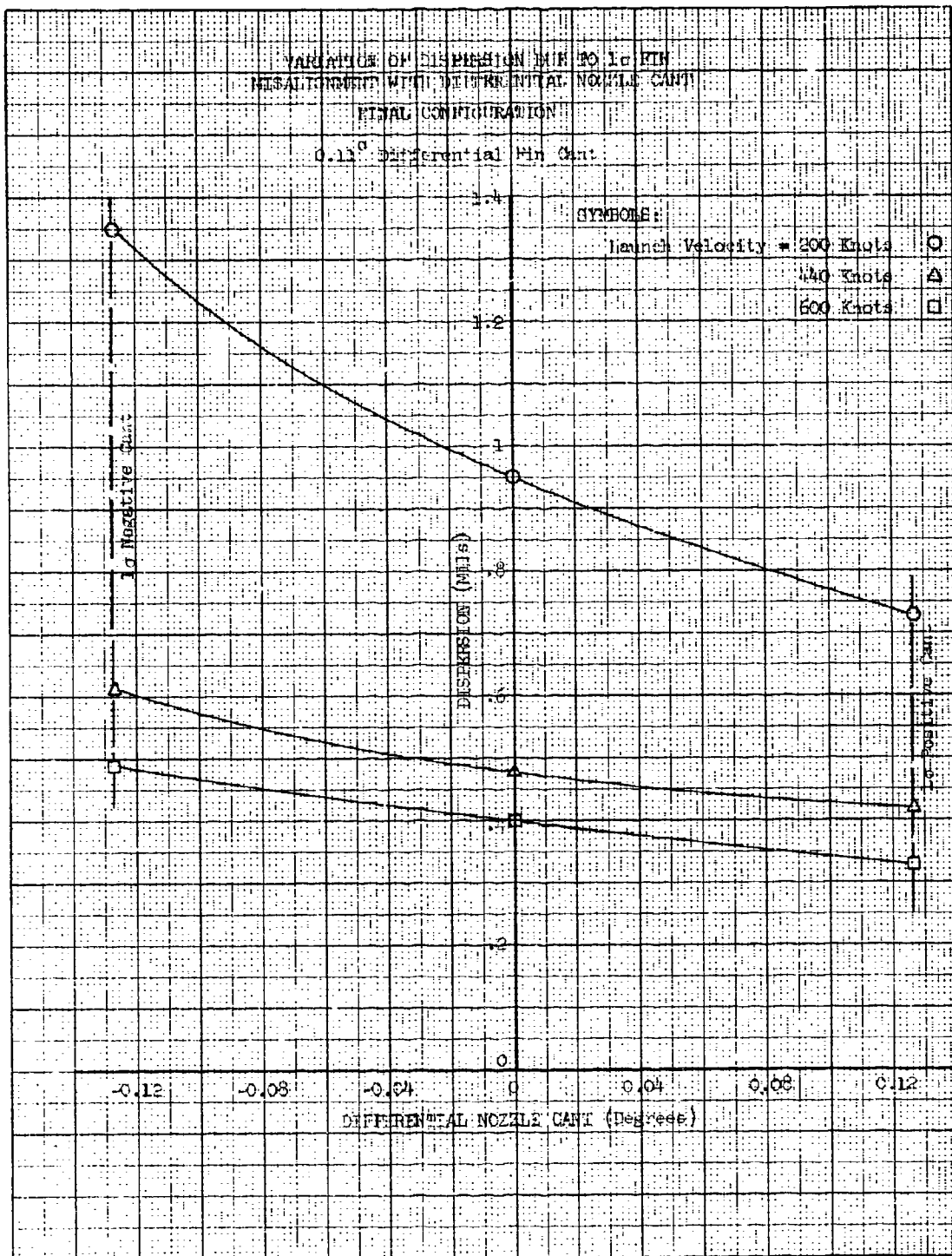


Figure 31  
Page 111

UNCLASSIFIED

UNCLASSIFIED

Report AFRPL-TR-69-90, Appendix A

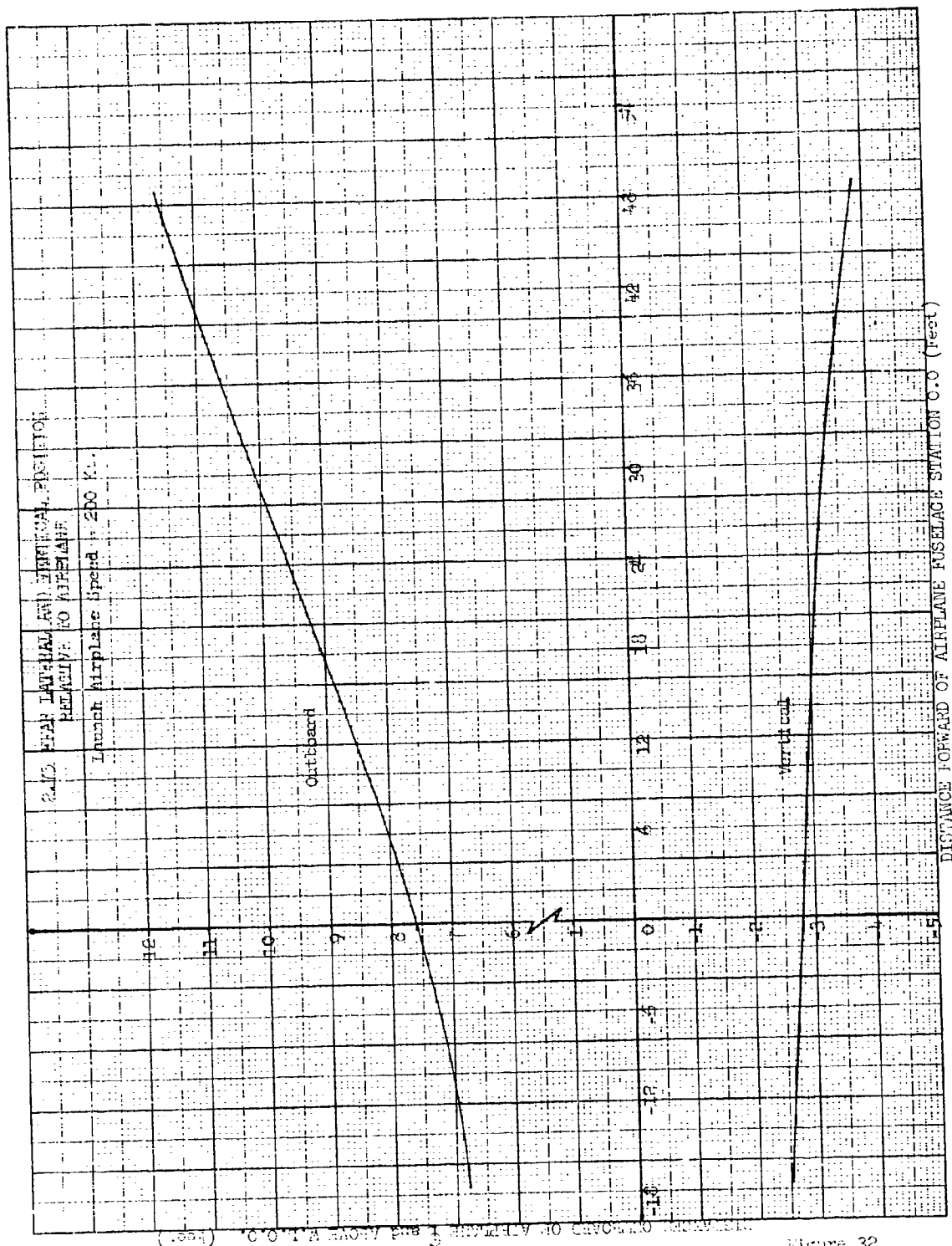
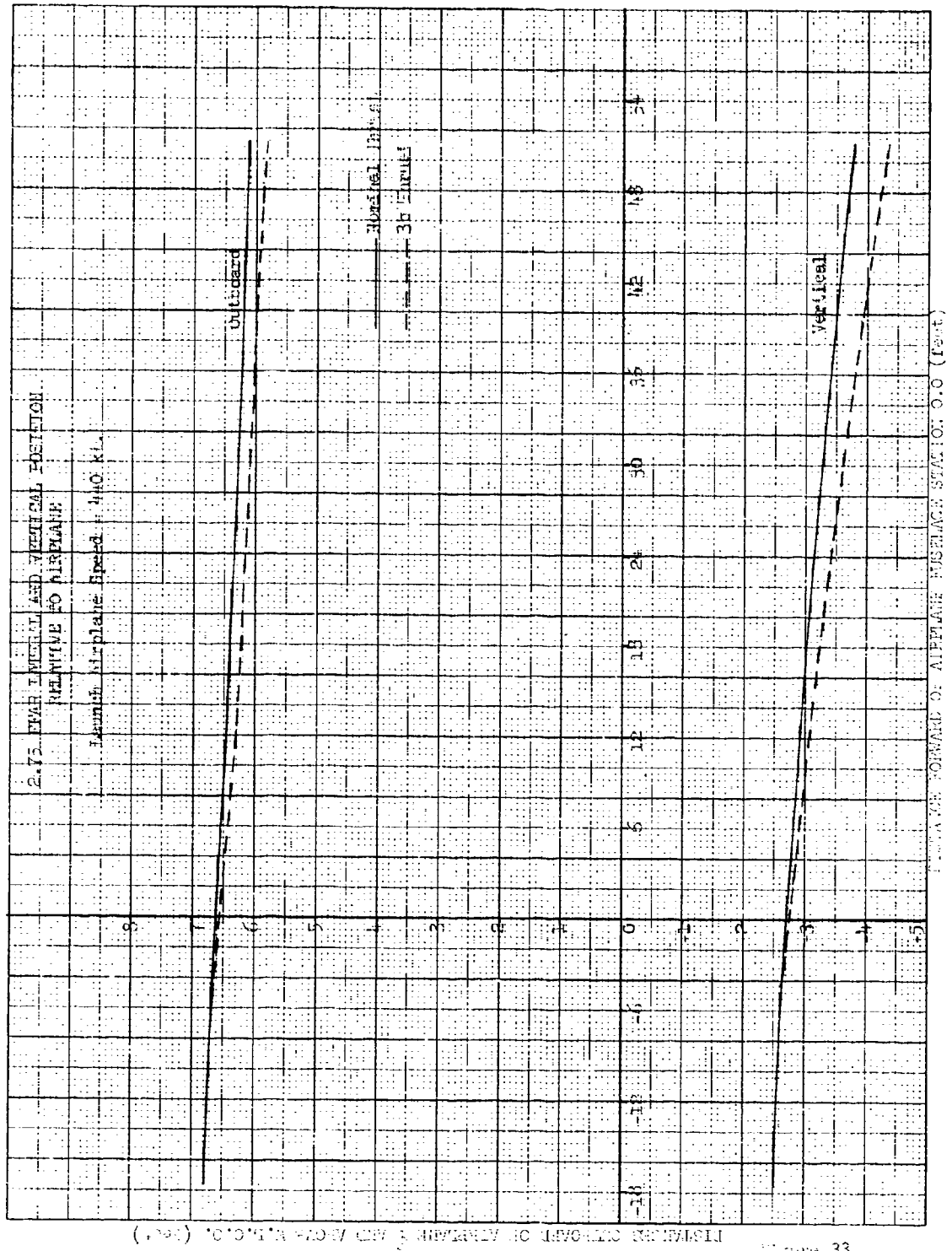


Figure 32  
Page 112

**UNCLASSIFIED**

UNCLASSIFIED

Report AFRPL-TR-69-90, Appendix A



UNCLASSIFIED

Figure 33  
Page 113

UNCLASSIFIED

Report AFRPL-TR-69-90, Appendix A

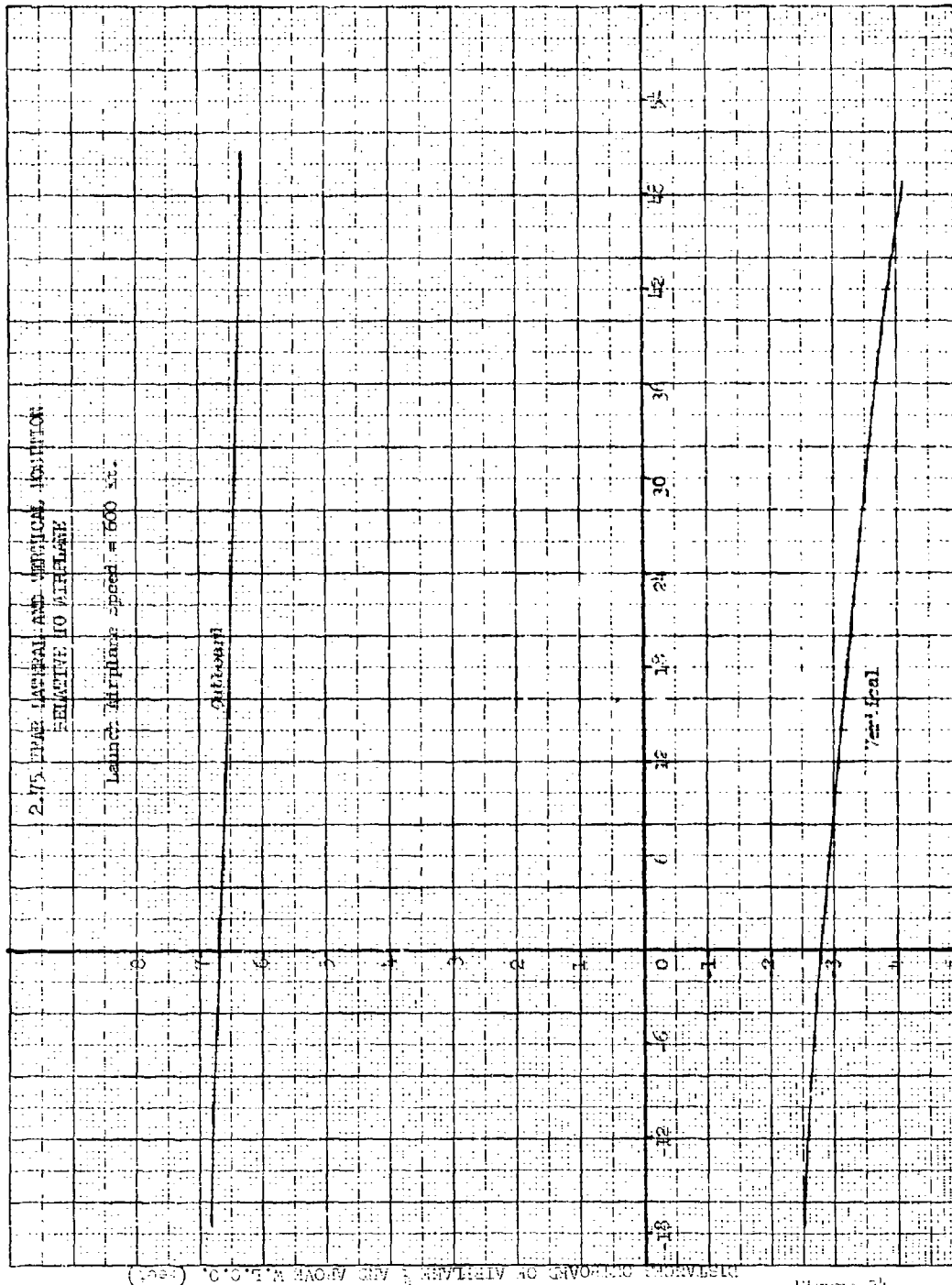


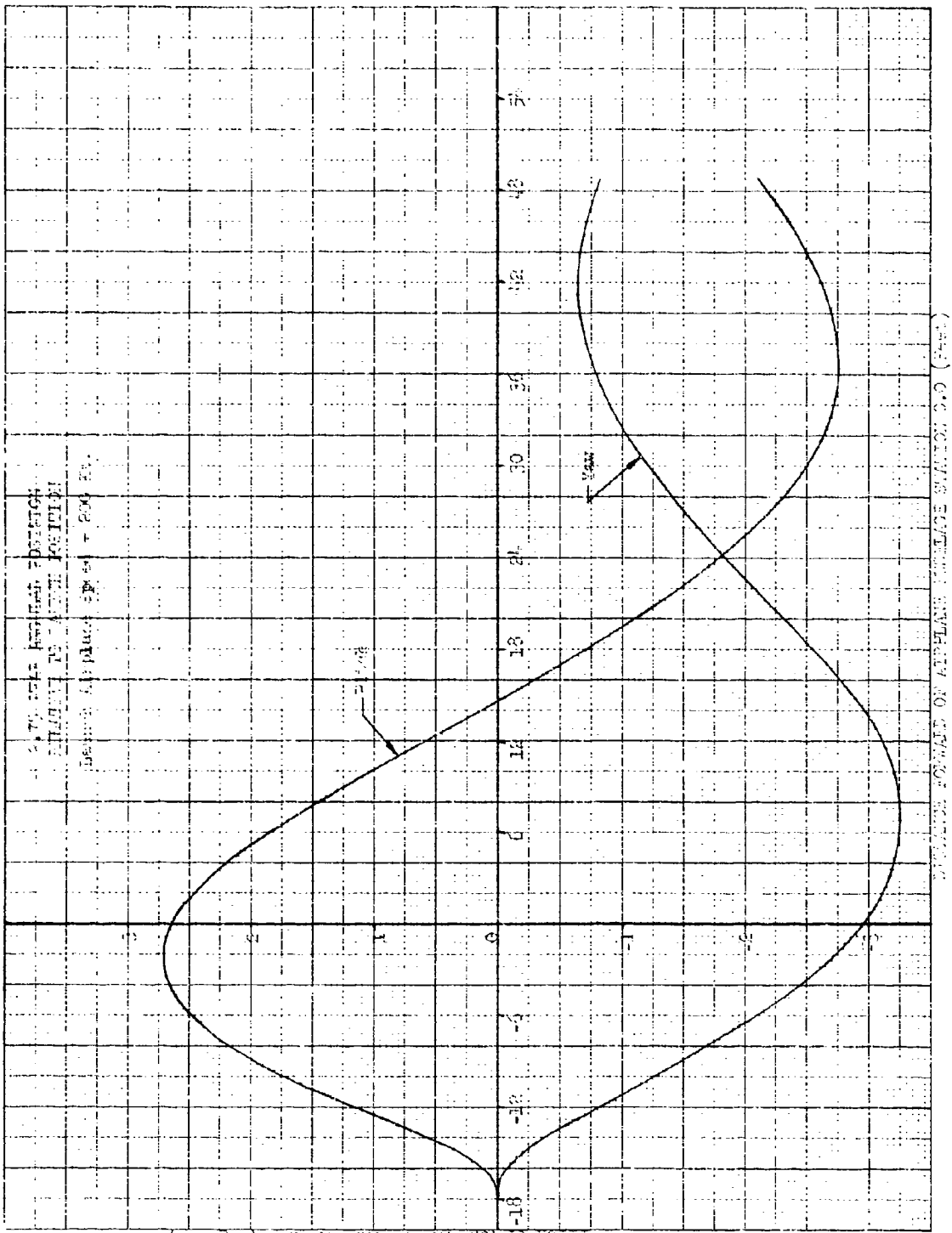
Figure 34  
Page 114

UNCLASSIFIED



UNCLASSIFIED

Report AFRPL-TR-69-90, Appendix A

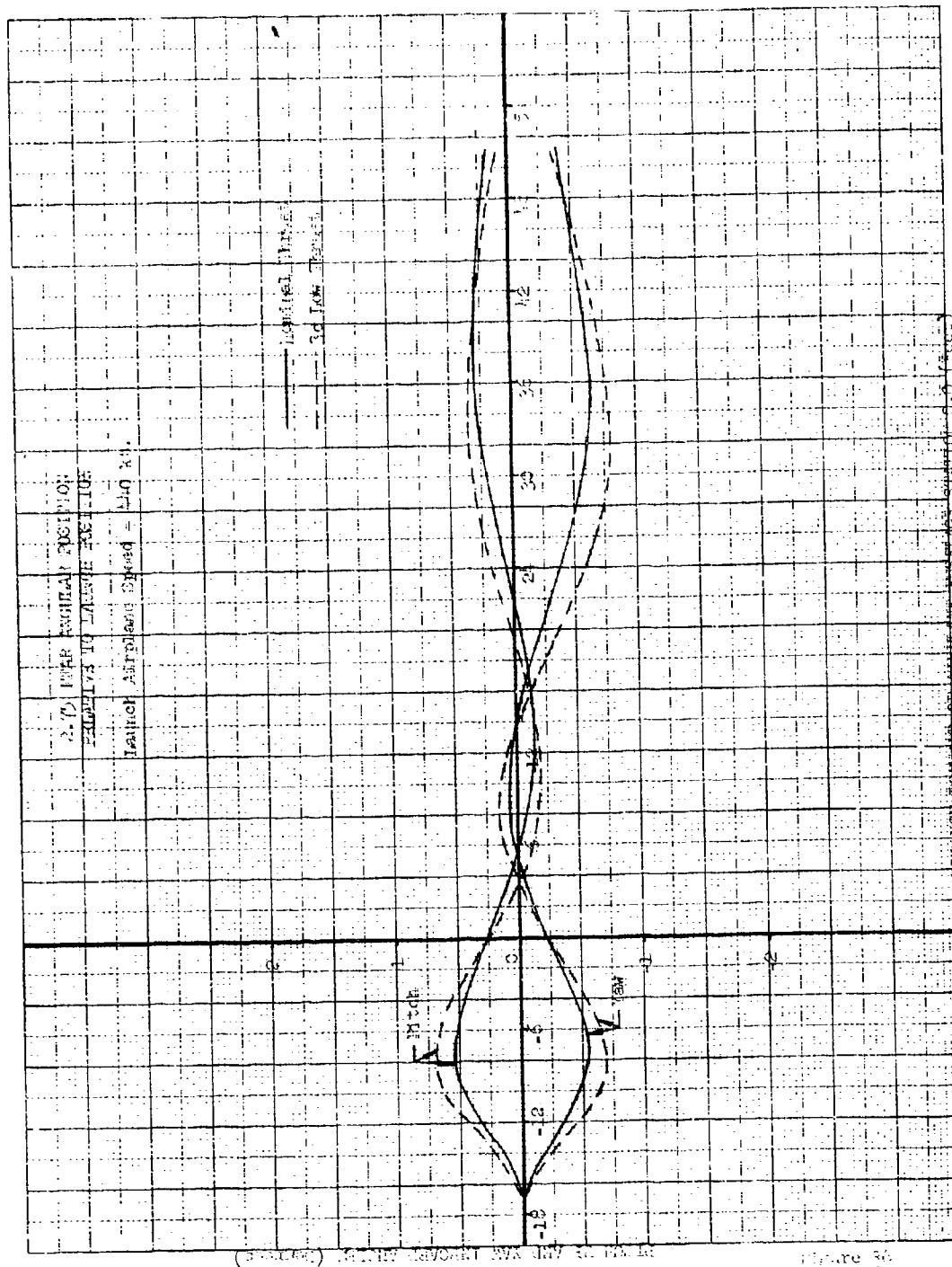


UNCLASSIFIED

Sheet 20  
Page 117

UNCLASSIFIED

Report ATRPL-TR-69-90, Appendix A



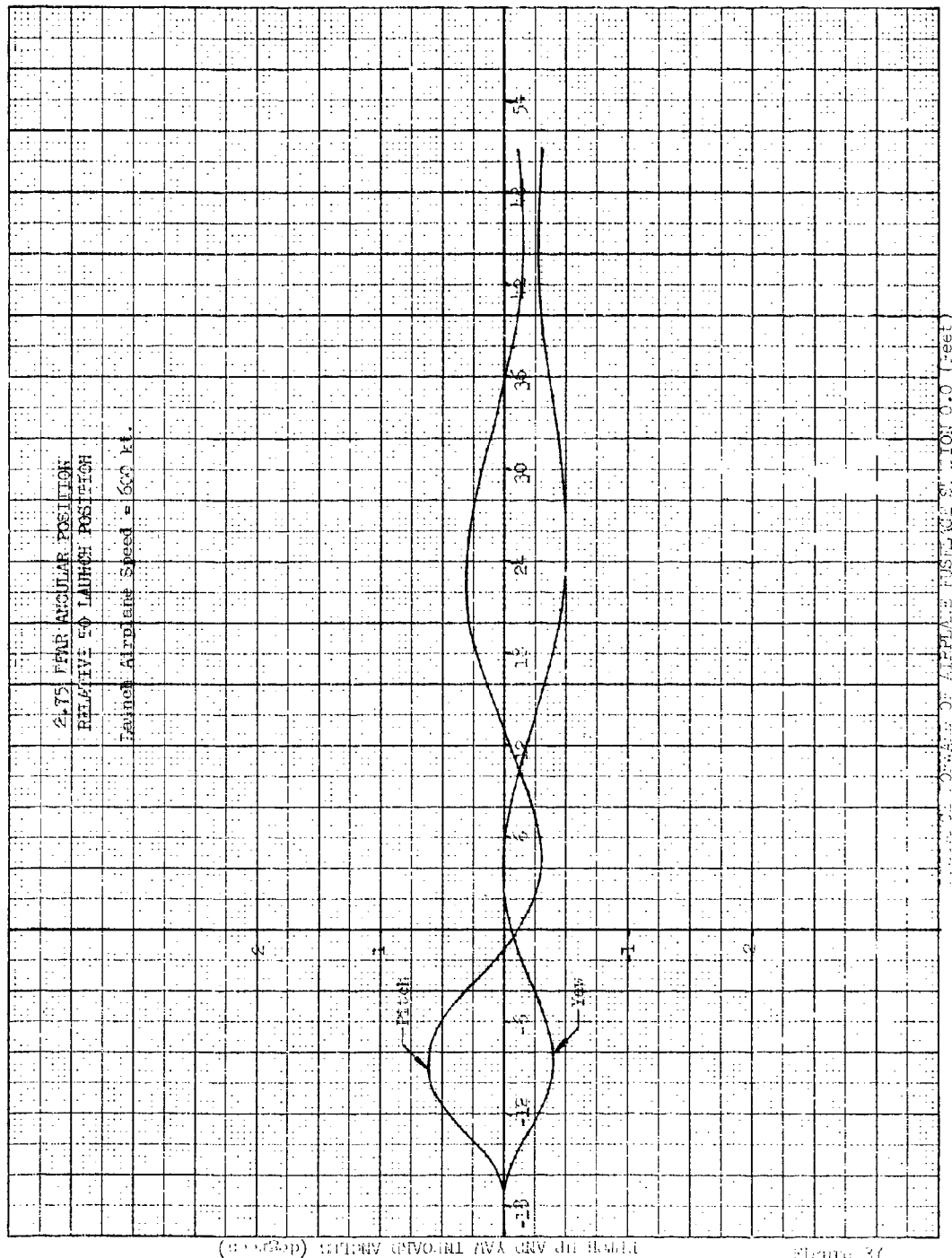
(30 km/s) 30 km/s

Figure 36  
Page 116

UNCLASSIFIED

UNCLASSIFIED

Report AFRPL-TR-69-90, Appendix A



(continued) AIRCRAFT YAW AND PITCH ANGLES

Figure 3/

Page 117

UNCLASSIFIED

**UNCLASSIFIED**

Report AFRPL-TR-69-90

**APPENDIX B**

**STRESS ANALYSIS**

**UNCLASSIFIED**

**UNCLASSIFIED**

Report AFRPL-TR-69-90, Appendix B

STRUCTURAL ANALYSIS OF

2.75 INCH DIAMETER

ROCKET MOTOR

February 1968

Revised May 1968

Contract FC 4611-67-C-0114

(W.O. 3297)

Prepared by:

Approved by:

*J. D. McConnell*

J. D. McConnell, Manager  
Structural Analysis, 3252  
Applied Mechanics

A. T. Caffo

*R. E. Leary*

R. E. Leary

*R. N. Shearly*

R. N. Shearly

**UNCLASSIFIED**

# UNCLASSIFIED

Report AFRPL-TR-69-90, Appendix B

## TABLE OF CONTENTS

	<u>Page</u>
I. INTRODUCTION	1
II. STRUCTURAL DESCRIPTION	2
III. STRUCTURAL DESIGN CRITERIA	4
A. GENERAL REQUIREMENTS	4
B. SPECIFIC DESIGN CONDITIONS	4
C. MATERIALS AND ALLOWABLES	5
IV. THERMAL ANALYSIS OF NOZZLES	19
V. STRUCTURAL ANALYSIS	23
A. MOTOR CASE	23
B. AFT CLOSURE ASSEMBLY	36
C. PROPELLANT GRAIN	69
REFERENCES	74

UNCLASSIFIED

# UNCLASSIFIED

Report AFRPL-TR-69-90, Appendix B

## LIST OF FIGURES

1. Structural Arrangement of 2.75-In.-Dia Rocket Motor Assembly
2. Mechanical Properties of MXC-313 Molding Compound
3. Coefficient of Thermal Expansion for Carbitex-700
4. Master Relaxation Modulus Curve for ANB-3241-2 Propellant
5. Shift Factor vs Temperature for ANB-3241-2 Propellant
6. Modulus vs Reduced Strain Rate for ANB-3241-2 Propellant
7. Allowable Firing Strain for ANB-3241-2 Propellant at  $-65^{\circ}\text{F}$  with 12 Percent Prestrain
8. Bond Tensile Stress vs Minimum Time to Failure for ANB-3241-2 Propellant
9. Allowable Bond Shear for ANB-3241-2 Propellant with Superimposed Hydrostatic Pressure
- 10a. Temperature Profiles Through Throat of 2.75 Nozzle
- 10b. Isotherms for Carbitex Nozzle Insert at  $t = 2.5$  Seconds
11. Motor Case Geometry and "Cut" Locations for Computer Solution - Forward End
12. Motor Case Geometry and "Cut" Locations for Computer Solution - Aft End
13. Lockwire Installation - 2.75-In. Rocket Motor
- 14a. Compressive Stresses at Inside Surface of Carbitex Insert at  $t = 2.5$  Sec - Case I
- 14b. Tensile Stress at Outside Surface of Carbitex Insert at  $t = 2.5$  Sec - Case I
- 15a. Compressive Stresses at Inside Surface of Carbitex Insert at  $t = 2.5$  Sec - Case II
- 15b. Shear Stress Distribution at Carbitex - Plastic Interface at  $t = 2.5$  Sec - Case II
16. Propellant Grain Configuration, 2.75-In. Motor

- iii -

UNCLASSIFIED

**UNCLASSIFIED**

Report AFRPL-TR-69-90, Appendix B

**DRAWING LIST**

<u>Component Description</u>	<u>Part No.</u>	<u>Change Letter</u>
Interface Control Envelope - 2.75 FFAR	1146578	
Rocket Motor Assembly	1146668-1	
O Ring	1127114	
Igniter and Closure Assembly	1146673-1	
Clip Assembly	1146031-1	B
Shunt Wire	1146336-1	
Igniter Assembly	1146693-1	A
Squib, MK 1, MOD 1	656714	
Chamber, Igniter	1146095-1	
End Plug, Igniter	1146096-1	
Cap, Insulator	1146370-1	C
Initiator Charge	1146877-1	
Washer	1146875-1	
Disc	1146876-1	
Fin and Closure Assembly	1146678-1	
Cross Head	456909	
O Ring	650950	
O Ring	650953	
Contact Disc	1253129	
Fin Retainer	1253131	
Nut	MS 20365-1032	
Pin, Straight	1146056-1	
Fin Blade	1146210-1	A
Closure Assembly	1146639-4	A
Plate, Nozzle	1146335-1	A
Sleeve	1146365-1	
Washer	1146613-3	
Insert, Throat	1146659-19	B
Weather Seal	1146913-1	A
Piston Assembly	1146916-1	
Wire	1146915-1	
Wire	1146915-2	
Sleeve	1146917-1	
Piston Assembly	1146932-1	
Piston Assembly	9220797	
Connector	9220788	
Chamber and Grain Assembly	1146759-1	B
Chamber, Insulated	1146637-1	B
Motor Tube	1569403	
Insulator, Released	1146636-1	A
Insulator, Fwd	1146033-1	
Lockwire	1146924-1	
Masterline Drawing - 2.75 FFAR	1146103	

**UNCLASSIFIED**



# UNCLASSIFIED

Report AFRPL-TR-69-90, Appendix B

## SUMMARY OF LIMITS FACTORS OF SAFETY

<u>Item</u>	<u>Drawing No.</u>	<u>Material</u>	<u>Design Condition</u>	<u>Type Stress</u>	<u>M.S.</u>	<u>Page No.</u>
Motor Case	BUMEPS 1569403	2014 Alum	High Temp Firing - Ult	Tensile + Bending	-0.12	31
Nozzle Plate	1146335-2	7075 Alum	High Temp Firing - Ult	Bending	0.99	
Propellant Grain		ANB-3241-2	(Reference, Table 5, page 73)			

UNCLASSIFIED

# UNCLASSIFIED

Report AFRPL-TR-69-90, Appendix B

## I. INTRODUCTION

This report covers the structural analysis of the 2.75 inch diameter Folding Fin Aircraft Rocket (FFAR), hereinafter referred to as the 2.75 inch rocket motor. This motor is being developed and produced for the Air Force by the Aerojet-General Corporation under Contract FO 4611-67-C-0114 (Reference 1). Whereas the structural analysis covers the complete motor assembly it should be emphasized that the actual motor case or chamber is supplied to Aerojet as government-furnished equipment.

Conventional methods of structural analysis are used throughout this report and, unless defined in the text, all notation conforms to that used in MIL-HDBK-5 (Reference 2).

In order to best handle the specialized structural problems associated with solid rocket motors extensive use has been made of the digital computer programs which have been developed by Aerojet-General. Brief descriptions of these programs are contained within this report and additional information covering the formulation is available upon request.

UNCLASSIFIED

# UNCLASSIFIED

Report AFRPL-TR-69-90, Appendix B

## II. STRUCTURAL DESCRIPTION

The 2.75 inch rocket motor consists of a deep drawn aluminum chamber with a threaded forward skirt for warhead attachments. An aft closure assembly containing four nozzles is attached to the cylindrical chamber by means of a steel lockwire. In addition to the four nozzles the aft closure assembly provides support for four aerodynamic fins. These fins are folded within the 2.75 inch envelope diameter prior to launch, and are actuated by a small gas operated piston in the center of the aft closure. Upon motor firing the fins are forced open to a 45 degree angle with respect to the motor centerline. In addition to providing aerodynamic stability, the fins are designed with a small cant angle which imparts a rotation about the missile center line.

The propellant grain is cylindrical in cross section and designed to burn only on the inside surface.

A sketch showing the overall structural arrangement is contained in Figure 1.

UNCLASSIFIED

Report AFRPL-1R-69-90, Appendix B

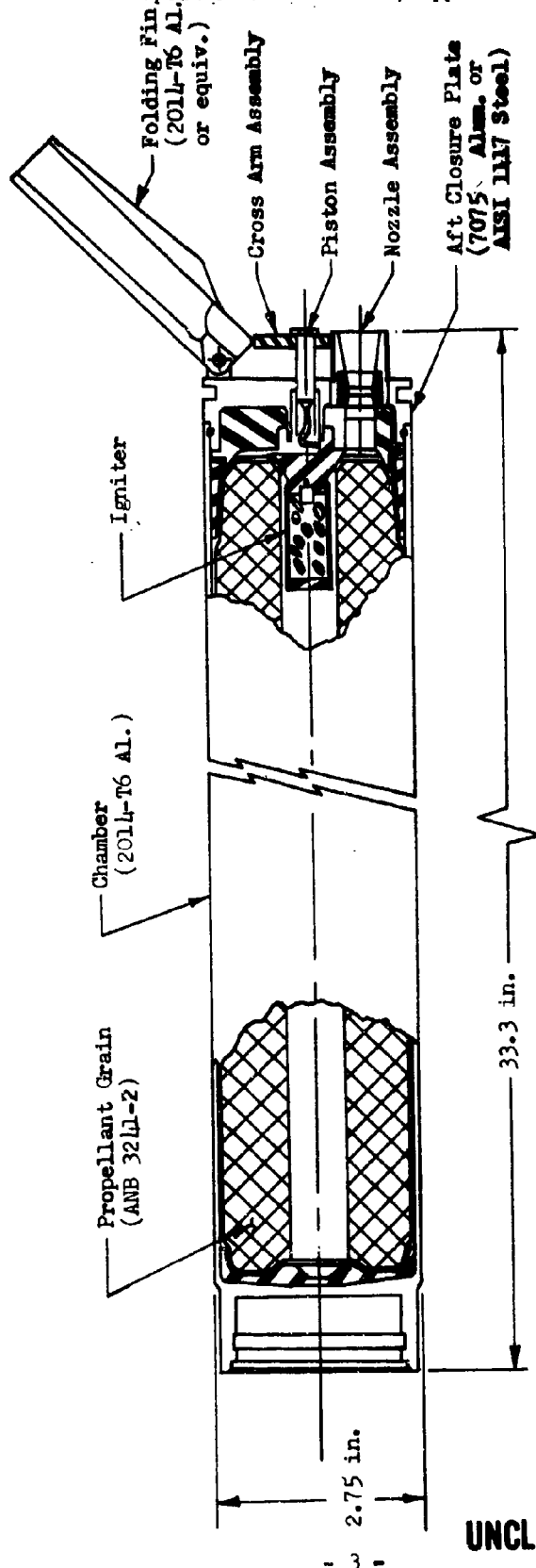


Figure 1

Structural Arrangement of 2.75 Inch Diameter  
Rocket Motor Assembly

UNCLASSIFIED

# UNCLASSIFIED

Report AFRPL-TR-69-90, Appendix B

## III. STRUCTURAL DESIGN CRITERIA

### A. GENERAL REQUIREMENTS

In accordance with the revised technical requirements of Reference (1), a safety factor of 1.5, based upon the ultimate strength of the material, shall be used for the structural analysis of all metal parts. In addition, Part III-B-1-f of the same document states that: "The motor shall be capable of successful operation over a temperature range of -65 to +150°F."

### B. SPECIFIC DESIGN CONDITIONS

Based upon an evaluation of available data and known requirements the following specific design conditions were selected for detail structural analysis.

#### 1. Hydrotest

In this condition the chamber assembly is fitted with a test plug and subjected to an internal pressure of 2000 psi. The resultant stresses for this condition were compared to the minimum yield strength of the chamber material.

#### 2. Low Temperature Storage

In this condition the loaded motor was considered exposed to the lowest environmental temperature of -65°F. This condition produces the maximum tensile stress in the propellant to liner bond system and these stresses were checked against the measured strength of the bond system.

#### 3. High Temperature Flight

In this condition the motor was considered subjected to the maximum expected operating pressure (MEOP) in combination with flight loads.

- 4 -

UNCLASSIFIED

## UNCLASSIFIED

Report AFRPL-TR-69-90, Appendix B

Based on ballistic calculations plus development firing data the MEOP for a motor conditioned to 150°F is 1990 psi. This value includes an estimated three standard deviations from the mean to account for statistical variations. The only flight loads of significance in the structural design are the aerodynamic loads on the fins. Aerodynamic studies plus tests at the Arnold Engineering Development Center in Tullahoma, Tennessee, have established the maximum lift and drag load per fin to be 50.50 and 26.76 lb, respectively. These loads are considered to act at the center of pressure of the fin which is 2.09 in. from the hinge pin and 0.45 in. from the leading edge.

### 4. Low Temperature Firing

In this condition consideration was given to firing a motor conditioned to -65°F. This condition produces the maximum strain in the propellant grain and the maximum shear stress in the propellant to liner bond.

### C. MATERIALS AND ALLOWABLES

Details concerning the specific composition and allowable strength of each component is contained in the structural analysis section of this report. For convenience, however, some of the more important information is listed below.

#### 1. Motor Case

The 2.75 inch diameter motor case is government furnished equipment, and is made from 2014 T6 aluminum with specified tensile strengths of 58,000 psi yield and 66,000 psi ultimate.

UNCLASSIFIED

# UNCLASSIFIED

Report AFRPL-TR-69-90, Appendix B

## 2. Nozzle Assembly

The materials of primary interest in the nozzle assembly are the Carbitex-700 used for the four throat inserts and the MXC-313 carbon fiber molding compound which supports the Carbitex inserts. Unfortunately, neither of these materials has been completely characterized over the full operating temperature range. Some laboratory test values are available, however, and these were used as a basis to estimate the necessary properties to perform a structural analysis. The actual values used in the analysis are as indicated below:

### a. MXC-313

This material was considered to be homogeneous and isotropic, but its properties were considered to be quite temperature dependent. Plots of estimated modulus, coefficient of thermal expansion and Poisson's Ratio as functions of temperature are shown on Figure 2.

### b. Carbitex-700

This material is a fibrous graphite having highly directional properties. Based on dynamic modulus measurements over a limited temperature range it was assumed that the modulus would be constant over the entire operating temperature range and have a value of 1,800,000 psi in the plane of the laminates and 900,000 psi across the laminates.

Poisson's Ratio was also assumed constant at 0.150 and considered to have the same value in all directions. The coefficient of thermal expansion was considered to vary with temperature in accordance with the plots shown in figure 3.

UNCLASSIFIED

UNCLASSIFIED

Report AFRPL-TR-69-90, Appendix B

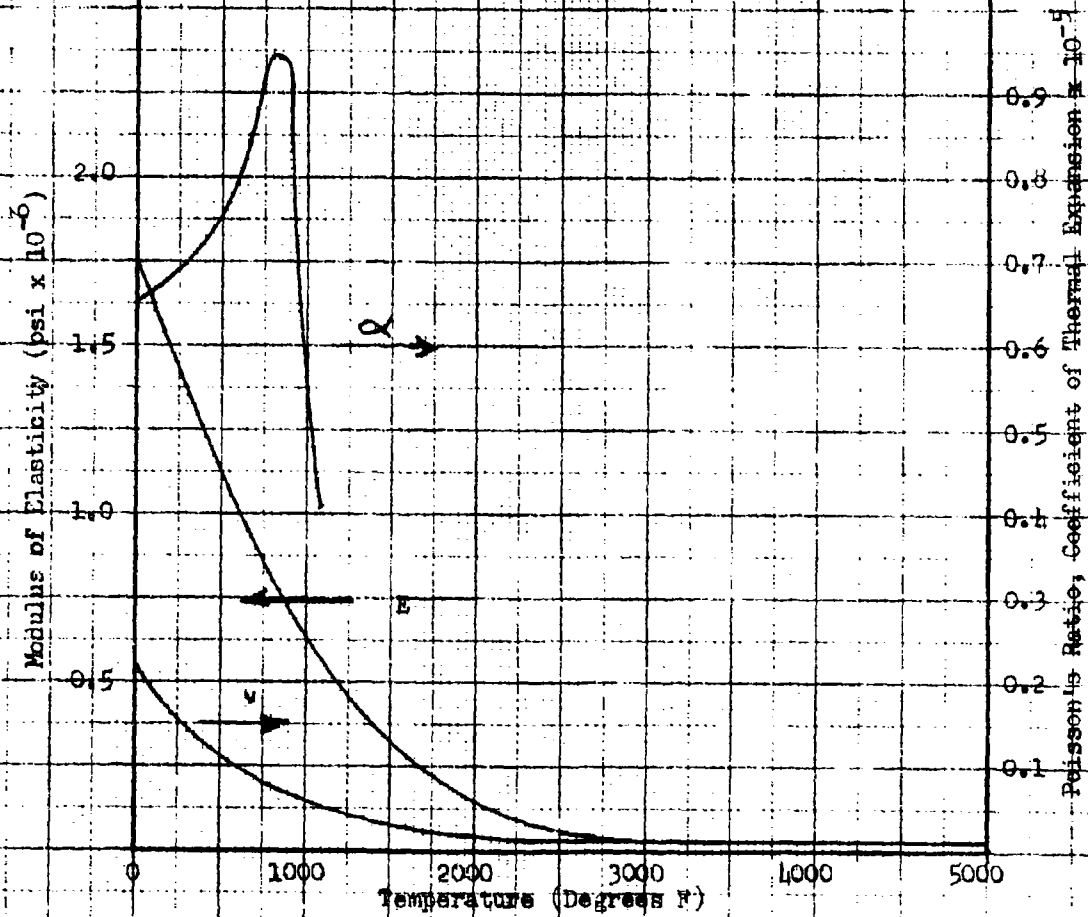


Figure 2  
Mechanical Properties  
of MXC-313 Molding Compound

UNCLASSIFIED



UNCLASSIFIED

Report AFRPL-TR-69-90, Appendix B

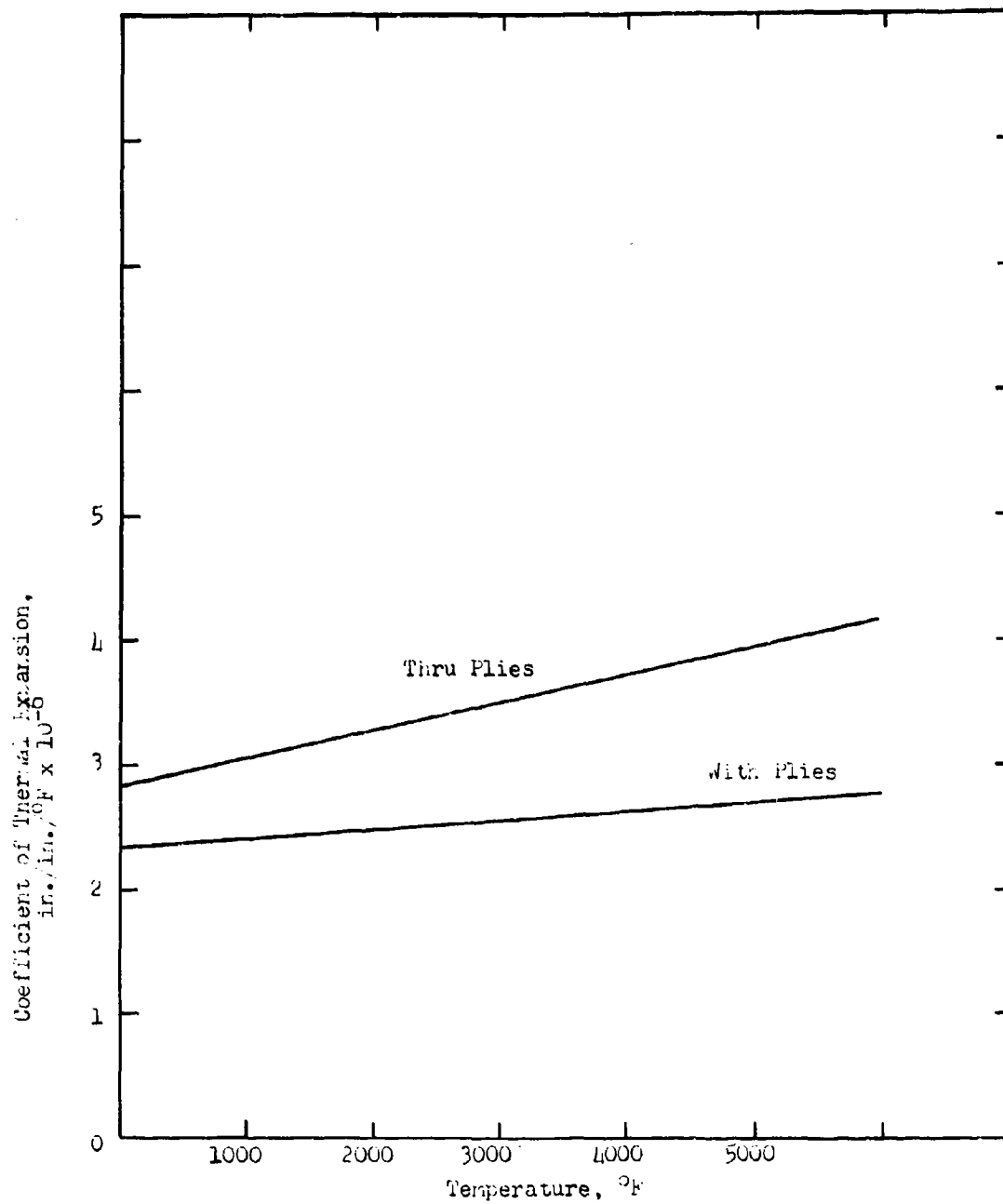


Figure 3  
Coefficient of Thermal Expansion  
for Carbitex-100

- 0 -

UNCLASSIFIED

# UNCLASSIFIED

Report AFRPL-TR-69-90, Appendix B

## 3. Propellant Grain

The 2.75-in. motor utilizes ANB-3241-2 propellant. A fairly complete mechanical property characterization of this propellant was conducted in conjunction with the cumulative damage program, and the results of this work which are required for the structural analysis are reproduced here for convenience.

### a. Coefficient of Thermal Expansion

The volume coefficient of thermal expansion was determined by means of measurements of propellant density at various temperatures over the range -80 to 80°F. The slope of a density-temperature plot provides the desired value. The linear coefficient is taken to be one-third of the volumetric. The average linear value for ANB-3241-2 determined from tests of specimens from three batches is  $6.1 \times 10^{-5} \text{ } ^\circ\text{F}^{-1}$ . While this is somewhat higher than the value of 5.4 used in the initial stress analysis a change in the analysis is not considered warranted. This is primarily due to the close correlation between the measured strains on the full-scale cycling motors and the initial calculation using  $\alpha = 5.4 \times 10^{-5} \text{ } ^\circ\text{F}^{-1}$ . The average measured strain on five motors was 12.3% versus the calculated value of 12.7%.

### b. Modulus

Stress relaxation tests were performed with end-bonded uniaxial specimens at -75, -40, 0, 40, 77, 110 and 150°F. Strains of 0.5 - 1.0% were applied at a rate of  $0.25 \text{ min}^{-1}$  and held for 10 min while the decay in stress was measured. The data obtained were plotted in the form of relaxation modulus versus time for each test temperature. Superposition of the data was accomplished by correcting the modulus by the ratio,  $T_s/T$ . ( $T_s$  = reference

UNCLASSIFIED

# UNCLASSIFIED

Report AFRPL-TR-69-90, Appendix B

temperature = 298°K (77°F),  $T$  = test temperature in °K) and manually shifting the curves along the time axis until they superimposed at the reference temperature. The resulting "master curve," shown in Figure 4, provides the modulus data needed for the thermal stress analysis. The shift factors required to superpose the data are shown in Figure 5.

Modulus values pertinent to the analysis of high rate loading conditions such as handling, acceleration and firing are obtained from a plot of modulus versus reduced strain rate ( $\dot{\epsilon} a_T$ ) as shown in Figure 6 for a reference temperature of 77°F. Moduli for other temperatures can be simply determined from this plot by multiplying the strain rate of interest by the appropriate  $a_T$  from Figure 5 and entering the curve of Figure 6 at that point.

## c. Allowable Stresses and Strains

The methods used to estimate the allowable strains and stresses for the propellant and bonds are based on simulating in the laboratory, by means of careful specimen design and environmental control, the critical motor conditions and treating the resulting data to account for the expected variability in properties. The basic relation used in calculating the allowables is given below:

$$X_a = \bar{X}K [1 - (3 + a) V] \quad (1)$$

where:

$X_a$  = allowable stress or strain

$\bar{X}$  = mean measured property obtained under appropriate test conditions

$K$  = stress concentration or multiaxiality correction factor

$a$  = statistical parameter which depends upon number of samples tested and level of confidence required

$V$  = coefficient of variation for property being measured

- 10 -

UNCLASSIFIED

# UNCLASSIFIED

Report AFRPL-TR-69-90, Appendix B

## (1) Strain Allowables

Because of the complications presented by such things as strain-temperature-time path dependency the evaluation of thermal cycling capability cannot be handled simply using uniaxial or biaxial tests. The best approach has been the use of analogue motors, with cylindrical bores of various sizes, thermally cycled to failure. In the case of the 2.75-in. motor the small size makes it convenient to test the full-scale article. A total of 31 motors are scheduled for cycling. To date, one set of five full-scale motors and four short-length motors from Batch 68-46 have been cycled between 150 and -65°F. The results to date are summarized below.

<u>Motor No.</u>	<u>Measured Strain at -65°F, %</u>	<u>Cycles Completed</u>	<u>Remarks</u>
2601 <sup>(1)</sup>	12.4	10	Cracked on 11th cycle
2602	12.3	20	Test continuing
2603	12.4	20	Test continuing
2604	12.1	16	Cracked on 17th cycle
2614	12.1	19	Test continuing
68-46-1 <sup>(2)</sup>	13.6	5	Cracked on 6th cycle Void at base of crack
68-46-2	13.9	18	Cracked on 19th cycle
68-46-3	13.4	12	Cracked on 12th cycle
68-46-3	14.4	6	Cracked on 7th cycle

(1) Full-scale motors

(2) Short length motors (14-in. long)

These data for one propellant batch indicate a substantial safety margin for the specification requirement of three cycles. Similar tests will be performed on additional batches to establish variability.

The allowable inner bore hoop strain for firing at -65°F was estimated from the results of high rate tensile tests of pretrained

UNCLASSIFIED

# UNCLASSIFIED

## Report AFRPL-TR-69-90, Appendix B

specimens. The tests were conducted in a high pressure (1000 psig) environment to simulate the conditions at the inner bore during motor ignition. The prestrain on the specimens was about 12% corresponding to the expected maximum thermal strain at the inner bore at  $-65^{\circ}\text{F}$ . The results, calculated using Equation (1), are shown in Figure 7, a K value of 0.83 was used to correct the uniaxial values to equivalent biaxial elongations.

### (2) Bond Stress Allowables

A preliminary evaluation of the bond capability for storage was made from the results of constant rate tension tests of poker-chip sandwich specimens prepared from ANB-3241-2 propellant and sandwich specimens prepared from ANB-3241-2 propellant and IRS-105-LX insulation. Tests were conducted at crosshead rates of 0.02, 0.2 and 2.0 in. per minute and temperatures of  $-65$  and  $150^{\circ}\text{F}$ . The results plotted in the form of stress versus reduced time to failure for a reference temperature of  $-65^{\circ}\text{F}$  are presented in Figure 8. The estimated allowable stress was obtained from these data by use of Equation (1) with K taken to be 1.1. In addition, the time values were corrected by a factor  $A = 0.1$ , to account for the fact that during the constant rate test the maximum stress is not applied to the specimen for the full duration of the test.

Based on observed behavior of a number of other similar propellant systems the allowable long time bond shear allowable is estimated to be 80% of the bond tensile value.

Poker-chip bond specimens tested in shear at several rates, and with superimposed pressure, provide the data needed for calculation of the allowable bond shear stresses for motor firing. Again Equation (1) was used with a K factor of 1.2. The results for firing temperatures of  $-65$  and  $150^{\circ}\text{F}$  are shown in Figure 9.

UNCLASSIFIED

Report AFRPL-TR-69-90, Appendix B

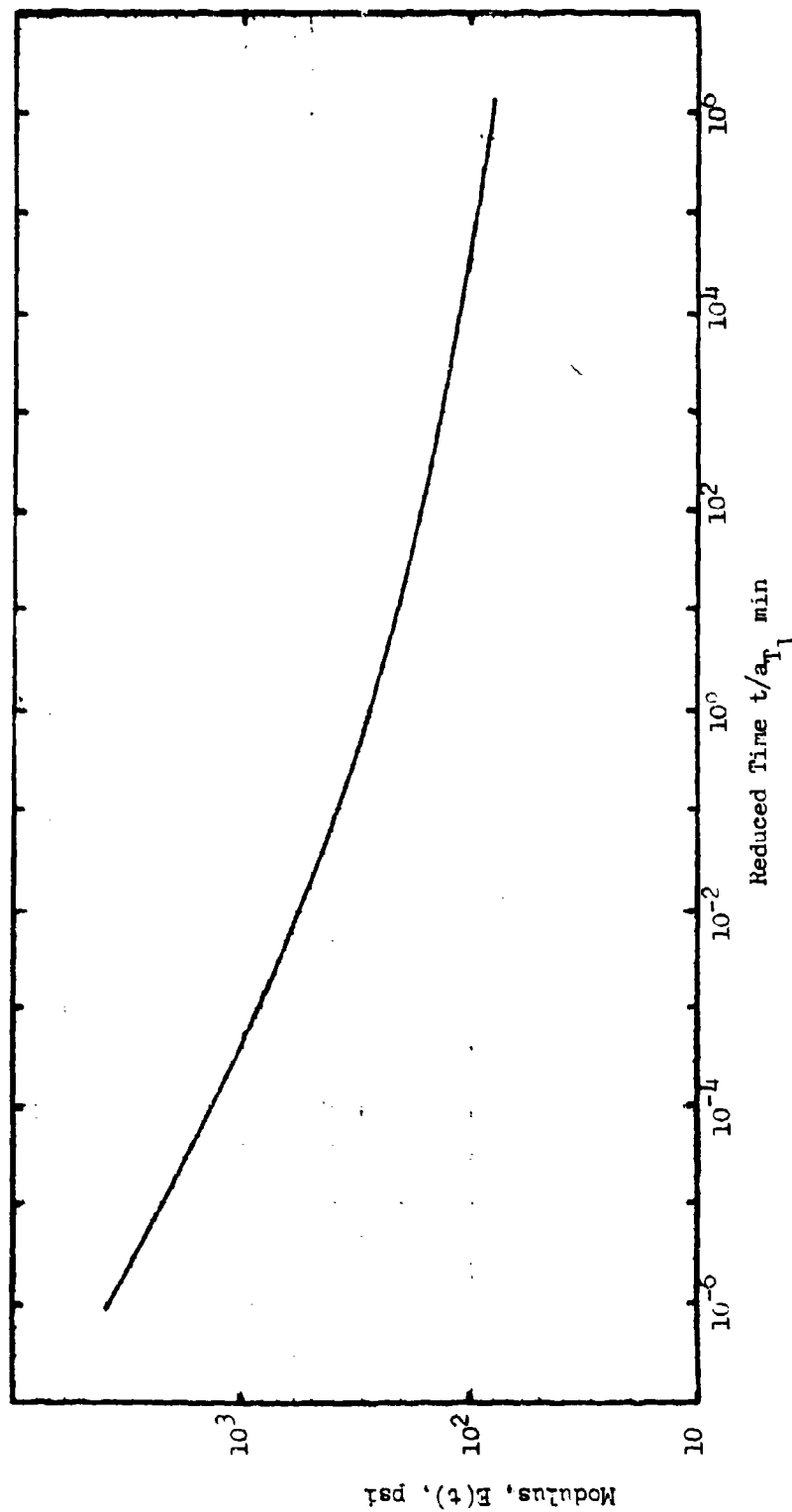


Figure 4  
Master Relaxation Modulus Curve  
for ANB-32/11-2 Propellant

UNCLASSIFIED

# UNCLASSIFIED

Report AFRPL-TR-69-90, Appendix B

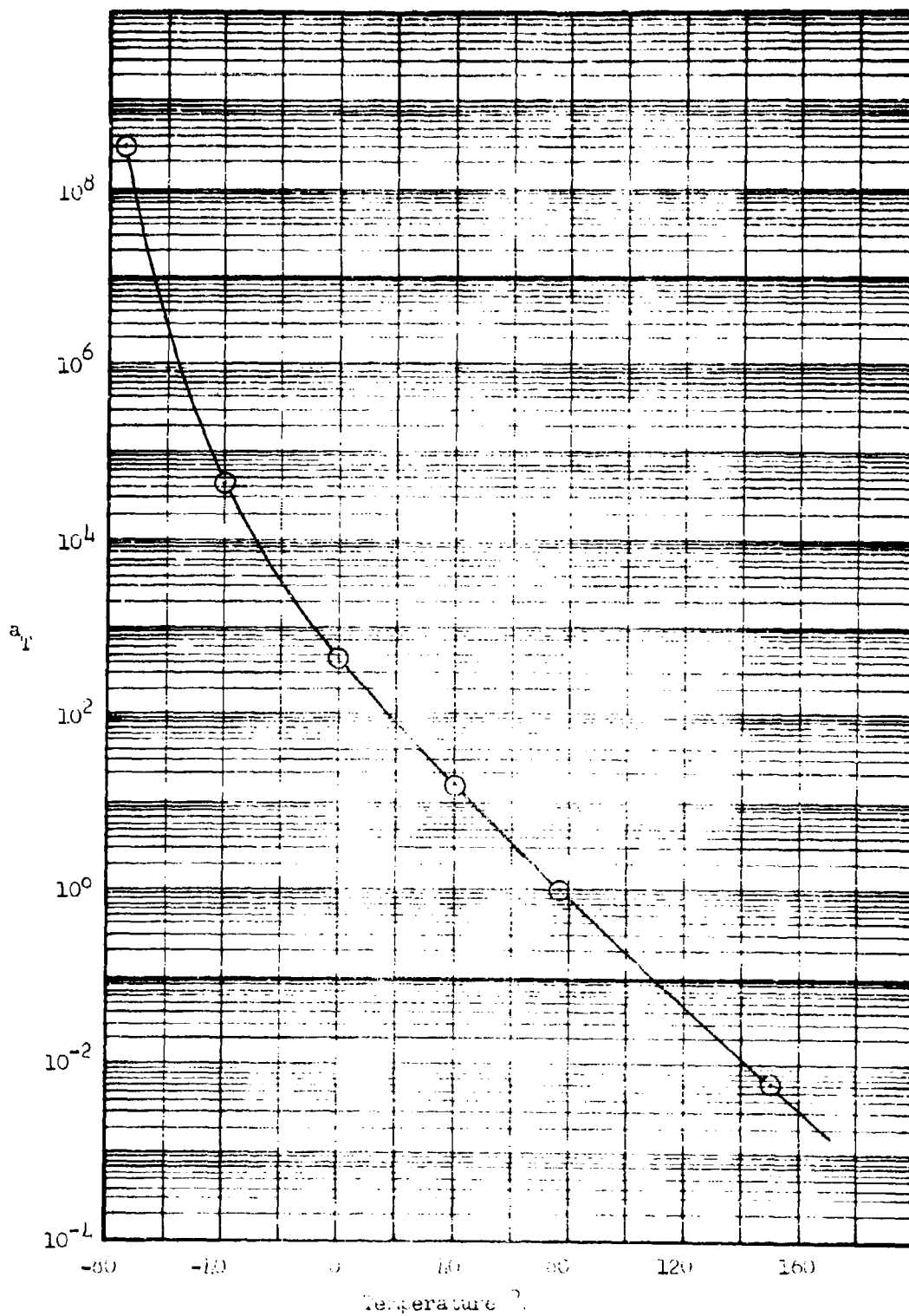


Figure 5  
Shift Factor vs Temperature  
for ANB 3241-2 Propellant

UNCLASSIFIED

Report AFRPL-TR-69-90, Appendix B

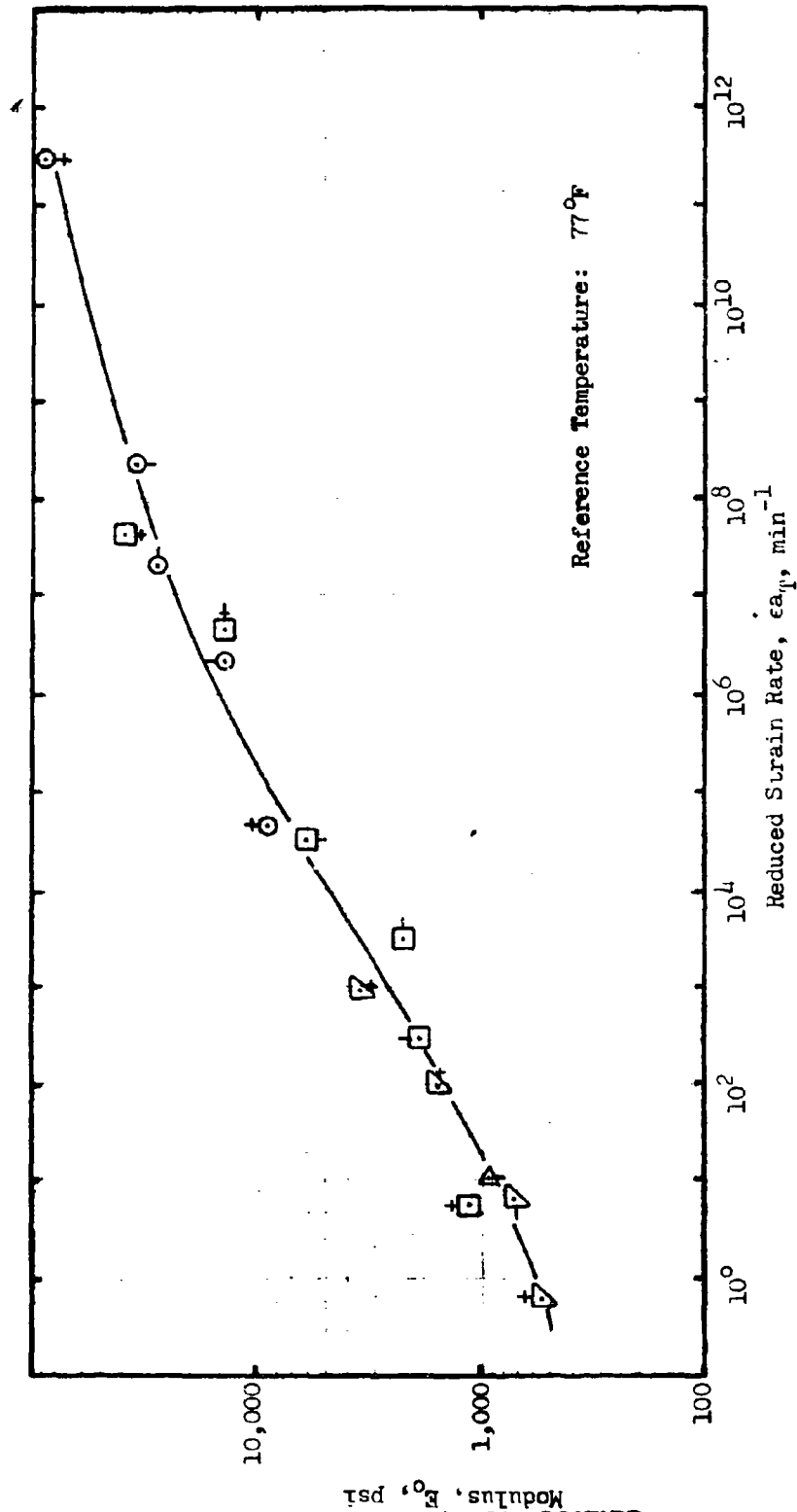


Figure 6  
Modulus vs Reduced Strain Rate  
for AHB 3241-2 Propellant



UNCLASSIFIED

Report AFRPL-TR-69-90, Appendix B

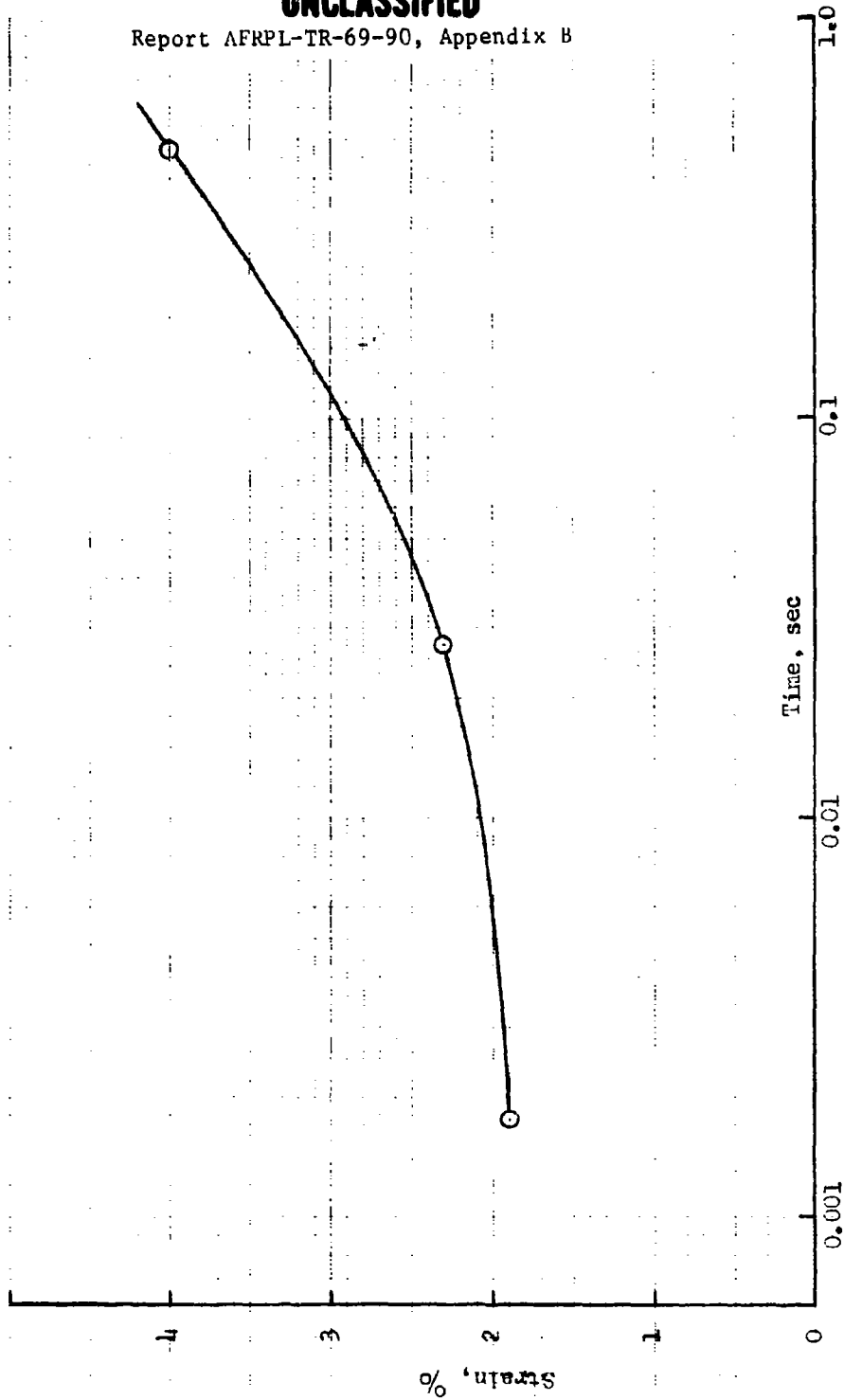


Figure 7  
Allowable Incremental Firing Strain for ANB-32/L-2  
Propellant at -65°. Strain is in Addition to  
Approximately 12 Percent Thermal Prestrain

UNCLASSIFIED

Report AFRPL-TR-69-90, Appendix B

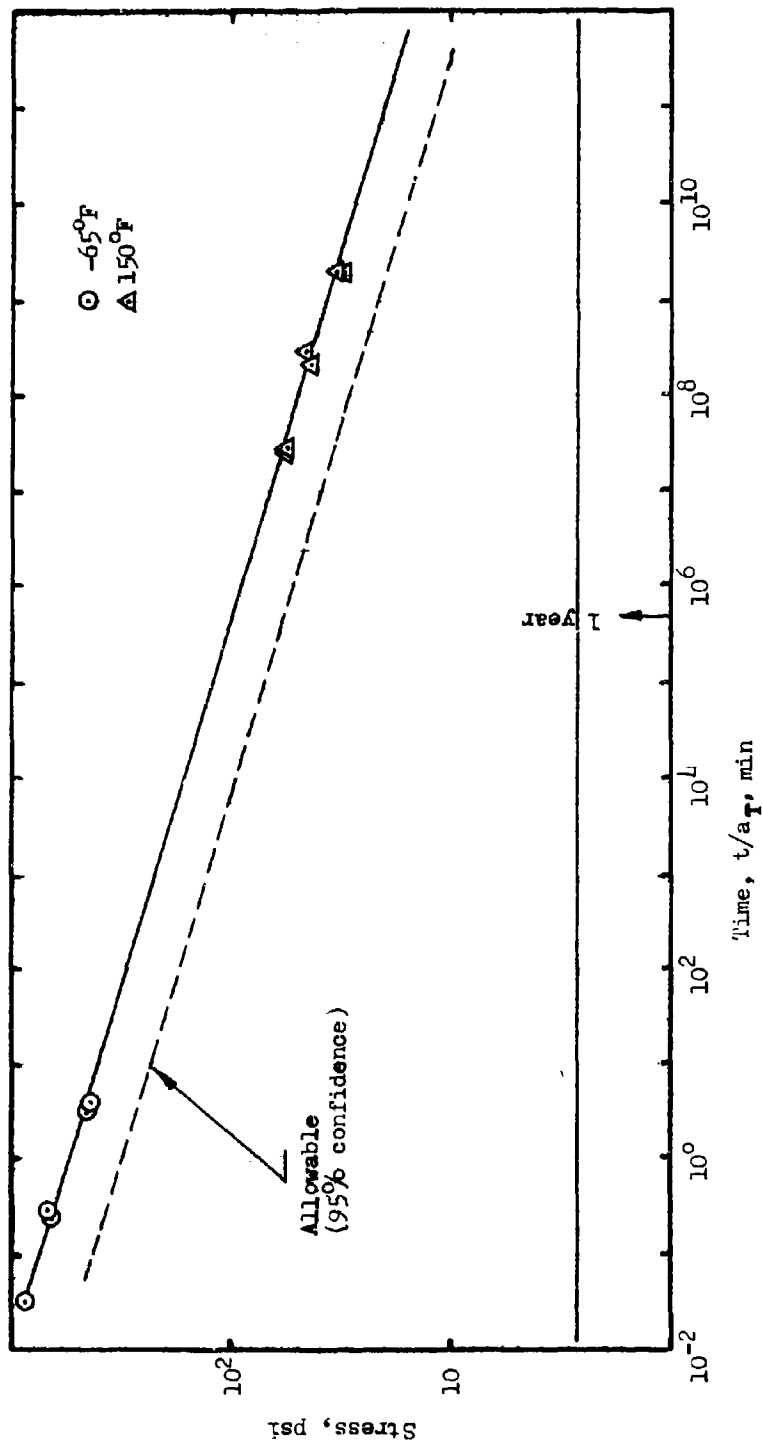


Figure 8  
Bond Tensile Stress vs Minimum Time to  
Failure for ANB-3241-2 Propellant

UNCLASSIFIED

UNCLASSIFIED

Report AFRPL-TR-69-90, Appendix B

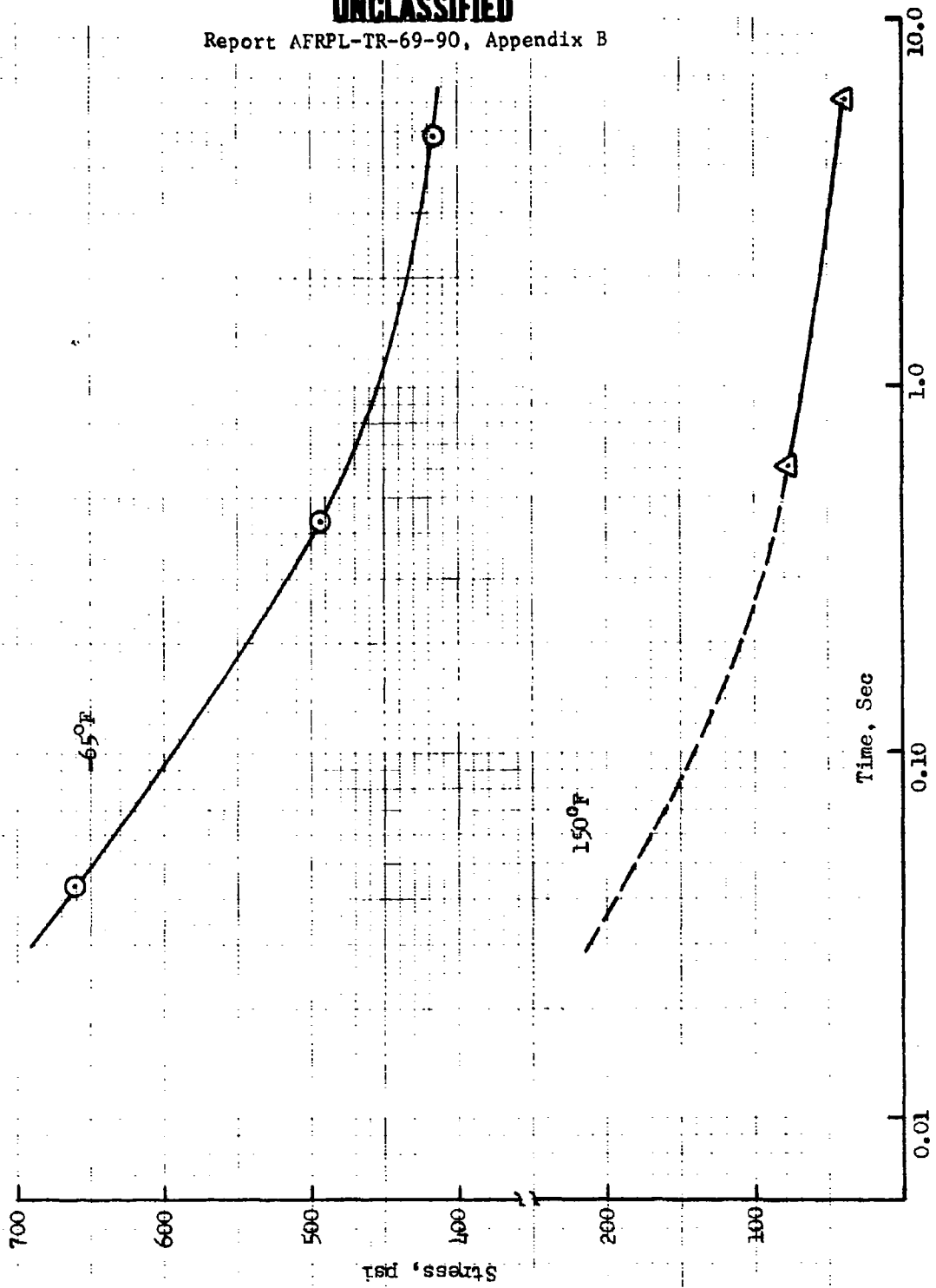


Figure 9  
Allowable Bond Shear for ANR-3/L1-2 Propellant  
with Superimposed Hydrostatic Pressure

# UNCLASSIFIED

Report AFRPL-TR-69-90, Appendix B

## IV. THERMAL ANALYSIS OF NOZZLES

The thermal analysis of a rocket nozzle consists of predicting the transient temperature distribution in the various nozzle components. However, when an ablative surface material is used, the ablation depth and char depth are also significant factors. The analytical prediction of these quantities requires the evaluation of the surface heat flux, which subsequently is used to evaluate the boundary conditions necessary for solution of the transient conduction equation.

The surface heat flux due to convection is governed by the relation:

$$Q_c = h_c(T_{aw} - T_w), \quad (2)$$

where :  $Q_c$  = convective heat flux, Btu/sq ft sec,  
 $h_c$  = convective heat transfer coefficient, Btu/sq ft sec<sup>°R</sup>,  
 $T_{aw}$  = adiabatic wall temperature, °R, and  
 $T_w$  = wall temperature, °R

During this thermal analysis, the Colburn equation, originally developed for fully developed flow in circular ducts, was used to evaluate the convective heat transfer coefficient of Equation 2. Although the flow in nozzles does not correspond to the flow in constant area circular ducts, previous experience with numerous motors has shown that accurate results are obtained using the Colburn equation to evaluate the convective heat transfer coefficient. The dimensionless form of the Colburn equation corresponding to Reynold's analogy is:

$$\left(\frac{h_c}{\rho U C_p}\right) P_r^{2/3} = 0.023 \left(\frac{\rho U D}{\mu}\right)^{-1/5} \quad (3)$$

# UNCLASSIFIED

Report AFRPL-TR-69-90, Appendix B

where :  $\rho$  = local propellant gas density, lb/cu ft,  
 $U$  = local free stream velocity, ft/sec,  
 $C_p$  = specific heat at constant pressure, Btu/lb<sup>o</sup>R  
 $P_r$  = Prandtl number,  
 $D$  = local nozzle diameter, ft. and  
 $\mu$  = absolute viscosity, lb/ft sec

The mass flux,  $\rho U$ , in Equation 3, at the throat of a nozzle is given by

$$(\rho U)_{*} = C_w P_c \quad (4)$$

where :  $C_w$  = propellant mass flow coefficient, sec<sup>-1</sup>, and  
 $P_c$  = chamber pressure, lb/sq ft abs.

Utilizing the equation of continuity, the local mass flux becomes

$$\rho U = (\rho U)_{*} \left( \frac{A_{*}}{A} \right) \quad (5)$$

where :  $A$  = local nozzle area, sq ft, and  
 $A_{*}$  = throat area, sq ft

Equation 5 can be substituted in Equation 3 and simplified to obtain the relationship:

$$h_c = \frac{0.023 C_w P_c C_p}{\left( \frac{C_w P_c D_{*}^{1/5}}{\mu} \right) P_r^{2/3}} \left( \frac{A_{*}}{A} \right)^{0.9} \quad (6)$$

Analytical and experimental studies of motors similar to the motor of this study have indicated that particle impingement and radiation made negligible contributions to the surface heat flux compared with the convective contribution. Based on this finding, Equation 2 can be used to approximate the total heat flux.

# UNCLASSIFIED

Report AFRPL-TR-69-90, Appendix B

The adiabatic wall temperature,  $T_{aw}$ , contained in Equation 2 is given by the relationship:

$$\frac{T_{aw}}{T_o} = \frac{2+R(\gamma-1)M^2}{2+(\gamma-1)M^2} \quad (7)$$

where:  $R$  = recovery factor,  
 $\gamma$  = isentropic coefficient,  
 $M$  = local Mach. number, and  
 $T_o$  = total temperature,  $^{\circ}F$

The recovery factor,  $R$ , for a turbulent boundary layer is obtained from the Seban equation

$$R = P_r^{1/3} \quad (8)$$

The heat flux to the nozzle wall is then obtained by substituting Equations 6 and 7 in Equation 2.

Using the heat input rates as noted above, the resulting temperature profiles in the nozzle structure are calculated by a General Thermal Analysis program written for the IBM 360/65. This computer program is capable of solving the general transient conduction equation which for a nozzle considering axial heat flow is given by:

$$C_p \frac{\partial T}{\partial \theta} = \frac{\partial}{\partial r} \left( k \frac{\partial T}{\partial r} \right) + \frac{k}{r} \frac{\partial T}{\partial r} + \frac{\partial}{\partial z} \left( k \frac{\partial T}{\partial z} \right) \quad (9)$$

The computer solution utilizes a modification of the Dusenberre explicit finite difference equations for heat flow in multi-layer solids. The difference equations incorporates variable thermal properties as defined by the above conduction equation.

In the case of the 2.75 inch motor the above equation was solved in one dimensional form with results as indicated in Figure 10a. These results were then extrapolated to obtain the isotherms in the Carbitex insert as indicated in Figure 10b.

21  
UNCLASSIFIED

UNCLASSIFIED

Report AFRPL-TR-69-90, Appendix B

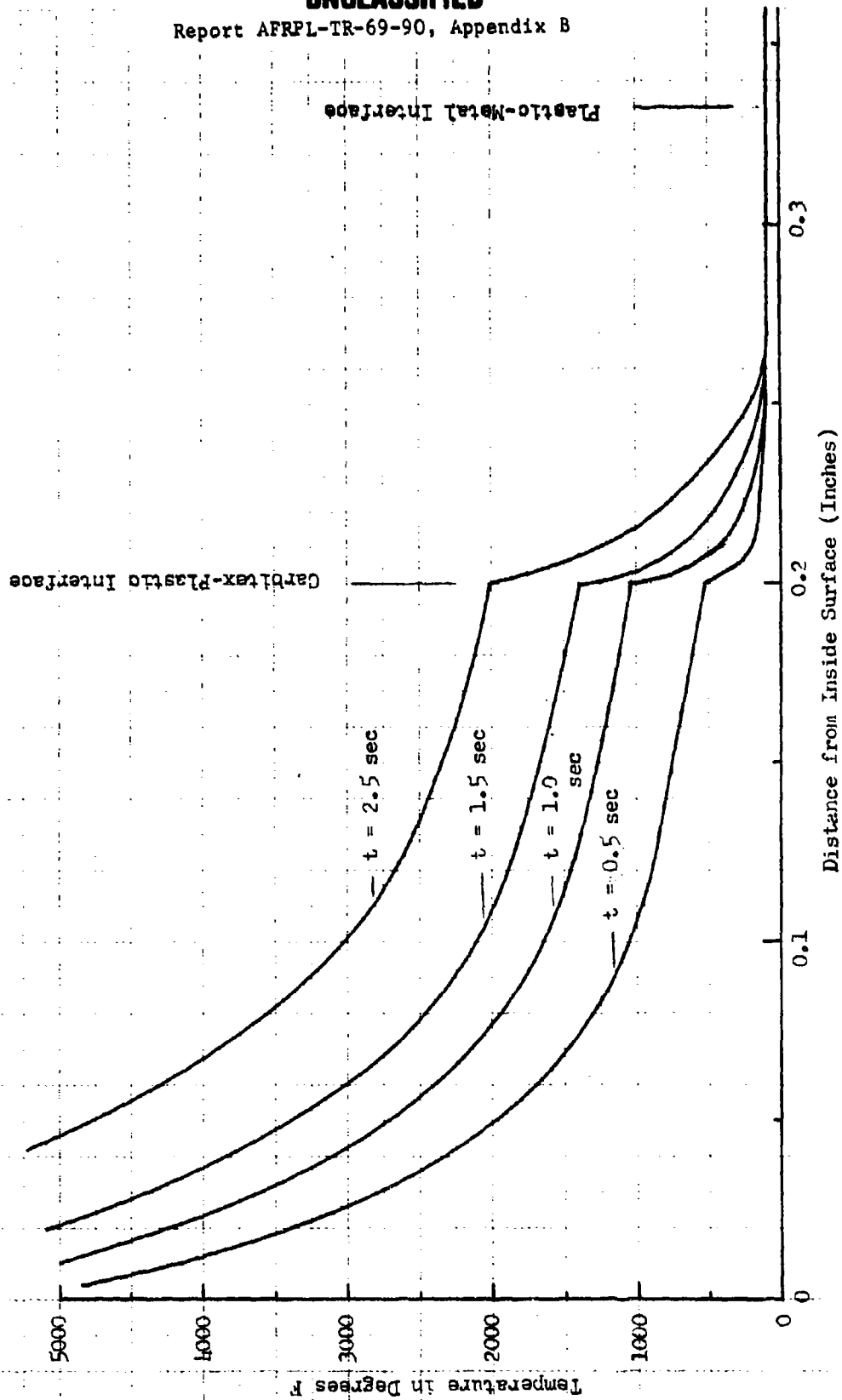


Figure 10 a  
temperature Profiles Through Throat of 2.75 Nozzle

UNCLASSIFIED

UNCLASSIFIED

Report AFRPL-TR-69-90, Appendix B

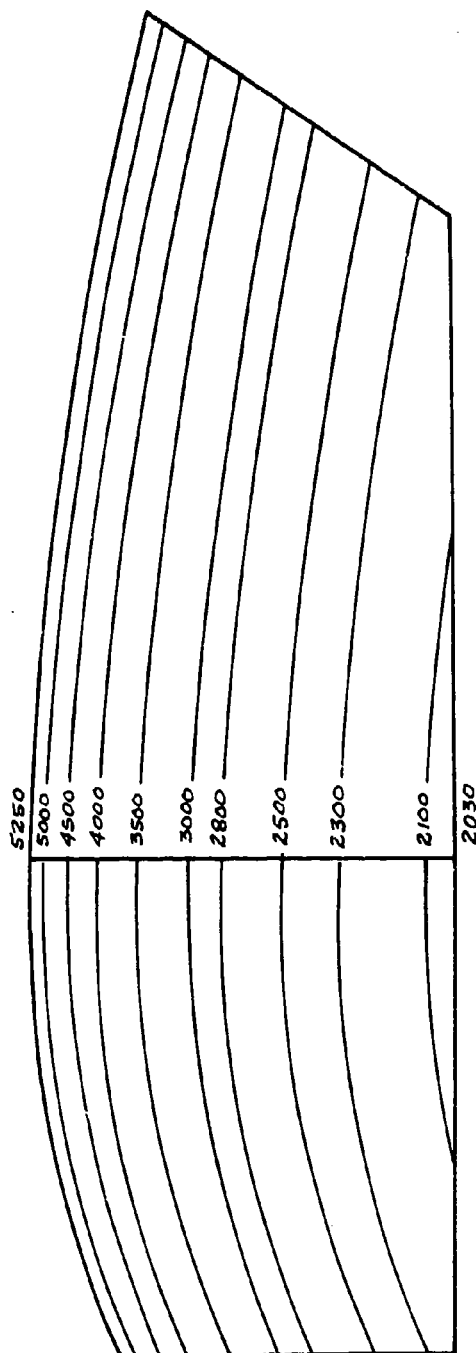


Figure 10 b  
Isotherms for Carbitex Nozzle Insert  
at  $t = 2.5$  Seconds

- 22b -

UNCLASSIFIED



# UNCLASSIFIED

Report AFRPL-TR-69-90, Appendix B

## V. STRUCTURAL ANALYSIS

For convenience, the structural analysis of the 2.75 inch rocket motor has been separated into three major assemblies, i.e., motor case, aft closure assembly and propellant grain. Where necessary, these items have been further broken down into component parts for the purpose of detailed stress calculations.

### A. MOTOR CASE

The analysis contained in this section is primarily concerned with the 2011T6 aluminum chamber, as defined by Bureau of Naval Weapons Dwg 1569403, and the steel lockwire (Reference BuWeps Dwg 457822). For completeness, however, consideration is also given to the mating flange of the aft closure plate (Reference AUC Dwg 1146335).

In order to evaluate the bending stresses due to geometrical discontinuities the analysis made use of a computer program developed by Aerojet-General for thin shell analysis. This program is entitled: "Elastic Axisymmetric Pressure Vessel Analysis Program." Details of this program are contained in Section 14.21 of Reference (3) and a brief abstract of the program is presented herewith:

The program is used for the analysis and design of motor case configurations with particular application to regions where a change from one type of shell geometry to another occurs and causes localized discontinuity stresses.

The structural analysis is accomplished by dividing the configuration into a series of small shell elements. The computer input data includes a complete description of the geometry, pressure plus other applied loads, material properties, and temperature for each of the basic elements. The computer program makes a complete numerical elastic stress

UNCLASSIFIED

## UNCLASSIFIED

Report AFRPL-TR-69-90, Appendix B

analysis of the integral configuration by writing equations to relate the deflections and rotations to the moments and shears at the edge of the basic elements. This solution is based upon the same analytical methods used in a routine hand solution, but the ability of the computer to handle a large number of equations allows for a more comprehensive coverage of the problem.

The computer output data consist of: radial deflection, the angular rotation, the discontinuity moment and shear, and the hoop and meridional stresses for each location considered.

The pressure vessel analyses presented herein utilize the deflected geometry of the loaded shell in order to ensure the greatest possible accuracy of solution. The final deflected geometry of the shell is determined by an iterative process. This same refinement can be accomplished by the direct application of the equations of M. Hetenyi which have the advantage of a closed form solution, but which are not readily applicable to the complex elemental shapes and plastic deformation of the 2.75-in. motor.

The plastic analysis of the pressure vessel structure at both the design limit and design ultimate loading conditions was formulated by first assuming full elastic action in all areas. Wherever the elastic stresses were found to exceed the yield allowable of the material the critical axial stress was subtracted from the allowable stress and the permissible amount of bending moment was programmed to exist within a sufficient region of the shell such that the final plastic analysis contained no stresses above yield. This technique resulted in fictitious step differences in shell rotations between the forward and aft sides of several of the structural analysis points. The shape of the stress-strain curve beyond yield was assumed to be flat. The magnitude of the permanent set at each location was determined by a judicious spreading of the calculated rotational disparity over the area of the shell where the yield tensile allowable had been exceeded.

# UNCLASSIFIED

Report AFRPL-TR-69-90, Appendix B

Detailed sketches of the actual geometry used in the analysis along with the location of the "cuts" employed in the computer solution are contained in Figures 11 and 12.

Solutions were obtained for both the limit (1990 psi internal pressure) and ultimate (2985 psi internal pressure) loading conditions. Results of these solutions are contained in Tables 1 through 4. A review of these tables indicates that the chamber as designed does not meet the 1.5 safety factor requirement for the ultimate load condition. The critical section occurs at the bottom of the lockwire groove and is based upon a minimum thickness of 0.032 in. In order to meet the 1.5 requirement this thickness would have to be increased to 0.037 in. minimum.

Certain detail evaluations which were not covered in the overall chamber solution are as follows:

## 1. Forward Closure

The forward closure consists of the structure between joints 28 and 29 as shown in Figure 11.

As shown in Figure 11 the minimum dome thickness is 0.230 in. On the same figure the draft angle of the dome is shown to be 5° maximum. In this analysis the entire dome was conservatively taken to be the minimum thickness of 0.230 in.

For the design ultimate loading condition the maximum edge stress is:

$$\sigma_{U-\max} = \frac{6k_{T.U.}}{t^2} = \frac{6(516)}{(0.230)^2} = 62,000 \text{ psi}$$

UNCLASSIFIED

UNCLASSIFIED

Report AFRPL-TR-69-90, Appendix B

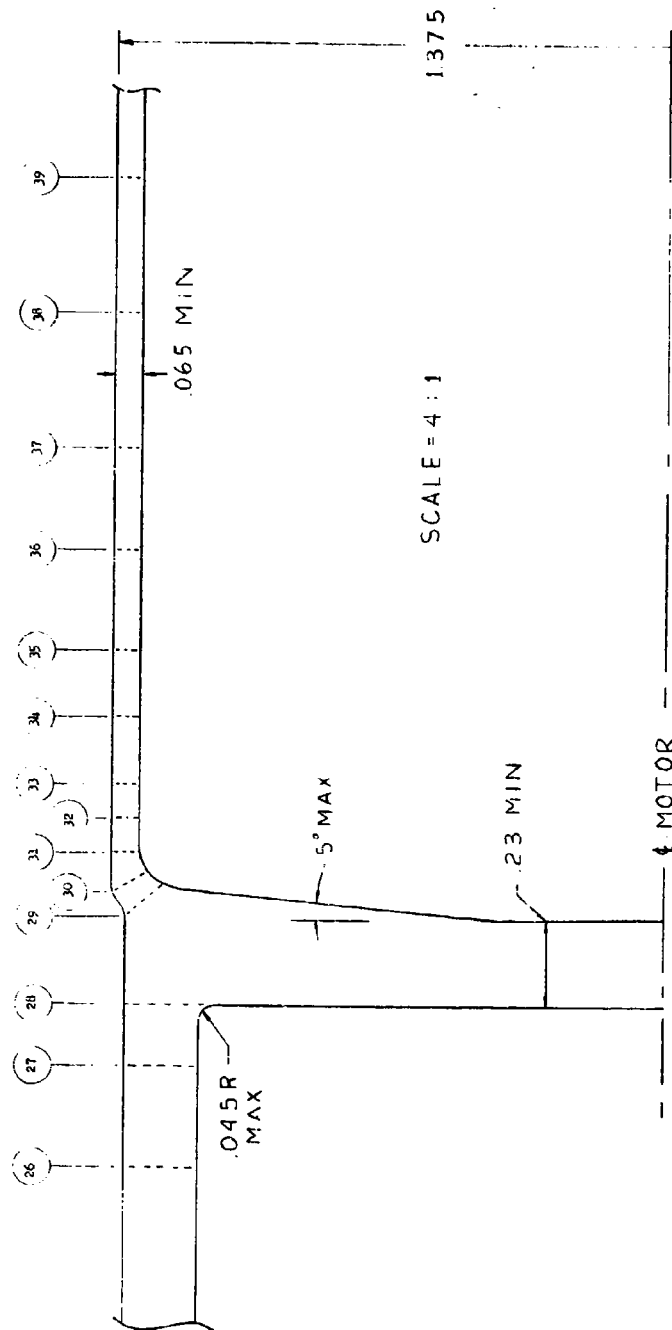
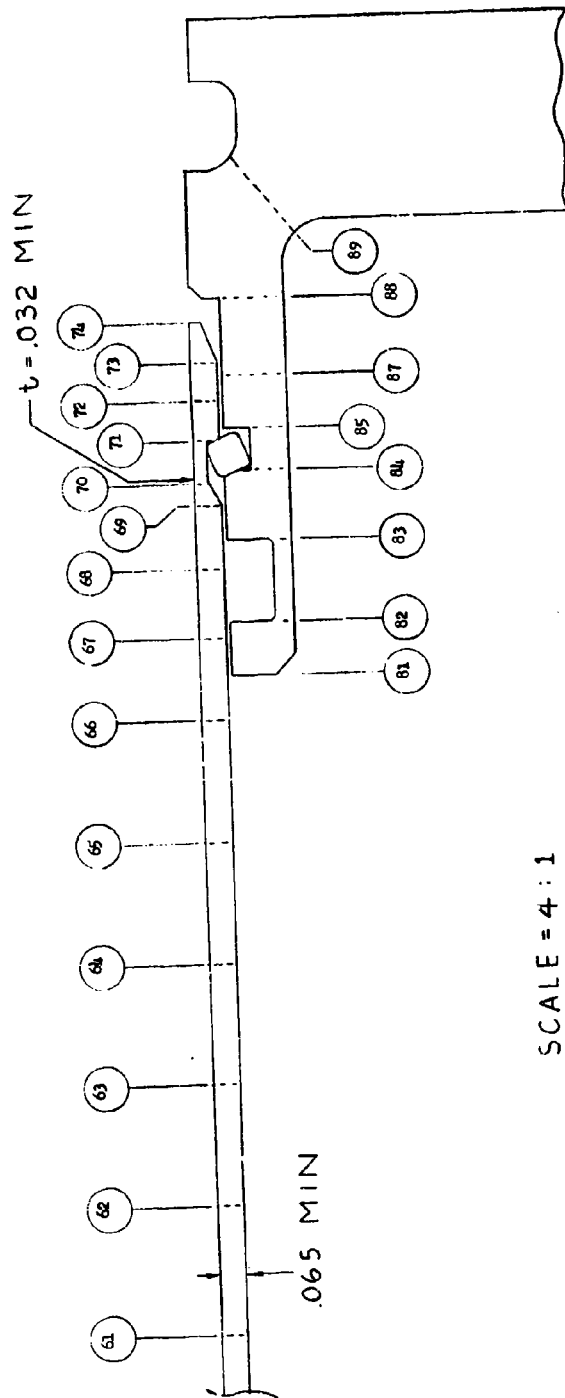


Figure 11. Motor Case Geometry and "Cut" Locations for Computer Solution, Forward End

UNCLASSIFIED

UNCLASSIFIED

Report AFRPL-TR-69-90, Appendix B



SCALE = 4 : 1

⌀ MOTOR

Figure 12. Motor Case Geometry and "Cut" Locations for Computer Solution, Aft End

UNCLASSIFIED

UNCLASSIFIED

Report AFRPL-TR-69-90, Appendix B

Table 1. 2.75-in. Motor Shell Forward  
Section Limit Press

CRITICAL MARGIN OF SAFETY = .0062 AT CUT 31

SUMMARY OF GENERAL DATA.

YOUNG'S MODULUS =  $11 \times 10^6$  PSI  
ALLOWABLE DIRECT STRESS = 50200 PSI  
THERMAL STRESSES ARE NOT INCLUDED

SUMMARY OF GEOMETRY AND STRESSES.

CUT IDENT.	RADIUS TO CUT (INCHES)	THICKNESS OF CUT (INCHES)	MERIDIONAL STRESS OUTER	MERIDIONAL STRESS INNER	HUOP STRESS OUTER	HUOP STRESS INNER	MARGIN OF SAFETY
21	1.30	.072	7	-7	47	47	HIGH
22	1.28	.105	58	-58	44	39	HIGH
23	1.28	.105	74	-74	43	0	HIGH
24	1.28	.105	-1565	1565	-279	-323	HIGH
25	1.28	.105	1031	-1731	-702	-23	HIGH
26	1.23	.207	13074	-13074	4018	3999	HIGH
27	1.23	.207	25913	-25913	9745	1900	0.3031
28	1.23	.098	13500	19700	10590	-4552	1.1711
29	1.28	.090	-1004	37810	-280	2479	1.8434
30	1.33	.090	-15300	56251	-401	7243	.4009
31	1.33	.065	18721	22151	-2862	12927	.0002
32	1.33	.065	32961	7091	12012	13041	1.5390
33	1.33	.065	33122	7749	27442	19915	.7050
34	1.33	.065	25193	15079	41010	34190	.3456
35	1.33	.065	20114	20757	43570	40724	.2910
36	1.33	.065	20179	20742	41515	41700	.3489
37	1.33	.065	20439	20432	40788	41002	.3721
38	1.33	.065	20436	20432	40042	40040	.3775
39	1.33	.065	20436	20430	40040	40040	.3761

UNCLASSIFIED

UNCLASSIFIED

Report AFRPL-TR-69-90, Appendix B

Table 2. 2.75-in. Motor Shell Aft Joint Limit  
Press 7075T73 Aluminum Closure

CRITICAL MARGIN OF SAFETY = .0004 AT CUT 70									
SUMMARY OF GENERAL DATA.									
YOUNG'S MODULUS = $11 \times 10^6$ PSI									
ALLOWABLE DIRECT STRESS = 56260 PSI									
THERMAL STRESSES ARE NOT INCLUDED									
SUMMARY OF GEOMETRY AND STRESSES.									
CUT IDENT.	RADIUS TO CUT (INCHES)	THICKNESS OF CUT (INCHES)	MERIDIONAL STRESS CUTEN	MERIDIONAL STRESS INNER	Hoop Stress Outer	Hoop Stress Inner	MARGIN OF SAFETY		
61	1.34	.065	20451	20451	40909	40909	.3753		
62	1.34	.065	20453	20450	40890	40889	.3759		
63	1.34	.065	20369	20533	40856	40905	.3754		
64	1.34	.065	20176	20724	40970	41134	.3677		
65	1.34	.065	21067	19836	41775	41405	.3468		
66	1.34	.065	26138	14764	41940	38527	.3415		
67	1.34	.065	28445	12457	36528	31732	.5402		
68	1.34	.065	17174	23729	23366	25333	1.2208		
69	1.34	.065	13333	27569	14444	18715	1.0407		
70	1.35	.032	41235	56235	21231	25731	.0004		
71	1.35	.032	56235	41235	39716	35216	.0004		
72	1.34	.065	26413	-26413	37288	21441	.5088		
73	1.34	.065	6109	-6109	29862	26197	.8840		
74	1.35	.027			24301	24301	1.3152		
81	1.21	.169			225	225	HIGH		
82	1.16	.055	-4355	4355	-6794	-4181	6.2710		
83	1.16	.055	-36590	36590	-17372	4583	.3501		
84	1.16	.102	43979	-21070	15980	-3534	.1233		
85	1.16	.102	42216	-19307	18271	-185	.1702		
87	1.21	.169	12677	1418	6607	5170	2.8362		
88	1.21	.169	1659	12636	3343	6636	2.9096		
89	1.16	.244	-2544	20669	59	7024	1.3900		

UNCLASSIFIED

UNCLASSIFIED

Report AFRPL-TR-69-90, Appendix B.

Table 3. 2.75-in. Motor Shell Forward  
Section Ultimate Press

CRITICAL MARGIN OF SAFETY = -.0218 AT CUT 35									
SUMMARY OF GENERAL DATA.									
YOUNG'S MODULUS = 11X(10) <sup>6</sup> PSI									
ALLOWABLE DIRECT STRESS = 64000 PSI									
THERMAL STRESSES ARE NOT INCLUDED									
SUMMARY OF GEOMETRY AND STRESSES.									
CUT IDENT.	RADIUS TO CUT (INCHES)	THICKNESS OF CUT (INCHES)	MERIDIONAL STRESS OUTER	MERIDIONAL STRESS INNER	HOOP STRESS OUTER	HOOP STRESS INNER	MARGIN OF SAFETY		
21	1.36	.072	11	-11	75	75	HIGH		
22	1.28	.105	93	-93	70	63	HIGH		
23	1.28	.105	118	-118	64	13	HIGH		
24	1.28	.105	118	-118	-445	-510	HIGH		
25	1.28	.105	-2497	2497	-1534	-36	HIGH		
26	1.23	.207	1644	-1044	7360	6379	7.6885		
27	1.23	.207	20855	-20855	15544	5531	2.0688		
28	1.23	.207	41334	-41334	17540	-7260	.5484		
29	1.28	.030	31433	13035	3840	-1440	1.0361		
30	1.33	.030	15308	34328	-2382	4836	.6273		
31	1.33	.065	5044	5044	-4701	6602	.1376		
32	1.33	.065	48014	15094	24510	15940	.4631		
33	1.33	.065	28248	1000	40763	40207	.0988		
34	1.33	.065	49049	11058	64000	51204	-.0103		
35	1.33	.065	50484	24823	64000	61930	-.0218		
36	1.33	.065	29885	31423	64000	62517	.0237		
37	1.33	.065	50176	31131	61163	61450	.0415		
38	1.33	.065	30609	30638	61273	61263	.0445		
39	1.33	.065	30654	30654	61323	61323	.0437		

UNCLASSIFIED



UNCLASSIFIED

Report AFRPL-TR-69-90, Appendix B

Table 4. 2.75-in. Motor Aft Joint Ultimate  
Press 7075T73 Aluminum Closure

CRITICAL MARGIN OF SAFETY = -0.1244 AT CUT 70

SUMMARY OF GENERAL DATA.

6

YOUNG'S MODULUS =  $11 \times 10^6$  PSI  
ALLOWABLE DIRECT STRESS = 64000 PSI  
(THERMAL STRESSES ARE NOT INCLUDED)

SUMMARY OF GEOMETRY AND RESULTS.

CUT IDENT.	RADIUS TO CUT (INCHES)	THICKNESS OF CUT (INCHES)	MERIDIONAL STRESS OUTER	MERIDIONAL STRESS INNER	HOOP STRESS OUTER	HOOP STRESS INNER	MARGIN OF SAFETY
61	1.24	.005	30677	30677	51363	51363	.0430
62	1.24	.005	30679	30674	51336	51335	.0434
63	1.24	.005	30559	30744	51288	51358	.0431
64	1.24	.005	30206	31088	51447	51694	.0374
65	1.24	.005	31499	29854	52633	52140	.0218
66	1.24	.005	35423	21930	53117	57870	.0140
67	1.24	.005	44294	17059	55274	47104	.1579
68	1.24	.005	29471	31382	34956	35689	.7933
69	1.24	.005	25844	37509	18627	22726	.7662
70	1.25	.005	73093	73093	29470	29470	-.1244
71	1.25	.005	73093	73093	54928	54928	-.1244
72	1.24	.005	36711	-36711	62279	40252	.0276
73	1.24	.005	7141	-7141	45515	41230	.4061
74	1.25	.007			23181	23181	1.7609
81	1.21	.109			6917	6917	7.5150
82	1.16	.035	2573	-2573	-10501	-12345	3.7711
83	1.16	.055	-49359	49397	-48338	-18699	.1923
84	1.12	.102	49357	-15030	32027	12698	.1924
85	1.12	.102	38211	-3847	27485	14868	.5414
87	1.21	.109	9779	12694	12851	14327	3.1992
88	1.21	.109	-6081	28324	3341	13903	1.0795
89	1.16	.244	-7422	34126	-377	12088	.7259

UNCLASSIFIED

# UNCLASSIFIED

Report AFRPL-TR-69-90, Appendix B

The stress at the dome centerline is determined through the use of the stress formulas of Cases 1 and 12 on pages 194 and 196 of Reference (4). The maximum design ultimate dome centerline stress is:

$$\begin{aligned}\sigma_{U-\max} &= \frac{3PR^2}{8mt^2} (3M + 1) - \frac{6M_{T.U.}}{t^2} \\ &= \frac{3(2985)(1.13)^2(9.30)}{8(2.7'')(0.230)^2} - 62,000 \\ &= 28,000 \text{ psi}\end{aligned}$$

The ultimate allowable tension stress for the maximum environmental temperature of 150°F is 97% of the 66,000 psi room temperature allowable. The resulting minimum margin of safety including a 1.5 modulus of rupture improvement factor is

$$M.S._U = \frac{0.97(66,000)(1.5)}{30,300} - 1 = +0.55$$

For the design yield loading condition the maximum edge stress is:

$$\sigma_{Y-\max} = \frac{6M_{T.Y.}}{t^2} = \frac{6(368)}{(0.230)^2} = 41,800 \text{ psi}$$

The design yield stress at the dome centerline is

$$\begin{aligned}\sigma_{Y-\max} &= \frac{3PR^2}{8mt^2} (3m + 1) - \frac{6M_{T.Y.}}{t^2} \\ &= \frac{3(1990)(1.13)^2(9.30)}{8(2.77)(0.230)^2} - 41,800 \\ &= 18,200 \text{ psi}\end{aligned}$$

The yield allowable tension stress for the maximum environmental temperature of 150°F is 97% of the 58,000 psi room temperature allowable. The resulting minimum margin of safety including a 1.2 modulus of rupture improvement factor is

$$M.S._Y = \frac{0.97(58,000)(1.2)}{41,800} - 1 = +0.61$$

32  
UNCLASSIFIED

## UNCLASSIFIED

Report AFRPL-TR-69-90, Appendix B

### 2. Central Cylindrical Section

The central cylindrical section is critical for simple hoop tensile stress. The minimum barrel thickness as shown in Figure 11 is 0.065 in.

For the design ultimate loading condition the maximum stress is:

$$\sigma_{U-\max} = \frac{PR}{t} = \frac{2985(1.336)}{0.065} = 61,366 \text{ psi}$$

The ultimate allowable stress for the maximum environmental temperature of 150°F is 97% of the 66,000 psi room temperature allowable.

The resulting minimum margin of safety is:

$$\begin{aligned} M.S._U &= \frac{\text{allowable stress}}{\text{applied stress}} - 1 \\ &= \frac{0.97(66,000)}{61,366} - 1 = +0.043 \end{aligned}$$

For the design yield loading condition the maximum stress is:

$$\sigma_{Y-\max} = \frac{PR}{t} = \frac{1990(1.336)}{0.065} = 40,909 \text{ psi}$$

The yield allowable stress for the same maximum environmental temperature of 150°F is 97% of 58,000 psi room temperature allowable. The resulting minimum margin of safety is:

$$\begin{aligned} M.S._Y &= \frac{\text{Allowable stress}}{\text{Applied stress}} - 1 \\ &= \frac{0.97(58,000)}{40,909} - 1 = +0.375 \end{aligned}$$

This analysis conservatively neglects the effect of biaxial gain which could improve the membrane burst stress by as much as 15 percent.

### 3. Lockwire Assembly

The aft joint lockwire provides the structural connection between the aluminum shell and the steel aft closure. The lockwire to chamber assembly is shown in Figure 13. The lockwire is completely detailed in the Bureau of Naval Weapons Dwg L57822. The minimum mechanical properties for the 1006 low carbon steel alternate material are:

UNCLASSIFIED

UNCLASSIFIED

Report AFRPL-TR-69-90, Appendix B

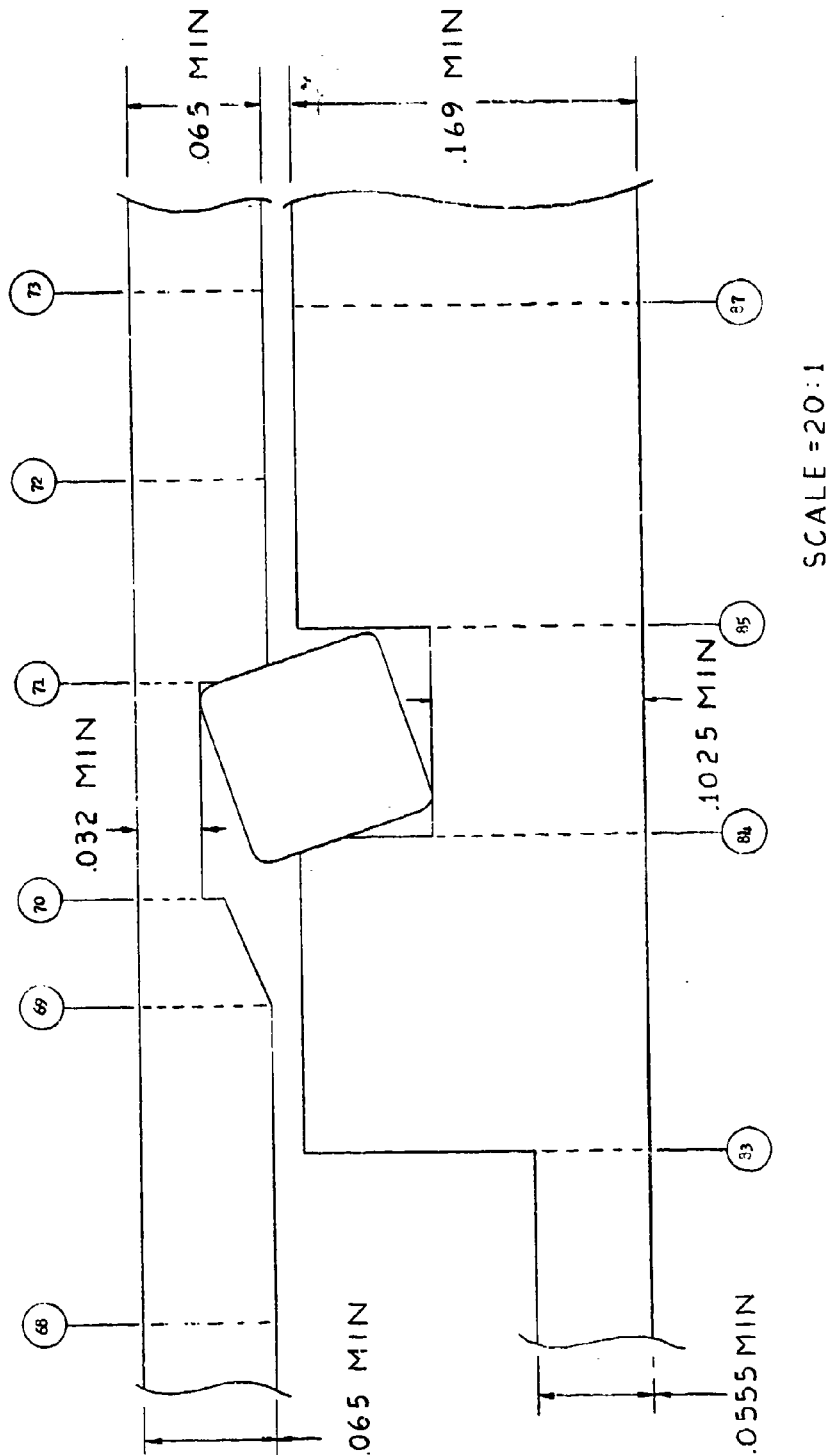


Figure 13. Lockwire Installation -  
2.75-in. Rocket Motor

UNCLASSIFIED

# UNCLASSIFIED

Report AFRPL-TR-69-90, Appendix B

$F_{tu}$	= 43,000 psi	$F_{sy}$	= 16,400 psi
$F_{ty}$	= 24,000 psi	$F_{bu}$	= 70,000 psi
$F_{oy}$	= 24,000 psi	$F_{by}$	= 45,000 psi
$F_{su}$	= 30,000 psi		

At the initial application of internal pressure the aluminum shell and the closure interface with the lockwire through line contact. As the pressure increases, the lockwire rotates and all three parts yield in bearing. At all times during the initial pressure loading, the bearing stress of the low carbon steel lockwire approaches the ultimate bearing strength of the material. The width of the contact surfaces shown in Figure 13 were determined by the above criterion. The application of the aft closure ejection load on the sloped surface of the rotated lockwire results in a differential radial deflection of the aluminum shell and the aft closure which in turn results in greater rotation of the lockwire. If the joint were unstable, this strapping effect would continue until enough differential radial deflection was obtained to permit the lockwire to rotate  $90^\circ$  and become completely ineffective. The lockwire joint herein analyzed was found to be stable by an iterative technique. The final differential radial deflection of the shell and the resulting lockwire rotation were assumed. The application of the ejection load resulted in the assumed radial deflections thereby verifying the structural assumption.

It is obvious that the above bearing stress condition does not lend itself meaningfully to the conventional type margin of safety calculations. In the most basic sense, however, the margin of safety should express the degree of structural stability. Following this reasoning it can be said that even considering the most adverse tolerances permitted the lockwire joint was found to be stable for the ultimate pressure loading condition.

UNCLASSIFIED

# UNCLASSIFIED

Report AFRPL-TR-69-90, Appendix B

The lockwire must also resist the direct shear load across the joint tending to eject the aft closure. The shear stresses and margins of safety are calculated below:

## Design Ultimate Pressure

$$\sigma_{\text{shear ult.}} = \frac{PR}{2t} = \frac{2985(1.3)}{2(0.094)} = 20,600 \text{ psi}$$

$$\text{M.S. ult.} = \frac{\text{Allowable stress}}{\text{Applied stress}} - 1 = \frac{30,000}{20,600} - 1 = +0.46$$

## Design Yield Pressure

$$\sigma_{\text{shear yield}} = \frac{\text{Allowable stress}}{\text{Applied stress}} - 1 = \frac{16,400}{13,800} - 1 = +0.19$$

### B. AFT CLOSURE ASSEMBLY

The aft closure assembly contains the closure plate, the nozzle assembly, the folding fin assembly, the igniter and the piston and crosshead assembly. All of these items are covered in considerable detail in this section of the report.

UNCLASSIFIED

# UNCLASSIFIED

Report AFRPL-TR-69-90, Appendix B

## 1. Nozzle Thermal Analysis

The initial design of the 2.75-in. rocket nozzle utilized an ATJ graphite throat insert supported by a carbon fiber molding compound (Fibrite Corporation's MXC-313). During development firings a number of instances of graphite cracking were observed as well as some cases of insert ejection. At that time an extensive analytical and experimental program was undertaken to determine the cause of the problem and to effect a solution.

The analytical effort included extensive two-dimensional heat transfer studies and two-dimensional thermal stress analyses which were reported in Reference (9). While this analytical work was not conclusive in explaining all of the observed cracks it did indicate very high compressive stresses on the inside surface and moderately high tensile stresses on the outer surface of the graphite. These results, combined with the good performance of Carbitex 700 inserts in test firings were considered justification for a change to the Carbitex inserts.

Uncertainty of material properties for Carbitex over the operational temperature range make it difficult to perform a reliable thermal stress analysis of the insert area and the integrity of the part is considered substantiated mainly on the basis of the 5 successful firings which have been conducted as of this date. In order to obtain an indication of the stress distribution in the Carbitex, however, a two-dimensional solution of the problem was attempted. This was accomplished by means of Aerojet's computer program E-111405. This is a finite element program for axisymmetric solids which permits consideration of orthotropic material properties. In summary, this program considers the continuous structure to be replaced with a system

UNCLASSIFIED

## UNCLASSIFIED

Report AFRPL-TR-69-90, Appendix B

of quadrilateral rings (elements). Displacement compatibility between elements is maintained by forcing the condition that within each element the displacement must vary linearly; i.e., constant strain within each element. Formulation of the equilibrium equations results in a set of linear equations which are solved for the unknown nodal displacements. Utilizing the nodal displacements, stresses and strains are then computed for each element.

Utilizing the temperature distribution from Figure 10, and the material properties from Section III-C, solutions were obtained for two assumed boundary conditions on the Carbitex insert. Two conditions were evaluated because of the sensitivity of back side stresses to the conditions assumed and the uncertainty of the actual conditions which actually do exist. The important concern on these boundary conditions is the shear transfer or lack of it that exists at the Carbitex-plastic interface. The assumed boundary conditions for the two cases considered were as follows:

### Case I

Carbitex insert was assumed to have no radial or shear restraint from the MXC-313 molding compound.

### Case II

The Carbitex insert was assumed to remain bonded to the MXC-313 molding compound throughout the full 2.5 sec firing duration.

The results of the Case I solution are contained in Figures 11a and 11b. These indicate the usual high elastic compressive stresses on the inner surface of the Carbitex; but it can be rationalized that these stresses, which exist only on a thin layer, are relieved by plasticity and surface ablation. The longitudinal tensile stress on the back side is also high, however, as indicated on Figure 11b.

UNCLASSIFIED



# UNCLASSIFIED

Report AFRPL-TR-69-90, Appendix B

Since the 1500 psi tensile stress is an order of magnitude higher than the estimated tensile allowable across plies, and since sectioned nozzles show no cracking, it must be assumed that the boundary condition assumed for Case I was not applicable.

Results of the Case II solution (Carbitex bonded to plastic) are contained in Figures 15a and 15b. Again the inside surface shows very high compression but the tension on the outer surface has been completely removed due to the shear transfer between the Carbitex and the plastic.

Since nozzles sectioned after firing show no evidence of separation at the interface it seems logical to assume that the bond between the materials is sufficient to withstand the shear stresses shown on Figure 15b even at the maximum operating temperature. This may be due to an actual migration of the plastic into the Carbitex at the high molding pressure utilized in the fabrication process.

In summary, while the analysis presented here cannot be considered as complete substantiation of the design, it can be regarded as indicating a rational explanation of the successful performance of the experimental program.

UNCLASSIFIED

UNCLASSIFIED

Report AFRPL-TR-69-90, Appendix B

Forward Edge of Insert at Axial Station  
1.38 In.

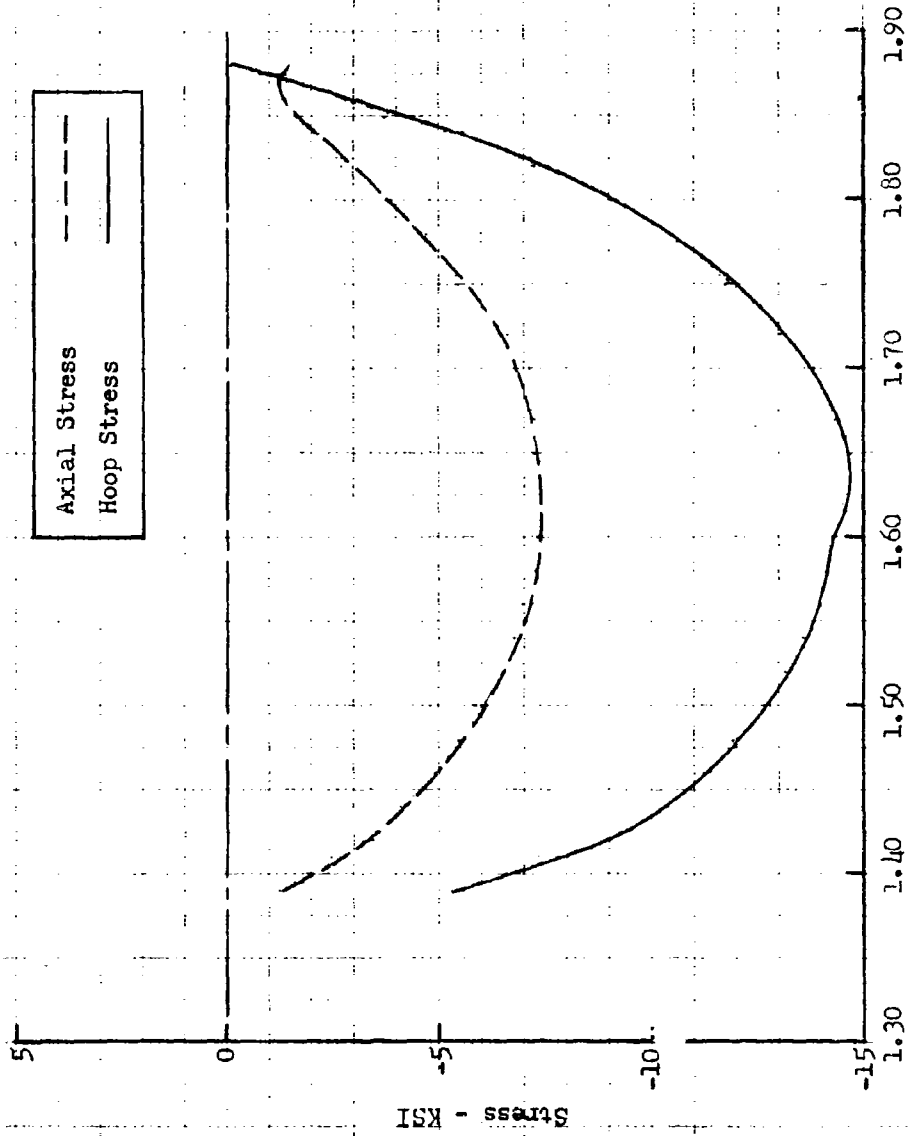


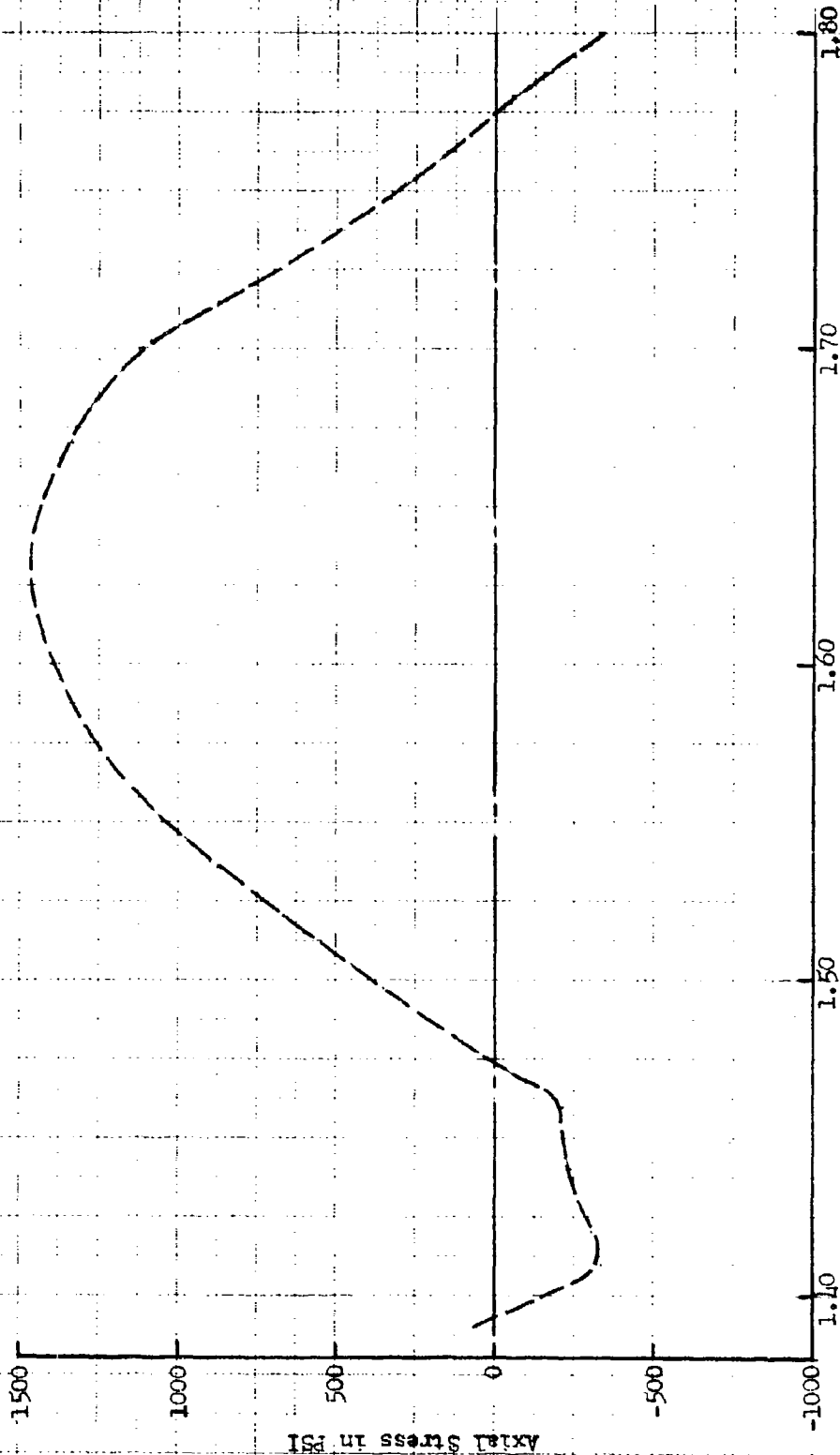
Figure 11a  
Compressive Stresses at Inside Surface of Carbitex  
Insert at  $t = 2.5$  Sec - Case I

UNCLASSIFIED

UNCLASSIFIED

Report AFRPL-TR-69-90, Appendix B

Forward Edge of Insert at Axial Station  
1.38 In.



Axial Distance - Inches  
Figure 11b  
Tensile Stress at Outside Surface of Carbitex  
Insert at  $t = 2.5$  Sec - Case I

UNCLASSIFIED

**UNCLASSIFIED**

Report AFRPL-TR-69-90, Appendix B

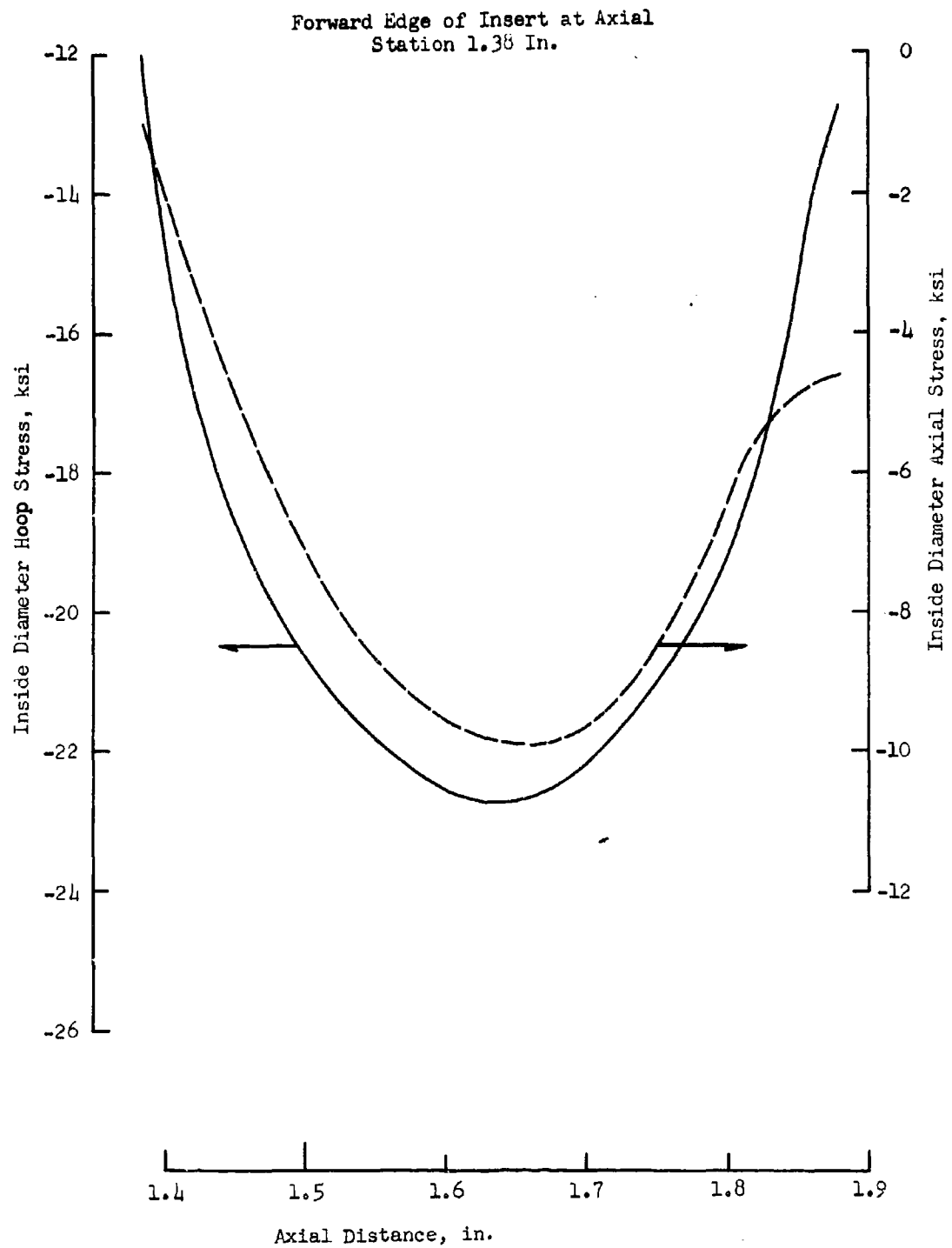


Figure 15a  
Compressive Stresses at Inside Surface of  
Carbitex Insert at  $t = 2.5$  Sec - Case II

- 42 - **UNCLASSIFIED**

UNCLASSIFIED

Report AFRPL-TR-69-90, Appendix B

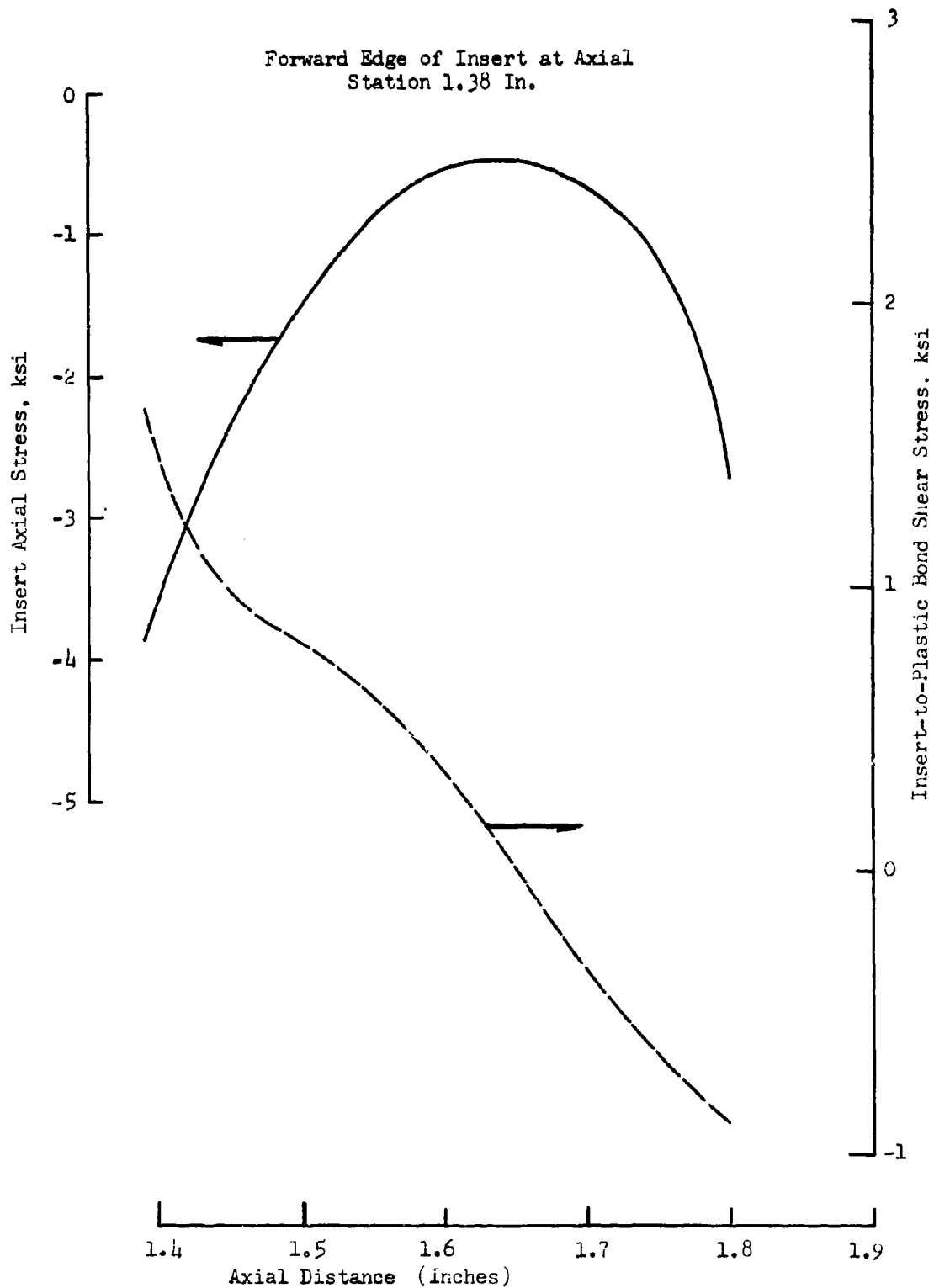


Figure 15b  
Shear Stress Distribution at Carbitex -  
Plastic Interface at  $t = 2.5$  Sec - Case II

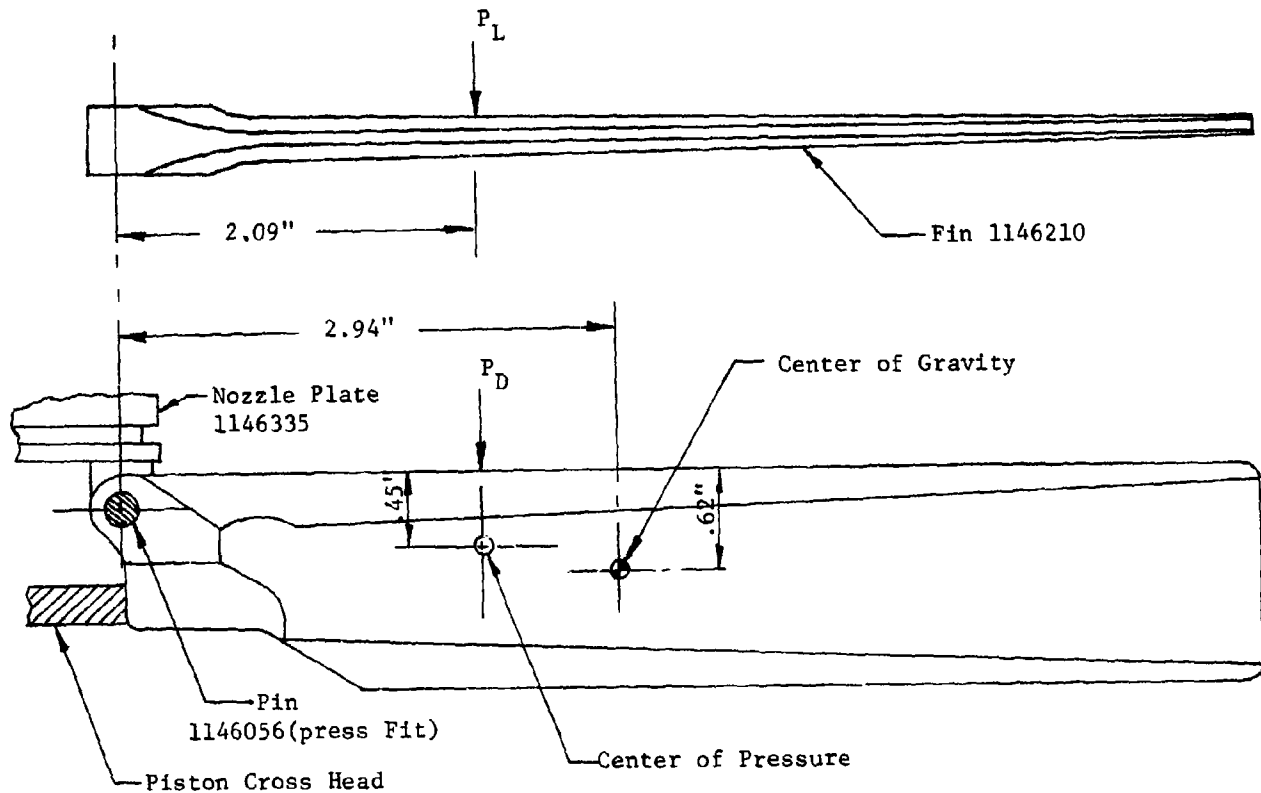
UNCLASSIFIED

# UNCLASSIFIED

Report AFRPL-TR-69-90, Appendix B

## 2. Blade, Fin Drawing No. 1146210

Geometry and Loads



Material: 2014 T6 Aluminum or Equivalent

$F_{ty} = 40000 \text{ psi}$

$F_{tu} = 62000 \text{ psi}$

UNCLASSIFIED

# UNCLASSIFIED

Report AFRPL-TR-69-90, Appendix B

## Operating Conditions

The following data was obtained from studies performed by Aerojet's Space Division. Load values are per fin.

Aerodynamic Lift: ( $P_L$ ) 50.4 lb @ center of pressure

Aerodynamic Drag: ( $P_D$ ) 26.76 lb @ center of pressure

Flight Acceleration Loads:

Transverse: 5.64 g

Axial: 43.35 g @ t = 1.89 sec.

Spin: 10 rps

## Flight Loads

In addition to the lift ( $P_L$ ) and drag ( $P_D$ ) loads above there are also acceleration and centrifugal loads, which are assumed to act at the center of gravity of the fin. Lab personnel at Space General measured the weight of a fin and located the C.G. (see sketch on previous page)

Weight: 52.4 grams or about 0.116 lbs.

Transverse G Load:  $F_t = 5.64 \times .116 = 0.65 \text{ lbs}$

Axial G Load:  $F_A = 43.35 \times .116 = 5.03 \text{ lbs}$

Centrifugal Force:  $F_c = \frac{WV^2}{g r}$

Where:  $g = 32.2 \text{ ft/sec}^2$

UNCLASSIFIED

# UNCLASSIFIED

Report AFRPL-TR-69-90, Appendix B

$$r = \frac{2.94''}{12''} = 0.245 \text{ ft}$$

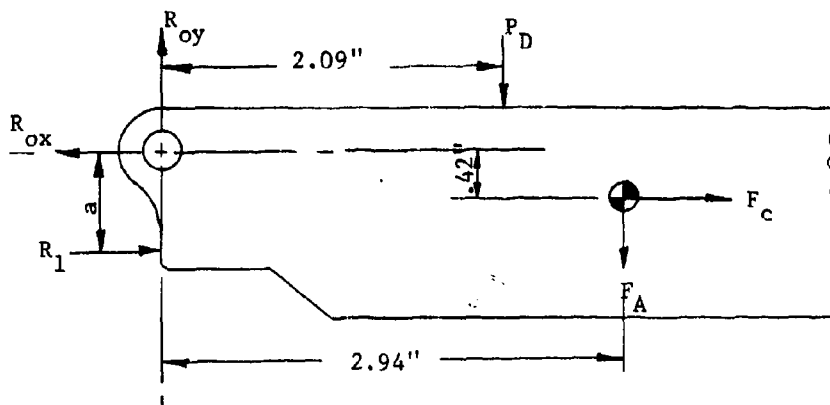
$$V = 2\pi rN \quad \text{where } N = 10 \text{ rps}$$

$$V = 2\pi \times .245 \times 10 = 15.4 \text{ fps}$$

$$\text{Then: } F_c = \frac{.116(15.4)^2}{32.2 \times .245} = 3.5 \text{ lbs}$$

## Stresses - Lug for Pin

### Axial and Centrifugal Loading



$$[\Sigma M_o = 0] \quad a = 0.60''$$

$$26.76 \times 2.09 + 5.03 \times 2.94 - 3.5 \times .42 = R_1 \times .60; R_1 = 115 \text{ lbs}$$

$$[\Sigma F_x = 0] \quad R_{ox} = 115 + 3.5 = 118.5 \text{ lbs}$$

$$[\Sigma F_y = 0] \quad R_{oy} = 26.76 + 5.03 = 31.79 \text{ lbs.}$$

$$\text{Resultant Load } R_t = \sqrt{(118.5)^2 + (31.79)^2} = \underline{123 \text{ lbs.}}$$

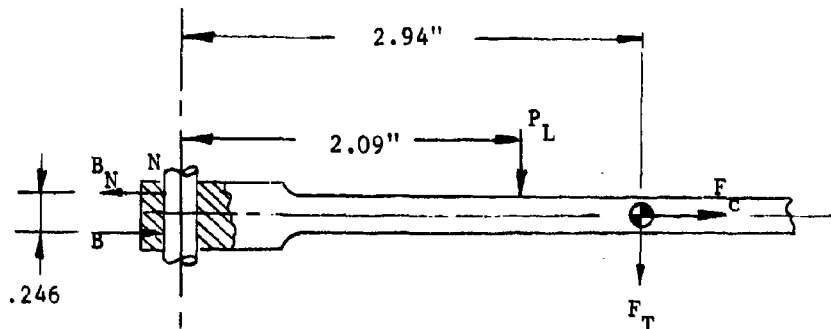
UNCLASSIFIED



# UNCLASSIFIED

Report AFRPL-TR-69-90, Appendix B

## Transverse and Centrifugal Loading



Assume pin reactions on lug are taken out as point loads as indicated. (assumed acting @ 1/3 points)

$$[\Sigma M_N = 0] \quad (50.4 \times 2.09) + (.65 \times 2.94) - (3.5 \times .123) = .246 B$$

$$B = 431 \text{ lbs}$$

$$[\Sigma F_x = 0] \quad B_N = 431 + 3.5 = \underline{434.5 \text{ lbs}}$$

### Total Load on Lug $T_O$

Assume that  $B_N$  above acts uniformly across lug and is directly additive to resultant reaction load  $R_t$  on previous page.

Then total load on lug is:

$$T_O = R_t + B_N$$

$$T_O = 123.0 + 434.5$$

$$T_O = \underline{557.5 \text{ lbs}}$$

UNCLASSIFIED

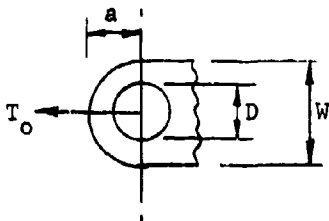
# UNCLASSIFIED

Report AFRPL-TR-69-90, Appendix B

Analysis of lug and pin assembly will be made in accordance with the method outlined in Reference 6.

## Dimensions:

Sketch shows equivalent lug.



$$a_{\min} = .187''$$

$$D_{\max} = .188''$$

$$W = .375''$$

$$t_{\min} = .369''$$

$$\frac{a}{D} = 1.0 \quad \frac{W}{D} = 2.0 \quad \frac{D}{t} = .51$$

$$A_{br} = Dt = .0694 \text{ in}^2 \quad A_t = (W-D)t = (.375 - .188).369 = .0694 \text{ in}^2$$

$P_{bru} \sim \text{Ultimate Load} \sim \text{Shear Bearing Failure}$

From Figure 13 of Reference 6: For  $\frac{a}{D} = 1$  and  $\frac{D}{t} = 2$

$$K_{br} = 0.84$$

$$P_{bru} = K_{br} A_{br} F_{tu_x}$$

$$\text{From Drawing No. 1146053 } F_{tu_x} = 62000 \text{ lbs/in}^2$$

$$\text{Then } P_{bru} = .84 \times .0694 \times 62000 = 3610 \text{ lbs}$$

UNCLASSIFIED

# UNCLASSIFIED

Report AFRPL-TR-69-90, Appendix B

## P<sub>tu</sub> Ultimate Load ~ Tension Failure

From Figure 12 of Reference 6: For  $\frac{W}{D} = 2.0$

$$K_t = .93$$

$$P_{tu} = K_t A_t F_{tu}$$

$$P_{tu} = .93 \times .0694 \times 62000$$

$$P_{tu} = \underline{4000 \text{ lbs}}$$

## P<sub>y</sub> Yield Load

$$P_{bru} < P_{tu} \therefore (P_u)_{\min} = P_{bru} = 3610 \text{ lbs}$$

$$\frac{(P_u)_{\min}}{A_{br} \times F_{tu_x}} = \frac{3610}{.0694 \times 62000} = 0.839$$

From Figure 15 of Reference 6:  $C = 1.1$

$$P_y = C \frac{F_{ty_x}}{F_{tu_x}} (P_u)_{\min}$$

From Drawing No. 1146053  $F_{ty_x} = 40000$

$$P_y = 1.1 \frac{40000}{62000} 3610 = \underline{2560 \text{ lbs}}$$

UNCLASSIFIED

# UNCLASSIFIED

Report AFRPL-TR-69-90, Appendix B

## Margin of Safety

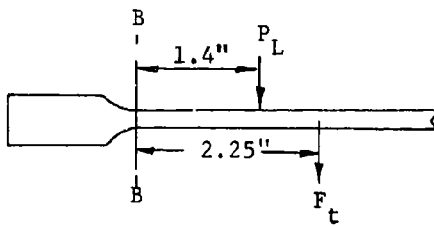
$$\text{Maximum lug load } T_c = 557.5 \text{ lbs}$$

$$\text{Minimum Allowable Load } P_{bru} = 3610 \text{ lbs}$$

$$\text{M.S.} = \frac{P_{bru}}{DF \times T_o} - 1$$

$$\text{M.S.}_u = \frac{3610}{1.5 \times 557.5} - 1 = \underline{\underline{3.19}} \leftarrow$$

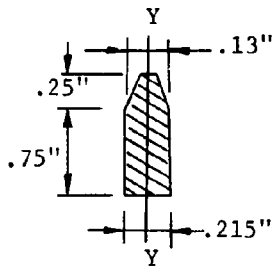
## Bending of Blade Due to Lift and Transverse Loads



$$M_{BB} = (1.4 \times 50.4) + (3.5 \times 2.25)$$

$$M_{BB} = 78.38 \text{ in-lbs}$$

Approx.  $I_{yy}$



Section B-B

$$I_{yy} = \frac{10^{-3}}{12} [ .75(2.15)^3 + .25(1.3)^3 ]$$

$$I_{yy} = 7.5 \times 10^{-4} \text{ in}^4$$

$$f_b = \frac{M_{BB} \times C}{I_{yy}} = \frac{78.38 \times .107}{7.5 \times 10^{-4}}$$

$$f_b = \underline{\underline{11200 \text{ lbs/in}^2}}$$

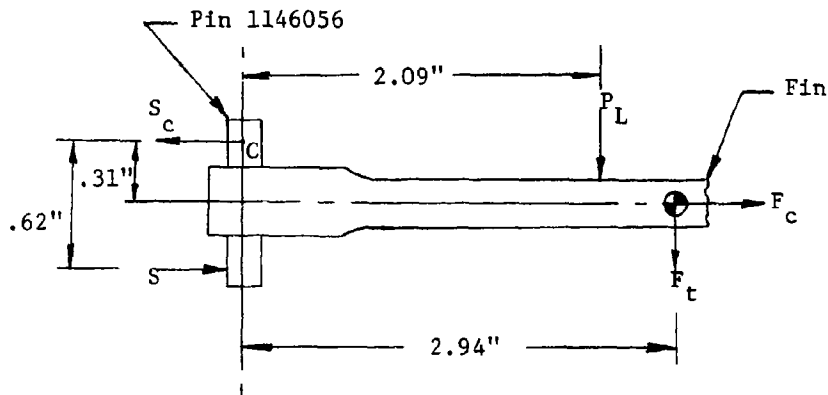
$$\text{M.S.} = \frac{F_{tu}}{DF \times f_b} - 1 = \frac{62000}{1.5 \times 11200} - 1 = \underline{\underline{2.69}} \leftarrow$$

# UNCLASSIFIED

Report AFRPL-TR-69-90, Appendix B

## 3. Pin, Straight, Drawing No. 1146056

Pin is a press fit in fin and slip fit in lugs on nozzle plate. From Page 45, the total pin reaction due to loads  $P_D$ ,  $F_A$  and  $F_C$  was  $R_T = 123$  lbs. The reaction due to  $P_L$ ,  $F_T$  and  $F_C$  is calculated below.



$$[\Sigma M_c = 0] \quad (50.4 \times 2.09) + (.65 \times 2.94) - (3.5 \times .31) = 5 \times .62$$

$$S = 171.5 \text{ lbs}$$

$$[\Sigma F_x = 0] \quad S_c = 171.5 + 3.5 = \underline{175.0 \text{ lbs}}$$

Assume this load directly additive to the 123 lb load where they act in the same direction. The 123 lb load is reacted by both sides of pin or:

$$\text{Load/Side} = \frac{123}{2} = 62.5 \text{ lbs}$$

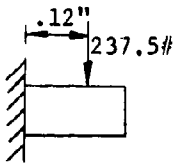
$$\text{Net pin load} = 175 + 62.5 = \underline{237.5 \text{ lbs}} = N$$

UNCLASSIFIED

# UNCLASSIFIED

Report AFRPL-TR-69-90, Appendix B

Assume pin cantilevered as shown:



Pin is modified from MS16556-643

3/16" dia cres steel pin with a Rockwell  
hardness of 36 to 42

$$M = 237.5 \times .12 = 28.5 \text{ in-lbs}$$

$$S = \frac{\pi d^3}{32} = \frac{\pi (1.875 \times 10^{-1})^3}{32} = .648 \times 10^{-3} \text{ in}^3$$

$$f_b = \frac{M}{S} = \frac{28.5}{6.48 \times 10^{-4}} = \pm 44000 \text{ lbs/in}^2$$

For minimum hardness of 36 Rockwell "C"

$$f_{tu} \approx 160,000 \text{ lbs/in}^2$$

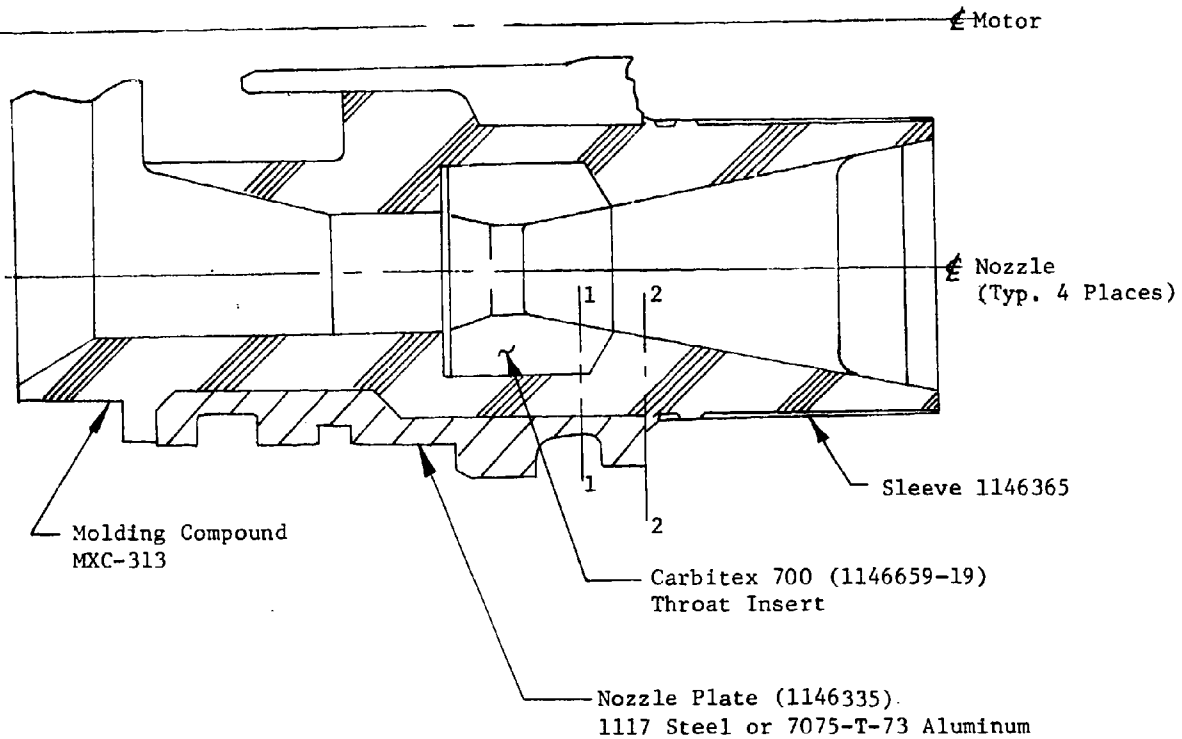
$$M.S. = \frac{f_b}{DF \times F_{tu}} - 1 = \frac{160000}{1.5 \times 44000} - 1 = \underline{\underline{1.42}} \leftarrow$$

UNCLASSIFIED

# UNCLASSIFIED

Report AFRPL-TR-69-90, Appendix B

## 4. Closure Assembly (Ref. Drawing No. 1146639)

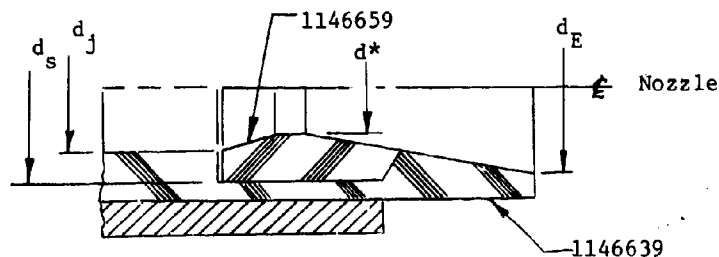


From the above sketch it can be seen that the molding compound is retained in the nozzle plate by mechanical interference as well as bond shear. In the event of a bond failure however, the full ejection load on the insert would have to be carried in tension by the molding compound at Section 1-1. This section will now be checked for that load.

# UNCLASSIFIED

Report AFRPL-TR-69-90, Appendix B

## Calculation of Ejection Load



The ejection load on a rocket nozzle can be computed from the following expression:

$$F_{ej} = P_j A_j (1 + \gamma M_j^2) - P_E A_E (1 + \gamma M_E^2) + \frac{\pi P_j}{4} (d_s^2 - d_j^2) + \frac{\pi P_\alpha}{4} (d_E^2 - d_s^2)$$

### From Drawings

$$d_s = .675" \quad d_s^2 = .455$$

$$d_j = .350" \quad d_j^2 = .122$$

$$d^* = .271"$$

$$d_E = .796"$$

$$P_j = 1990 \text{ psi}$$

$$P_E = P_\alpha = 14.7 \text{ psi}$$

### Various Equation Terms:

$$A_j = .7854 (.35)^2 = .0963 \text{ in}^2$$

$$A_E = .7854 (.675)^2 = .358 \text{ in}^2$$

UNCLASSIFIED



**UNCLASSIFIED**

Report AFRPL-TR-69-90, Appendix B

$$A_E = .7854 (.796)^2 = .498 \text{ in}^2$$

$$A^* = .7854 (.271)^2 = .0576 \text{ in}^2$$

From compressible flow tables for  $\gamma = 1.2$ :

$$\text{For } \frac{A_j}{A^*} = \frac{.0963}{.0576} = 1.670 \quad M_j = .38$$

$$\text{For } \frac{A_E}{A^*} = \frac{.498}{.0576} = 8.650 \quad M_E = 3.18$$

Ejection Load Becomes:

$$F_{ej} = 1990 (.0963)[1 + 1.2(.38)^2] - 14.7 (.498)[1 + 1.2(3.18)^2] \\ + .7854 \times 1990 (.675^2 - .350^2) + .7854 \times 14.7 (.796^2 - .908^2)$$

$$F_{ej} = 224 - 96 + 520 - 2$$

$$F_{ej} = \underline{646 \text{ lbs}}$$

$$f_t = \frac{646}{\frac{\pi}{4}(.908^2 - .675^2)} = 2300 \text{ psi}$$

Manufacturer's data (Fiberite Corp.), indicate a room temperature tensile strength for MXC-313 of 7200 psi. Based on silica reinforced phenolics, and temperatures indicated on Figure 10a, it is estimated that the minimum strength might be reduced 50%, i.e.,  $F_{tu} = 0.5 \times 7200 = 3600 \text{ psi}$

$$\text{M.S.} = \frac{3600}{2300} - 1 = 0.57 \leftarrow$$

**UNCLASSIFIED**

# UNCLASSIFIED

Report AFRPL-TR-69-90, Appendix B

## Check Sleeve (Drawing No. 1146365)

This part will be conservatively checked for the maximum internal pressure in the exit cone.

$$r = 0.45''$$

At Section 2-2 (Reference Page 53)

$$t = .007'' \text{ minimum}$$

$$\text{Mat.} = \text{MT-1010 - MT-1020 Steel}$$

$$d_2 = 0.430 \text{ in}$$

$$F_{ty} = 30,000$$

$$\frac{A_2}{A^*} = \frac{.430^2}{.271^2} = 2.52$$

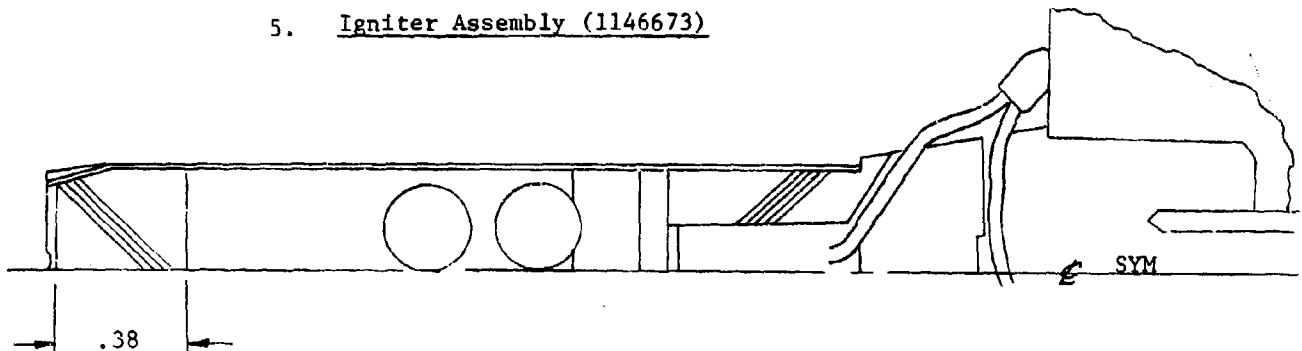
$$\frac{P_2}{P_t} = 0.084 \text{ (Reference Comp. Flow Tables } \gamma = 1.2)$$

$$P_2 = .084 \times 1991 = 167 \text{ psi}$$

$$f_t = \frac{167 \times .45}{.007} = 10,700 \text{ psi}$$

$$\text{M.S.} = \frac{30,000}{10,700} - 1 = 1.80 \leftarrow$$

## 5. Igniter Assembly (1146673)



A check will be made to insure that the polystyrene plug will shear out before the aluminum tube will rupture.

# UNCLASSIFIED

Report AFRPL-TR-69-90, Appendix B

## Pressure to Eject Plug

Plug is of polystyrene and is bonded to the chamber. Shear strength of adhesive is estimated to be 3000 psi. Shear strength of polystyrene is 40-90 psi per mfg. data.

∴ Plug will fail in shear in polystyrene.

$$\text{Area in shear, } A_s = \pi \times .58 \times .38 = .691 \text{ in}^2$$

$$\text{Maximum load to eject plug} = .691 \times 90 = 62.2 \text{ lbs}$$

Pressure required to eject plug:

$$p_{\max} (.7854)(.58)^2 = 62.2$$

$$p_{\max} = \underline{236 \text{ psi}} \text{ maximum}$$

## Stress in 1146095 Chamber @ $p_{\max}$

$$t = .007" \text{ min}$$

$$f_t = \frac{p r}{t}$$

$$f_t = \frac{236 \times .313}{.007} = \underline{10500 \text{ lbs/in}^2}$$

Tube is 6061: Assume condition "O" ~ conservative

$$F_{tu_{\min}} = 14000 \text{ lbs/in}^2$$

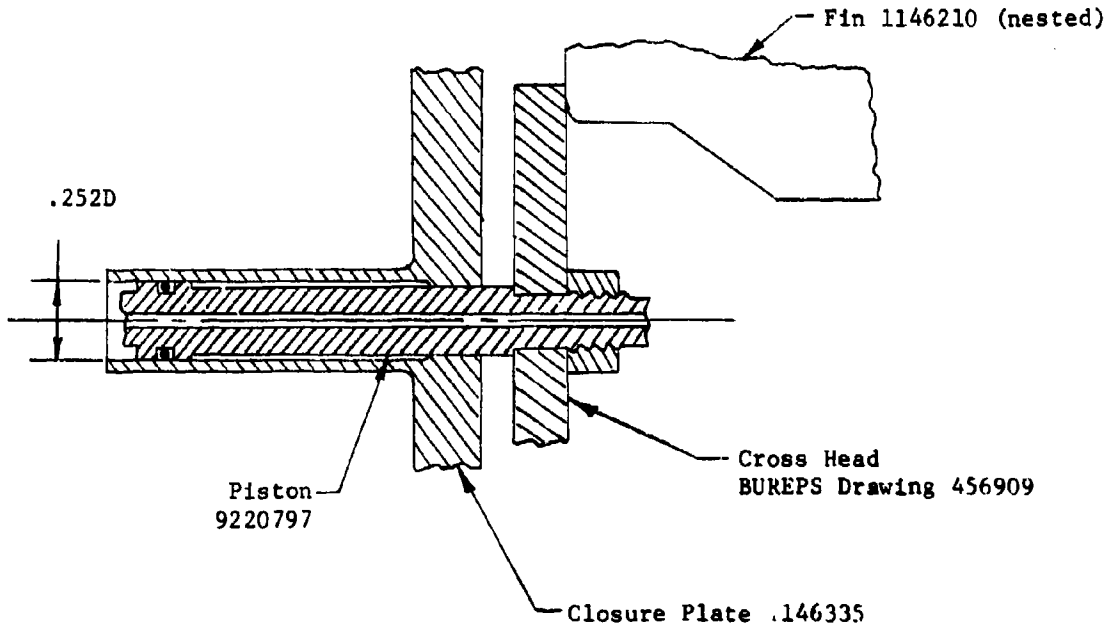
∴ Plug will eject before bursting chamber.

UNCLASSIFIED

# UNCLASSIFIED

Report AFRPL-TR-69-90, Appendix B

## 6. Piston and Cross-Head Assembly



### Piston Load $P_p$

Piston is actuated by chamber pressure and applies a load on the fins through the cross-head.

$$p_c = 1990 \text{ psi}$$

$$P_p = .7854(.252)^2 1990 = 99.3 \text{ lbs}$$

A detail piston drawing is not available, however, from mating parts and other information the following dimensions were estimated:

$$\text{O.D.} = .215''$$

$$\text{I.D.} = .060''$$

# UNCLASSIFIED

Report AFRPL-TR-69-90, Appendix B

$$\text{Area in Compression} = A_p = .7854 [(.215)^2 - (.06)^2] = .0336 \text{ in}^2$$

$$f_c = \frac{99.3}{.0336} = 2960 \text{ lbs/in}^2 \quad \text{M.S.} = \text{High}$$

## Cross Head-Fins Folded ~ Bending Load

From previous page the load on the central part of the cross head is 99.3 lbs.

Per BUREPS Drawing No. 456909, piston is proof tested with a central load of 500 lbs.

$$\text{M.S.} = \frac{500}{1.5 \times 99.3} - 1 = \underline{2.36} \leftarrow$$

## Cross Head-Fins Extended ~ Compression Load

With the fins in the extended position, an axial load exists on the legs of the cross head. This load was calculated to be 118.5 lbs on Page 45.

Per Drawing No. 456909, the legs are subjected to a proof load of 1000 lbs.

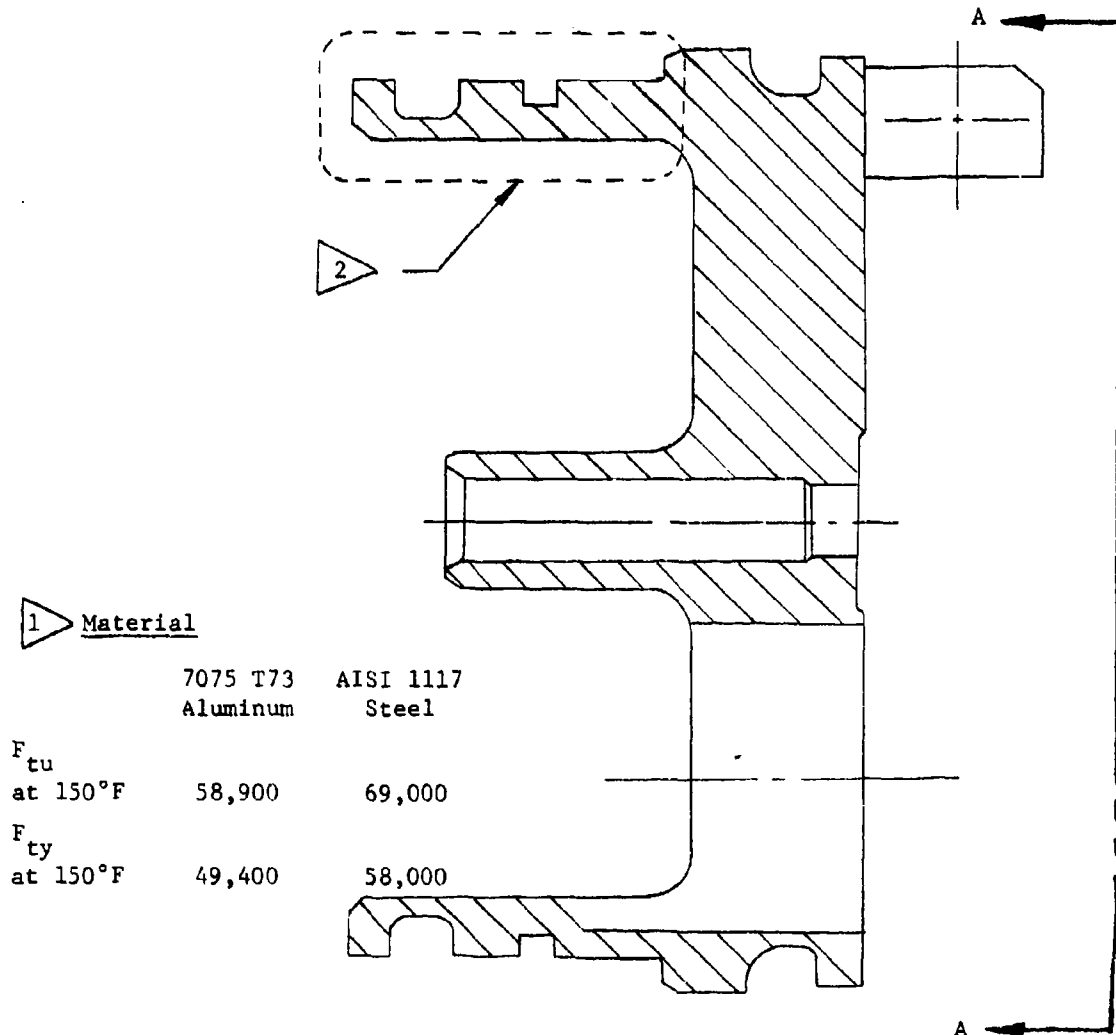
$$\text{M.S.} = \frac{1000}{1.5 \times 118.5} - 1 = \underline{\text{High}} \leftarrow$$

UNCLASSIFIED

# UNCLASSIFIED

Report AFRPL-TR-69-90, Appendix B

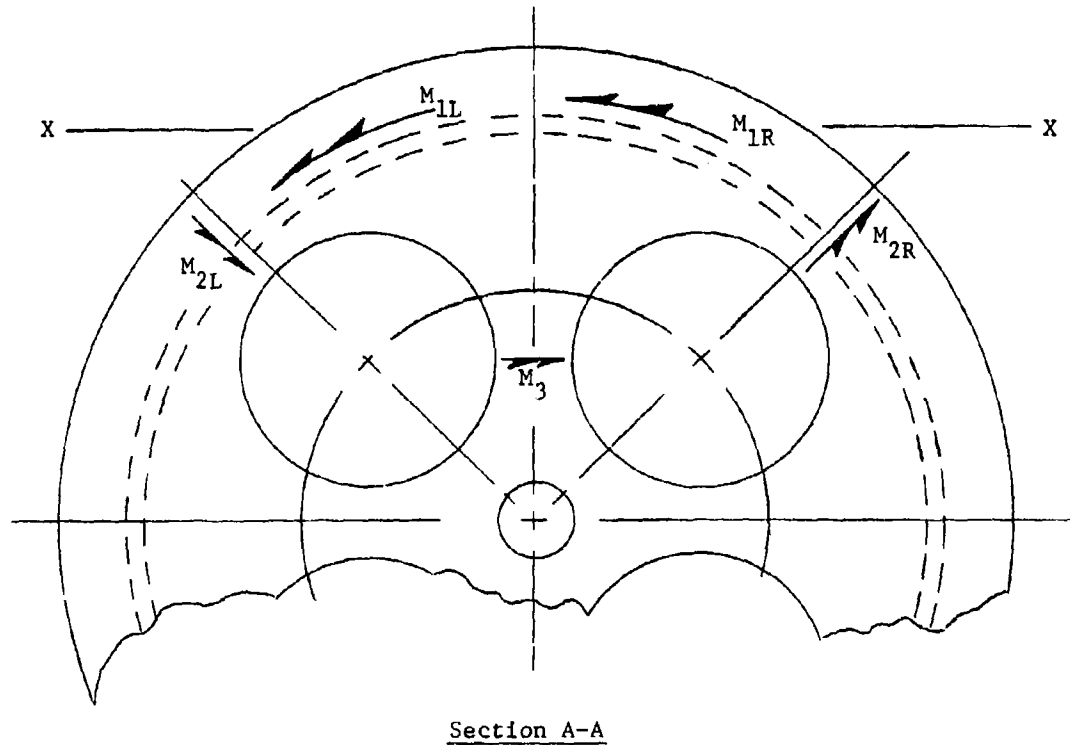
## 7. Nozzle Plate, Drawing No. 1146335-1



- 1 At the present time both aluminum and steel are under consideration for the nozzle plate material. This analysis deals specifically with the aluminum design. Based on a comparison of material properties and margins of safety, however, the alternate steel design is also considered to be substantiated.
- 2 The structural analysis of the nozzle plate presented herein does not include substantiation of the enclosed lockwire attachment flange. This has been more conveniently evaluated as part of the motor case assembly.

**UNCLASSIFIED**

Report AFRPL-TR-69-90, Appendix B



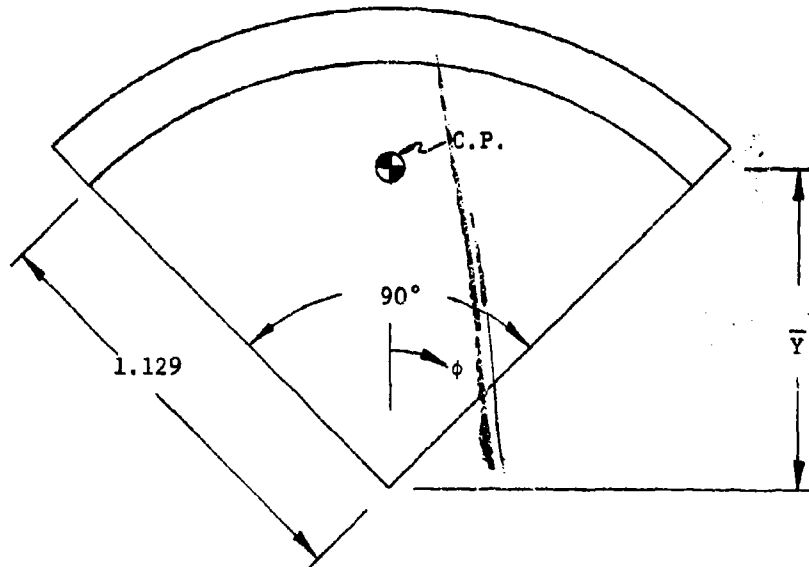
The perforated plate (Section A-A), which acts as an end closure, will be analyzed by "yield line" theory. The failure mechanism due to the normal pressure loading will be assumed to be general yielding along the critical 1-2-3 planes indicated above. Just prior to general yielding the pie shaped sector 1-2-3 must support the total applied loads by a reaction along ARC 1 plus the edge moments indicated as  $M_1$ ,  $M_2$ , and  $M_3$ . Total moments for this sector will be summed about the X-X axis and the total applied moment will be compared to the total reactive moment when full yielding is reached at all points around the 1-2-3 sector.

**UNCLASSIFIED**

# UNCLASSIFIED

Report AFRPL-TR-69-90, Appendix B

The total applied moment about the X-X axis consists entirely of the pressure loading.



Assume pressure acts uniformly on sector with radius = 1.129 inches, applied load (limit)

$$P = \frac{p\pi R^2}{4} = \frac{1990 \pi (1.129)^2}{4} = 2000 \text{ lbs}$$

moment arm

$$= R - \bar{Y} = R - \frac{2R \sin(\pi/4)}{3(\pi/4)}$$

UNCLASSIFIED



# UNCLASSIFIED

Report AFRPL-TR-69-90, Appendix B

$$= 1.129 - \frac{2(1.129)(.707)}{3(\pi/4)}$$

$$= 1.129 - .680 = .449$$

Applied Moment (limit)

$$M_{\text{applied yield}} = 2000(.449) = 898 \text{ in-lbs}$$

Applied Moment (Ultimate)

$$M_{\text{applied yield}} = (1.5)(898) = 1350 \text{ in-lbs}$$

The reactive moment about the X-X axis consists of the effects of the edge loads plus the edge moments as calculated below:

## Edge Reaction

Edge Reaction Load (Limit)

$$W = \frac{pR}{2} = \frac{1990(1.129)}{2}$$

$$= 1125 \text{ lbs/in}$$

UNCLASSIFIED

**UNCLASSIFIED**

Report AFRPL-TR-69-90, Appendix B

Moment about X-X Axis

$$\begin{aligned}
 M_{X-X} &= 2 \int_0^{\pi/4} WR^2 (1 - \cos \phi) d\phi \\
 &= 2 WR^2 [\phi - \sin \phi]_0^{\pi/4} \\
 &= .156 WR^2
 \end{aligned}$$

$$\begin{aligned}
 M_{X-X(\text{limit})} &= .156(1125)(1.129)^2 \\
 &= 224 - \text{in lbs}
 \end{aligned}$$

$$\begin{aligned}
 M_{X-X(\text{ult.})} &= 1.5(224) \\
 &= 336 - \text{in lbs}
 \end{aligned}$$

Edge Moment ( $M_1$ )

$$\begin{aligned}
 M_1 &= \frac{F_{\text{allow}} t^2 (1.5)}{6} = \frac{F_{\text{allow}} (.244)^2 (1.5)}{6} \\
 &= .0149 F_{\text{allow}}
 \end{aligned}$$

Moment about X-X Axis

$$\begin{aligned}
 M_{X-X} &= 2M, R \cos (\pi/4) \\
 &= 2(.0149)F_{\text{allow}}(1.129)(.707) \\
 &= .0238 F_{\text{allow}}
 \end{aligned}$$

**UNCLASSIFIED**

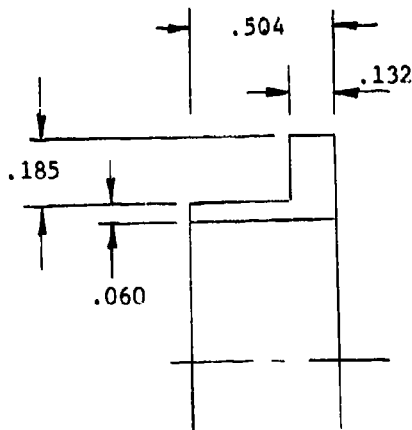
# UNCLASSIFIED

Report AFRPL-TR-69-90, Appendix B

$$\begin{aligned} M_{X-X(\text{limit})} &= .0238(49400) \\ &= 1180 - \text{in lbs} \end{aligned}$$

$$\begin{aligned} M_{X-X(\text{ult})} &= .0238(58900) \\ &= 1400 - \text{in lbs} \end{aligned}$$

Edge Moment ( $M_2$ )



$$M_{2L} = M_{2R} = F_{\text{allow}} \left[ \leq \frac{Bt^2}{4} \right]$$

$$= F_{\text{allow}} \left[ \frac{.060(.504)^2}{4} + \frac{.185(.132)^2}{4} \right]$$

$$= F_{\text{allow}} (.00382 + .00081)$$

$$= .00463 F_{\text{allow}}$$

$$\begin{aligned} M_{X-X(\text{limit})} &= 2 M_{2L} \cos(\pi/4) \\ &= 2(.00463)(49400)(.707) \\ &= 324 - \text{in lbs} \end{aligned}$$

$$\begin{aligned} M_{X-X(\text{ult})} &= 2(.00463)(58900)(.707) \\ &= 387 - \text{in lbs} \end{aligned}$$

UNCLASSIFIED

# UNCLASSIFIED

Report AFRPL-TR-69-90, Appendix B

## Edge Moment ( $M_3$ )

Moment about X-X Axis

$$\begin{aligned} M_{X-X} &= \frac{F_{\text{allow}} b t^2 (1.5)}{6} \\ &= \frac{F_{\text{allow}} (.152)(.504)^2 (1.5)}{6} \\ &= .00965 F_{\text{allow}} \end{aligned}$$

$$\begin{aligned} M_{X-X(\text{limit})} &= .00965(49400) \\ &= 477 \text{ - in lbs} \end{aligned}$$

$$\begin{aligned} M_{X-X(\text{ult})} &= .00965 (58900) \\ &= 570 \text{ - in lbs} \end{aligned}$$

## Margins of Safety

$$\begin{aligned} \text{M.S. (limit)} &= \frac{\text{Reactive Moment}}{\text{Applied Moment}} - 1 \\ &= \frac{224 + 1180 + 324 + 477}{898} - 1 = \underline{+1.45} \end{aligned}$$

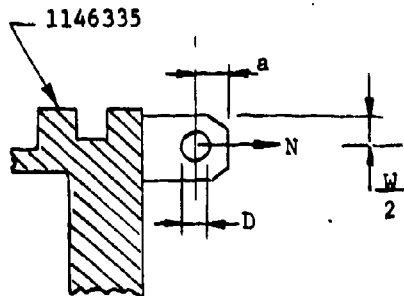
$$\begin{aligned} \text{M.S. (ult)} &= \frac{\text{Reactive Moment}}{\text{Applied Moment}} - 1 \\ &= \frac{336 + 1400 + 387 + 570}{1350} - 1 = \underline{+0.99} \end{aligned}$$

UNCLASSIFIED

# UNCLASSIFIED

Report AFRPL-TR-69-90, Appendix B

## Lugs for Fins



$a \approx .22''$  min. scaled from Drawing

$\frac{W}{2} = .15''$  (dimension @ min. leg)

$D = .191''$

$t = .18''$

$$\frac{a}{D} = \frac{.22}{.191} = 1.15$$

$$\frac{W}{D} = \frac{.30}{.191} = 1.57$$

$$\frac{D}{t} = \frac{.191}{.18} = 1.06$$

$$A_{br} = Dt = .191 \times .18 = .0344 \text{ in}^2$$

$$A_t = (W-D)t = (.30 - .191) \times .18 = .0196 \text{ in}^2 \quad (\text{conservative})$$

$$N = 237.5 \text{ lb (from anal. for pin)}$$

## $P_{bru}$ Ultimate Load ~ Shear Bearing Failure

From Reference 6

$$K_{br} = 1.04$$

$$P_{bru} = K_{br} A_{br} F_{tu_x}$$

For 7075-T73

From Reference [2]

$$F_{ty_{x_{min}}} = 52000 \text{ lbs/in}^2 \quad F_{tu_{x_{min}}} = 61000 \text{ lbs/in}^2 \quad (\text{annealed values})$$

$$P_{bru} = 1.04 \times .0344 \times 61000 = 2180 \text{ lbs}$$

-67-  
UNCLASSIFIED

**UNCLASSIFIED**

Report AFRPL-TR-69-90, Appendix B

P<sub>tu</sub> Ultimate Load, Tension Failure

From Reference 6

$$K_t = .97$$

$$P_{tu} = K_t A_t F_{tu} = .97 \times .0196 \times 61000 = 1160 \text{ lbs}$$

P<sub>y</sub> Yield Load

$$P_{tu} < P_{bru} \therefore (P_u)_{\min} = P_{tu} = 1160$$

$$\frac{(P_u)_{\min}}{A_{br} \times F_{tu_x}} = \frac{1160}{.0344 \times 61000} = .552$$

$$C = 1.1$$

$$P_y = C \frac{F_{ty_x}}{F_{tu_x}} (P_u)_{\min} = 1.1 \frac{52000}{61000} 1160 = 1090 \text{ lbs}$$

Margin of Safety

Maximum lug load = 237.5 lbs (from Page 11)

Minimum allowable load: P<sub>tu</sub> = 1160 lbs

$$M.S. = \frac{P_{tu}}{DF \times N} - 1$$

$$M.S. = \frac{1160}{1.5 \times 237.5} - 1 = \underline{2.26} \leftarrow$$

**UNCLASSIFIED**

# UNCLASSIFIED

Report AFRPL-TR-69-90, Appendix B

## C. PROPELLANT GRAIN

An important consideration for all solid rocket motors is the thermal environment in which the motor is required to operate. This is primarily due to the differential coefficient of thermal expansion between solid propellants and conventional rocket case materials. In many designs this difference is nearly an order of magnitude and the 2.75-in. rocket is no exception. In addition, the extreme temperature and strain rate dependence of solid propellant mechanical properties usually requires that both ends of the environmental range be carefully investigated.

The actual modes of failure which are usually observed in case bonded rockets are: (a) failure of the bond due to excessive tensile and/or shear stresses at the low operating temperature, (b) failure of the bond due to shear stresses during firing at either the high or low temperature, and (c) cracking of the inner bore of the grain due to either long time low storage or temperature cycling between the high and low temperature requirements. After reviewing the design requirements of the 2.75-in. rocket as specified in Reference 1, the following specific conditions were selected for detailed structural evaluation.

- (1) Long time Storage at  $-65^{\circ}\text{F}$
- (2) Firing at  $-65^{\circ}\text{F}$
- (3) Firing at  $150^{\circ}\text{F}$
- (4) Thermal Cycling Between  $150^{\circ}\text{F}$  and  $-65^{\circ}\text{F}$   
(three cycles)

The stresses and strains due to these thermal and pressure loads were calculated and, where applicable, the results have been compared with appropriate laboratory test data.

# UNCLASSIFIED

Report AFRPL-TR-69-90, Appendix B

## 1. Method of Analysis

The structural analysis was performed using Computer Program 1099, "Stress Analysis of General Axisymmetric Bodies." This program is a finite difference solution of Southwell's stress function theory for axisymmetric solids of revolution. Southwell's governing equations are differential equations in two stress functions. These equations satisfy both equilibrium and compatibility conditions of the grain. The grain is assumed to be a homogeneous, isotropic, elastic material subjected to axisymmetric loads.

The finite difference technique is employed since the general solution of the differential equations is not known. A suitable grid is established on the longitudinal section of the grain and discrete values of both stress functions are identified at each intersection point. The particular boundary conditions are established using, in general, normal and shear stresses on the free boundaries and matching strains on the constrained boundaries. The governing and boundary equations are written in finite difference form yielding "n" linear simultaneous equations in "n" unknowns. The discrete stress function values are obtained from this system of equations by the Gaussian elimination process on an IBM 360/65 computer. The stress function values are substituted back into the finite difference equations for evaluation of the stresses and strains at all grid points.

## 2. Results

A summary of the maximum stresses and strains obtained for the various design conditions is contained in Table 5. In all cases the allowable values are equal to or greater than the requirements and the grain is considered to be structurally adequate for all its design conditions.

UNCLASSIFIED



## UNCLASSIFIED

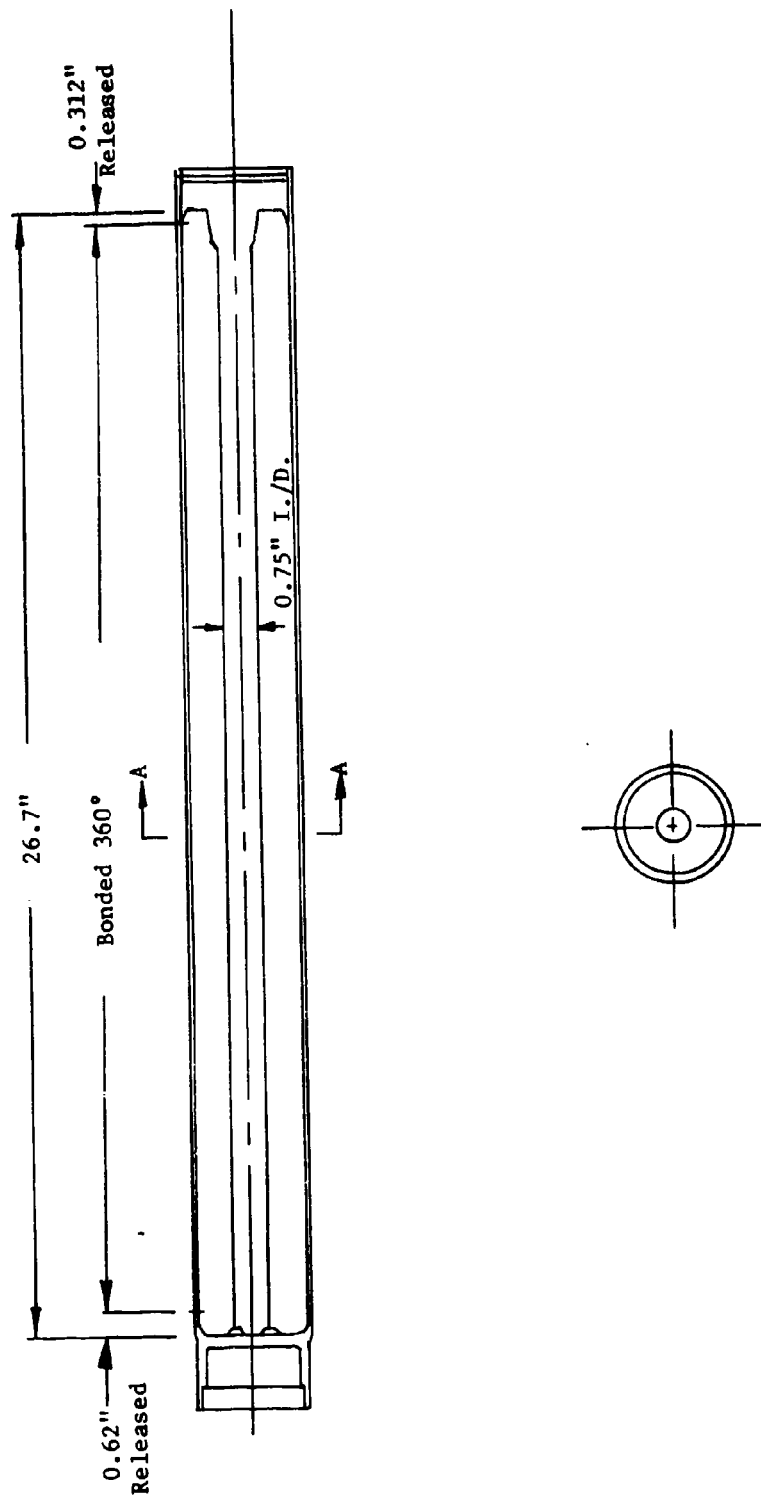
Report AFRPL-TR-69-90, Appendix B

In addition to the conventional structural analysis contained herein a "cumulative damage" analysis was also conducted on the 2.75-in. rocket motor. Recent work at Aerojet has shown that this approach can be used to make theoretical predictions of the actual number of cycles which a grain can withstand between various temperature limits. Details of this cumulative damage analysis, which considers the interaction of transient heat conduction and thermoviscoelastic propellant behavior, are contained elsewhere in the "Design Disclosure" documentation. Results of this work do, however, further confirm the ability of the 2.75 grain to withstand the required three cycles between 150 and -65°F.

UNCLASSIFIED

UNCLASSIFIED

Report AFRPL-TR-69-90, Appendix B



SECTION A-A

PROPELLANT GRAIN CONFIGURATION, 2.75 INCH MOTOR

FIGURE 16

UNCLASSIFIED

UNCLASSIFIED

Report AFRPL-TR-69-90, Appendix B

Table 5. Maximum Stresses and Strains in 2.75-In. Motor Grain  
Inner Bore = 0.75-In. Full Length

	Interface Shear Stress			Interface Tensile Stress			Inner Bore Hoop Strain		
	Calculated (psi)	Allowable (psi)	M.S.	Calculated (psi)	Allowable (psi)	M.S.	Calculated (%)	Allowable (%)	M.S.
Storage at -65°F (Ep = 400 psi)	23.4	74	2.16	32.7	92	1.82	12.7	>12.7	1
Firing at -65°F p = 1500 psi (Ep = 35,000)	113	560	0.35	Compression			2.7	3.2	2
Flight at +150°F p = 1990 psi AA = 40 g's Spin = 10 rps (Ep = 400 psi)	10.9	120	Large	Compression			3.6	3	Ample

1 Substantiation of strain capability for storage and cycling condition is based on cycling test program described on page 11. Margin of safety on actual strain value is not considered applicable.

2 Margin of safety for low temperature firing condition is based on allowable incremental strain which can be imposed on prestrained propellant (reference, Figure 7).

3 Allowable high rate strain at 150°F has not been established by test but is estimated to be well in excess of required 3.6 percent.

UNCLASSIFIED

# UNCLASSIFIED

Report AFRPL-TR-69-90, Appendix B

## REFERENCES

1. Negotiated Contract FO L611-67-C-0014 dated 2 June 1967, between Edwards Air Force and Aerojet-General Corp.
2. Military Handbook MIL-HDBK-5A dated 8 February 1966, "Metallic Materials and Elements for Aerospace Vehicle Structures"
3. Structures Manual, Aerojet-General Corporation, Sacramento Facility
4. Roark, R. J.: "Formulas for Stress and Strain," Third Edition, McGraw-Hill Book Co., Inc., New York, 1954
5. Croy, E. L. and Schumacher, J. G., "An Analysis of Thick Cylinders in the Plastic Range," Aerojet-General Technical Memorandum 240 SRP dated 7 December 1962
6. Melcon, M. A. and Hoblit, F. M., "Developments in the Analysis of Lugs and Shear Pins," Product Engineering - June 1953
7. Messner, A. M., "Propellant Grain Stress Analysis," Proc. 17th JANAF-ARPA-NASA Solid Propellant Group Meeting, May 1961
8. Messner, A. M. and Shearly, R. N., "Stress Analysis of Axisymmetric Propellant Grain with Arbitrary End Geometries," Aerojet-General Corporation, Technical Memo 201, SRP, October 1962 (Confidential)
9. 2.75-In. FFAR Monthly Status Report. Contract FO L611-67-C-0114 10 May 1968 (Confidential)

UNCLASSIFIED

**UNCLASSIFIED**

Report AFRPL-TR-69-90

**APPENDIX C**

**WEIGHTS AND BALANCE**

**UNCLASSIFIED**

# UNCLASSIFIED

Report AFRPL-TR-69-90, Appendix C

## WEIGHTS AND BALANCE

The calculated Improved 2.75-in. motor weights and c.g. data are shown in Figures 1 and 2. Figure 3 is a summary of the most recent available actual weights.

UNCLASSIFIED

# UNCLASSIFIED

Report AFRPL-TR-69-90, Appendix C

Line	Item	Pre-Fire Condition			Post-Fire Condition		
		Weight, lb	Arm, in.*	Moment, in.-lb	Weight, lb	Arm, in.*	Moment, in.-lb
1	Motor Tube	(2.36)	(13.80)	(32.57)	(2.36)	(13.80)	(32.57)
2							
3	Internal Insulation	(0.48)	(17.08)	(8.20)	(0.40)	(16.95)	(6.78)
4	Fwd Insulator	0.06	3.00	0.18	0.06	3.00	0.18
5	Aft Insulator	0.08	29.90	2.39	0.08	29.90	2.39
6	Cap, Insulator	0.03	30.55	0.92	0.02	30.60	0.61
7	Liner	0.30	15.60	4.68	0.23	15.50	3.57
8	Release Agent	0.01	3.10	0.03	0.01	3.10	0.03
9							
10	Closure Assembly	(1.15)	(31.71)	(36.47)	(1.04)	(31.75)	(33.02)
11	Plate	0.85	31.80	27.03	0.85	31.80	27.03
12	Sleeves	0.02	32.75	0.66	0.02	32.75	0.66
13	Inserts and Seals	0.05	32.00	1.60	0.03	32.00	0.96
14	Washers	0.01	31.70	0.32	-	-	-
15	Molding Compound	0.22	31.20	6.86	0.14	31.20	4.37
16							
17	Fin Assembly	(0.60)	(34.95)	(20.97)	(0.59)	(34.32)	(20.25)
18	Fin Blades	0.48	35.45	17.02	0.48	34.65	16.63
19	Pins	0.02	32.55	0.65	0.02	32.55	0.65
20	Piston	0.02	32.15	0.64	0.02	32.75	0.66
21	Crosshead and Nuts	0.07	32.40	2.27	0.07	33.00	2.31
22	Retainer	0.01	39.20	0.39	-	-	-
23							
24	Igniter Assembly	(0.02)	(30.20)	(0.60)	-	-	-
25							
26	Lockwire and O-Ring	(0.03)	(31.20)	(0.94)	(0.03)	(31.20)	(0.94)
27							
28	TOTAL INERTS	(4.64)	(21.51)	(99.75)	(4.42)	(21.17)	(93.56)
29							
30	Propellant	(8.05)	(16.63)	(133.88)	-	-	-
31	Chamber	8.03	16.60	133.30	-	-	-
32	Igniter	0.02	28.80	0.58	-	-	-
33							
34	TOTAL MOTOR	(12.69)	(18.41)	(233.63)	(4.42)	(21.17)	(93.56)

\* Measured from forward edge of motor tube (Motor Station 0.00)

Improved 2.75-in. FFAR Weight and Balance Status

Figure 1

Page 2

# UNCLASSIFIED

# UNCLASSIFIED

Report AFRPL-TR-69-90, Appendix C

<u>Line</u>	<u>Item</u>	<u>Part Number</u>	<u>Revision</u>	<u>Weight, lb</u>
1	Motor Tube	1569403	GFM	(2.36)
2				
3	Internal Insulation			(0.48)
4	Fwd Insulator	1146033-1	N/C	0.06
5	Aft Insulator	1146637-1	B	0.08
6	Cap, Insulator	1146370-1	C	0.03
7	Liner	IBS 105-3		0.30
8	Release Agent	RTV 587		0.01
9				
10	Closure Assembly	1146639-4	A	(1.15)
11	Plate	1146335-1	N/C	0.85
12	Sleeves	1146365-1	N/C	0.02
13	Inserts and Seals	1146659-19, 1146913-1	B, N/C	0.05
14	Washers	1146613-1	N/C	0.01
15	Molding Compound	MXC 313		0.22
16				
17	Fin Assembly			(0.60)
18	Fin Blades	1146210-1	A	0.48
19	Pins	1146056-1	N/C	0.02
20	Piston	9220783	GFM	0.02
21	Crosshead and Nuts	456909, MS 20365-1032	GFM	0.07
22	Retainer	1253131	GFM	0.01
23				
24	Igniter Assembly	1146693-1	A	(0.02)
25				
26	Lockwire and O-Ring	457822, 1146924	GFM	(0.03)
27				
28	TOTAL INERTS			(4.64)
29				
30	Propellant			(8.05)
31	Chamber	ANB-3241-2		8.03
32	Igniter	BPN		0.02
33				
34	TOTAL MOTOR	1146668-1	A	(12.69)

Improved 2.75-in. FFAR Detail Weight Statement

Figure 2

Page 3

UNCLASSIFIED



# UNCLASSIFIED

Report AFRPL-TR-69-90, Appendix C

<u>Lot Number</u>	<u>Pre-fire Condition</u>			<u>Post-fire Condition</u>	
	<u>Inert</u>	<u>Prop.</u>	<u>Total Motor**</u>	<u>Total Motor**</u>	<u>Inerts Exp.</u>
Lot 6 Weight	4.12	8.00	12.12	3.88	0.24
Range	0.09	0.09	0.02	0.08	0.09
Lot 7 Weight	4.06	8.06	12.12	***	***
Range	***	0.11	***	***	***
Calculated	4.15	8.03	12.18	3.92	0.23

\* All weights expressed in lb.

\*\* All weights are less fin blades, pins and retainer (0.51 lb).

\*\*\* No data available at this time.

Improved 2.75-in. FFAR Actual Weight Data\*

Figure 3

Page 4

# UNCLASSIFIED

**UNCLASSIFIED**

**Report AFRPL-TR-69-90**

**APPENDIX D**

**ENVIRONMENTAL TEST**

**UNCLASSIFIED**

# UNCLASSIFIED

## Report AFRPL-TR-69-90, Appendix D

### 1.0 GENERAL

- 1.1 Purpose of Tests: The purpose of the test program was to subject 20 FFAR rocket motors to temperature cycling, humidity, vibration and altitude cycling, in accordance with the specification listed below.
- 1.2 Manufacturer: Aerojet-General Corporation  
Propulsion Division  
Sacramento, California
- 1.3 Manufacturer's Designation: 2.75-in. FFAR PFRT Rocket Motor,  
Part Number 1146668
- 1.4 Specification Reference: Aerojet Test Specification TDS-00091,  
MIL-C-45662.
- 1.5 Government Contract: F 04-611-67-C-0114
- 1.6 Security Classification: Unclassified
- 1.7 Quantity of Items Tested: 40
- 1.8 Testing Completed: 15 August 1968
- 1.9 Testing Conducted by: Ogden Technology Laboratories, Inc.  
Remote Test Facility  
Beaumont, California
- 1.10 Disposition of Specimens: Returned to Aerojet-General Corporation  
Sacramento, California
- 1.11 Abstract: Forty FFAR rocket motors were subjected to humidity testing. Twenty FFAR rocket motors were subjected to temperature cycling, vibration and altitude cycling.

UNCLASSIFIED

# UNCLASSIFIED

Report AFRPL-TR-69-90, Appendix D

## 2.0 TEST DATA

### 2.1 Ambient Conditions

Unless otherwise stated in the body of this report, all tests were conducted at an ambient temperature of  $70 \pm 20^\circ\text{F}$ , a relative humidity of less than 90% and a barometric pressure of  $30 \pm 2$  in. of mercury (Hg).

### 2.2 Tolerances on Test Conditions and Instrumentation

During the tests as described in this report, all tolerances on test conditions and instrumentation did not exceed the following parameters:

Temperature	$\pm 5^\circ\text{F}$
Relative humidity	$\pm 5\%$
Vibration (g)	$\pm 5\%$
Frequency	$\pm 10\%$ or 1 cycle, whichever is greatest
Pressure	$\pm 5\%$
Time	$\pm 1\%$ or 10 sec

### 2.3 Test Equipment

All test equipment used in the performance of the tests described in this report were calibrated in accordance with the standard calibration practices of Ogden Technology Laboratories, Inc. Calibration is conducted at intervals sufficient to assure continued accuracy and repeatability of recorded measurements. Calibration standards are traceable to the National Bureau of Standards and certification and calibration records are maintained on file for study by authorized personnel upon request.

All vibration and shock equipment is calibrated immediately before each successive use, as a complete system, in addition to the regularly scheduled test calibrations.

### 2.4 Axis Designation

Longitudinal: Parallel with the longitudinal axis of the specimen.  
Transverse: Perpendicular to the longitudinal axis.

### 2.5 Visual Examination

Prior to and following each test the FFAR motors underwent a visual examination in which the samples were checked for corrosion, rust or pitting, and any degradation caused by testing.

### 2.6 Test Setup

Typical test setups are shown on Figures 1 through 5.

# UNCLASSIFIED

Report AFRPL-TR-69-90, Appendix D

## 3.0 DISCUSSION OF TESTS

### 3.1 Temperature Cycle

#### 3.1.1 Requirements

Twenty FFAR rocket motors were subjected to the temperature cycling test in accordance with Paragraph 13.3 of the Specification TDS-00091.

#### 3.1.2 Procedure

Prior to start of the temperature cycling test, each of the 20 FFAR rocket motors were visually inspected. These motors were then placed in a pre-conditioned temperature chamber at 150°F and maintained at this temperature for a minimum of 4 hr. Within 5 minutes the motors were transferred to a chamber that was preconditioned at -65°F and maintained for a minimum period of 4 hr. This procedure was continued until all motors had undergone three complete hot and cold cycles.

#### 3.1.3 Results

Following the three temperature cycles a visual examination was performed on all motors. None of the motors showed any visual evidence of external damage or deformation as a result of the temperature cycle test. All motors were X-rayed and the original films were forwarded to Aerojet-General Corporation.

### 3.2 Humidity Test

#### 3.2.1 Requirement

Forty FFAR rocket motors were subjected to the humidity test as specified in Paragraph 13.6 of Specification TDS-00091.

#### 3.2.2 Procedure

Prior to the start of the humidity test 20 FFAR rocket motors were subjected to a visual inspection. The 20 motors were installed in a humidity chamber and the chamber temperature was increased to 120°F at a relative humidity of 95%. This condition was maintained for a minimum period of 360 hr.

#### 3.2.3 Results

The test was stopped on the first 20 motors submitted, by authority of Aerojet-General Corporation. Serial numbers of these motors and the hours of test are tabulated as follows:

<u>Units, Serial Number</u>	<u>Hours</u>
2710, 2718, 2716, 2742, 2726	233
2727, 3109, 3101, 3110, 3106	195
3111, 3117, 3143, 3145, 0902	143
0904, 0905, 0908, 0909, 0911	

UNCLASSIFIED

# UNCLASSIFIED

## Report AFRPL-TR-69-90, Appendix D

An additional 20 samples were submitted and completed the humidity test.

During the post-humidity test visual inspection, the following conditions were found: corrosion on nozzles, pitted paint, oxidation on fins, and corrosion on fin hinge points.

### 3.3 Vibration

#### 3.3.1 Requirements

Twenty FFAR rocket motors were subjected to the temperature and vibration test as specified in Paragraph 13.4 of the Specification TDS-00091.

Group A at +70°F  
Group B at -65°F  
Group C at -65°F  
Group D at +150°F  
Group E at +150°F

The units were grouped as follows:

<u>Group A</u>	<u>Group B</u>	<u>Group C</u>	<u>Group D</u>	<u>Group E</u>
SN 11-31	10-12	10-85	10-88	10-44
11-38	10-77	10-07	10-92	10-48
10-03	11-06	11-11	10-09	10-51
10-33	11-37	11-30	11-21	11-35

#### 3.3.2 Procedure

Prior to the start of the vibration test 20 FFAR rocket motors were subjected to a visual inspection. These motors were then mounted in a vibration fixture, four motors at a time, and subjected to the vibration test.

#### 3.3.3 Results

Following the vibration test none of the 20 motors showed any visible evidence of external damage or deformation as a result of the vibration test.

Following the visual inspection, Groups A, B, C, and D were X-rayed and the original films were submitted to Aerojet-General Corporation.

Group E was shipped to Aerojet-General Corporation prior to X-ray.

### 3.4 Altitude Cycling

#### 3.4.1 Requirements

Twenty FFAR rocket motors were subjected to the altitude cycling in accordance with Paragraph 13.5 of the Specification TDS-00091 at the temperatures listed in Table I.

# UNCLASSIFIED

# UNCLASSIFIED

Report AFRPL-TR-69-90, Appendix D

## 3.4.2 Procedure

Prior to the start of the altitude cycling test, each of the 20 motors was subjected to a visual inspection. These motors were then placed in a temperature chamber and conditioned to the temperatures as tabulated below. Within a 10-minute period the motors were transferred to a preconditioned temperature altitude chamber and subjected to five cycles of test site ambient pressure and 2.1 in. Hg. The time period at each extreme was 30 minutes. The actual pressure change time was a maximum of 5 minutes.

<u>Test Temperature, °F</u>	<u>Group</u>
+70	A
-65	B, C
+150	D, E

## 3.4.3 Results

Following the five altitude cycles all motors were subjected to a visual inspection. None of the motors showed any visible evidence of external damage or deformation as a result of the altitude cycling test.

UNCLASSIFIED

# UNCLASSIFIED

Report AFRPL-TR-69-90, Appendix D



Typical Test Description Temperature Cycling  
Improved 2.75-1.1. Motion Form - 100-10-10

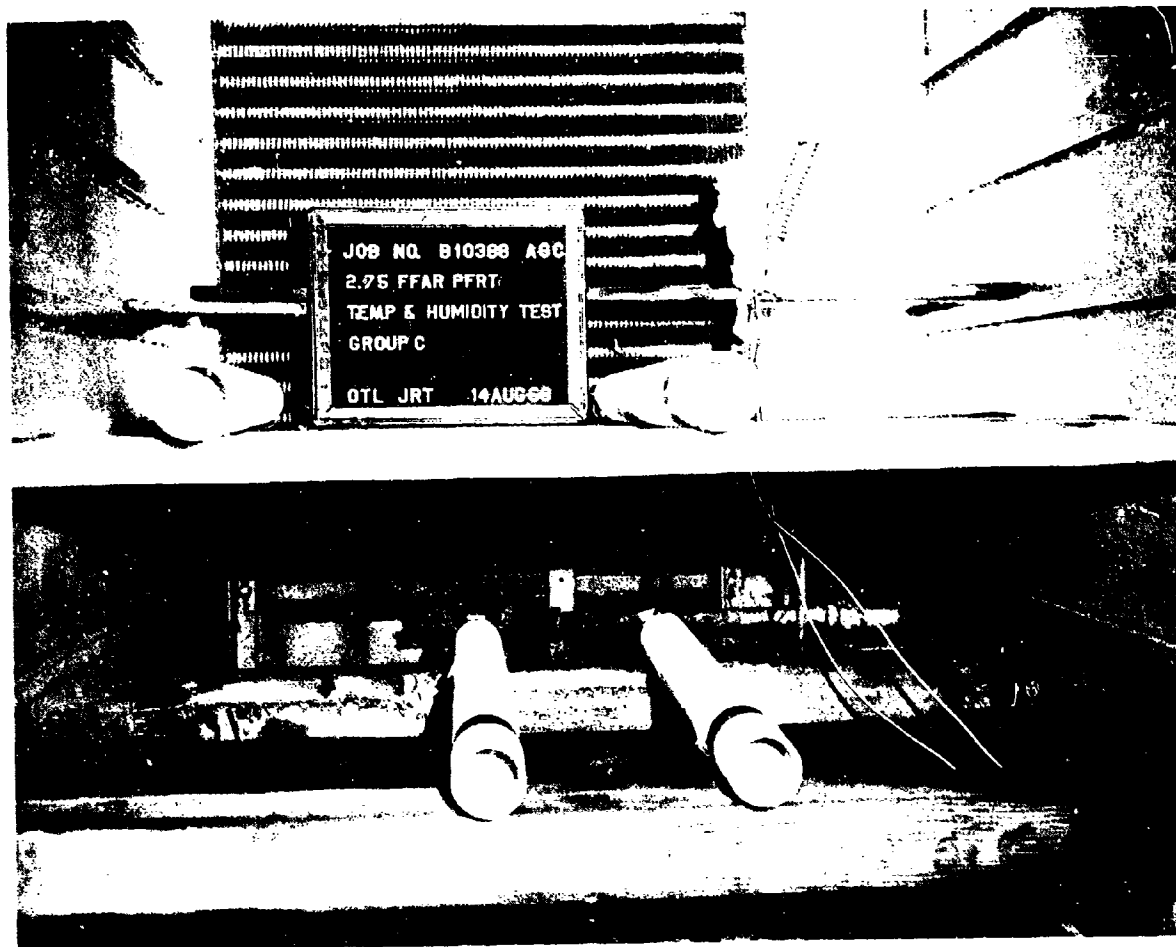
Figure 1  
Page 6

UNCLASSIFIED



UNCLASSIFIED

Report AFRPL-TR-69-90, Appendix D



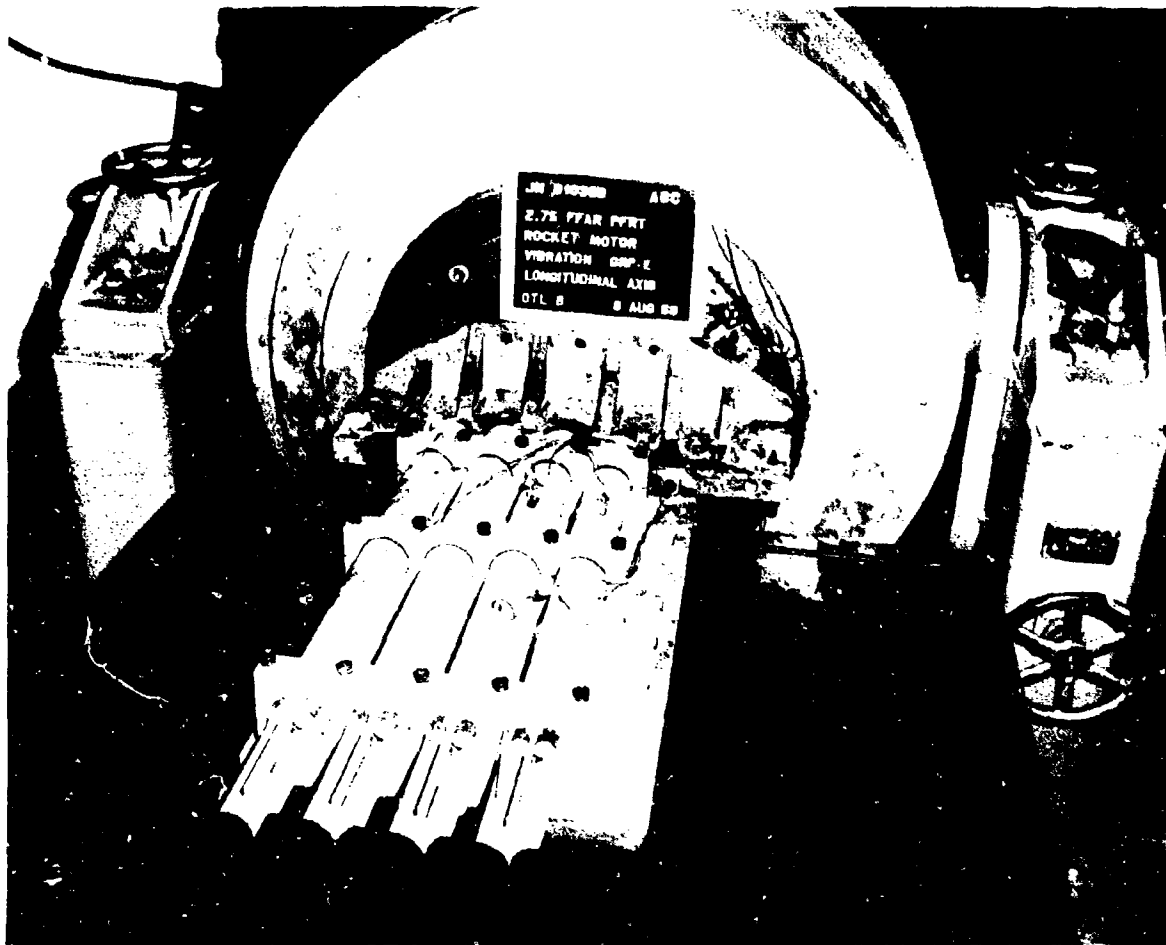
Typical Test Setup for Humidity Testing  
of Improved 2.75-In. Motor

Figure 2  
Page 7

UNCLASSIFIED

UNCLASSIFIED

Report AFRPL-TR-69-90, Appendix D



Typical Test Setup for Launch Direct Vehicle  
on Large and 2.5-In. Motor

Figure 3  
Page 8

UNCLASSIFIED

UNCLASSIFIED

Report AFRPL-TR-69-90, Appendix D



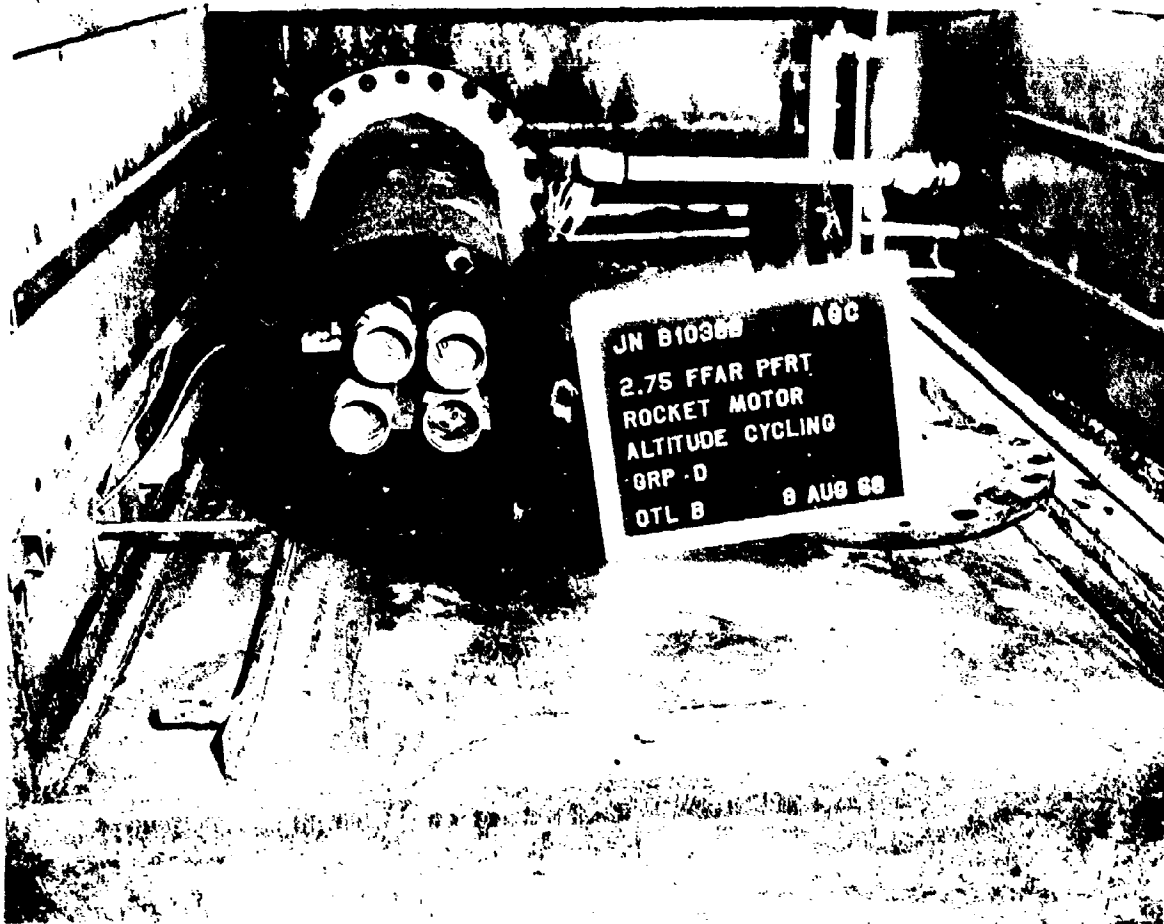
Typical Test Setup for Transverse Vibration  
of Improved 2.75-In. Motor

Figure 4  
Page 9

UNCLASSIFIED

UNCLASSIFIED

Report AFRPL-TR-69-90, Appendix D



2.75 FFAR PFRT Rocket Motor  
Altitude Cycling Test

Figure 5  
Page 10

UNCLASSIFIED